The pressure drag and momentum flux during a cold frontal passage over the Alps

Bertrand Carissimo

The pressure drag and momentum flux during a cold frontal passage over the Alps

by

Bertrand C. Carissimo

A dissertation presented to the
Faculty of Princeton University
in candidacy for the degree of
Doctor of Philosophy

Recommended for acceptance by the
Program in Atmospheric and Oceanic Sciences

October, 1987

Abstract

The strong pressure drag, the momentum flux and the air flow changes occurring during the interaction of a cold front with a meso-scale mountain are investigated using a combination of observations from the Alpine Experiment and theoretical models.

The surface pressure observations are analyzed every three hours to derive the pressure drag and reveal that peak values are reached when tight pressure gradients are located on steep orography. These values would be underestimated by conventional synoptic analyses or coarse resolution numerical models.

The momentum flux above the topography is estimated from aircraft measurements taken during the strong drag events. Compared with the surface pressure drag, the observed momentum fluxes are small. They are in line however with the values computed in this situation by a "wave drag" parameterization. The accuracy of these fluxes is also discussed.

In order to understand these observations, the dynamics of the interaction between a cold front and the mountain is further investigated. Additional observations show that the pressure fall and rise accompanying the front in flat terrain is insufficient to fully account for the pressure drop across the mountain and for the drag magnitudes observed.

A dynamical explanation for the large observed drag during frontal passage is therefore sought using a simple layer model. Although this model is somewhat deficient in simulating the prefrontal stage in the interaction, it is capable of reproducing the observed frontal retardation and the drag evolution. This model also shows that a substantial increase in the post-frontal drag can be created by the blocking of cold air if it is strong and remains localized on the upstream slope of the mountain.

An additional series of numerical experiments with a continuously stratified model is performed to compare the air flow over the mountain with and without the presence of a front and the evolution of the front with and without the mountain. The vertical shear in the wind across the front, by its ability to create a secondary frontal circulation interacting with the mountain, is shown to be capable of producing an increase in the prefrontal drag.

Acknowledgements

It is with deep gratitude that I would like to thank Dr. Raymond Pierrehumbert. His continuous support, helpful discussions and constant optimism have made this dissertation possible.

I also would like to thank Drs. Abraham Oort, John McGinley and Isodoro Orlanski for their critical comments and guidance troughout this work and Bruce Wyman for his generous assistance.

It is also a pleasure to acknowledge the help and friendship I have received from other people at the Geophysical Fluid Dynamics Laboratory who have contributed in making my stay a wonderful learning experience.

Finally I would like to extend a special thanks to my familly and friends who provided moral support all along.

Praeses et Curatores Vniuersitatis Princetoniensis
Omnibus has litteras lecturis
Salutem in Domino.

Quandoquidem decet eis qui ad altissimum gradum doctrinae ac disciplinae ascenderint amplissimum gradum academicum deferri ut et praemia suis meritis digna adipiscantur et disciplina ipsa honore augeatur, quando autem

Bertrand C. Carissimo

non tantum in eruditione ingenioque tam praeclare enitet sed in scientia scientiarum ad caelum et oceanum pertinentium tam praecipue eminet ut summos publicos honores probe mereatur: idcirco nos Praeses et Curatores Vniuersitatis Princetoniensis eidem titulum gradumque

Philosophiae Doctoris

tribuimus et singulis iuribus priuilegiis honoribus ad summum gradum quaqua pertinentibus fruendi potestatem detulimus.

Cuius rei haec membrana sigillo nostrae Vniuersitatis rata et nominibus Praesidis et Scribae munita testimonio sit.

Datum Aulae Nassouicae
die XXIV Octobris
Anno Domini MCMLXXXVII

William G. Bowen *Praeses.*

Robert H. Weiss *Scriba.*

Table of Content

General Introduction

The surface drag caused by pressure differences across mountain ranges is one of the two mechanisms by which the atmosphere is dynamically coupled to the solid earth and its importance is comparable to surface friction. The torque created by the zonal component of this pressure drag, important to the general circulation of the atmosphere and commonly referred to as the mountain torque, has been the subject of several studies. For example the recent work of Wahr and Oort (1984), which gives an historical account of previous work, obtained global estimates by analyzing the monthly mean station reports onto an evenly spaced grid of 5º longitude by 2.5 º latitude. It was however pointed out that the data resolution and coverage is insufficient for certain areas, raising the important issue of the contribution of smaller scale orography and its variability on time scales shorter than a month.

On the other hand there is evidence from the Alpine Experiment (ALPEX) of the Global Atmospheric Research Program (GARP), that a particular mesoscale mountain (which incidentally can fit in a grid box of the above analysis!) can create a significant and highly variable pressure drag on the atmosphere in relation to synoptic events. Davies and Phillips (1985) have computed the local north-south component of the drag using an array of microbarograph set up in the central part of the Alps, in the Gotthard pass. Hafner and Smith (1985) have obtained the total drag on the mountain by carefully selecting a few representative stations, estimating the volume of the mountain and applying Archimedes' law in the horizontal.

In Chapter I the total pressure drag during the ALPEX period is obtained by a method similar to that used in the global study of Wahr and Oort (1984) and compared with the previous studies of Hafner and Smith (1985) and Davies and Phillips (1985). Our study provides an independent estimate of the drag which is not specifically designed for the Alps

and is therefore applicable to other regions as well. In addition we will see that it can be easily used for the comparison of numerical models with observations.

The effect of this pressure drag, unlike the effect of surface friction, can be felt at very high levels in the atmosphere through the momentum transport by vertically propagating gravity waves. This potentially important effect is however very difficult to estimate from observations. Up to now the only practical method has been instrumented research aircraft providing in situ measurements. Such studies have been performed for example for the Rocky Mountains by Lilly and Kennedy (1973) and Lilly (1978) and for the Pyrenees by Hoinka (1983) and Cox (1985). In all these studies however the surface pressure drag was not available for comparison. In Chapter II we will exploit the unique design of ALPEX which provided for such a comparison and compute the momentum flux for north-south aircraft flight legs at mid-tropospheric level in the central part of the Alps. The accuracy of the momentum estimates derived from aircraft is limited by the measurements of the vertical velocity as discussed by Lilly and Kennedy (1973). This question will be examined further here based on the intercomparison flight between the three ALPEX aircraft.

The motivation, in the planning of ALPEX, for a better understanding of mountain effects came in part from the recognized deficiencies in the representation of orography in numerical models. This subject has recently received a growing attention following the work of Wallace et al.(1983), geographically linking some of the systematic error in forecasts with the topography. As a result several semi-empirical parameterizations of the effects of small scale, unresolved topographic features have been proposed and used with some beneficial effects: the envelope orography (Wallace et al.,1983) and the wave drag parametrisation (Palmer et al., 1986; Pierrehumbert 1987). To improve these parametrizations requires a broader observational basis which can be provided by the ALPEX data set. As a first step in that direction we will compare and discuss the pressure drag in the observations with a numerical simulation carried out using a high resolution limited area model. In addition the

momentum flux derived from the aircraft observations will also be compared with the values prescribed by the wave drag parameterization under development at the Geophysical Fluid Dynamics Laboratory (Princeton).

So far we have seen the importance of determining the surface pressure drag and the momentum flux from the large scale point of view. However a large fraction of the drag variability is due to a recurring pattern that is observed in relation with the passage of cold fronts over the Alps which is accompanied by increased precipitation on the north side and the formation of a low pressure in the south eventually leading to lee-cyclogenesis over the Gulf of Genoa. The dynamics of the interaction between an approaching cold front and the mountain will therefore be investigated with the primary objective to provide an understanding of the time variation of the pressure drag.

The observed features of the interaction will be reviewed in Chapter III. The drag evolution can be traced to the space-time history of the surface pressure based on microbarograph records. The different stages of the interaction are also illustrated with cross sections through the front , synoptic maps and comparison of upper air temperature and wind time series for the north and south sides of the mountain. An example of isentropic analysis will also be discussed.

In Chapter IV we will continue our investigation of the front-mountain interaction using a simple layer model. Without the mountain, this is the classical model of fronts used for example in the instability studies of Orlanski (1968) and Kasahara and Rao (1972). The interaction of the front with the mountain was previously studied with the same model by Arakawa and Okano (1976) and Davies (1984) but for regimes of limited applicability for the Alps. The pressure drag was not discussed in these investigations. In our model the front is approximated by a material interface between the warm and cold air which is sloping and intersecting the ground forming a surface front. Both analytical and numerical techniques will be used to explore the different regimes of the interaction and to compare them to the

previous studies and the observations. Particular emphasis will be given to the understanding of the observed frontal retardation on the upstream side of the mountain and of the surface pressure drag evolution. Because of the simplicity of this model the drag can easily be related to other features in the flow.

Subsequently a more realistic numerical model is used in Chapter V to examine the influence of continuous stratification and secondary circulations on the interaction. Bannon (1983, 1984) and Zehnder (1986) have looked at frontogenesis over topography in the quasi- or semi- geostrophic limit, an approximation which is not appropriate for the Alps because the Rossby number is greater than one. The more general problem of frontogenesis over topography involves the horizontal flow field set up by the mountain which is inherently three dimensional (McGinley, 1982) and poorly understood at present. Instead of frontogenesis we will consider the interaction with a fully developed front which is quasi-stationary in the absence of the mountain, as in the study by Orlanski and Ross (1977). The case of uniform flow over the mountain has been discussed using the same model by Pierrehumbert and Wyman (1985). In the presence of vertical shear in the wind component across the front (U) a secondary circulation develops that tends to weaken the flow ahead of the front and strengthen it behind it. This circulation can play an important role in the interaction with the mountain and it is investigated in considerable detail. As before particular attention is given to the evolution of surface pressure and the underlying dynamics. As opposed to the simple model of Chapter IV, this model supports vertically propagating gravity waves and the momentum flux will be compared with the observations for cases with and without front.

Chapter I: The observed pressure drag on the Alps

1. INTRODUCTION

The determination of the mountain drag force on the atmosphere was among the main objectives of the Alpine Experiment (ALPEX) (see Kuettner, 1986). The experiment design included several sections across the topography, instrumented with microbarographs and accompanied, in some cases, by overhead flights by research aircrafts.

Davies and Phillips (1985) have computed the local pressure drag across the Gotthard section using high frequency microbarograph surface pressure data. A notable feature in their time series is the strong drag (>5Pa), reversing in 12 to 24 hours, in coincidence with frontal passage and cyclogenesis over the Alps. They also find that the drag across the section is well correlated with the pressure difference between Stuttgart, on the North side, and Milano, on the South side, although the magnitude of the drag corresponding to a linear pressure gradient between these two stations is much too small. The large drag is due to the localization of the presssure drop within the Alpine inner region, giving rise to large presssure gradients that will certainly be underestimated by synoptic analyses.

These extremely strong values and rapid reversal of the drag represent a good test of adequate representation of topography in numerical simulations. They have been used by Tibaldi and Dell'Osso (1986) who showed that the model resolution is an important factor to reproduce the drag but also that the use of an envelope orography can lead to an overestimate of its magnitude.

A different method was used by Hafner and Smith (1985) to compute the pressure drag vector caused by the entire Alpine range. Their method is based on a division of the Alps into subregions both in the horizontal and vertical directions. On each of these

subregions Archimedes' law is applied in the horizontal direction, requiring an estimate of the topography volume and a locally constant pressure gradient. Strong variations, both in magnitude and direction, are found in relation with synoptic events in a manner consistent with the results of Davies and Phillips.

In this chapter we first present an evaluation of the drag vector due to the entire Alpine range, for the ALPEX period, using all the reported surface pressure data. The values of the drag we obtain are compared with those of Davies and Phillips (1985) who used only microbarograph data and those of Hafner and Smith (1985) who used only surface pressure data from thirteen carefully selected stations.

In section 2 we present the method of estimating the drag. Maps of analyzed pressure, obtained as an intermediate step, are discussed. The drag time series is presented in section 3 and a comparison with other studies follow. A composite of the strong drag events occuring in March is constructed in section 4. In section 5 we examine the influence of resolution upon the estimated drag and in section 6 we discuss the diurnal variations that are found in the time series. In section 7 we present a comparison of analysed drag with a case of numerical simulation, which is followed in section 8 by a summary of our results.

2. PRINCIPLE OF PRESSURE DRAG EVALUATION

2.1 Method:

The total force on an immersed body is composed of contributions from the tangential stress, at the body surface, and from the normal stress (Batchelor, 1967). The contribution from the tangential stress, the frictional drag, will not be considered further here. In some applications the total force due to the normal stress is further divided into different contributions such as the drag and lift in aerodynamics. Given the complex situations found

in mountain meteorology we will not attempt to separate its different contributions, but rather consider it as one force and we will refer to its horizontal component as the pressure drag (although in some cases the terminology of lift might be more appropriate!):

$$\mathbf{F} = \int_S p\,\mathbf{n}\,d\sigma \qquad \text{(I.1.a)}$$

$$\mathbf{D} = -\mathbf{F}_H = -\int_S p\,\nabla h\,dx\,dy \qquad \text{(I.1.b)}$$

where:

F is the total force acting on the mountain,

D is the drag acting on the atmosphere.

p is the surface pressure

h is the mountain height

n is the vector normal to the surface element $d\sigma$

S is the limited domain of integration

Instead of following Hafner and Smith (1985) who transformed this integral in order to further simplify it by assuming a constant gradient, we directly compute this integral from data. We therefore need an estimate of the fields of surface pressure and topography gradient. We next describe how these quantities are obtained.

2.2 Surface pressure analysis:

The surface pressure cannot be analysed directly because its horizontal variation depends not only on the horizontal variation of the pressure field but also on the horizontal variation of the topography. A truly rigorous evaluation would require a three dimensional analysis of the pressure field, in order to determine its value at the surface, which in turn would require the use of upper air soundings which are clearly insufficient in number to adequately resolve the Alps (Richner, 1986).

Instead we follow a method inspired by Wahr and Oort (1984) which requires only the surface pressure data: p(x,y,h(x,y),t). The scheme consists of removing the time and domain averaged pressure P(h(x,y)) at each station before doing the analysis on the resulting deviation pressure p'(x,y,t) (= p - P). This procedure amounts to approximating the local vertical pressure gradient by the known average pressure gradient during the vertical interpolation. For simplicity in this study we have replaced the average pressure (P) by the standard atmospheric pressure.

The deviation pressure (p') is analysed on a 0.5 º grid in the domain 5E-16E by 41N-49N. The analysis procedure we have used is described by Barnes (1973) and is designed to accelerate the convergence of schemes of the type developped by Cressman and minimize the noise created by an irregular data distribution.

In this method the reported pressures are first reduced, if necessary, to station pressure using a lapse rate of 6.5K/km. As all Alpine countries have different reduction methods (LAPETH, 1986), this procedure might introduce errors. In general, however, the reported level is usually very close to the station level. For example, sea level pressure is reported only for low altitude stations whereas mountainous stations report surface pressure or geopotential height for the nearest standard level, therefore minimizing the reduction error.

The limited domain of this study introduces difficulties compared with the global study by Wahr and Oort (1984). If the boundaries were all at the same level (as in a periodic domain) then the contribution from the average pressure (a function of z only) would be zero, and the drag computed from the deviation (p') or surface pressure (p) would be the same. However, because the northern side of the Alps is higher than the southern side, the drag due to the average pressure, which physically corresponds to the horizontal component of the force resulting from the weight of the atmosphere, is not zero because the domain is not flat on average. Its value is very large for our domain: the boundary heights typically differ by

300 m for a domain size of 600 km. The average slope is therefore 5. 10^{-4} and gives a drag of approximately 50 Pa per unit area. This is a very large but constant value that depends solely on the geometrical characteristics of the domain.

Hafner and Smith (1985) avoided a similar problem by defining a sloping base for the Alps that was not taken into account for their volume computation whereas Davies and Phillips (1985) caried out the integration for heights greater than 400m.

In order to investigate the effect of resolution on the drag values computed, we have repeated the analysis retaining various degrees of details. Our fine analysis retains details on the scale of the average distance between surface data points (approximately R=50 km). This analysis is relatively noisy due to non uniform data distribution. A coarse analysis which retains details on the scale of R=200 km will be used to investigate the effect of resolution.

Figure I.1. a to c show examples of the analysis for March 4-5,1982 , corresponding to the passage of a cold front. On March 4 at 00 GMT and March 5 at 00 GMT the very strong pressure gradients can be seen on the topography and will give rise to very high drag values for these two times. These gradients have completely reversed in 24h.

By contrast the situation on March 4 at 12 GMT shows almost no pressure gradient accross the topography and will therefore lead to weak drag. This particular sequence, with these tight pressure gradients located on the topography, is reproduced in all cases of frontal passage during the two months of ALPEX. They can be compared with other observations of orographically perturbed pressure: Smith (1981), Hoinka (1985) and Steinacker (1981).

In Fig. I.1.d the NMC analysis of sea level pressure for March 5, 00 GMT is shown for comparison. Due to its low resolution compared to the present analysis it is unable to reproduce the tight gradients above the topography.

2.3 Topography gradients:

The topography we use is the high resolution Navy topography (10'*10') , smoothed

to the same resolution as the analysed pressure fields. The gradients are obtained directly from the topography by convolution with the derivative of the filter function.

Figure I.2 shows an East-West cross section at 46º N for the topography at the different resolutions used. There is a sharp decrease in maximum height and magnitude of the gradients for the topography as resolution is decreased.

3. DISCUSSION OF RESULTS

Using the surface pressure and topography gradients obtained as described above we compute the drag vector using Eq. I.1 The time series for the magnitude and direction of this drag vector are presented in Figure I.3 for the entire ALPEX Special Observing Period of March and April 1982. The convention used for the direction of the drag is the same as the one used for the wind direction. For example a direction of 90º corresponds to an east to west drag acting on the atmosphere.

Davies and Phillips (1985) present a detailed summary for the weather events in March and April 1982, reproduced here in Fig. I.3.c, which shows that there is a strong correlation between drag variations and the occurence of synoptic events. The same correlation exists in the present study and we will only give a brief account of the sequence of weather events during the period to illustrate this fact. For a more complete review the reader is refered to the two work cited above and also to Buzzi, 1986.

Three different periods, characterized by a persistence of the large scale weather pattern, were identified:

- A first period (March 1-21), characterized by a baroclinically unstable westerly flow in which a series of cyclonic disturbances moved towards Europe. The associated frontal systems crossed the Alpine region from NW to SE and as many as six cases of lee cyclogenesis occured during this period (March 2, 4-5, 11, 13, 18, 20-21).

- A second period (22 March - 7 April) of transition with weaker and more variable wind that was not characterized by a persitent large scale weather pattern.

- A third period (8-30 April) characterized by a typical Euro-Atlantic blocking pattern with the blocking anticyclone located near Ireland. The flow in the proximity of the Alps came from a direction between NW and E. The blocking anticyclone retreated slightly to the West on three occasions (April 8-9, 24-35, 29-30) and associated outbreaks of polar air reached the Mediterranean causing lee cyclogenesis in the last two cases only, while on April 9th a lee trough developped but did not evolve into cyclogenesis.

These periods in weather events have remarkable analogues in the time series of Figure I.3 The first period is characterized by large drag values, important and simultaneous variations of drag magnitude and direction in close correspondence with the synoptic events mentioned above. A composite of these strong drag events will be presented in Section 4. In the second period, the transition period, the drag is weaker than in the first period, but variations in the direction are still important although more gentle. The third period is characterized by weak drag values, exept during the temporary disruption of the blocking pattern already mentionned . The drag direction is fairly constant throughout this third period.

Another notable feature of these drag time series is the diurnal oscillation in the magnitude, that can best be seen when the drag is weak in April, but still modulates the entire time series. A similar diurnal oscillation was also observed by Davies and Phillips for the Gotthard section and is discussed further in Section 6.

The largest drag occurs on March 2 , 11 and April 29 with values close to 12.5 10^{11} N. Only slightly smaller peaks occur on March 5, 16, 19 and april 9. These values are substantially larger than those of Hafner and Smith who reported maximum drag values of 7.7 10^{11} N on March 5 and 8.4 10^{11} N on March 10 for a domain approximately the same size, including the Alps. In order to compare our values with those of Davies and

Phillips we need an estimate of the drag per unit area. The area choosen for the comparison is crutial and, in order to be consistent, we will consider only the area of our domain which is higher than 500m , corresponding approximately to the base level of Davies and Phillips. This area is 3.0 10^{11} m^2 (as compared with 5.9 10^{11} m^2 for the entire domain) wich leads to a drag per unit area of 4.2 Pa, compared with values as high as 7.5 Pa for the Gotthard section. If this discrepancy is real it indicates that an estimate based on the value in the Gotthard section will lead to an overestimate of the peak drag values for the entire mountain range. On the other hand the higher values obtained in Davies and Phillips study could be due to the higher resolution used (27 stations for 400 km). This point is dicussed further in Section 5.

The drag on the Alps is comparable in magnitude to the hemispheric annual average estimated by Wahr and Oort (1984) as can be seen in Fig. I.3.d representing the annual mean mountain torque (1 Hadley ≡ 10^{18} N.m and represent the torque due to a force of approximately 2 10^{11} N at 45º latitude).

4. COMPOSITE OF THE STRONG DRAG EVENTS

In order to emphasize the similarities between the different strong drag events occuring during the first 20 days in March, we have constructed a composite, shown in Figure I.4, based on those cases (March 2, 4-5, 11, 18).

To construct the composite we first locate the minimum drag magnitude during each of the events as our reference time and simply average the drag for a 48h period around it.

Although the peak values are much reduced compared with some particular cases (see Fig. I.3.a) there is still a distinct pattern emerging from the composite. The drag reaches a first maximum in an almost northerly direction, followed by a sharp drop in magnitude (approximately 50%) and accompanied by a rapid rotation to south-easterly direction, in

which the drag magnitude reaches a second maximum, slightly larger than the first. The evolution between the two maxima has taken place in approximately 18h.

This picture of the time evolution is in agreement with the study of Hafner and Smith and is consistent with the signature of the temporal variation of the north-south component only, in the Gotthard pass, obtained by Davies and Phillips. This indicates that this phenomena is not localized in the section.

5. INFLUENCE OF RESOLUTION

In Figure I.5 we compare the drag magnitude obtained in our fine analysis (R=50 km) with the drag obtained in the coarse analysis (R=200 km), for the first eight days in March.

It is apparent in this figure that the strong peak values of the drag are constantly underestimated in the coarse analysis, sometimes by as much as 50%, whereas lower drag values are in better agreement. This also leads to more gentle time evolution. Similar results (not shown) are found for the rest of the period. The drag directions were also compared and are in much better agreement.

This important reduction of the peak values due to smoothing has important implications. First we observe that the topography is strongly affected by smoothing as shown in Figure I.2 , its main scale falling between 50 and 200 km. This is not however sufficient to reduce the drag: if the pressure varies on a scale larger than the scale of the mountain, and is therefore not affected by smoothing, then the drag is approximately equal to the horizontal pressure gradient multiplied by the volume of the mountain, which is conserved during the smoothing. This implies that the drag due to a large scale pressure gradient (>200 km) will not be sensitive to the smoothing of topography. This in turn tells us that the peak drag values are due to pressure variations on a scale on the order of the topographic scale.

This discussion naturally leads us to the question of what would be the drag computed with much higher resolution. In Davies and Phillips study the drag, computed with approximately 15km resolution in the Gottard pass is larger but one can easily argue that it is not representative of the entire mountain range and the comparison is therefore inconclusive.

6. DIURNAL DRAG VARIATIONS:

A composite of the diurnal cycle for the period of April 17 to 24 has been constructed and is shown in Fig. I.6.a. As mentioned above, a similar diurnal cycle, with minimum drag around 00 GMT and maximum drag around 15 GMT, was also found in the one dimensional drag calculation of Davies and Phillips for the Gotthard section. The relative magnitude of this oscillation and the peak drag values found here are consistent with that of Davies and Phillips, shown in Fig. I.6.b.

The additional information we have here on the drag direction (see Fig. I.3.b) indicates that there is no visible diurnal rotation and that the diurnal cycle is mainly in the north- south direction.

Davies and Phillips analysed this diurnal cycle using a Hovmöller diagram of the cross-sectional pressure as a function of time and found that the diurnal cycle in the drag is due primarily to the difference in the amplitude of the diurnal cycle of pressure on the north (0.2 mb) and the south sides(>1 mb) . They argued that this difference in amplitude could be due to differences in the geometry of the valleys that compose the Gotthard pass. In Figure I.7 we show the analysed deviation surface pressure at approximately the time of minimum and maximum drag for two consecutive days in the period of weak synoptic activity in April. Similar to the findings for the Gotthard pass (Davies and Phillips) a north-south asymetry is present in the amplitude of the surface pressure diurnal cycle but it involves the entire Alps and cannot therefore be attributed to a particular valley geometry. It is not clear at present

what are the causes of this asymetry but one possible cause could be the differences in the solar exposure of valleys on the north and south sides. Finally, we should point out that the analysis may be strongly biased toward giving strong diurnal variations as the surface pressure is more often measured in the valleys , which are subject to a stronger diurnal cycle. However this effect by itself is insufficient to explain the relevant magnitudes without the asymetry mentioned above.

7. COMPARISON WITH MODEL DRAG:

It was one of the original goals of ALPEX to use the drag computed from the array of microbarographs, for comparison with drag in numerical prediction models. Such a comparison was initiated by Tibaldi and Dell'Osso (1986) for the model of the ECMWF, using the drag computed by Davies and Phillips (1985).

In this section we present a comparison with the drag computed by the same method as for the observations in the numerical simulation of the cyclogenesis case of March 4-5, 1982 described in Pham (1985). The 36h simulation starts on March 4, 00 GMT and uses the limited area model of the French Weather Bureau, which has a resolution of 35km. A similar comparison could also be easily made with any numerical model in sigma-coordinate, for which the surface pressure is a prognostic variable.

Figure I.8 represents the deviation surface pressure for selected times during the numerical simulation and is directly comparable to Figure I.1 There are remarkable similarities between modeled and observed pressure such as the tight pressure gradient located on the topography that reverses between March 4, 00GMT and March 5, 00 GMT as discussed in Section 3.

Figure I.9 shows the comparison between model and observation fields for the drag magnitude and direction during the 36h period . This is one of the strong drag events

associated with frontal passage and cyclogenesis. We see that the change in drag direction from northerly to southerly is fairly well reproduced by the model and that the agreement is better for stronger drag values. The observed and modeled drag magnitude are almost identical for the first 18h of the simulation although the model drag starts slightly smalller, possibly due to initial smoothing of the pressure field. Thereafter there is an important, almost constant, overestimate of the drag by the model. As yet we have no definitive explanation for this difference and we can only present a few hypotheses in addition to possible model shortcomings. First the difference in resolution between the model (35km) and the observation (50km) might play a role as mentionned in Section 5 and be reflected in the difference in drag . In addition the use of enhanced orography as described by Pham (1985), because it increases the topography volume, might also cause an artificial increase the drag in the model similar to that reported by Tibaldi and Dell'Osso (1986).

8. SUMMARY:

The mountain pressure drag has been computed using all the reported surface pressure data in a limited domain including the Alps.

The pressure analysis has been performed using a deviation surface pressure which corresponds, for each station, to the difference between the surface pressure and the standard pressure at the surface. Therefore the computed drag differs from the actual drag by a constant value that represents the horizontal component of the force resulting from the weight of the atmosphere because the domain is not flat on average.

As also shown by previous studies, the drag time series is strongly correlated with the synoptic events, in particular with frontal passage and cyclogenesis. Our drag values are somewhat larger than those reported by Hafner and Smith (1985) for a domain aproximately the same size but they are smaller than the values of Davies and Phillips (1985)for the

Gotthard section if they are assumed to be representative for the fraction of our domain above 500m. These discrepancies might be attributed to differences in resolution as indicated by the important decrease in peak values of the drag when the resolution is decreased.

An important diurnal cycle, with minimum around 00 GMT and maximum around 15 GMT, is found in the magnitude of the drag during the period of weak synoptic activity in mid-April. The direction of the drag remains meridional during this cycle which is very similar to the one reported by Davies and Phillips (1985) in the Gotthard section, but involves the entire Alps.

Finally a comparison with a high resolution numerical simulation of the March 4-5 cyclogenesis case shows good agreement in the drag evolution. It shows also that the model reproduces the tight pressure gradients observed above the topography.

Figure captions for Chapter I:

Figure I.1: a), b) and c): contour maps of the deviation surface pressure (analysis grid 0.5º; contour interval: 1mb, negative contours are dashed) for the period of 4-5 March 1982. The topography above 1000m is stippled, with higher density stippling above 2000m. Coasts-lines are dotted. d): sea-level pressure on March 5, 00 GMT from the NMC analysis (analysis grid 2.5º; contour interval 4mb).

Figure I.2: Topography cross section at 46º N, from 5ºE to 16ºE, at different resolutions. The vertical plot extends from 0 to 4000m.

Figure I.3.a : Magnitude and direction of the pressure drag for the entire Alpine mountain for the month of March. (with resolution of 50 km)

Figure I.3.b : same as I.3.a but for the month of April.

Figure I.3.c: summary of weather events observed during ALPEX (from Davies and Phillips, 1985)

Figure I.3.d: annual mean mountain torque in Hadleys per 5º latitude (1 Hadley $\equiv 10^{18}$ N.m and represent the torque due to a force of 2. 10^{11} N at 45º latitude) from Wahr and Oort (1984).

Figure I.4: Composite of the drag evolution during frontal passage. Notice the two peaks in the drag evolution and the change of direction.

Figure I.5: Comparison of the drag magnitude obtained with different resolution (R = 50 km and R = 200 km). Peak drag values are reduced by 50 % at low resolution.

Figure I.6: a) composite of the diurnal cycle for the period April 17 to 24, 1982; b) diurnal cycle found by Davies and Phillips (1985).

Figure I.7: Contour maps of deviation surface pressure (contour interval: 1 mb) at the extrema of the drag diurnal cycle for 21 and 22 April, 1982.

Figure I.8: Contour map of deviation surface pressure (contour interval: 1 mb) obtained in the numerical simulation of 4-5 March, 1982. The topography is shown in the top left frame. (these results should be compared with Fig. I.1)

Figure I.9: Comparison of the observed drag (R=50 km) with the drag in the numerical simulation for March 4 to 5, 1982.

a

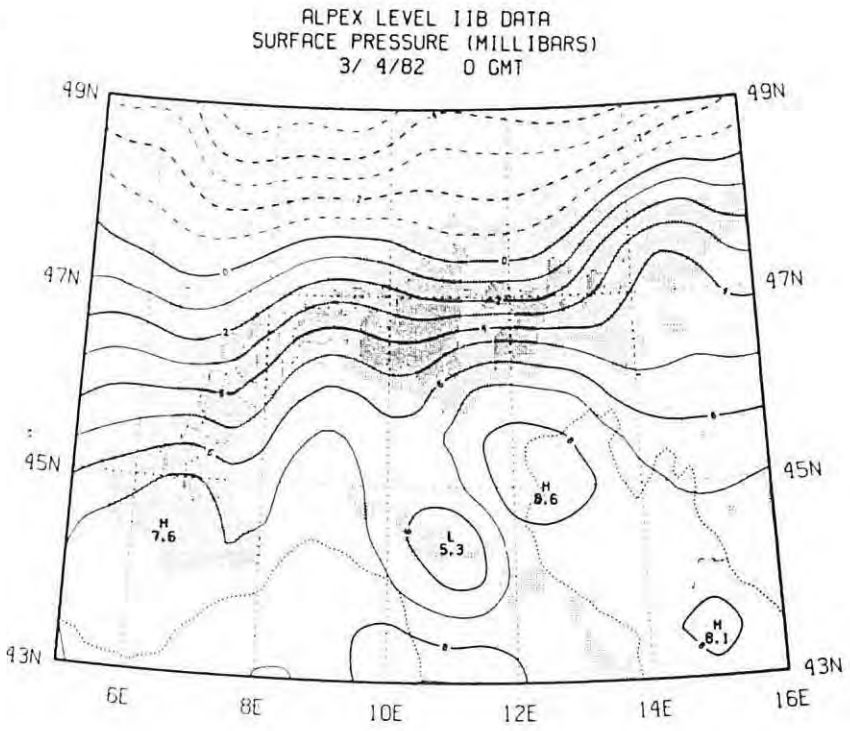

b

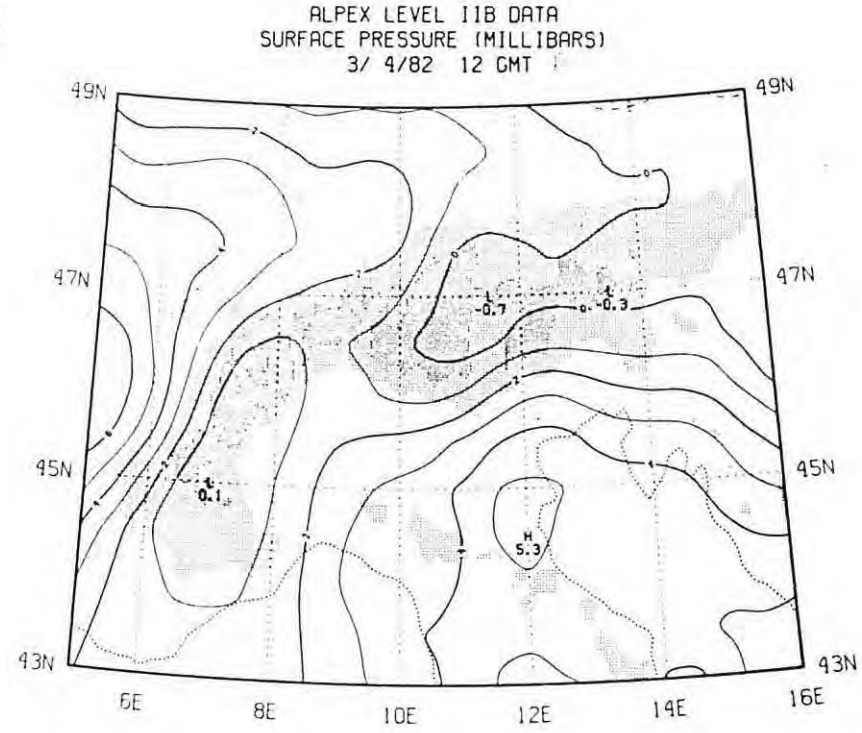

Figure I.1: a), b) and c): contour maps of the deviation surface pressure (analysis grid 0.5º; contour interval: 1mb, negative contours are dashed) for the period of 4-5 March 1982. The topography above 1000m is stippled, with higher density stippling above 2000m. Coasts-lines are dotted. d): sea-level pressure on March 5, 00 GMT from the NMC analysis (analysis grid 2.5º; contour interval 4mb).

c

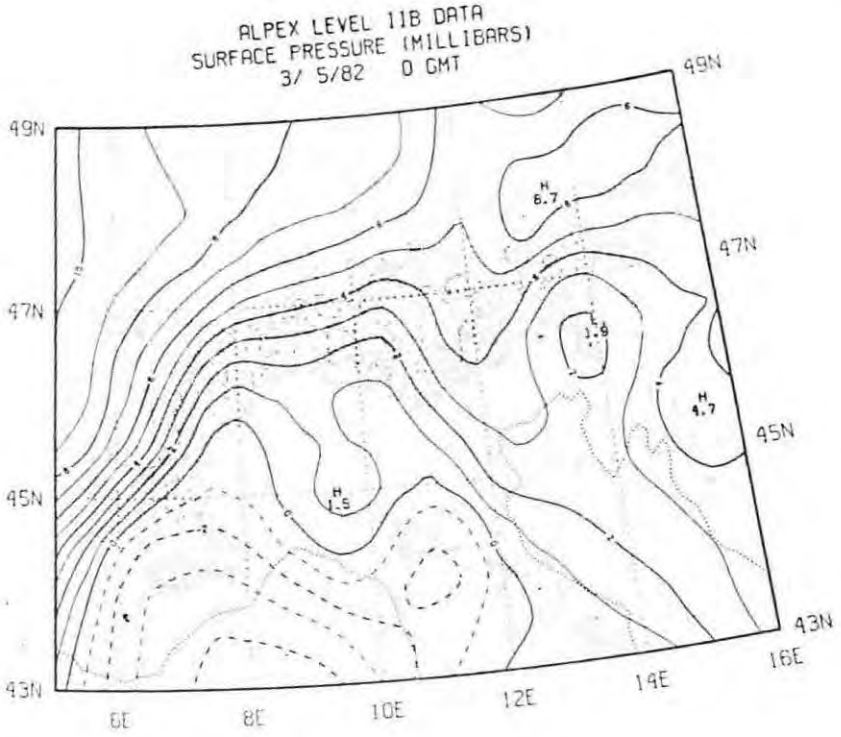

d

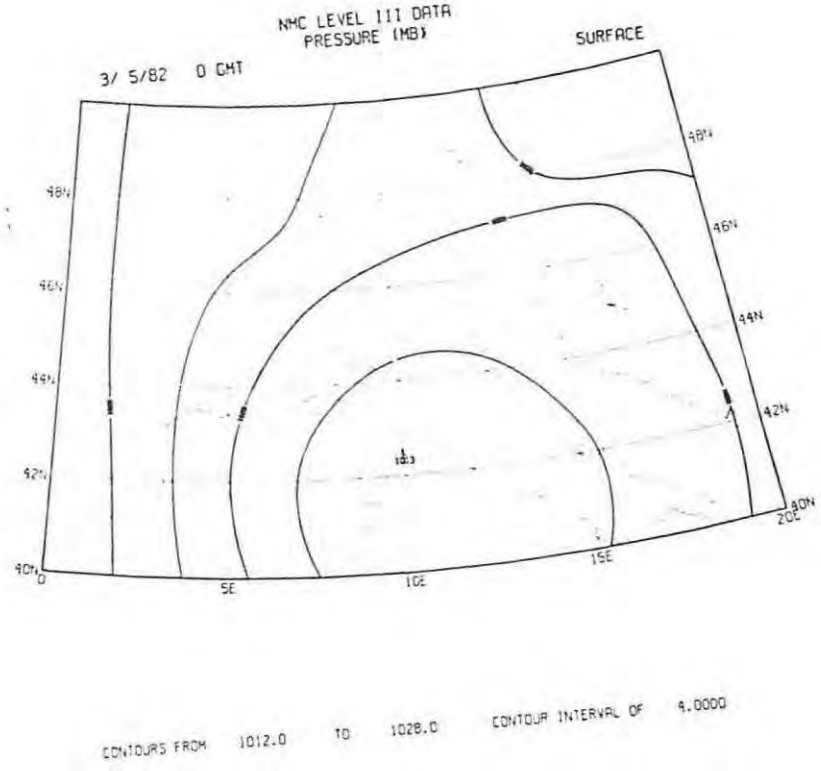

Figure I.1 (continue)

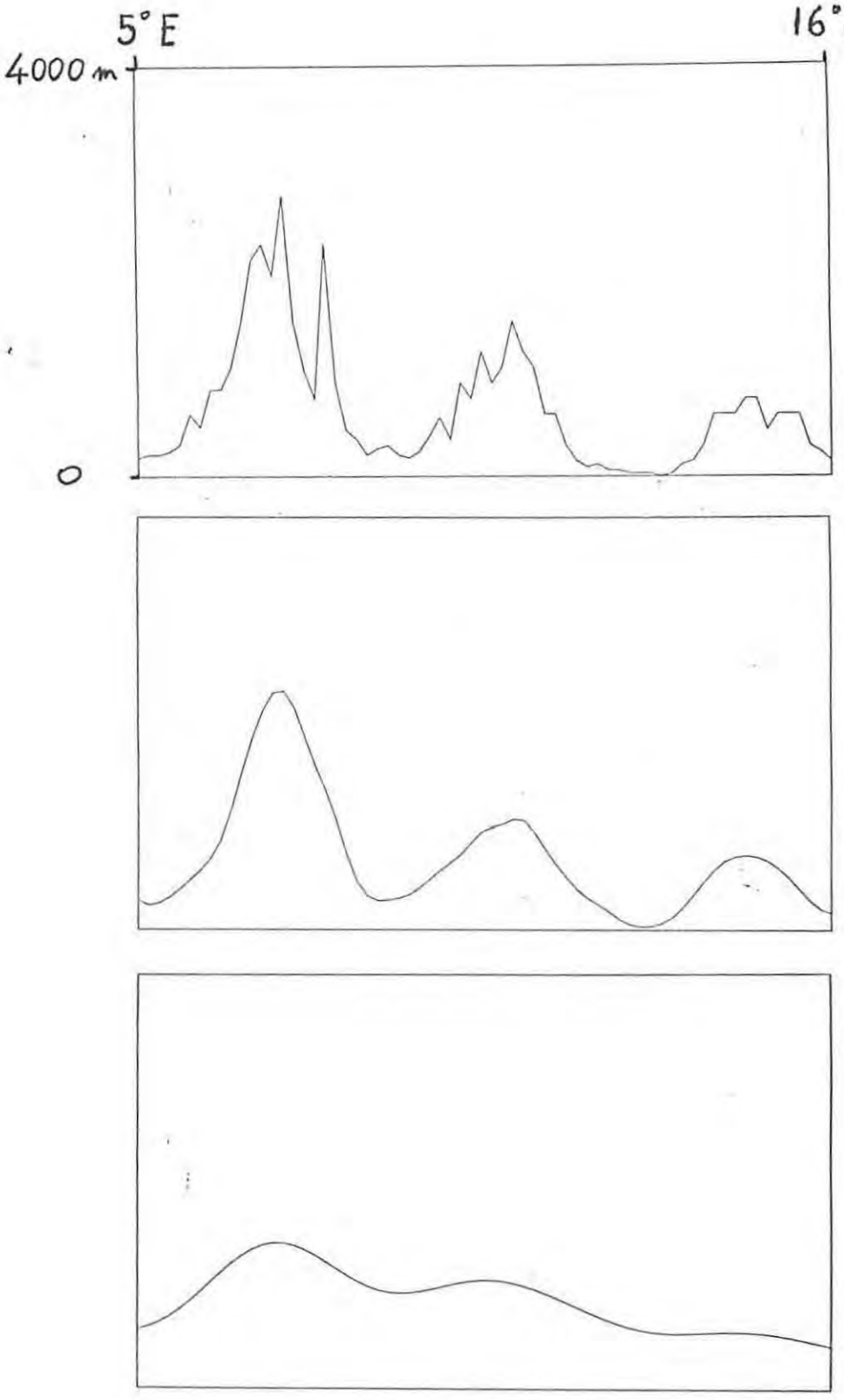

Figure I.2: Topography cross section at 46º N, from 5ºE to 16ºE, at different resolutions. The vertical plot extends from 0 to 4000m.

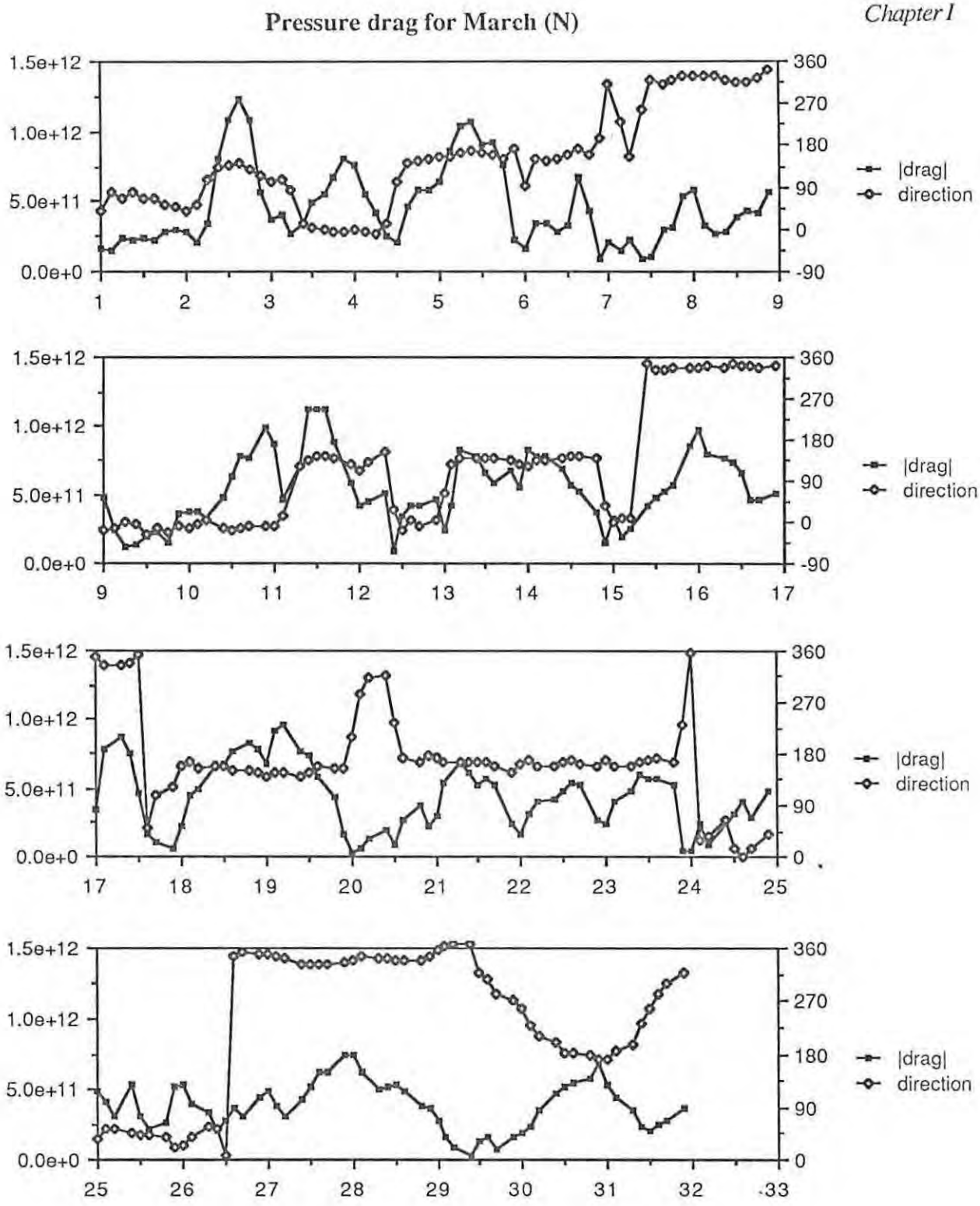

Figure I.3.a : Magnitude and direction of the pressure drag for the entire Alpine mountain for the month of March. (with resolution of 50 km)

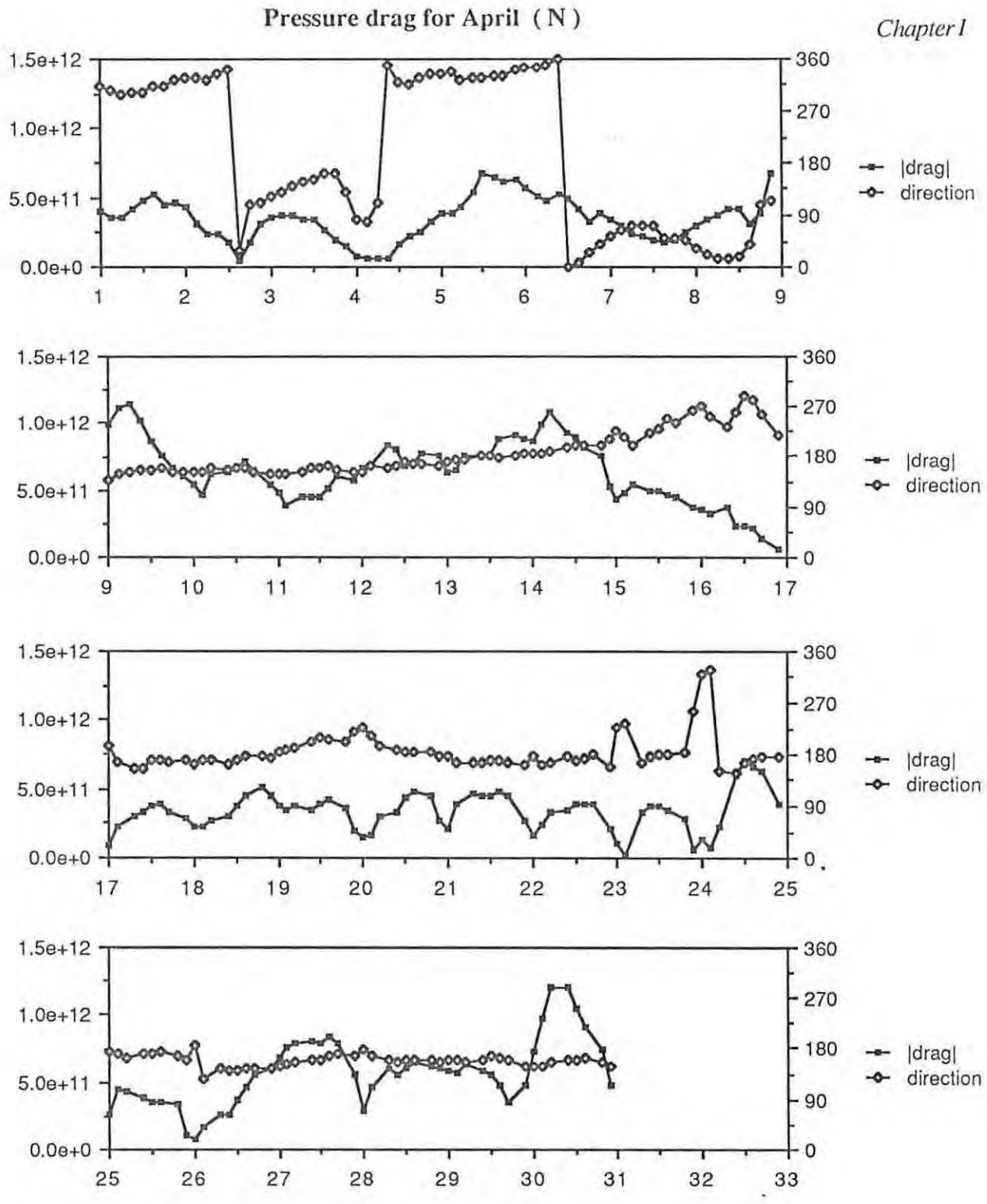

Figure I.3.b : same as I.3.a but for the month of April.

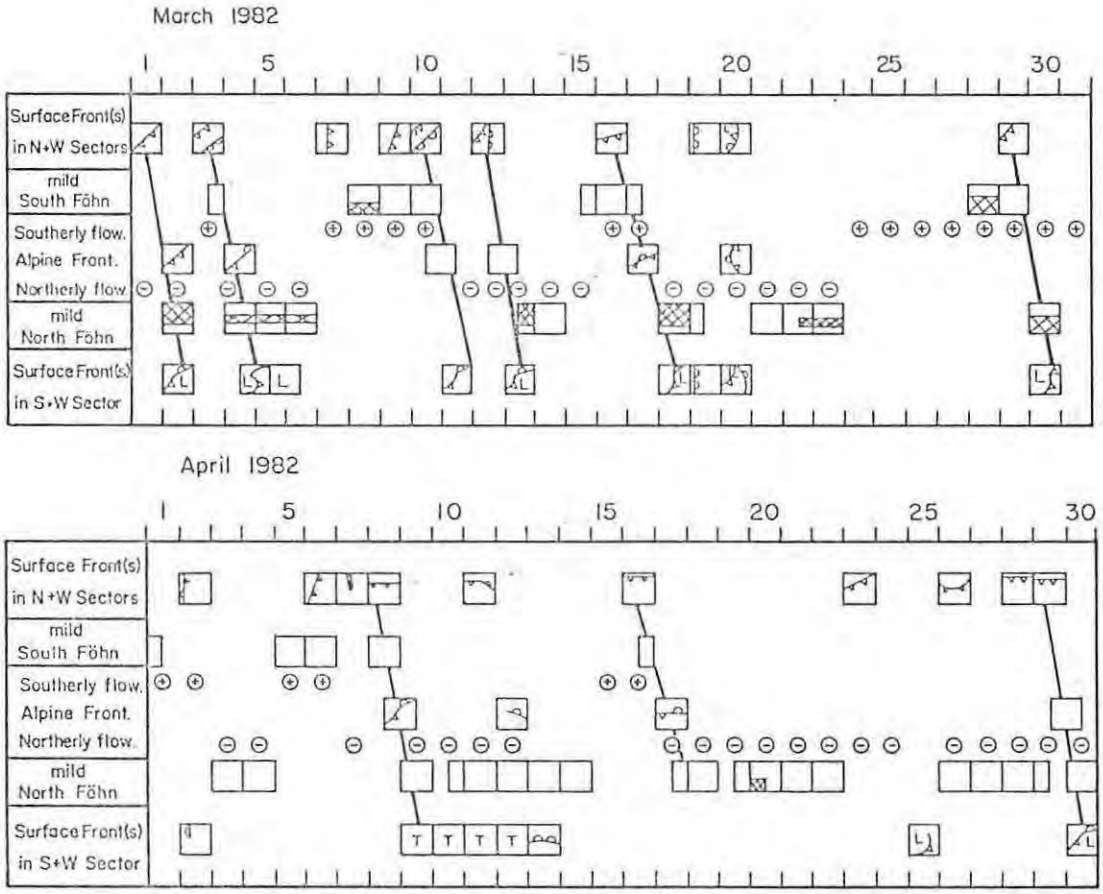

A tabular summary of the chronology of some key flow phenomena related to the pressure drag. The upper, central and lower panels document the significant frontal features that are, respectively, to the west or north of, astride of, or to the west or south of, the alpine ridge. In the lower panel the letters L and T signify lee cyclones and lee troughs. The "mild south-föhn" and "mild north-föhn" categories refer to the existence of appreciable (~2–3 K), not purely diurnal, potential temperature differences across the inner 100 km of the St. Gotthard. The föhnic nature of these categories is borne out by the N–S component of the wind at the 650 mb level above Oberwald indicated by the circle with plus (southerly) and circle with minus (northerly) symbols. The stippled domains indicate the regions of surface rain during mild föhn conditions with the upper, central and lower portions of each individual square corresponding, respectively, to north of, astride of, and south of the Gotthard.

Figure I.3.c: summary of weather events observed during ALPEX (from Davies and Phillips, 1985)

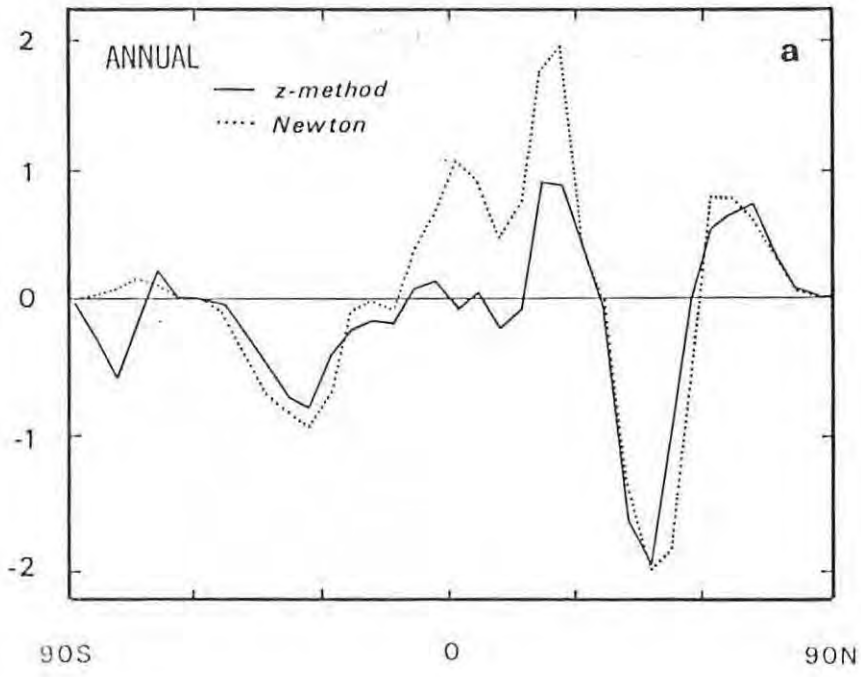

Figure I.3.d: annual mean mountain torque in Hadleys per 5º latitude (1 Hadley ≡ 10^{18} N.m and represent the torque due to a force of 2. 10^{11} N at 45º latitude) from Wahr and Oort (1984).

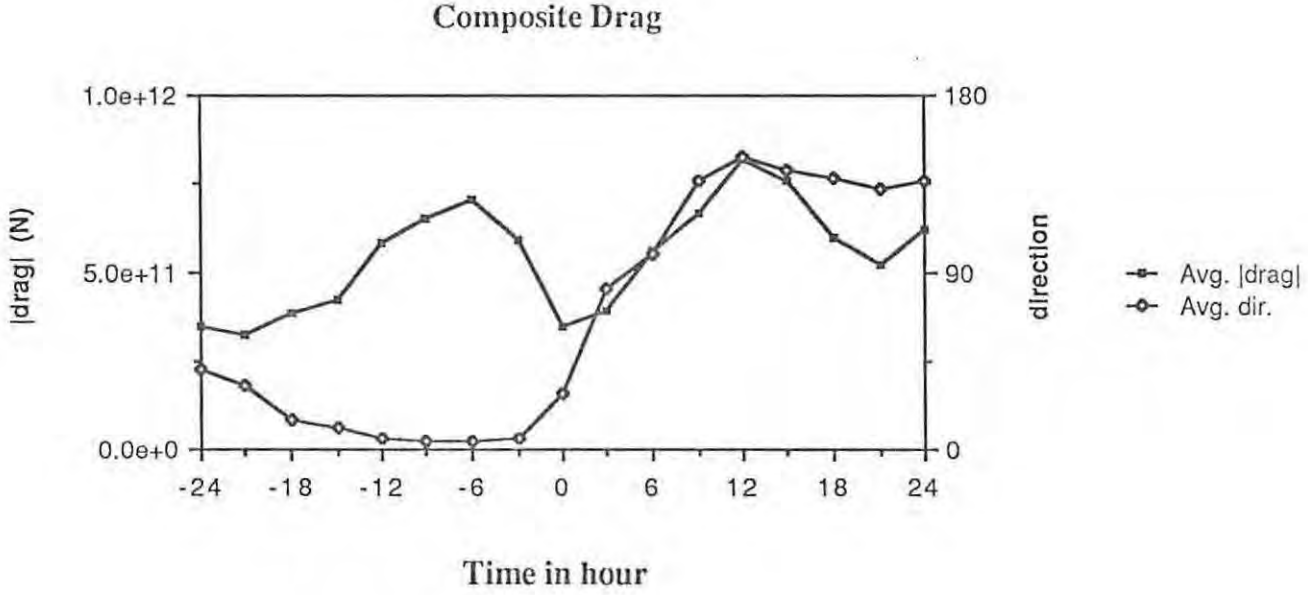

Figure I.4: Composite of the drag evolution during frontal passage. Notice the two peaks in the drag evolution and the change of direction.

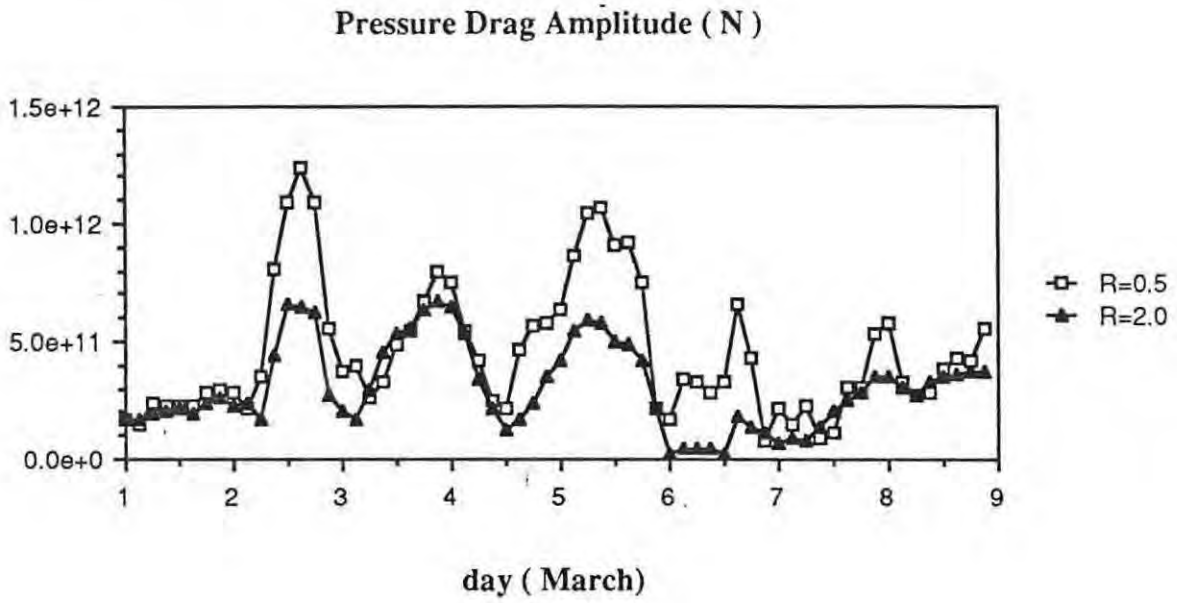

Figure I.5: Comparison of the drag magnitude obtained with different resolution (R = 50 km and R = 200 km). Peak drag values are reduced by 50 % at low resolution.

a

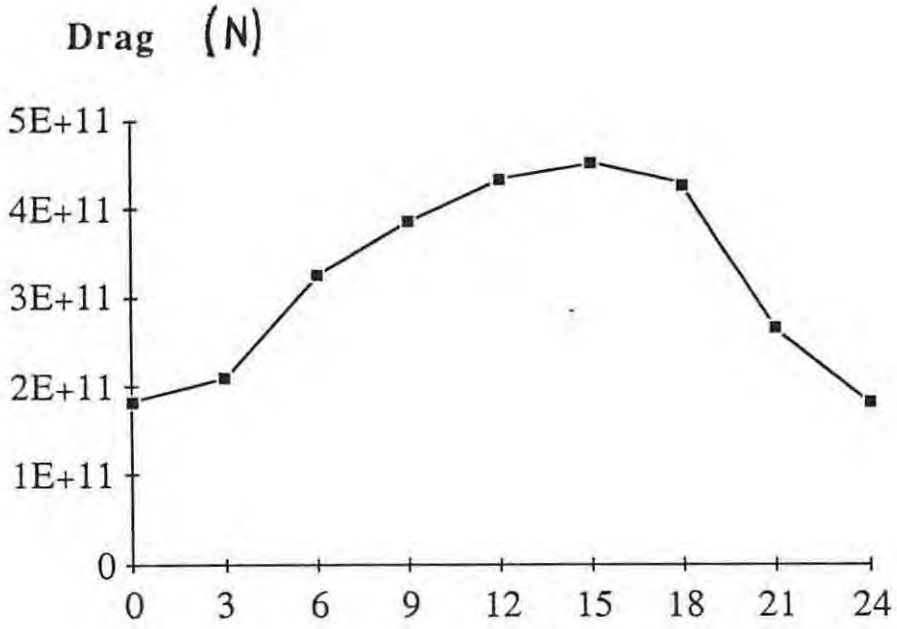

b

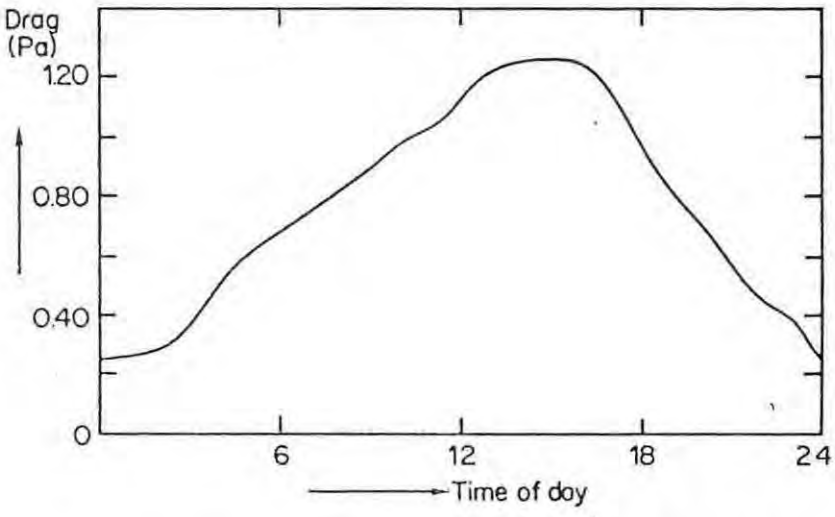

The diurnal cycle in the $\overline{(D/\Delta)}$ pressure drag values (see text for definition).

Figure I.6: a) composite of the diurnal cycle for the period April 17 to 24; b) diurnal cycle found by Davies and Phillips (1985).

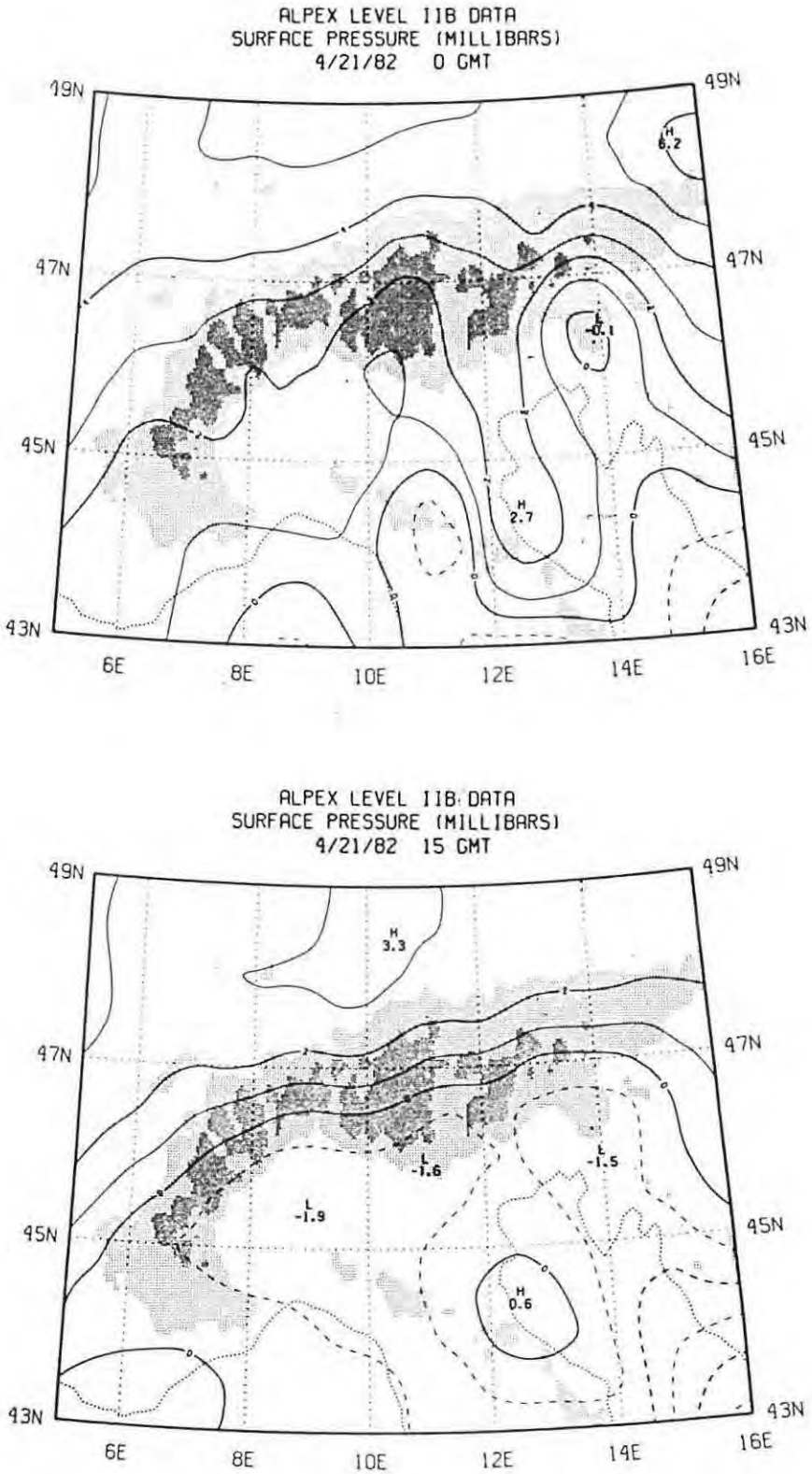

Figure I.7: Contour maps of deviation surface pressure (contour interval: 1 mb) at the extremums of the drag diurnal cycle for 21 and 22 April.

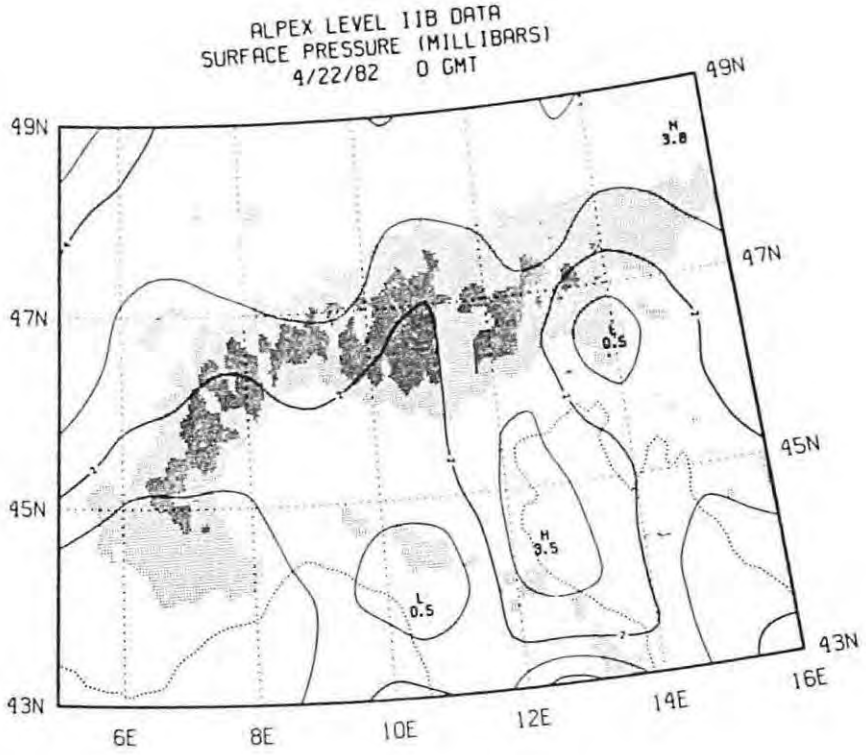

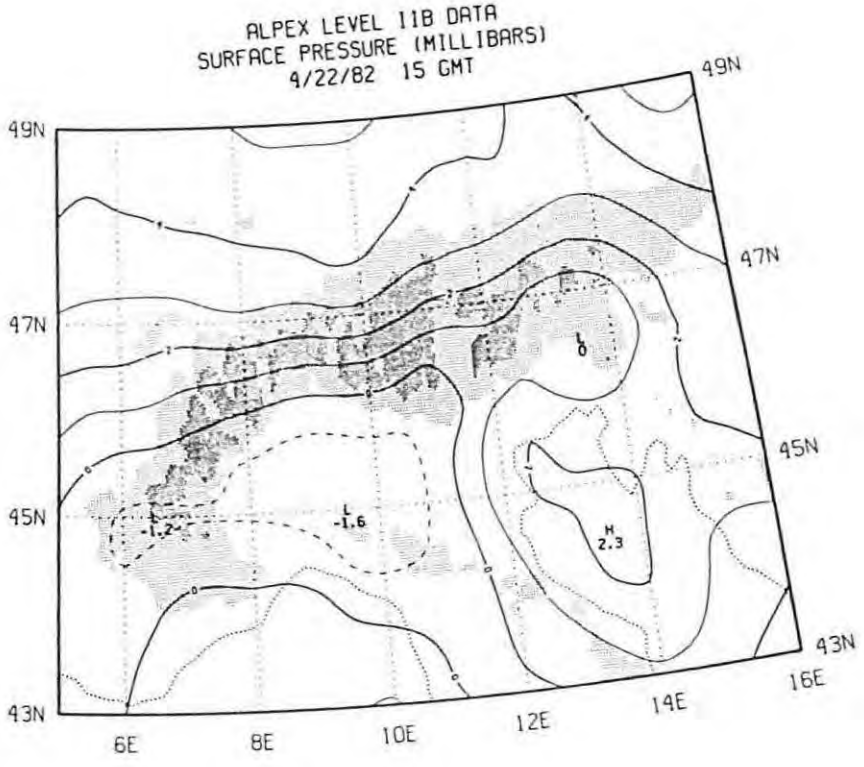

Figure I.7 (continue)

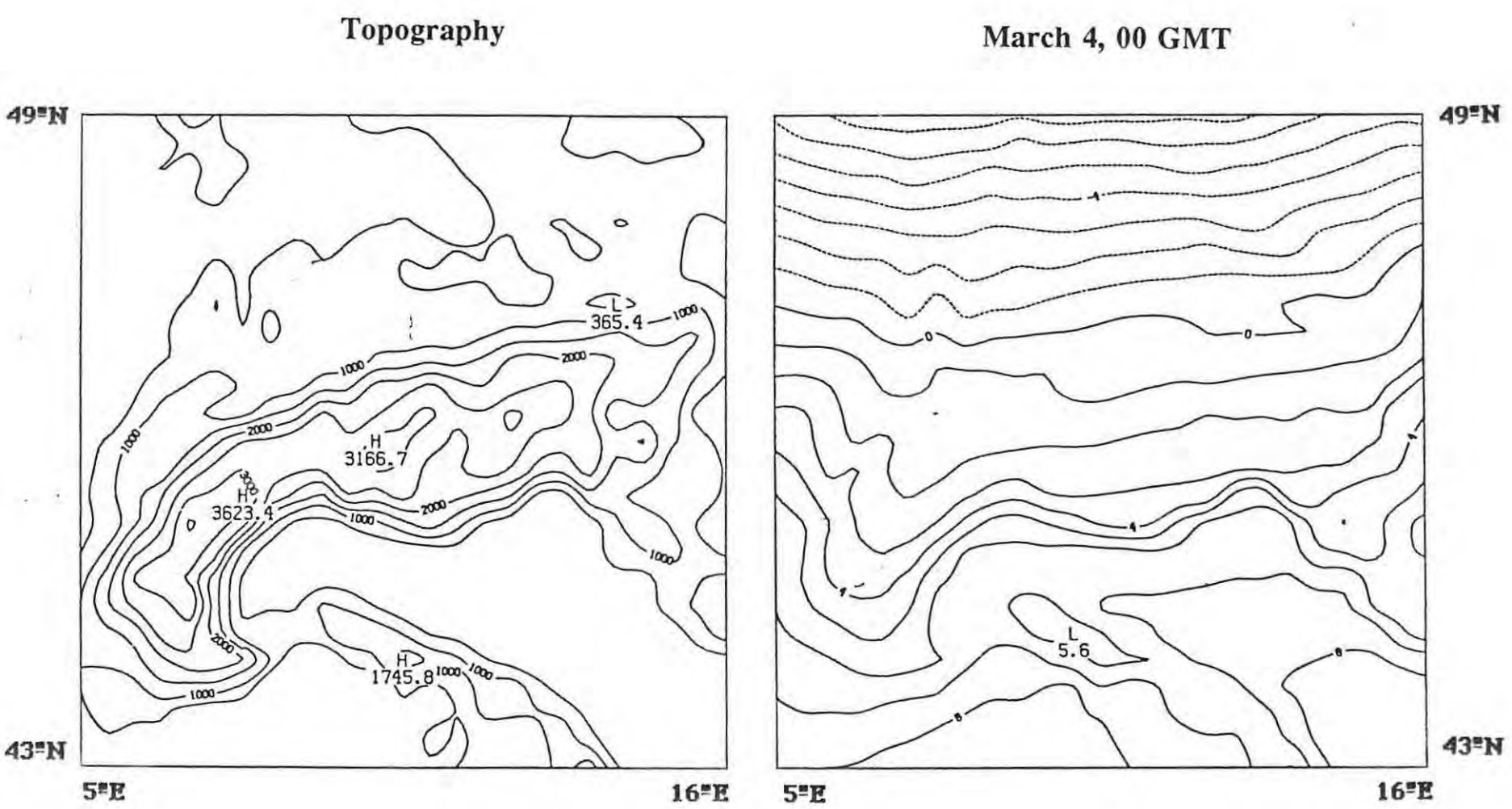

Figure I.8: Contour map of deviation surface pressure (contour interval: 1 mb) obtained in the numerical simulation of 4-5 March. The topography is shown in the top left frame. (these results should be compared with Fig. I.1)

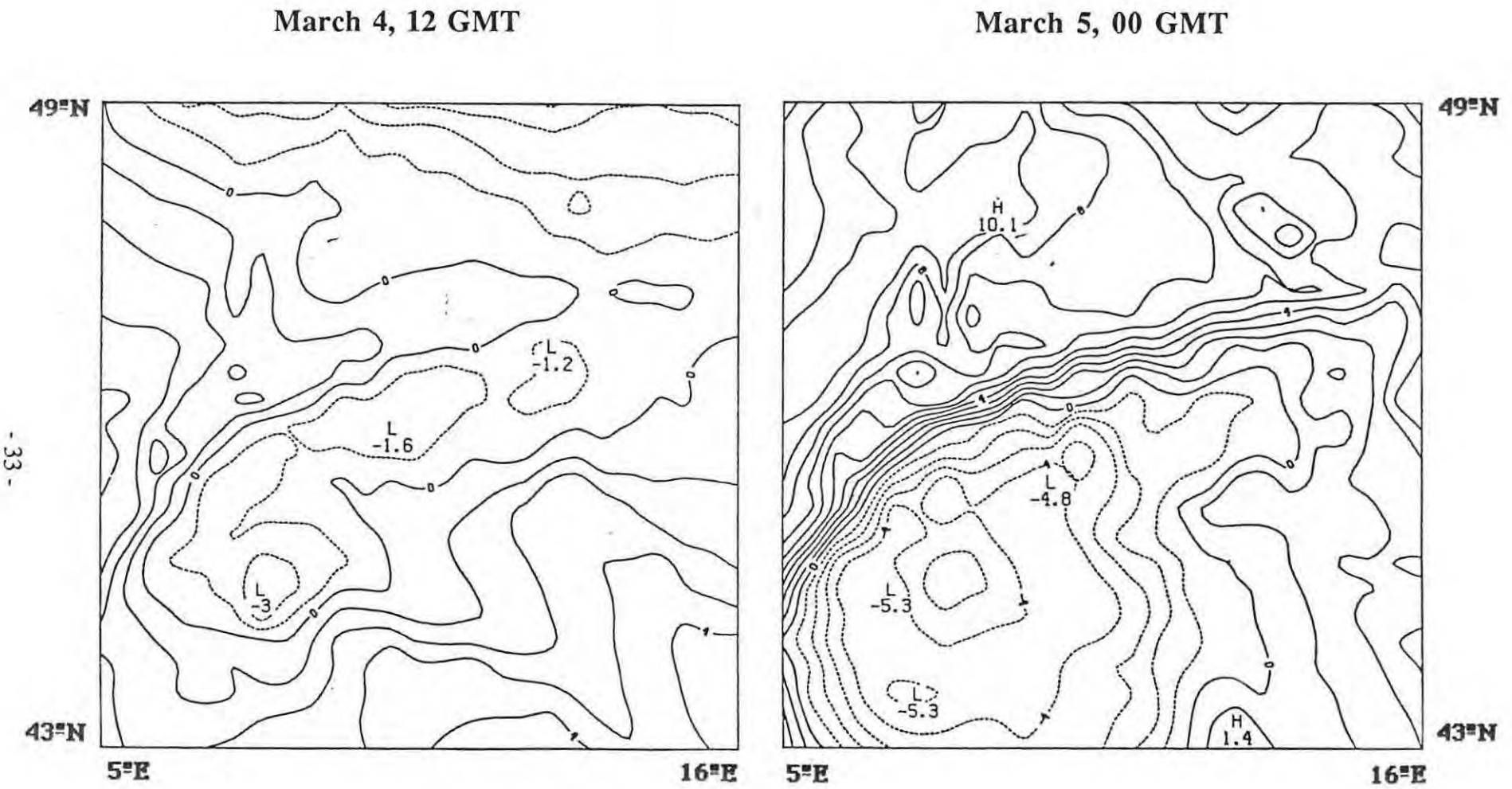

Figure I.8 (continue)

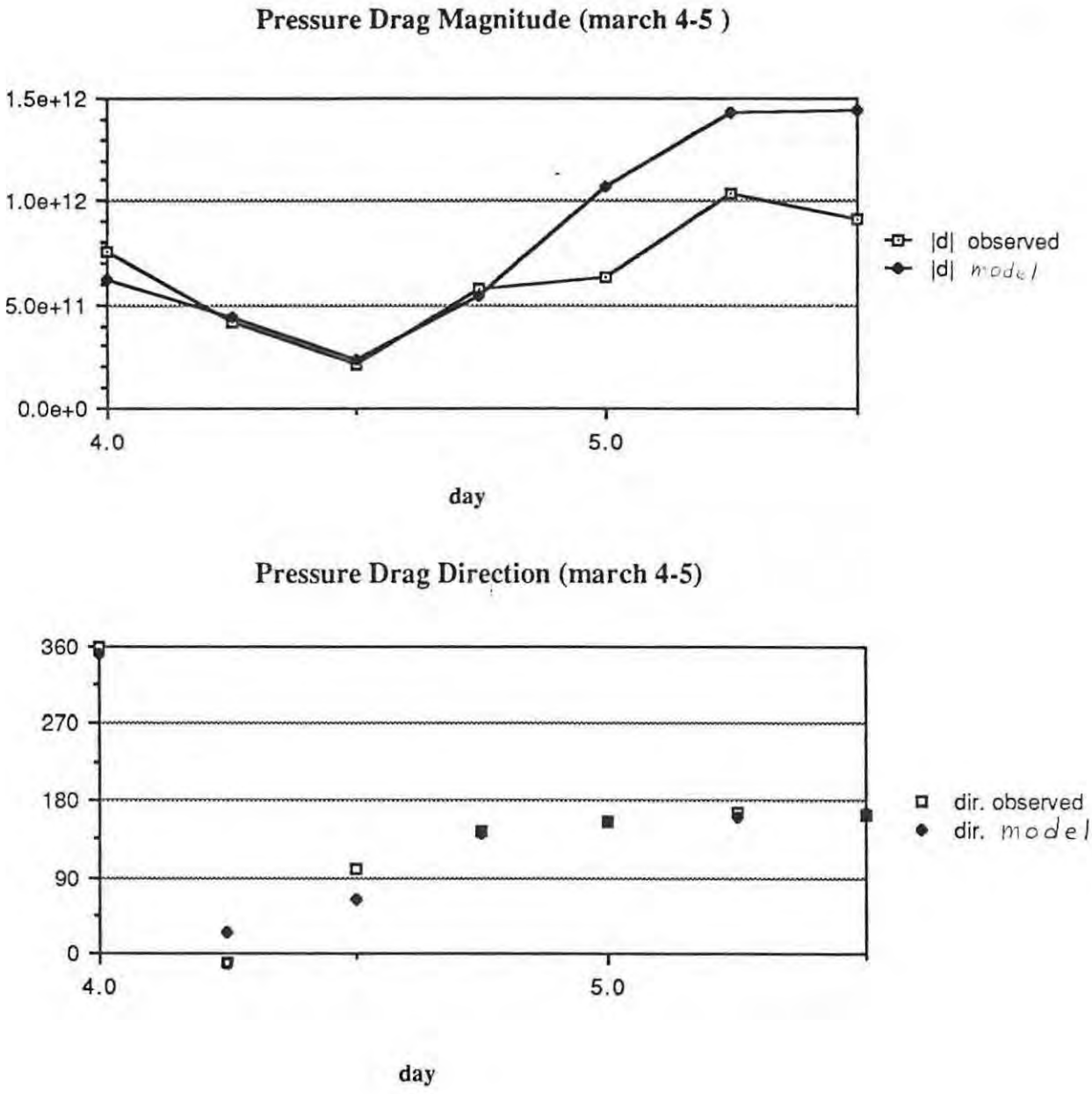

Figure I.9: Comparison of the observed drag (R=50 km) with the drag in the numerical simulation for March 4 to 5, 1982.

Chapter II: Aircraft observations of momentum flux

1. INTRODUCTION:

It was among the main objectives of ALPEX to compare the surface pressure drag exerted by the mountain with an estimate of the momentum flux measured at the mid-tropospheric level obtained using instrumented research aircraft. In this chapter we estimate the momentum flux based on north-south aircraft flights in the central part of the mountain, during the baroclinically active period in the first 20 days of March, which produced the episodes of strong drag that have been described in the previous chapter.

The determination of the wave momentum flux and its relation to the surface drag for various mountain ranges is a question of theoretical and practical importance, but one that has received little attention from the observational point of view. For the idealized situation of a two dimensional ridge with uniform stratification and constant wind it is easily shown, using the linear model developed by Queney (1947), that the surface drag exactly balances the wave momentum flux. However if the mountain is sufficiently high so that the mountain wave breaks and non linear, transient and dissipative effects become important then the flow enters a distinctly different state, referred to as the "high drag" state by Peltier and Clark (1979) who first demonstrated its existence. In this situation the momentum flux is absorbed at low level and the surface drag directly affects the low level momentum budget (Bacmeister, 1987). It is still an open question to determine how much of this idealized behavior is found in more realistic situations with strong shears, important transient behavior, non uniform stratification (such as in a front!) etc....

This question has also recently become of practical importance for the parametrization of mountain effects in large scale atmospheric models. The suggestion that the wave drag might play a significant role in the momentum budget of the atmosphere can be found for

example in Lilly (1972) who suggested that it might be necessary to parameterize it in GCMs. Such parameterizations, however, have only been recently implemented (Boer et al., 1984; Palmer et al., 1986; Pierrehumbert, 1987) and some insight into the reasons why can be found in Palmer et al.. These schemes have been guided mainly by the theoretical results in the idealized situation described above and justified partially by their beneficial effects. Some indirect evidence of the possible importance of wave drag has been presented: the geographical distribution of the residual in the zonal mean and vertically integrated, synoptic scale momentum budgets and also the surface pressure drag (Palmer et al.,1986). The only direct evidence amounts so far to a few scattered aircraft measurements. There is therefore an urgent need for both more aircraft observations and other means of direct estimation. Using the vertical soundings performed by the aircraft to obtain the different quantities required by the parameterization (Pierrehumbert, 1987), we will compare here the observed values with the parameterized values.

ALPEX Aircraft data have been previously analyzed for momentum flux calculation by Hoinka (1984, 1986) and Cox(1985) for the case of March 23 in the Pyrennees, during which a strong mountain wave was observed. There was however no measure of the surface pressure drag for comparison.

In section 2 we will present our data. In section 3 we will discuss the methods and results for the momentum flux calculation, which will be compared, in section 4, with the parameterization. This will be complemented in section 5 by a discussion of the aircraft intercomparison flights which will lead to an analysis of our results in the spectral domain. In section 6 we will summarize our results.

2. THE AIRCRAFT DATA

During the two months of the ALPEX Special Observing Period (SOP), three instrumented aircrafts: the NOAA P3, the NCAR ELECTRA and the DFVLR jet

FALCON provided high resolution data within the Alpine domain. These flights were organized into different missions which are described in Kennedy (1982). Among this large amount of data we will consider the fraction gathered on north-south cross mountain traverses, during the baroclinically active period of March 1-20, described in the previous chapter. These flight legs were flown in the central portion of the mountain, approximately above the Gotthard pass. The initial reports for these missions turned out to show so little evidence of a wave activity that the aircraft were eventually redirected to the Pyrenees (Kuettner, 1985). However even small momentum fluxes ($\approx$ 1 Pa) are important and there has been so far no quantitative estimate of the momentum flux based on those Alpine flights.

The data we use here are the validated level IIb, one second resolution, aircraft data. This data has been subjected to an extensive quality check (Kennedy and Frey, 1982). Because there are problems in measuring the meteorological variables when the aircraft is turning (Lenshow, 1982), we have excluded all the portions including heading changes from the data used here.

In order to understand the general problems with the aircraft data accuracy, we describe here briefly the principle of air motion measurements ; further details can be found in Lenshow (1982). The air speed is obtained by difference between the aircraft ground speed, derived from the inertial navigation system, and the airplane true airspeed measured by a pressure sensing probe (pitot tube). This involves a small difference between large numbers. The accuracy is therefore limited by the accuracy of the inertial navigation system, which deteriorates with time, and the precision of delicate sensors on the airplane working at very small angles of attack. For the Electra, the absolute accuracy in horizontal air speed has been estimated to be $\pm$ (1 + 0.5t) m/s where t is in hours after take off, and the relative accuracy (for short term fluctuations, < 2min) to $\pm$ 0.1 m/s.

The mean absolute vertical air velocity cannot be derived from these measurements, both because the accuracy of 0.1 m/s is insufficient, but also because its accuracy is limited by using the measured pressure altitude as a long term reference.

We have six flight legs over four separate days for the Electra that satisfy our criterion of being north-south traverse during periods of intense drag associated with frontal passage. Their characteristics are summarized in Table II-1.

In Fig. II.1 (from Kennedy, 1982) we can see the flight paths for each day, relative to the mountain. For example on March 4 the aircraft leaves the Geneva airport (indicated by GVA on the map) follows the northern side of the Alps eastward, then crosses the mountain southward from southern Germany to northern Italy and back, sampling the flow over the entire mountain width.

The aircraft altitude as a function of time (GMT in seconds) is shown in Fig. II.2 with an indication of the portions used in this study. The levels studied above the mountain range are from 570 mb to 450 mb. In Fig. II.3 we show the time series for the meridional wind V and the vertical wind W for three legs: 304S, 311 and 318S (by reference to the notation of Table II–1). The position of the main mountain crest is also indicated on these figures, together with the orientation of the leg relative to the mountain and the direction of the meridional wind. For the other legs (not shown) the situation is similar to that of leg 304S, with very weak perturbations, especially in vertical velocity.

The situation is quite different for the legs 311 and 318s where strong perturbations can be observed that are clearly related to the position of the main mountain crest and the direction of the meridional wind.

Table II-1

Leg:	Note	304S	304N	311	316	318N	318S
start	1	10h30	11h11	8h05	12h22	9h26	9h47
end	2	10h51	11h39	8h34	12h55	9h41	10h33
heading		south	north	south	north	north	south
alt. (mb)		575	550	570	550	550	450
g.s.(m/s)	3	121	140	135	134	138	106
U (m/s)	4	22	20	18	12	-5	2
V (m/s)		9	15	-10	3	11	29
Pressure drag:							
S.Time	5	9	12	9	12	9	12
Dx (Pa)	6	-0.15	-0.70	-2.63	0.63	-0.83	-0.81
Dy (Pa)		-0.81	0.14	2.70	-2.09	2.02	2.03
Momentum Flux:							
u'w'	7	-0.11	-0.02	-0.43	-0.04	-0.01	-0.18
v'w'		-0.06	0.01	-0.13	-0.01	0.04	0.03

Notes:
1) leg starting time (GMT)
2) leg ending time (GMT)
3) aircraft ground speed (m/s)
4) average U and V on the leg
5) nearest synoptic time for the surface drag
6) drag per unit area (area > 500 m)
7) average momentum flux on the leg

In Table II-1 we have also reported the drag values for the nearest synoptic time, based on our analysis of the previous chapter. These values represent averages over the entire mountain range and are smaller than the local values derived by Davies and Phillips (1985)

from the array of microbarographs in the Gotthard pass. These values are to be compared with the momentum flux estimates described next.

In Fig. II.4 we have indicated the timing of the aircraft flights relative to the evolution of the north-south component of the surface drag.

3. THE MOMENTUM FLUX:

The vertical fluxes of horizontal momentum were obtained using:

$$F = \int_{t1}^{t2} \rho u'w'Cdt \; / \; \int_{t1}^{t2} Cdt \qquad \text{(II.1)}$$

and similarly for v'w',

where: C is the aircraft ground speed,

t1,t2 are the beginning and end of the flight leg.

The perturbation values of the westerly wind u', the southerly wind v' and the vertical wind w' were obtained by removing the mean and the linear trend by a least square fit. This procedure is dictated by the impossibility to obtain a mean vertical velocity from the aircraft measurements and is identical to the procedure used by Hoinka (1984), Cox (1985) and Lilly (1978). This point will be discussed further later.

The momentum flux values are included in Table II-1. The values are small in comparison with the corresponding surface drag, indicating a significant departure from the idealized situation where they are expected to be equal. Furthermore there appears to be no systematic relationship between the drag magnitude and sign and the momentum flux obtained. For example there is a strong meridional drag and relatively strong meridional momentum flux on March 11 but on the opposite sign from what is expected and only a weak momentum flux accompanies the strong drag on March 18.

These weak momentum flux values aloft implies that the surface drag affects almost exclusively the momentum budget of the lower troposphere; this aspect will be discussed further in following chapters.

Our largest values are similar in magnitude to those of Hoinka (1984) and Cox(1985) in the Pyrennees, for which it was also found difficult to draw a consistent picture of the variations of momentum flux with height.

4. COMPARISON WITH PARAMETERIZED FLUXES:

In this section we compare the momentum flux we have estimated from aircraft data with the values that would be parameterized by the scheme currently under development in the GFDL GCM. This scheme has been described by Pierrehumbert, 1987 and Stern (private communication) and we will just outline here its characteristics.

The parametrization must first determine how much momentum flux is launched into the atmosphere. This base flux, that is the momentum flux at low level above the eventual breaking region, is given by:

$$\tau_0 = - \frac{\rho |U|^3}{Nl^*} \frac{Fr^2}{1+Fr^2} \qquad \text{(II.2)}$$

with $Fr = \frac{N\ h'}{|U|}$: the Froude number

N: Brunt Vaissala frequency

|U|: wind magnitude at low level

h': effective subgridscale mountain height (typically 500 m for the Alps)

l*: effective mountain length (here 100 km),

and has been determined on the basis of a combination of linear analysis, dimensional considerations and numerical simulations. In particular this parameterization seeks to

reproduce the saturation at large Fr that has been observed in the simulations and is caused by low level wave breaking. One word of caution must be inserted here regarding the possible inconsistency in the use of the subgridscale mountain height (h' = 500m) for comparison with observations, which include the total height of the mountain. We will see however later in this chapter that the aircraft resolve only the small scale contributions to the momentum flux.

The second part of the parameterization must then indicate where in the atmosphere this momentum flux will be deposited. This problematic issue has not been resolved at present and in the spirit of the simplicity of a sensitivity study the momentum flux absorption has been linearly distributed with height.

At the level flown by the aircrafts during the cross mountain legs, approximately 500 mb, the parameterized momentum fluxes are therefore on the order of:

$$\tau_x = 0.5\ \tau_0\ U/|U| \qquad \text{(II.3)}$$

$$\tau_y = 0.5\ \tau_0\ V/|U| \qquad \text{(II.4)}$$

In order to determine τ_0 we need to know N , U and V for the local flow. These could be estimated from the synoptic soundings but we preferred here to use the soundings performed by the aircraft, which are more accurate both in space and time.

These soundings, as indicated in Fig. II.2, were usually performed on the north or south side of the Alps following or preceding a cross mountain leg. Two examples of aircraft soundings for March 11 are shown in Fig. II.5. The wind is north-westerly at low level at the time of the flight and therefore the sounding 311N is upstream whereas 311S is downstream. In the north-south wind V there is some evidence of upstream low level blocking and strong downslope wind on the lee side, in agreement with the theoretical prediction for flow over mountain.

For each day, the low level wind and stratification required to estimate τ_0 have been determined by averaging the soundings at 800 mb on the north and south side of the mountain. The results are summarized in Table II-2, together with the parameterized momentum fluxes . These values should be compared with the values of u'w' and v'w' in Table II-1.

The parameterized fluxes are in general consistent both in sign and magnitude with the observed values. On March 11, however, the meridional fluxes, v'w', have opposite signs. The sign of the parameterized flux is consistent with the sign of the surface pressure drag.

Table II-2:

Leg:	304S	311	316	318N
N	0.013	0.009	0.008	0.006
U_0	13	22	5	5
V_0	0	-10	4	-4
τ_x	-0.17	-0.24	-0.04	-0.04
τ_y	0	0.11	-0.03	0.03

The uncertainties in the aircraft measured momentum flux are large (as discussed further below) and there is therefore the possibility that this discrepancy is not real. One must however recall that the flight leg 311 occurred near the end of a rapid transition, as attested by the pressure drag evolution in Fig. II.4. During this transition the north-south pressure drag component completely reverses in less than 12 h and there is no guarantee that the meridional momentum flux is exactly in phase with this reversal. If the discrepancy with the parameterized momentum flux is real it could possibly signal an important flaw in the current parameterization schemes: their inability to correctly treat transient flows over topography. This might not be too surprising given that these scheme are built on the stationary

assumption and might therefore be better suited to parameterize the time average effect of the orography.

5. SPECTRAL ANALYSIS:

We have already seen that there is an important limitation in aircraft measurements which is due to the impossibility of measuring mean vertical velocities (for periods greater than a few minutes). The question we therefore want to ask here is: which part of the spectrum contributes the most to the momentum flux. This is an important question because if, for example, the major contribution comes from long waves which are not resolved by the aircraft measurements, then our momentum flux estimate are likely to be inaccurate.

Before presenting the results of our spectral analysis we will first introduce the terminology used. We will then summarize the results of the intercomparison flight on April 19, 1982 between the three aircraft, that has been extensively analyzed by Richner (1985), and which will be the basis of our estimate of the aircraft accuracy as a function of frequency.

5.1 Terminology:

Given two time series: u'_i and w'_i

and their respective Fourier transforms: U_k and W_k,

we have the following definitions:

- the power spectrum: $S_k = U_k^* U_k$, represents the mean square value (variance) of the variable u' as a function of frequency.

Similarly, if we have two time series, the real and imaginary part of the complex cross spectrum give:

- the co-spectrum: $C_k = \text{Real}\{ U_k^* W_k \}$
- the quadrature-spectrum: $Q_k = \text{Im}\{ U_k^* W_k \}$

from which one can derive:

- the coherence-spectrum: $coh_k = (C_k^2 + Q_k^2) / (S_{u,k} S_{w,k})$, which is a measure of the correlation between the two time series for each frequency band.

Before the Fourier transform is applied it is necessary to perform a tapering of the time series to insure that it is periodic, which will be done here using a cosine taper applied to 10% of the series at each end. In addition we will also take a frequency average over 11 adjacent points in the spectral domain, a standard procedure to increase the statistical stability of the results.

5.2 Summary of the intercomparison flight:

On April 19, 1982 an intercomparison flight involving the three aircraft took place over the lake of Geneva. The aircraft flew in close formation (spaced about 25m apart) for about an hour and the resulting data has been extensively analyzed by Richner (1985) and summarized here.

Due to some problems with data from the P3, which have been partially corrected as a result of Richner's analysis, we will only discuss the comparison between the Electra and the Falcon. The analysis procedure used by Richner is similar to ours except that he took a frequency average over 25 points and he did not detrend the time series.

In Fig. II.6 we have reproduced Richner's comparison between the power spectra for the vertical wind for the Electra and the Falcon, together with the coherence spectrum between the two aircraft. The two power spectrum are quite different at high frequencies but also at low frequencies and this is confirmed by the coherence spectrum which shows an appreciable coherence between the two aircraft only for frequencies in the range $0.008 < \nu < 0.05$.

The loss of coherence at low frequency is due to the aircraft inability to measure the mean vertical motion. This deficiency is made quantitative here: the aircraft cannot measure accurately mean motions with periods greater than 125s (consistent with the 2 min mentioned

by Lenshow, 1982) which corresponds for an aircraft flying at 125 m/s to a wavelength of 15 km. In particular the aircraft cannot resolve vertical motions on the scale of the Alps.

At low frequency, this loss of coherence is not found in the horizontal wind, but at high frequency the same loss of coherence is found for all the three wind components at approximately $\nu = 0.05$, corresponding to wavelength of 2.5 km. This frequency is therefore not related to the distance between aircraft, which is 25m, but rather to the accuracy of the data (see Richner, 1985).

5.3 Results:

For each of the legs in Table II-1 we have performed a spectral analysis. We will first discuss the decomposition of the momentum flux into three regions in the spectral domain, determined on the basis of the results of the intercomparison flight:

- region A: $\nu < 0.008$ in which the long period vertical motion are not resolved by the aircraft

- region B: $0.008 < \nu < 0.05$ in which there is good coherence between aircraft measurements for all wind components ,

- region C: $0.05 < \nu$ in which there is poor coherence for all three wind components between aircraft measurements.

The results of this spectral decomposition of the momentum flux into these three domains is presented in Table II-3. When there is an appreciable momentum flux, such as on legs 304S, 311 and 318S, the major portion comes from region A, with a lesser part from region C (leg 311 in particular). In general only a small fraction of the flux comes from region B. In Fig. II.7 we see in more details the importance of the low frequencies in the plot of the cospectrum of V and W for the legs 311 and 318S. These curves are plotted on a variance-area conserving graph and the momentum flux in each spectral subdomain is therefore directly proportional to the area under the curve. These two curves are similar to the

ones for the other cases (not shown) and also to the spectral analysis performed by Cox(1985) for the case of March 23 .

Table II-3

Leg:	Note	304S	304N	311	316	318N	318S
u'w' tot	1	-0.10	-0.02	-0.47	-0.04	-0.01	-0.19
u'w' A	2	-0.09	-0.03	-0.34	-0.03	0.	-0.17
u'w' B	3	0.	0.01	-0.01	-0.01	-0.01	-0.01
u'w' C	4	-0.01	-0.01	-0.12	0.	0.	-0.01
v'w' tot	5	-0.06	0.01	-0.11	-0.01	0.04	0.02
v'w' A		-0.06	0.02	-0.19	-0.01	0.04	0.02
v'w' B		0.	0.	0.02	0.	0.02	-0.03
v'w' C		0.	-0.01	0.06	0.	0.	-0.01

Notes: 1) total u-momentum flux (in Pa)
2) u-momentum flux for : $\nu < 0.008$ Hz
3) for : $0.008 < \nu < 0.05$
4) for : $0.05 < \nu$
5) similar for v-momentum flux

The dominance of the low frequency part of the spectrum in the momentum flux is in itself a useful result but also indicates that our flux estimates are unreliable. The same is also true for the studies of Hoinka (1984, 1986) and Cox (1985) in the Pyrennees which used the same aircraft.

On theoretical grounds one expects, for typical atmospheric values, that wavelengths in the range 6 km ($=2\pi U/N$) to 600 km ($=2\pi U/f$) are vertically propagating and contribute to the momentum flux. But here only wavelengths less than 15 km are actually resolved by the aircraft.

The possibility exists that the true momentum flux values, which include the contribution from the mountain scales, will be much larger. One could argue that in Fig. II.3 b) and c) there is a mountain wave that is visible in the horizontal velocity V but not in the vertical velocity W, possibly due to the lack of resolution. Such a wave could contribute an important part to the momentum flux.

In addition the procedure of linear detrending of the time series is also questionned by these results. Removing the linear trend from the time series strongly distorts the low frequencies, as shown in Fig. II.8 for the V-wind on leg 311, which in turn affects the major contribution to the momentum flux. A more appropriate method would be to filter out the low frequency part (not much would be left as seen in Table II-3!) and this would settle the controversy on whether a detrending should be performed (Hoinka, 1984, 1986 and Cox, 1985).

6. SUMMARY:

Based on six north-south cross mountain flights at approximately the 500 mb level, we have computed an estimate of the momentum flux above the Alps. The timing of the flights relative to the surface drag evolution has been indicated.

In all cases the momentum flux is much smaller than the surface pressure drag. This would suggest that the dominant balance is between the surface pressure drag and the low level (below 500 mb) momentum budget. This issue will be discussed again in subsequent chapters.

A comparison with the values predicted by the wave-drag parameterization under development for the GFDL GCM has been presented. The low level wind and stratification have been determined based on the aircraft soundings. The parameterized values are generally consistent with the observations. In one instance however (the meridional flux on March 11),

the parameterization gives an opposite result and we have argued that this may be due to the rapid variation of the flow that can not be taken into account by the parameterization.

The analysis of the intercomparison flight performed by Richner (1985) has led us to a decomposition of the momentum flux into three regions in the spectral domain. Only in the middle spectral region, with wavelength approximately in the range 2.5 km < L < 15 km , there is good coherence between the aircraft and confidence in the measurements. For long waves the measurements are limited by the aircraft ability to measure vertical motions, whereas for short waves the limitations appear due to the accuracy of the measurements for the three wind components. In particular the aircraft cannot adequately resolve waves on the scale of the mountain.

In Table II-3 we have seen that the major contribution to the momentum flux comes from the low frequency region, which therefore brings a word of caution about the reliability of our estimates. One must say however that these results are generally consistent with expectations regarding their magnitude, direction and spatial scales.

Therefore we repeat here the results that we feel are robust: 1) the momentum flux at mid-tropospheric level is much smaller than the surface drag, 2) the contribution to the momentum flux from wavelengths in the range 2.5 km < L < 15 km is very small (this could have interesting implications such as in the use of ` a high resolution (10 km) limited area model to test the parameterisations); 3) The parameterization gives, in general, the right order of magnitude but can give erroneous values in some particular cases.

Figure captions for Chapter II:

Figure II.1: Flight tracks for the aircraft Electra (E) used in this study. The three digit code corresponds to the month and day of the flight. Approximate aircraft altitudes are indicated in hundred of feets. Dark shading on the maps indicate high mountain elevation. Only the north-south cross mountain legs will be considered here. (from Kennedy, 1982)

Figure II.2: Time-altitude plots corresponding to the flights in Fig. II.1, with thicker lines indicating the portions used in this study. The letters indicate soundings performed by the aircraft: on the north side (N) and on the south side (S).

Figure II.3: Examples of time series for the north-south wind (V) and the vertical wind (W) for the legs: a) southward leg on March 4 (304S), b) southward leg on March 11 (311) and c) southward leg on March 18 (318S) (see Table II-1 for more details).

Figure II.4: Timing of the aircraft legs (indicated by the arrows) relative to the evolution of the north-south component of the surface drag. The time is indicated in days for March.

Figure II.5: Aircraft soundings performed on March 11 on the north (N) and south (S) side of the mountain: a) potential temperature, b) westerly wind and c) southerly wind. Solid and dashed lines are used to distinguish the soundings.

Figure II.6: Power and coherence spectra for the vertical wind measured by the two aircraft Electra and Falcon during the intercomparison flight of April 19, 1982 (from Richner, 1985).

Figure II.7: Cospectrum for the north-south wind (V) and vertical wind (W) for a) the southward leg on March 11 (311) and b) the southward leg on March 18 (318S)

Figure II.8: An example of the effect of the linear detrending on the power spectrum for the north-south wind component on March 11.

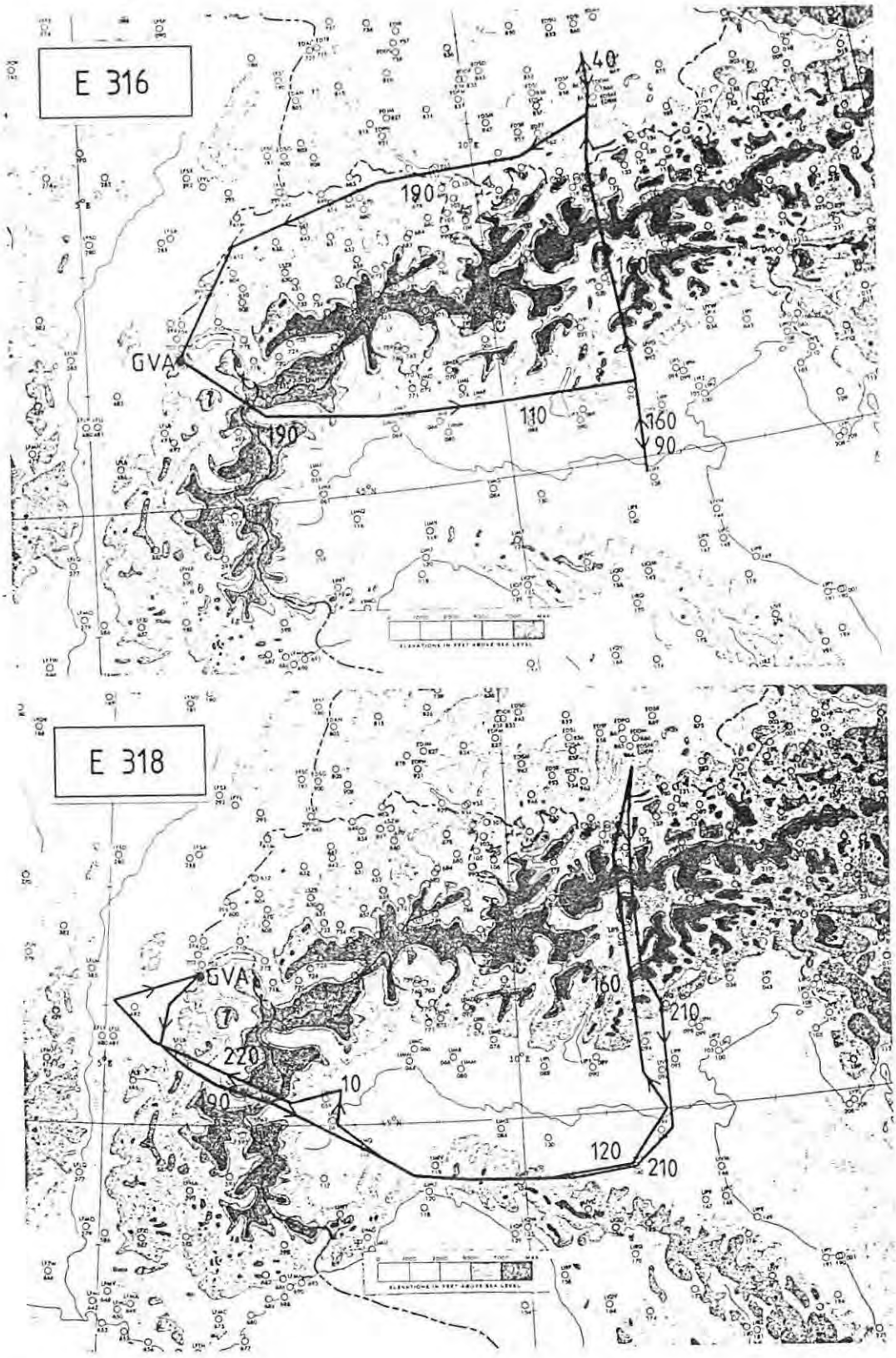

Figure II.1: Flight tracks for the aircraft Electra (E) used in this study. The three digit code corresponds to the month and day of the flight. Approximate aircraft altitudes are indicated in hundred of feets. Dark shading on the maps indicate high mountain elevation. Only the north-south cross mountain legs will be considered here. (from Kennedy, 1982)

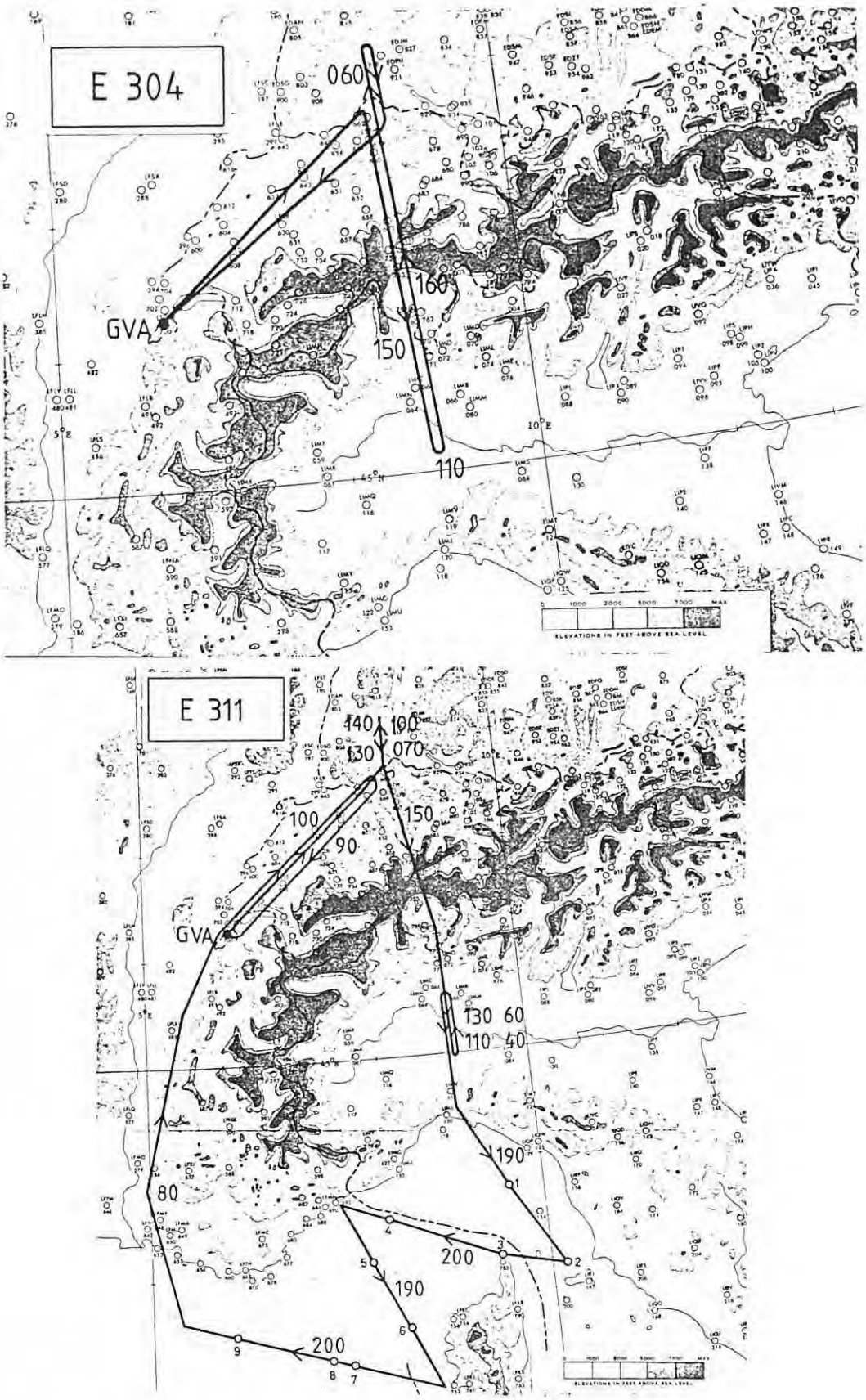

Figure II.1 (continue)

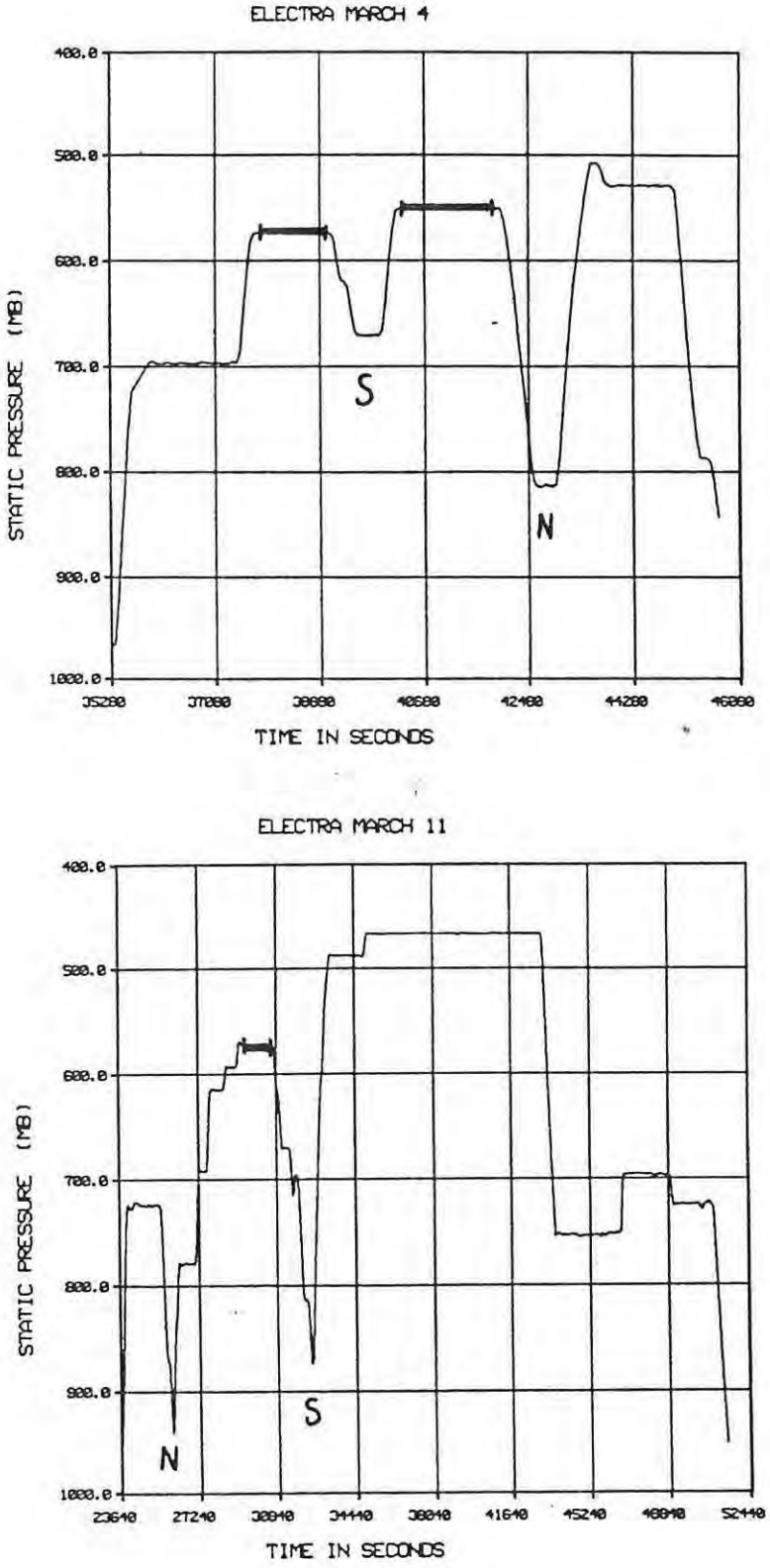

Figure II.2: Time-altitude plots corresponding to the flights in Fig. II.1, with thicker lines indicating the portions used in this study. The letters indicate soundings performed by the aircraft: on the north side (N) and on the south side (S).

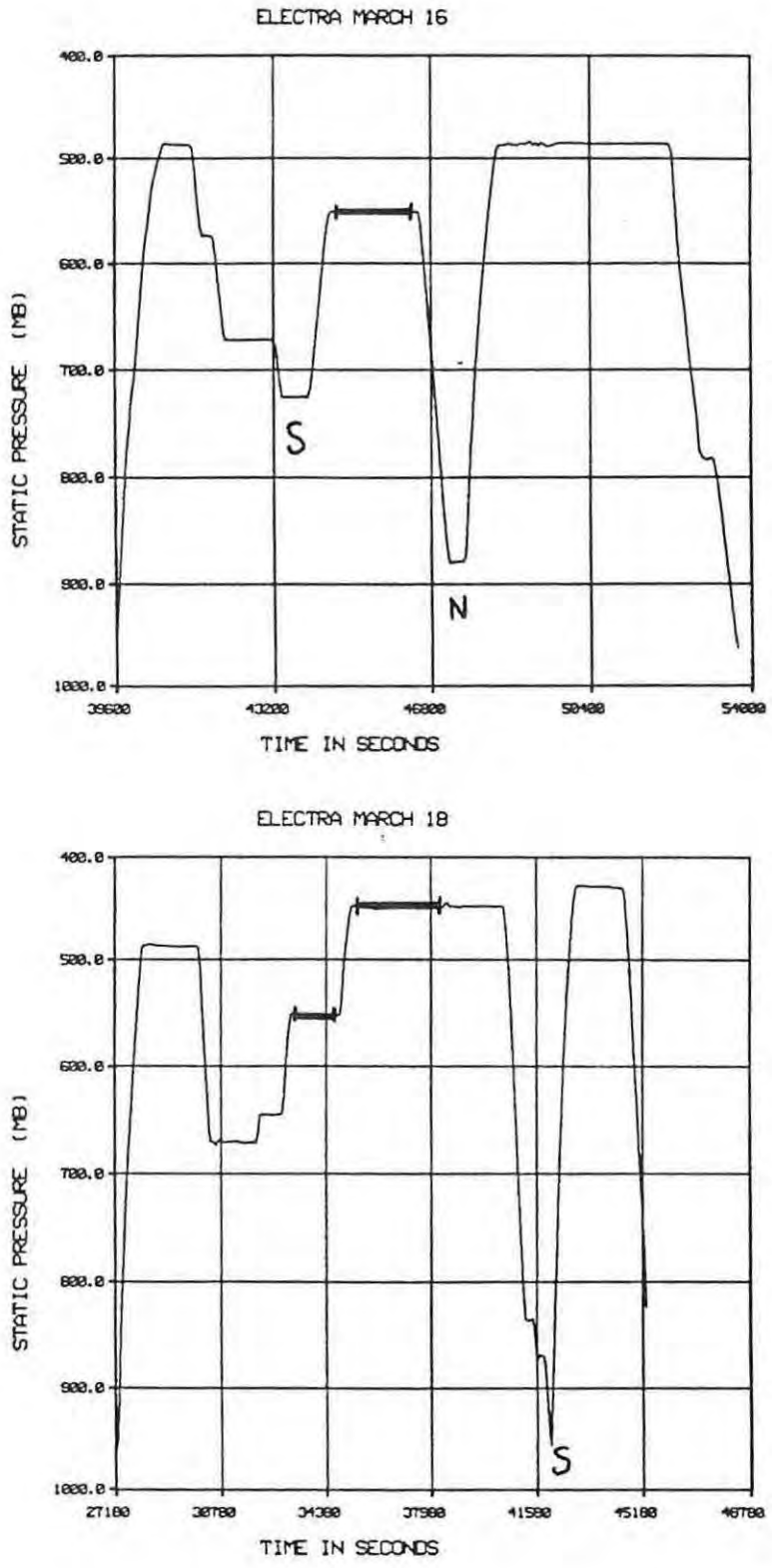

Figure II.2 (continue)

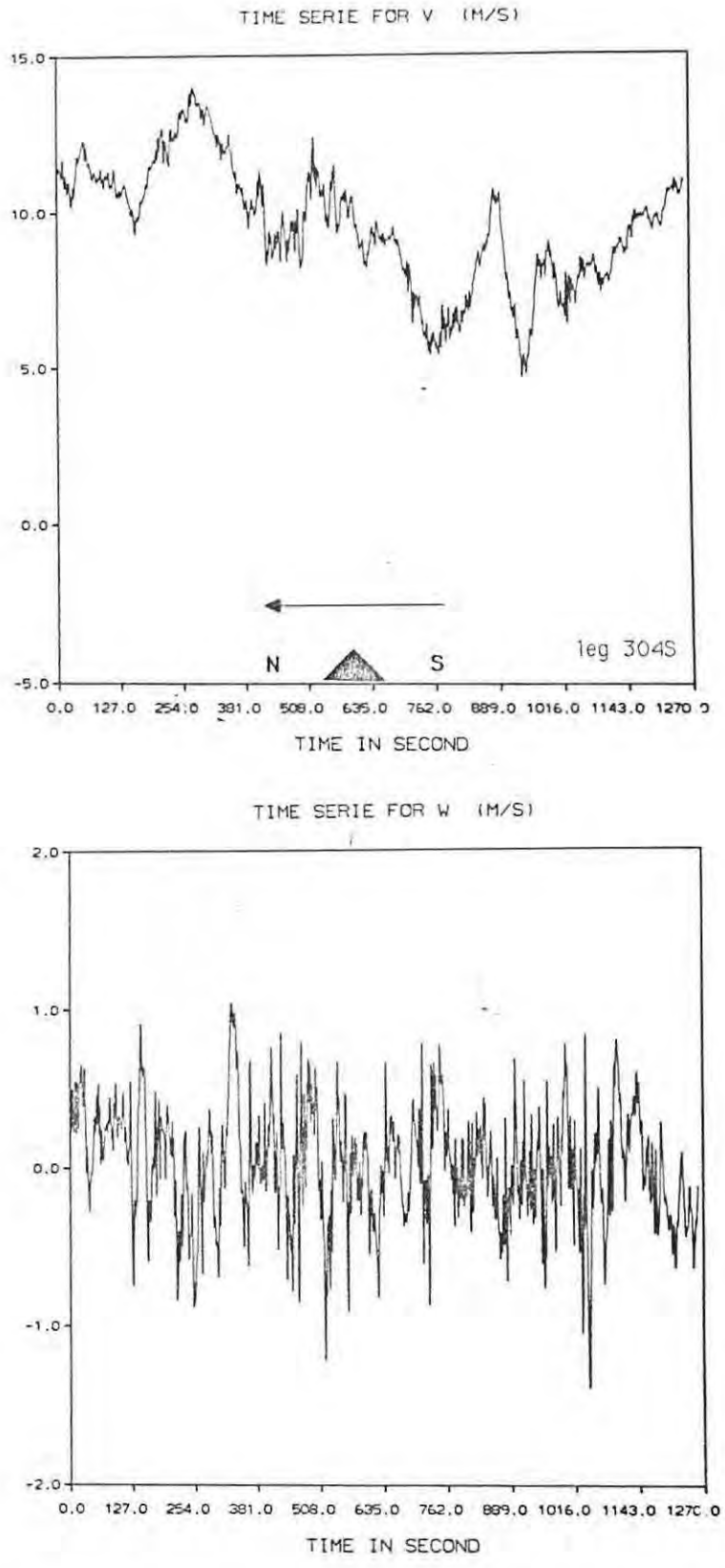

Figure II.3: Examples of time series for the north-south wind (V) and the vertical wind (W) for the legs: a) southward leg on March 4 (304S), b) southward leg on March 11 (311) and c) southward leg on March 18 (318S) (see Table II-1 for more details).

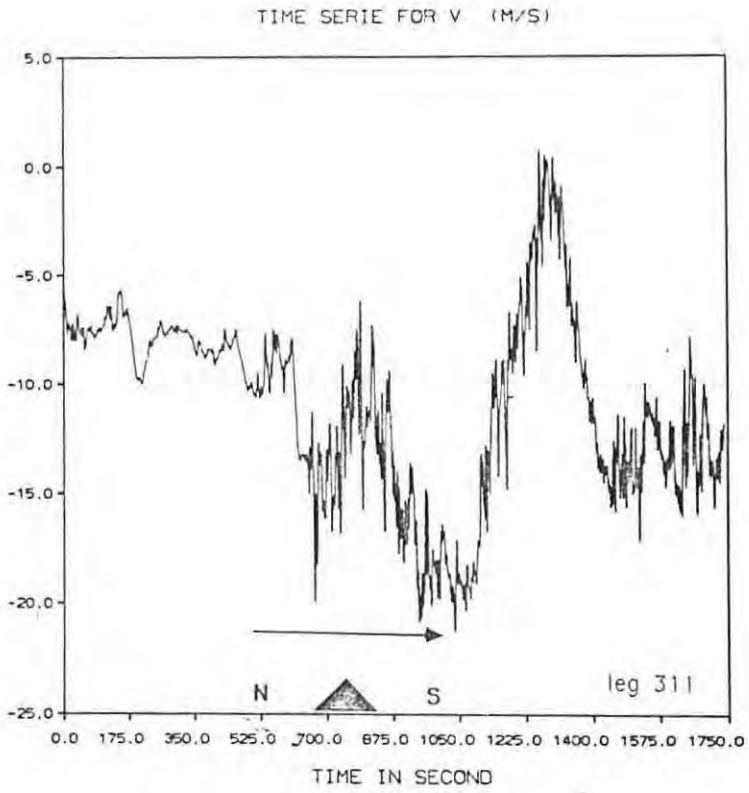

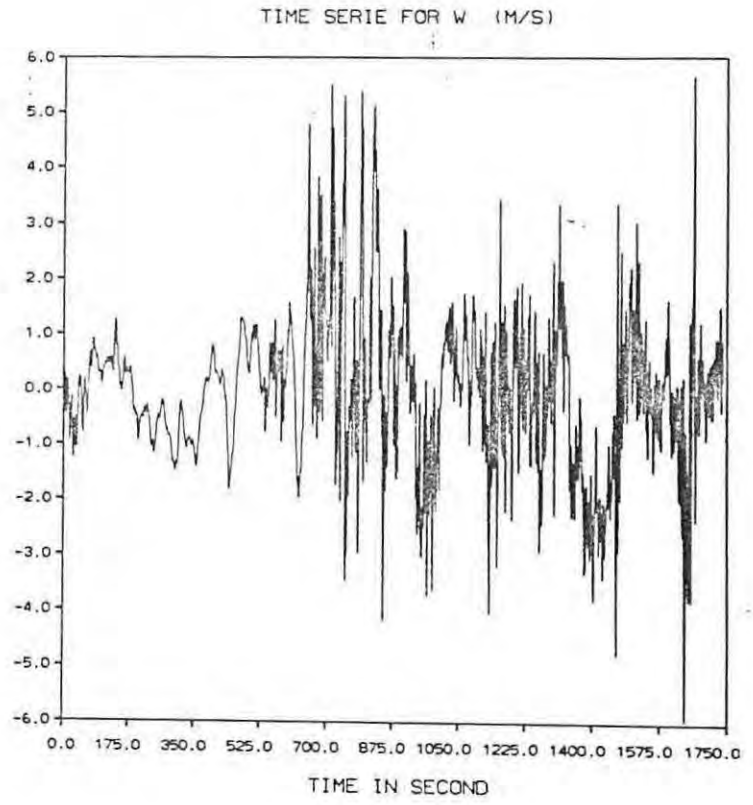

Figure II.3 (continue)

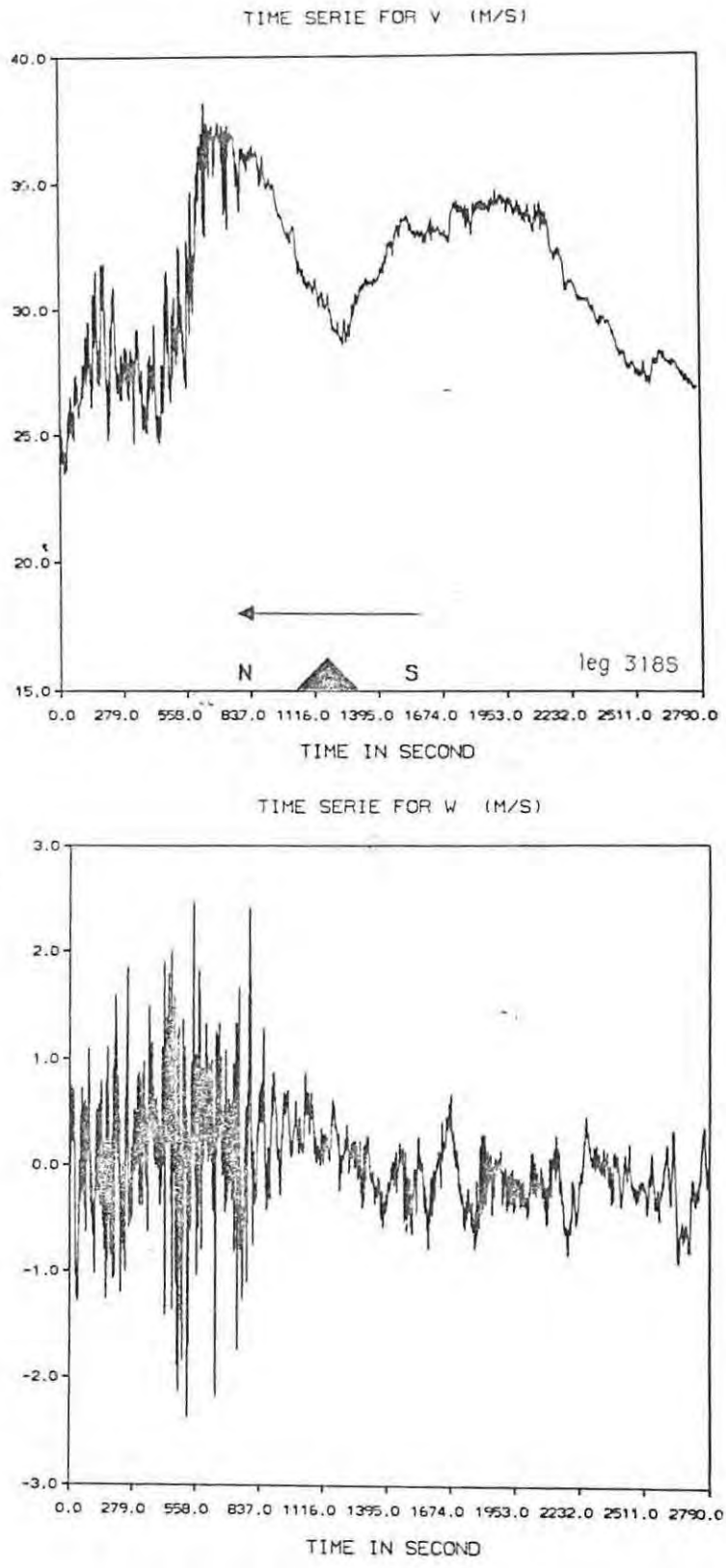

Figure II.3 (continue)

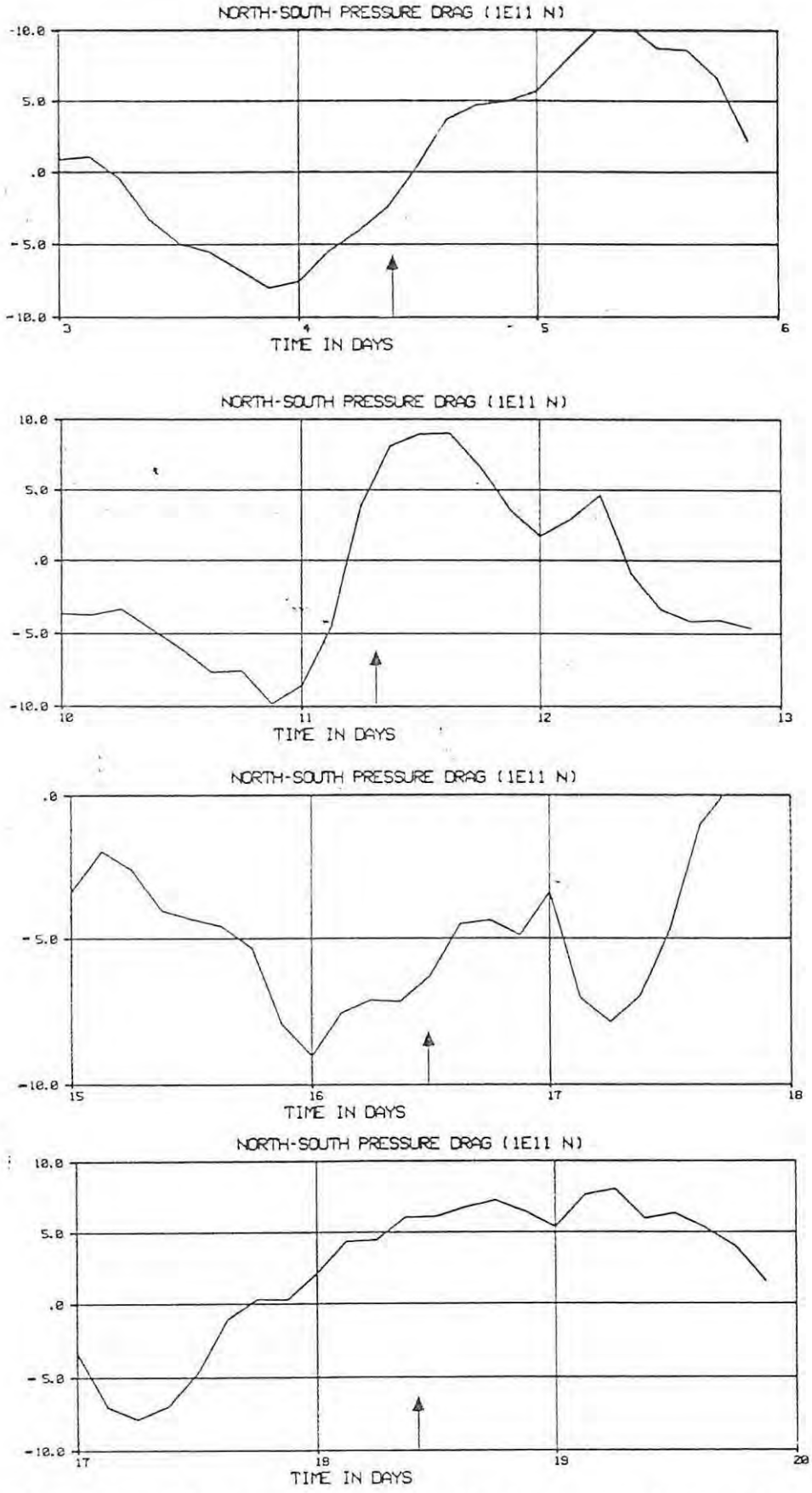

Figure II.4: Timing of the aircraft legs (indicated by the arrows) relative to the evolution of the north-south component of the surface drag. The time is indicated in days for March.

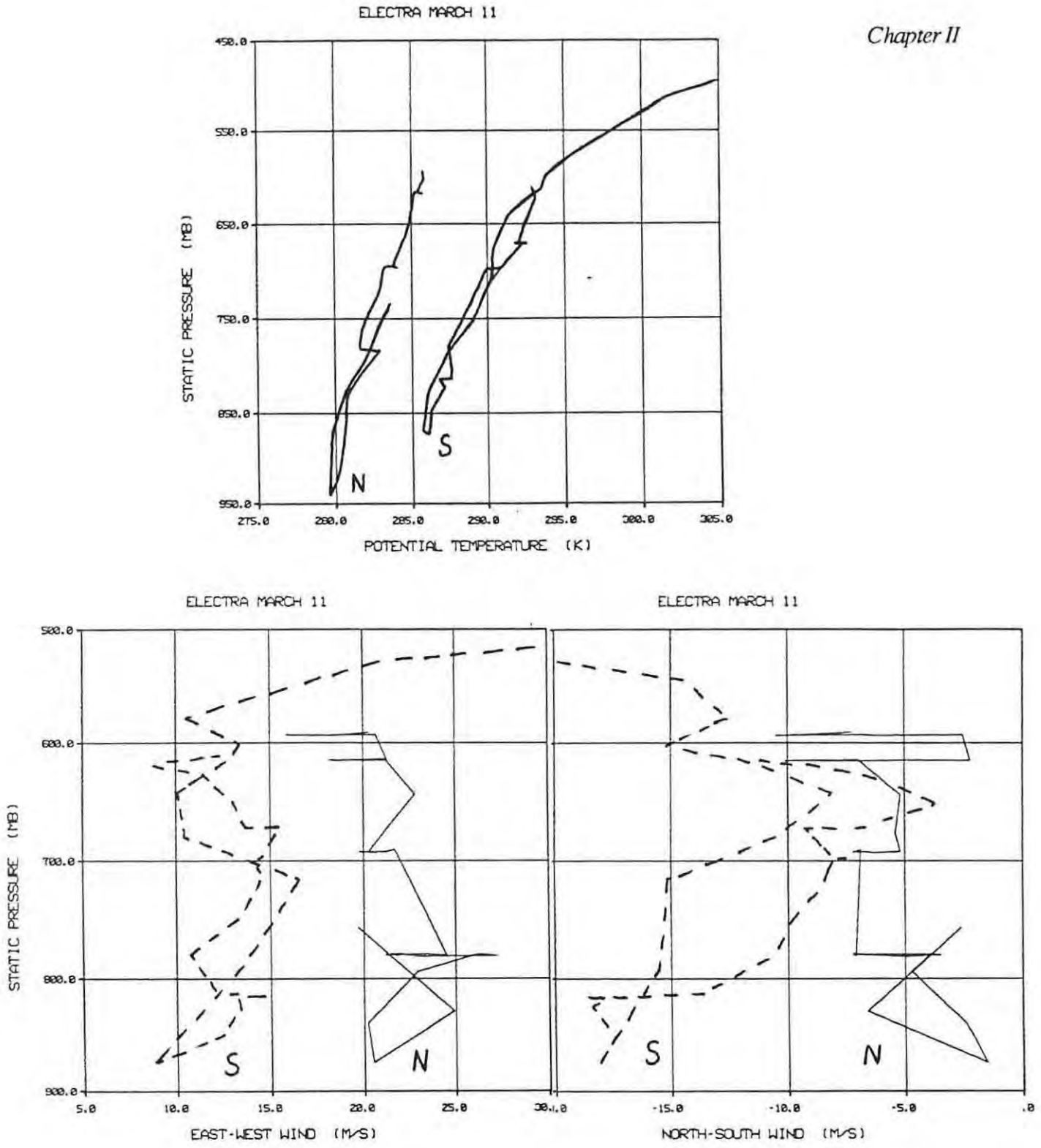

Figure II.5: Aircraft soundings performed on March 11 on the north (N) and south (S) side of the mountain: a) potential temperature, b) westerly wind and c) southerly wind. Solid and dashed lines are used to distinguish the soundings.

a) Electra

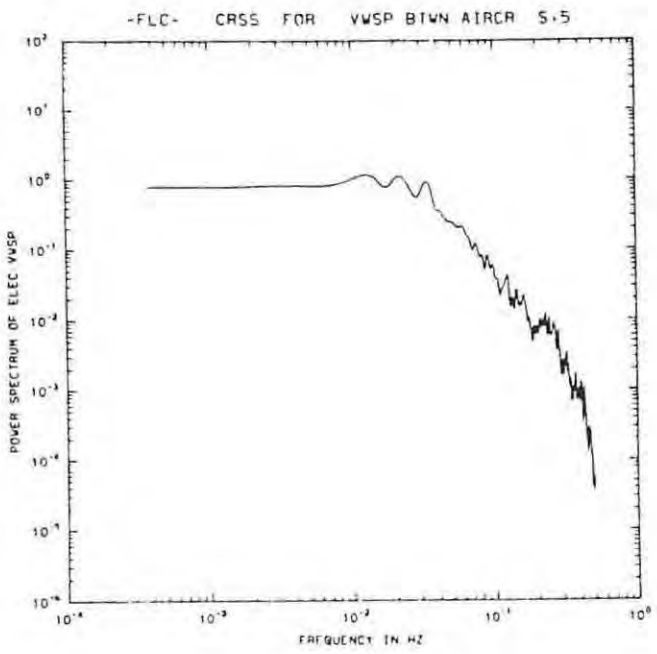

b) Falcon

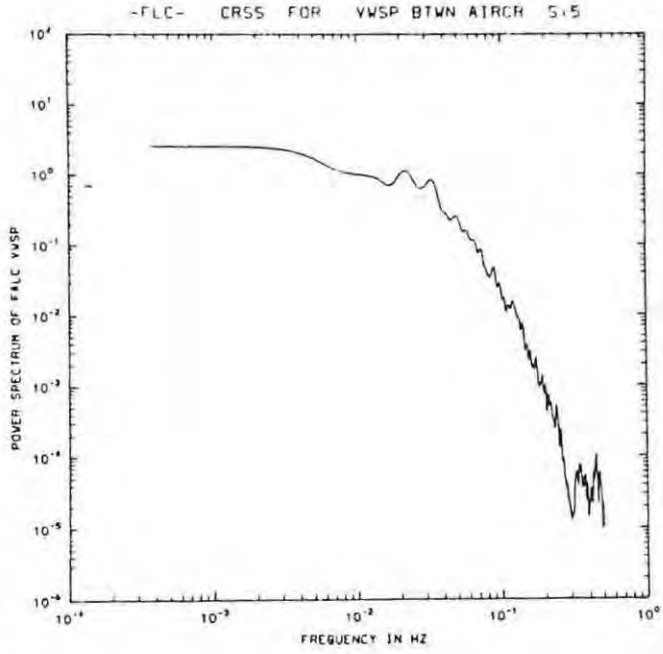

c) coherence Electra / Falcon

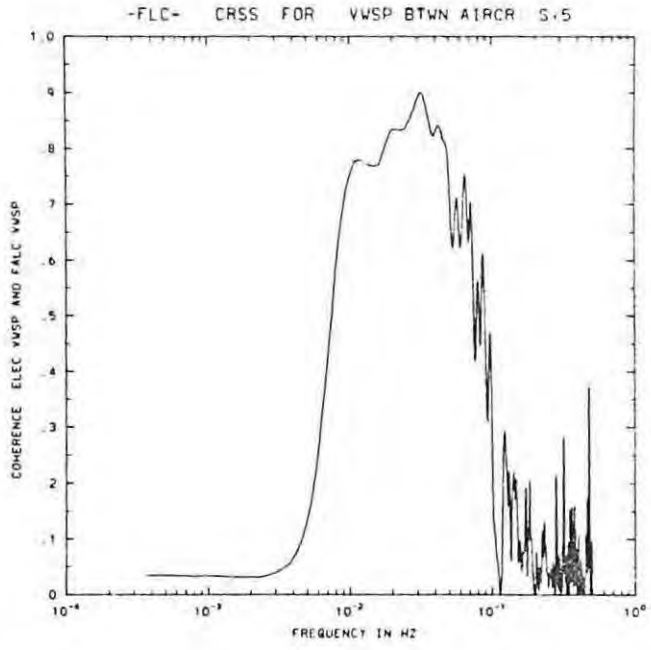

Figure II.6: Power and coherence spectra for the vertical wind measured by the two aircraft Electra and Falcon during the intercomparison flight of April 19, 1982 (from Richner, 1985).

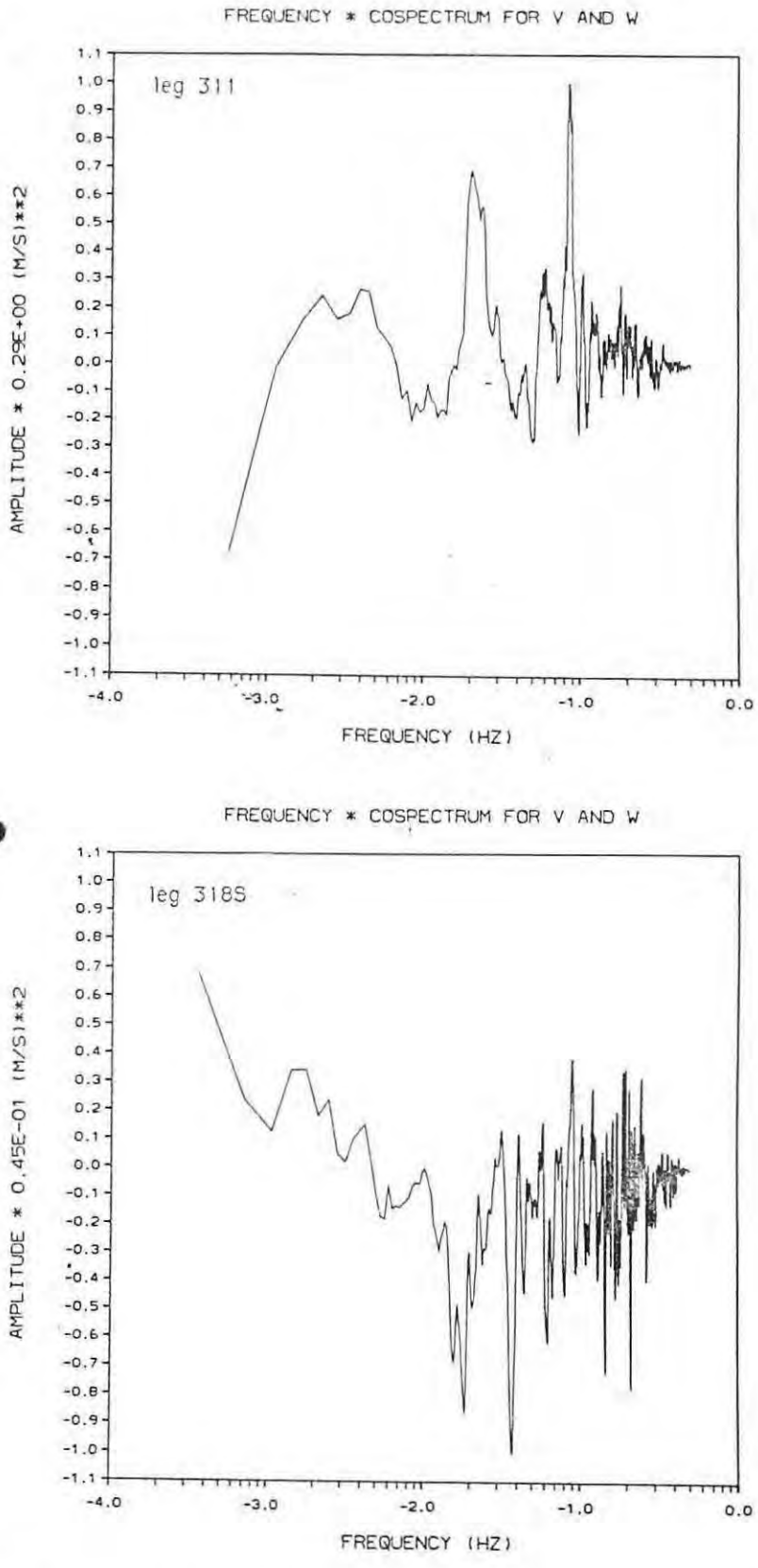

Figure II.7: Cospectrum for the north-south wind (V) and vertical wind (W) for a) the southward leg on March 11 (311) and b) the southward leg on March 18 (318S)

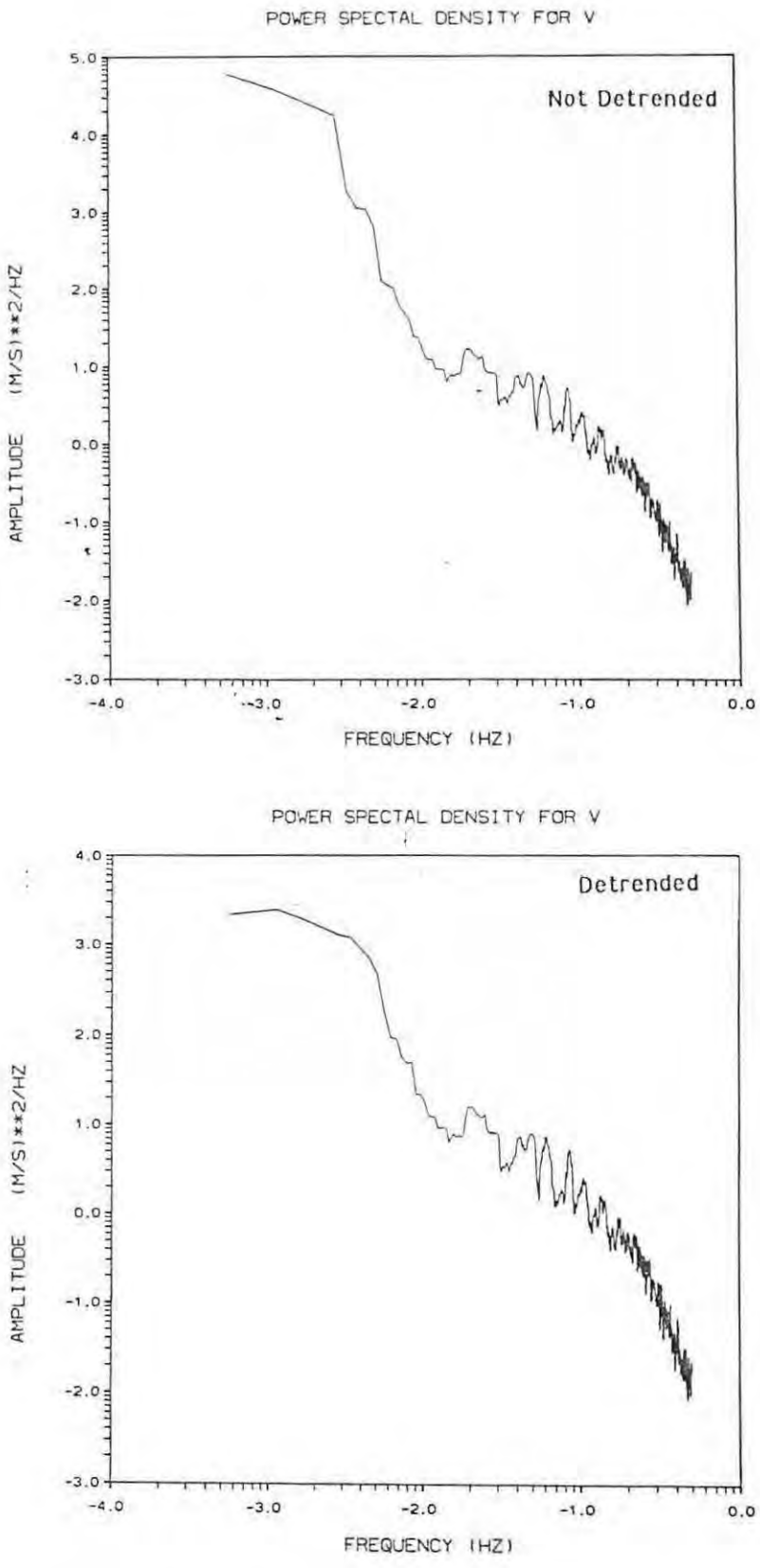

Figure II.8: An example of the effect of the linear detrending on the power spectrum for the north-south wind component on March 11.

Chapter III: Other observations of frontal passage

1. INTRODUCTION:

It was shown in the previous chapters that very strong drag has been observed in relation with frontal passage and cyclogenesis and that during those events little momentum flux was measured at the mid-tropospheric level. In the remainder of this thesis we will investigate the mechanisms creating these observed features. As a first step in this chapter we will examine in more details the phenomenon of frontal passage using available observations.

It is well known (e.g. Wallace and Hobbs, 1977) that during the passage of a cold front a fixed observer sees a pressure fall immediately followed by a pressure rise. The simple advection across the mountain of the surface pressure pattern associated with the front would create a drag reversal qualitatively similar to the observations. A question therefore immediately arises about this mechanism: can it explain the observed drag magnitude?. This aspect will be discussed in section 2.

We will see however, that the pressure gradients across the mountain during the interaction are much larger than typically associated with the front upstream of the mountain, implying strong topographic effects. In section 3, the features of the front-mountain interaction will therefore be further examined using the available observations. The synoptic analyses will show us the distortions of the surface front, surface pressure and the flow pattern that can clearly be related to the mountain. The evolution of the cold air advection will be tracked using potential temperature cross sections through the front and the mountain at different stages of the interaction. Some insight will also be gained from the comparison of the time series of temperature and wind for stations on the north and south side of the

mountain. In addition an example of isentropic analyses will also demonstrate how the advection of cold, high potential vorticity air is affected by the mountain.

Finally, in section 4, a discussion of these results and the outstanding questions will be presented.

2. THE DRAG EXPECTED FROM THE UNDISTORTED FRONT:

In this section we compare the pressure gradients associated with the front upstream of the mountain, before it feels the mountain effects, with the pressure gradient required to create the observed drag. This comparison will be illustrated by the example of March 4-5 but its relevance to other cases will be discussed.

Fig. III.1 is from Hoinka (1986) and represents a set of microbarograph plots in the Alpine region between March 3 and 5. The frontal passage, marked by the progression of the low pressure, is obvious between the northernmost stations: Stuttgart (STU) and Nuremberg (NUE) and those stations close to the baseline of the Alps: Weissenau (WEI) and Garmish (GAR). Subsequently the front moves across the following stations: Innsbruck (INN), Brixen (BRI) and Bologna (BOL) which are roughly in line with Garmish and Stuttgart. From these measurements, Hoinka (1986) obtains the following estimates for the frontal speed: 8m/s on the windward side, 3m/s across and 17 m/s on the lee side of the Alps. Combined with the observed magnitude of the pressure rise upstream of the mountain, observed for example at Stuttgart, of at most 5mb / 6hour, this leads to a value of the pressure gradient of approximately 2.5 mb / 100 km, with smaller values inferred from the pressure fall.

For comparison we now estimate the pressure gradient required to produce a pressure drag of 10. 10^{11} N on the Alps, typical of the peak values obtained in Chapter I. For a constant pressure gradient the pressure drag is given by approximately the gradient magnitude multiplied by the mountain volume (Archimedes' law), which is estimated to be

2.1 10^5 km^3 by Hafner and Smith (1985) and is similar to the value derived from the topography used here if the base is included (c.f. discussion in Chapt. I). Consequently the pressure gradient required for the observed pressure drag is approximately $\nabla P \approx$ 5 mb / 100 km, which approximately corresponds to what is observed in the surface pressure analyses shown in Chapt. I, but is larger than the values inferred from the synoptic sea-level pressure shown in the next section.

To further see the strong ageostrophic effects implied by these observations, one can compute the along front wind that would be in geostrophic balance with this pressure gradient. The required wind has a magnitude of 50 m/s which is unrealistically larger than any observed value during ALPEX for the wind just above the boundary layer.

An original analysis of these microbarographs measurements has been performed by Phillips (1984), in the form of an Atlas for the entire ALPEX period of time-distance (Hovmöller) diagrams of the surface pressure evolution, across the north-south Gotthard section. Two examples of these diagrams are reproduced in Fig. III.2 and cover the frontal passages of March 4-5, 11(in part) and 12-13 . Phillips (1984) also gives similar diagrams for the hourly precipitation data which are useful in locating the frontal perturbation .

Because the measurements are taken at different altitudes some form of pressure reduction was necessary to obtain these plots. The pressure at Altdorf (ALT; in the central part of the domain) was chosen as the standard pressure and, at each station, the pressure was normalized by the ratio of the averages for the two months period. This method present some problems discussed by Phillips (1984).

In Fig. III.2.a one can clearly see the build up of the cross mountain pressure gradient on late March 3 and early March 4, corresponding to the prefrontal drag. The front can be approximately tracked using the position of minimum pressure and is seen to encounter the mountain in the morning of March 4; thereafter it is considerably retarded. At the time of the encounter there is almost no pressure gradient across the mountain but it immediately starts

to rebuild but in the opposite direction. The maximum gradient is observed on March 5, creating the strong post-frontal drag. From this figure it is clear that the pressure gradient across the topography, at the time of largest magnitude, is much larger than any pressure gradient that can be associated with the front upstream of the mountain.

The situation is similar for other cases of frontal passages. For example Fig. III.2.b shows the latest stages of the very rapid frontal passage on March 11 and the entire passage on March 12-13. In addition it is easily verified from synoptic maps that in all cases the pressure gradient is supergeostrophic.

In summary of this discussion one can conclude that the magnitude of the pressure fall and rise associated with the front upstream of the mountain is insufficient (by approximately a factor of two) to account for the observed maximum drag values. These very strong pressure gradients are therefore a product of the front-mountain interaction which mechanisms will be examined in subsequent chapters. But before doing so we will look at more observations in the next section.

3. OBSERVATIONS OF THE FRONTAL DISTORTIONS:

Here we present some additional observations that are pertinent to the frontal distortion by the mountain. For a very complete study of a case of frontal passage and cyclogenesis, but unfortunately without equivalent for the ALPEX period, the reader is referred to Buzzi and Tibaldi (1978).

3.1 Synoptic Analyses:

The synoptic analyses presented here are reproduced from the Deutscher Wetterdienst daily bulletin.

Fig. III.3.a and b show the surface analysis for March 4, 12 GMT and March 11, 12 GMT respectively. Although too much confidence cannot be given to the analysis in the

mountainous area and to the location of the front, we will nevertheless emphasize here the similarities between these two cases, also found in the majority of frontal passages in the Alps. There is a deceleration of the front in the central part of the mountain that is suggested here and will be confirmed by more detailed analyses of the position of the surface front shown in Chapt. IV. On the lee side, a secondary cyclone forms with its own warm and cold sector advection. The formation of a high pressure nose on the upstream side of the mountain can also be noticed.

In Fig. III.4.a, b and c are shown the 850mb geopotential maps and wind barbs for 00 GMT on March 4, 5 and 11, respectively. The 850mb level is above the boundary layer and below the mountain top. In all the three cases presented here as well as in the other cases not shown, there is usually a significant cross isobaric flow close to the mountain indicating strong ageostrophic effects related to the topography. On March 4, in Fig. III.4.a, we are in the prefrontal regime with the pressure drag vector pointing southward. The flow is westerly north of the mountain but becomes south-westerly closer to it. In Fig. III.4.b, 24 h later, the situation has changed quite drastically. The flow is now almost northerly north of the Alps but becomes blocked and diverted as it approaches the mountain. At that time we are in the post frontal regime with the pressure drag on the atmosphere pointing northward. The prefrontal regime on March 11, 00 GMT shown in Fig. III.4.c gives an indication of the degree of similarity between cases when compared with Fig. III.4.a.

3.2 Cross sections :

Two cross sections analyses of potential temperature through the front and the mountain during the interaction are presented in Fig. III.5 and III.6. The sections in Fig. III.5 are for the case of March 4-5 from Hoinka (1986) and extend from Ireland to southern Italy (the 295K isentrope has been outlined for easier comparison). On March 3 , 00 GMT the isentropes are almost flat around the mountain but the approaching front can be seen in the extreme left part of the figure and is advected towards the right. Twelve hours

later the front has reached the mountain and the isentropes can be observed to begin to rise upstream of the mountain, indicating the blocking of cold air. Very little change is also observed on the lee side (right part of the figure).

On March 4 at 12 GMT the cold air blocking becomes more pronounced, with a dramatic increase in the height of the isentropes compared with the previous figure on the upstream side, but with still very little change on the downstream side. This indicates that the cold air advection remains largely confined to the upstream side. On March 5 at 00 GMT the front finally crosses the mountain.

A very similar scenario emerges in the series of cross sections, from (10W, 60N) to (20E, 35N), shown in Fig. III.6 from Zehnder (1986), for the case of March 1-2. The blocking effect of the alpine barrier is also clear in these sections when the isentropes rapidly rises but only upstream of the mountain.

3.3 Time series:

The blocking effect of the mountain can also be observed if we compare the synoptic station time series on the north and south sides of the mountain. In Fig. III.7, such a comparison is performed for the stations of Payerne (north; in Fig. III.7.a) and Milano (south; in Fig. III.7.b) for both the potential temperature and the meridional wind. The solid, dashed and dotted lines represent the 850 mb, 700 mb and 500 mb levels respectively. Other stations were compared and were found to give essentially similar results.

In the potential temperature series, the frontal passages of March 2, 4, 11, 13 and 18 (see chapt. I) can clearly be identified at all levels in Fig. III.7.a, on the north side. However on the south side, in Fig. III.7.b, while the frontal passages can still be identified at the 500 mb and 700 mb levels they are practically invisible at 850 mb. Although these differences between the north and the south at low level could be caused by diversion of the air around the mountain or by diabatic effects, the cross sections above indicates that the cold air advection never reaches Milano because it remains blocked on the north side. Another

point to be made regarding these series is that the warm advection preceding the cold front also does not reaches Milano causing very small temperature variations at the 850 mb level compared to the northern station of Payerne.

The comparison between the wind time series in Fig. III.7.a and b cannot be made so easily, perhaps due to the larger wind fluctuations. One can however notice a general difference between the north and the south with regards to the variability, in particular for the 850 mb level. A closer look also reveals that, preceding all frontal passages (March 2, 4, 11, 13 and 18), there is a peak in the southerly wind at the 850 mb level for the northern station of Payern, that is possibly related to the shallow south foehn commonly observed on the north side of the Alps in prefrontal conditions (Smith, 1986).

3.4 Isentropic Analyses:

Examples of isentropic analyses for the case of March 11, which were performed by B. Wyman at GFDL, are shown in Fig. III.8. They provide additional illustration of the effect of the mountain on the cold, high potential vorticity air advection. All the results presented here are for the 290K isentropic surface.

In Fig. III.8.a the pressure level of the surface is plotted for March 11, 00 GMT, indicating the presence of cold air. There is also a noticeable pressure gradient across the mountain on this isentropic surface, which implies that the cold air is confined to the north side of the mountain.

This confinement on the upstream side is most likely a consequence of the flow blocking, already revealed by the previous analyses, and is consistent with the advection pattern indicated in Fig. III.8.b by the Montgomery streamfunction. The streamfunction shows that the flow is retarded in the central part of the mountain, as inferred from the difluent pattern, but also diverted around the edges.

A further indication of the blocking behavior can be seen in the evolution of potential vorticity between 0 and 12 GMT in Fig. III.8.c and d. Under adiabatic and frictionless

conditions, approximately satisfied at the level considered, the potential vorticity is a conserved quantity which is advected like a passive tracer. The potential vorticity in Fig. III.8.c is therefore, to first approximation, advected by the flow shown in Fig. III.8.b to produce the pattern in Fig. III.8.d, where the effect of the mountain appears clearly: it has stopped the high potential vorticity advection.

One caveat must however be placed here about the reliability of these isentropic analyses. The upper air data network was found barely sufficient for such analyses in the Alpine region and the high gradients above the topography have the potential to create important interpolation errors. In addition other cases did not show such a clear effect although it could be argued that the case of March 11 is special in this respect.

4. DISCUSSION:

In this chapter we have seen from the observations that the synoptic gradients are too weak to account for the observed pressure drag. In addition the aircraft observations in the previous chapter have ruled out the possibility that a substantial part of the missing drag can be accounted for by vertically propagating waves. As a first step towards understanding these features we have also examined here additional observations of the front–mountain interaction.

From all our sources it appears that the observed blocking of cold advection is an important part of this phenomenon. It is also a primary candidate to explain the strong pressure drag. But there are however several points remaining to clarify.

The first basic issue is to understand the cold front blocking itself and in particular its differences with the blocking of a uniform flow, already extensively studied. We must then explain the relation between blocking and drag because it is not a priori clear to which extent the drag depends on the amount of fluid blocked upstream. In fact it is only the fluid above the mountain slopes that hydrostically contributes to the pressure drag. It is also important to

clarify the mechanism creating the strong drag in the prefrontal stage, when the front is still on the north side of the mountain. In this situation the upper wind is westerly but a shallow southerly foehn is often observed.

To address these questions we will proceed as follows. In the following chapter we will first examine a simple layer model of the cold front advection. With this model we will be particularly interested in understanding the frontal progression and the pressure drag.

However, important effects are left out in this simplified model, such as the vertical propagation of waves or the secondary circulation associated with the front. The relative importance of all these effects will therefore be investigated in Chapter V, using a continuously stratified model .

Figure captions for Chapter III:

Figure III.1: Microbarograph measurements taken between 3/3/82, 12 GMT and 3/5/82, 00 GMT. (from Hoinka, 1986)

Figure III.2: Space-time sections of adjusted pressure through the Gotthard pass: a) for March 3-5, b) for March 11-13. The trajectory of the low pressure associated with the front is indicated by the dashed line. The pressure gradient across the mountain changes sign during the frontal passage (from Phillips, 1984)

Figure III.3: Synoptic surface maps at 12 GMT (Deutscher Wetterdienst analysis) for: a) March 4 and b) March 11. The surface front is strongly retarded in the central part of the Alps.

Figure III.4: 850 mb geopotential height at 00 GMT (Deutscher Wetterdienst analysis) for: a) March 4, b) March 5 and c) March 11. a) corresponds to the prefrontal stage, with mean westerly advection while b) and c) represent the post frontal stage with mean north-westerly advection.

Figure III.5: Cross section of potential temperature through the front, from Ireland to southern Italy, between March 4, 00 GMT and March 5, 12 GMT (from Hoinka, 1986). The cold air blocking is made visible by the rising isentropes.

Figure III.6: Cross section of potential temperature from 60N,15E to 35N, 20W between March 1, 00 GMT and March 2, 12 GMT (from Zehnder, 1986).

Figure III.7: Time series of potential temperature and southerly wind for: a) Payerne (northern side) and b) Milano (southern side). Solid, dashed and dotted lines represent the 850 mb, 700 mb and 500 mb level respectively. There is a marked difference in the potential temperature evolution at low level between the north and south side.

Figure III.8: Isentropic analyses on the 290 K surface: a) pressure at 12 GMT, b) Montgomery streamfunction at 12 GMT, c) potential vorticity at 00 GMT and d) potential vorticity at 12 GMT (analyses by B. Wyman, GFDL). The potential vorticity in c) is aprroximately advected by the streamfunction of b) and shows in d) the effect of the mountain.

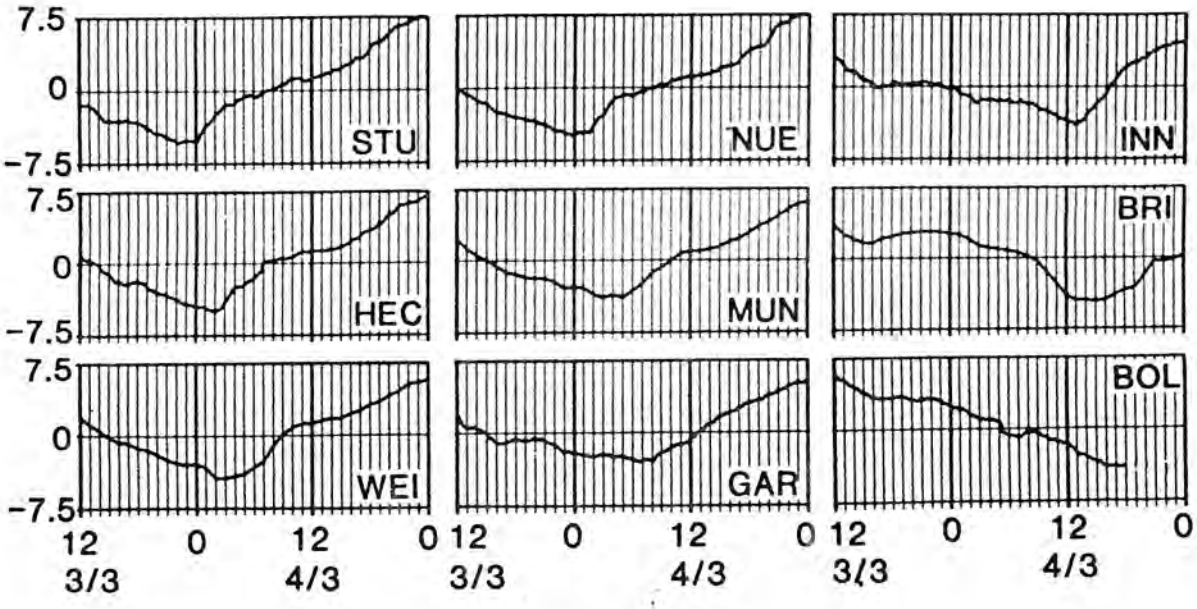

Figure III.1: Microbarograph measurements taken between 3/3/82, 12 GMT and 00 GMT 5/3/82. Shown are the pressure deviations (hPa) from the averaged values over this period. The abbreviations stand for Stuttgart (STU), Hechingen (HEC), Weissenau (WEI), Nuremberg (NUE), Munich (MUN), Garmisch (GAR), Innsbruck (INN), Brixen (BRI) and Bologna (BOL). (from Hoinka, 1986)

a

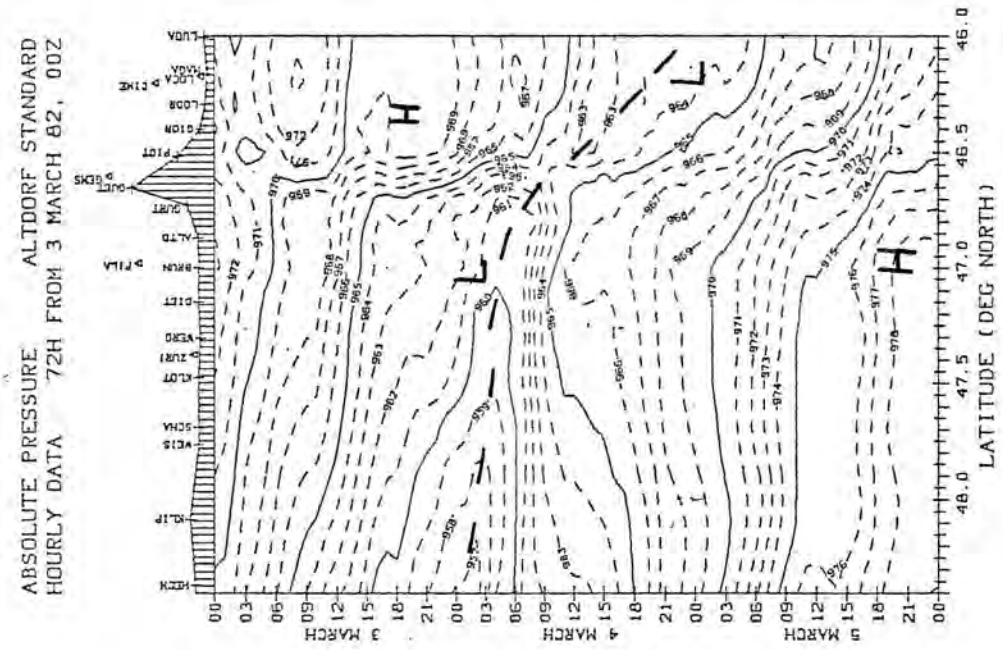

b

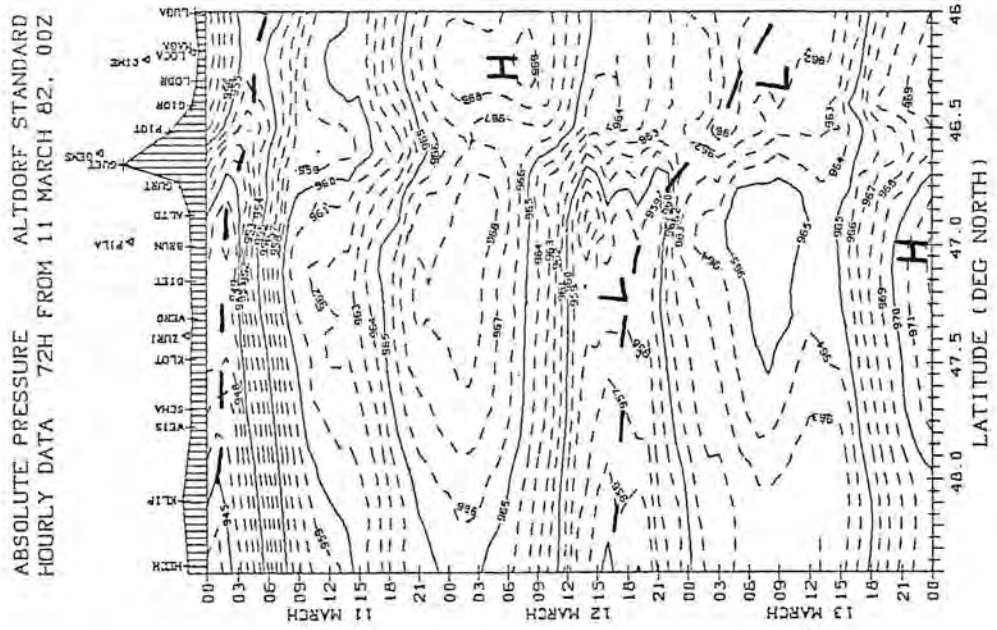

Figure III.2: Space-time sections of adjusted pressure through the Gotthard pass: a) for March 3-5, b) for March 11-13. The trajectory of the low pressure associated with the front is indicated by the dashed line. The pressure gradient across the mountain changes sign during the frontal passage (from Phillips, 1984)

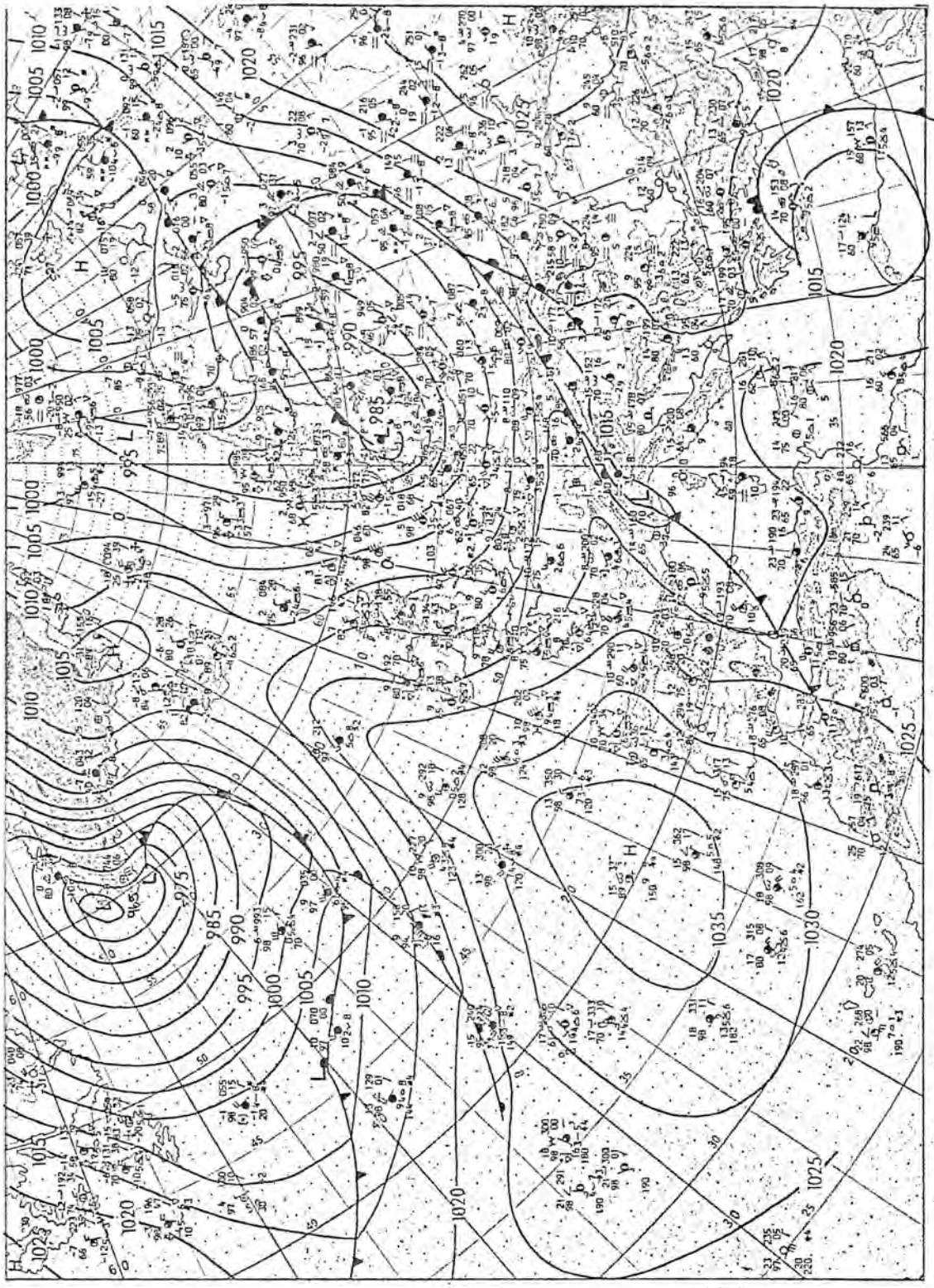

a

Figure III.3: Synoptic surface maps at 12 GMT (Deutscher Wetterdienst analysis) for: a) March 4 and b) March 11. The surface front is strongly retarded in the central part of the Alps.

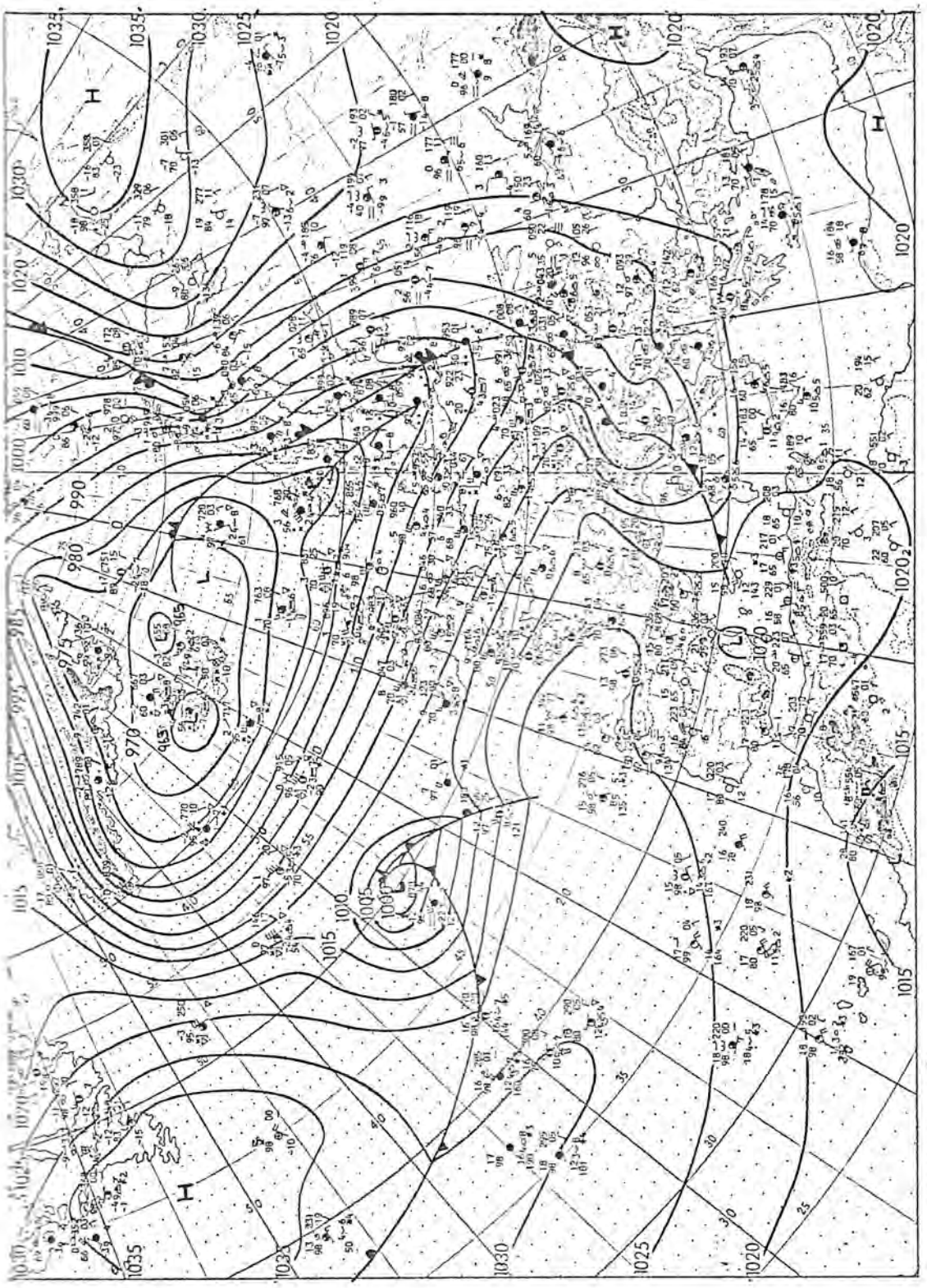

b

Figure III.3 (continue)

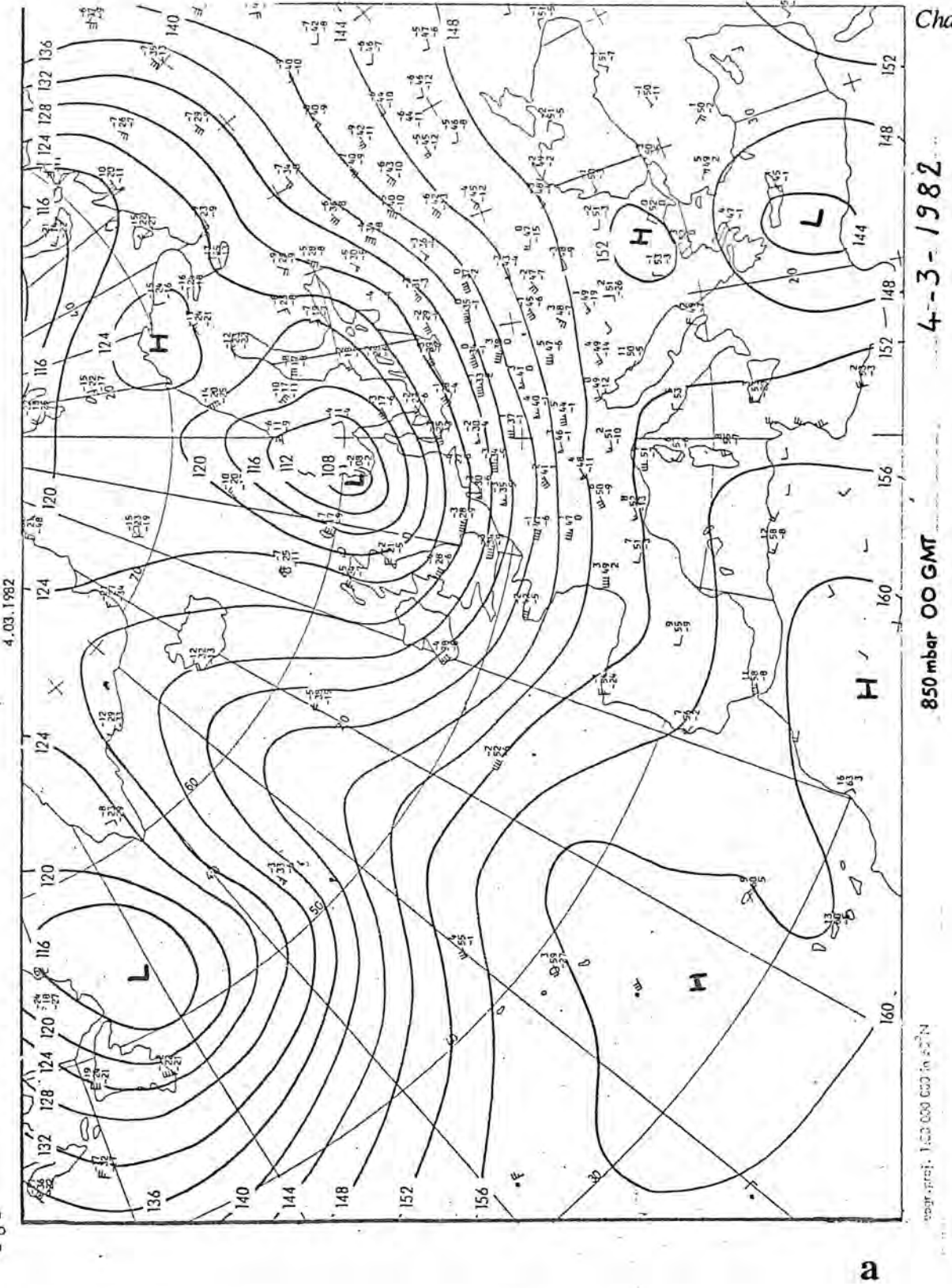

Figure III.4: 850 mb geopotential height at 00 GMT (Deutscher Wetterdienst analysis) for: a) March 4, b) March 5 and c) March 11. a) corresponds to the prefrontal stage, with mean westerly advection while b) and c) represent the post frontal stage with mean north-westerly advection.

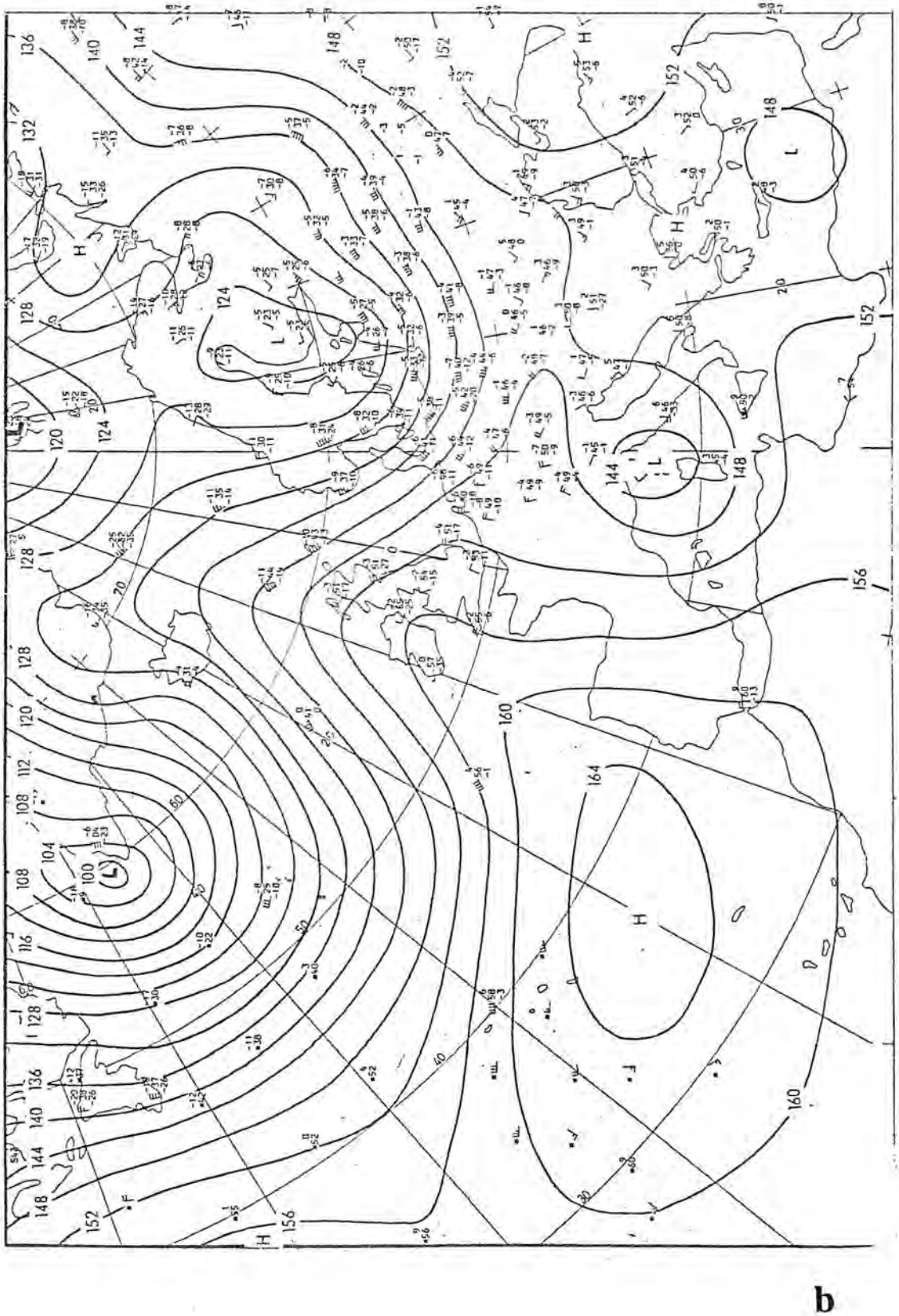

Figure III.4 (continue)

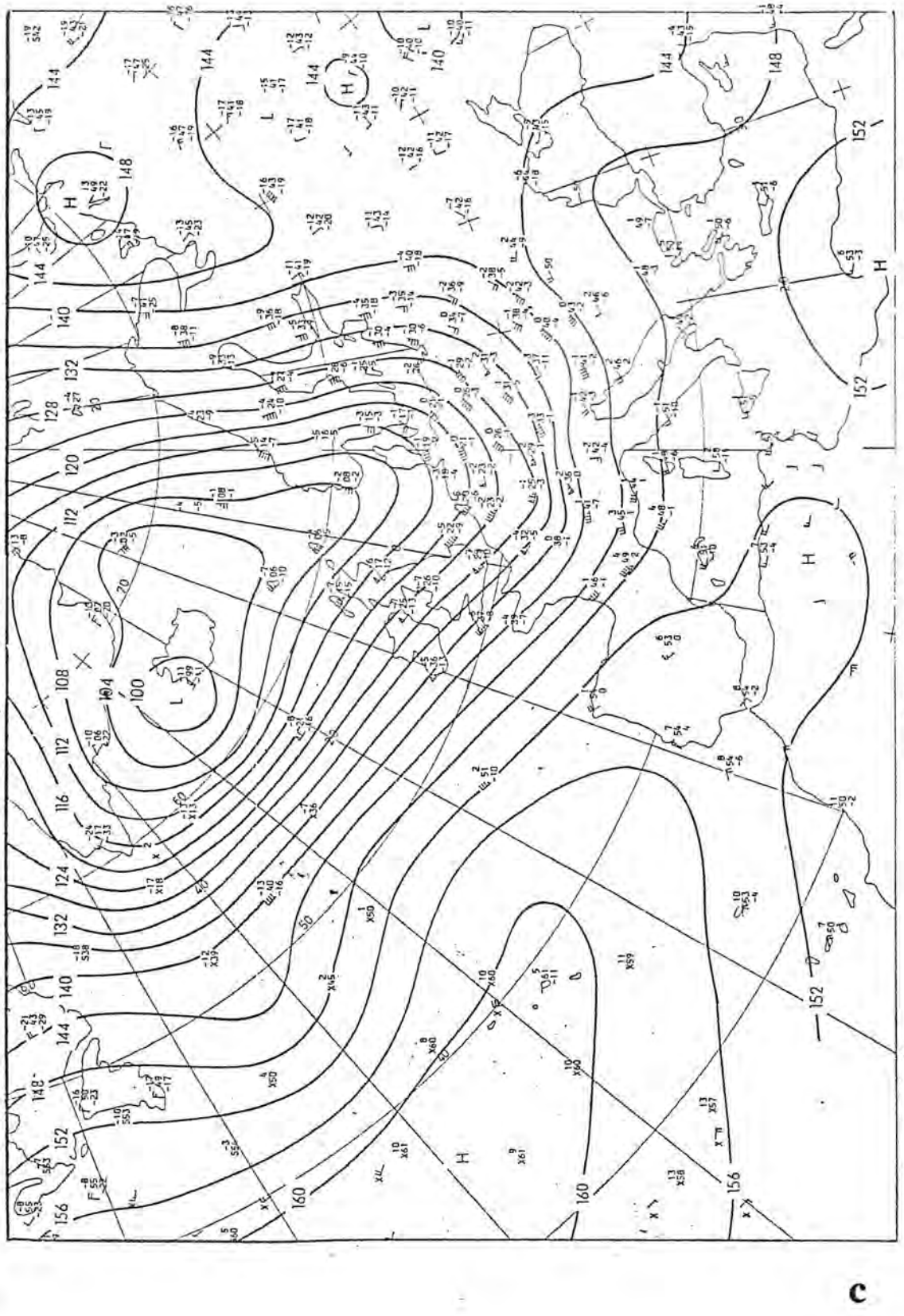

Figure III.4 (continue)

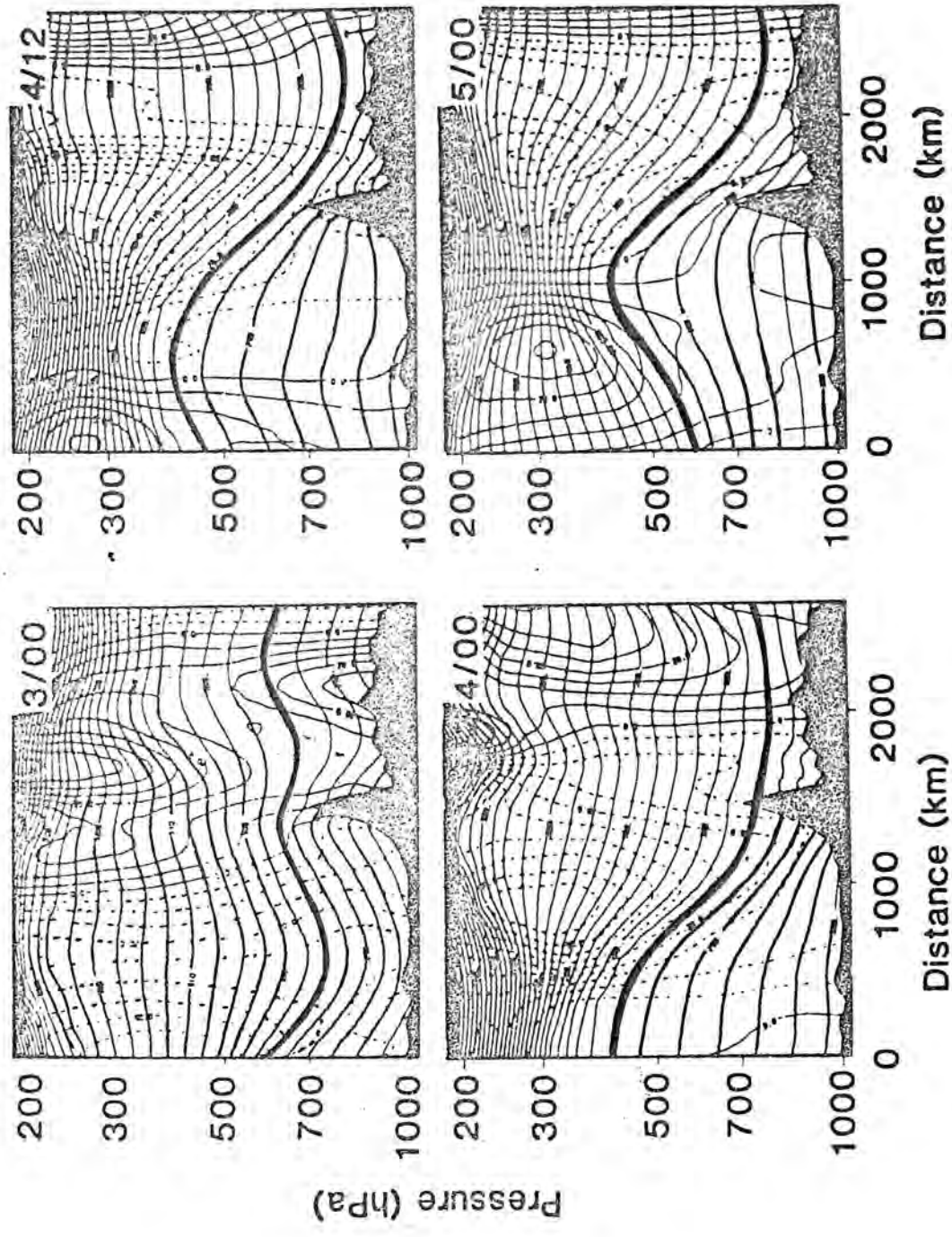

Figure III.5: Cross section of potential temperature through the front, from Ireland to southern Italy, between March 4, 00 GMT and March 5, 12 GMT (from Hoinka, 1986). The cold air blocking is made visible by the rising isentropes.

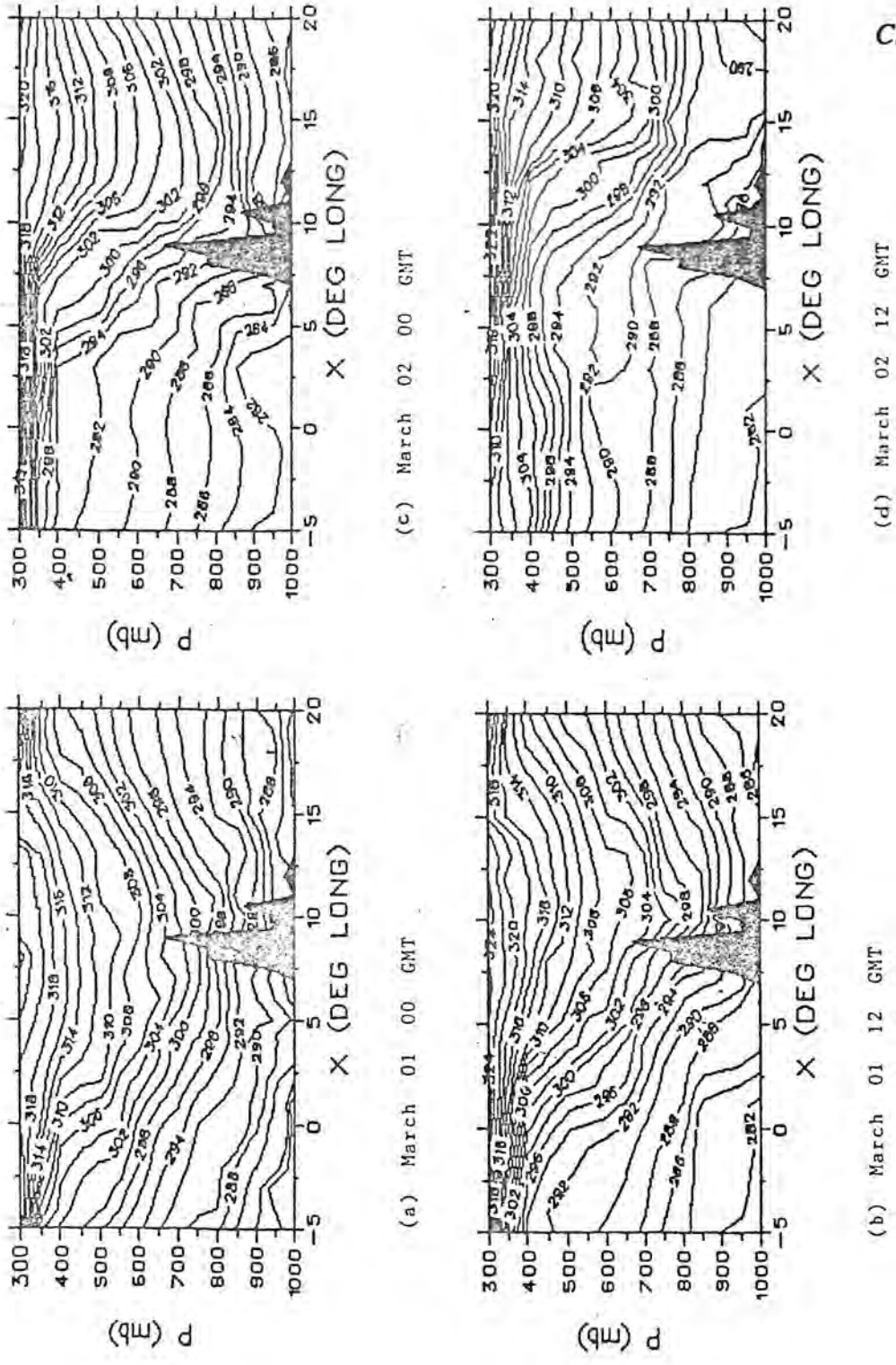

Figure III.6: Cross section of potential temperature from 60N,15E to 35N, 20W between March 1, 00 GMT and March 2, 12 GMT (from Zehnder, 1986).

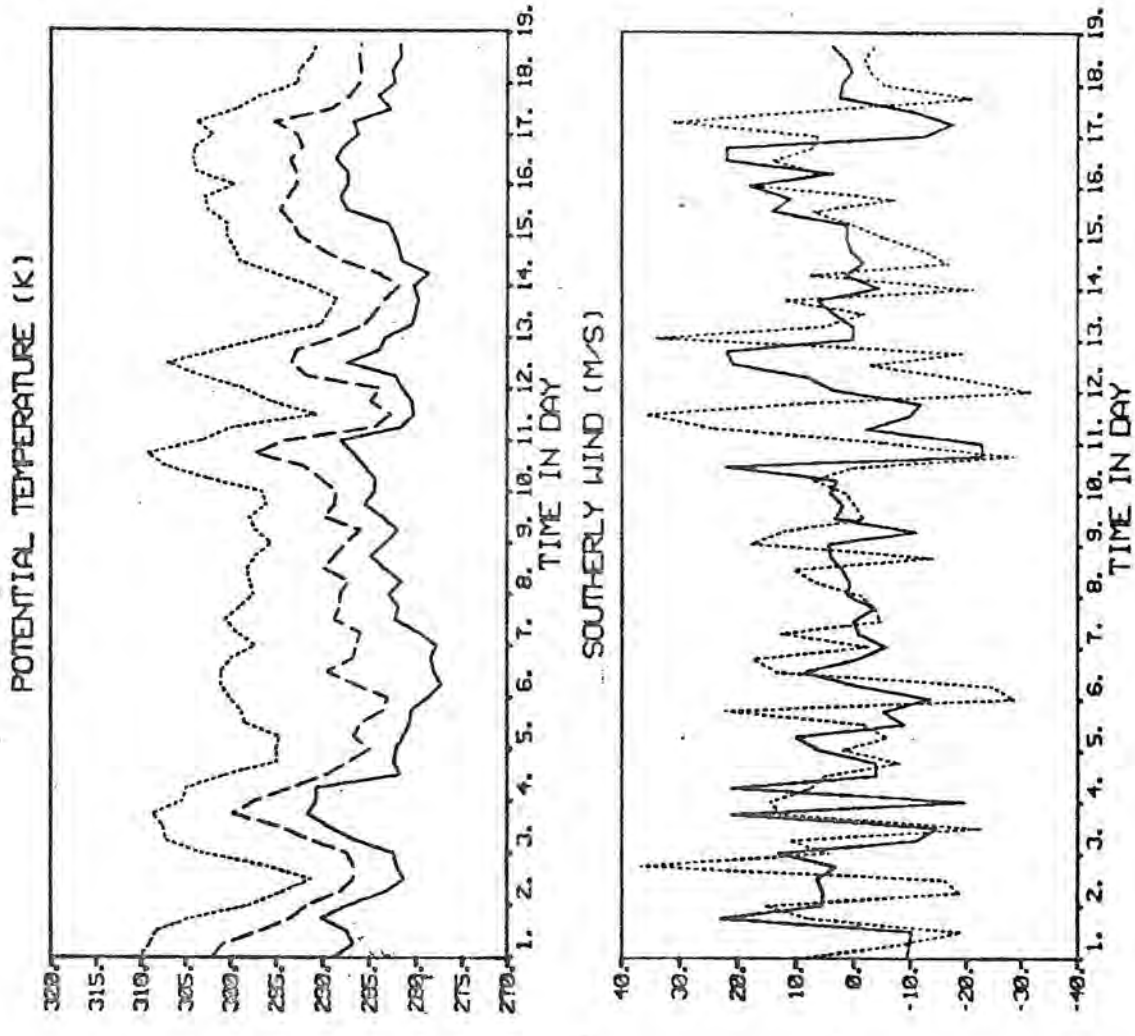

a **Payerne (Switzerland)**

Figure III.7: Time series of potential temperature and southerly wind for: a) Payerne (northern side) and b) Milano (southern side). Solid, dashed and dotted lines represent the 850 mb, 700 mb and 500 mb level respectively. There is a marked difference in the potential temperature evolution at low level between the north and south side.

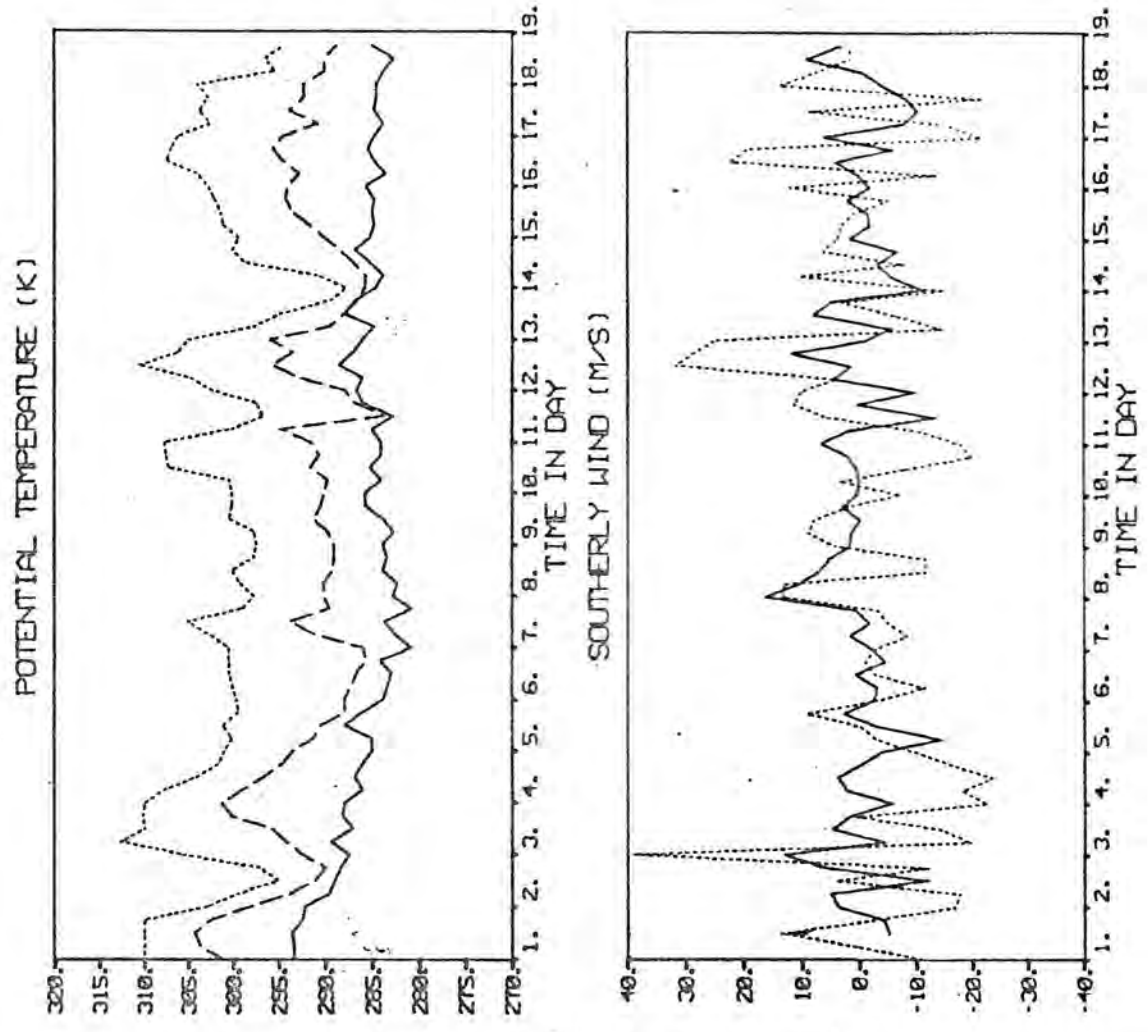

b **Milano (Italy)**

Figure III.7 (continue)

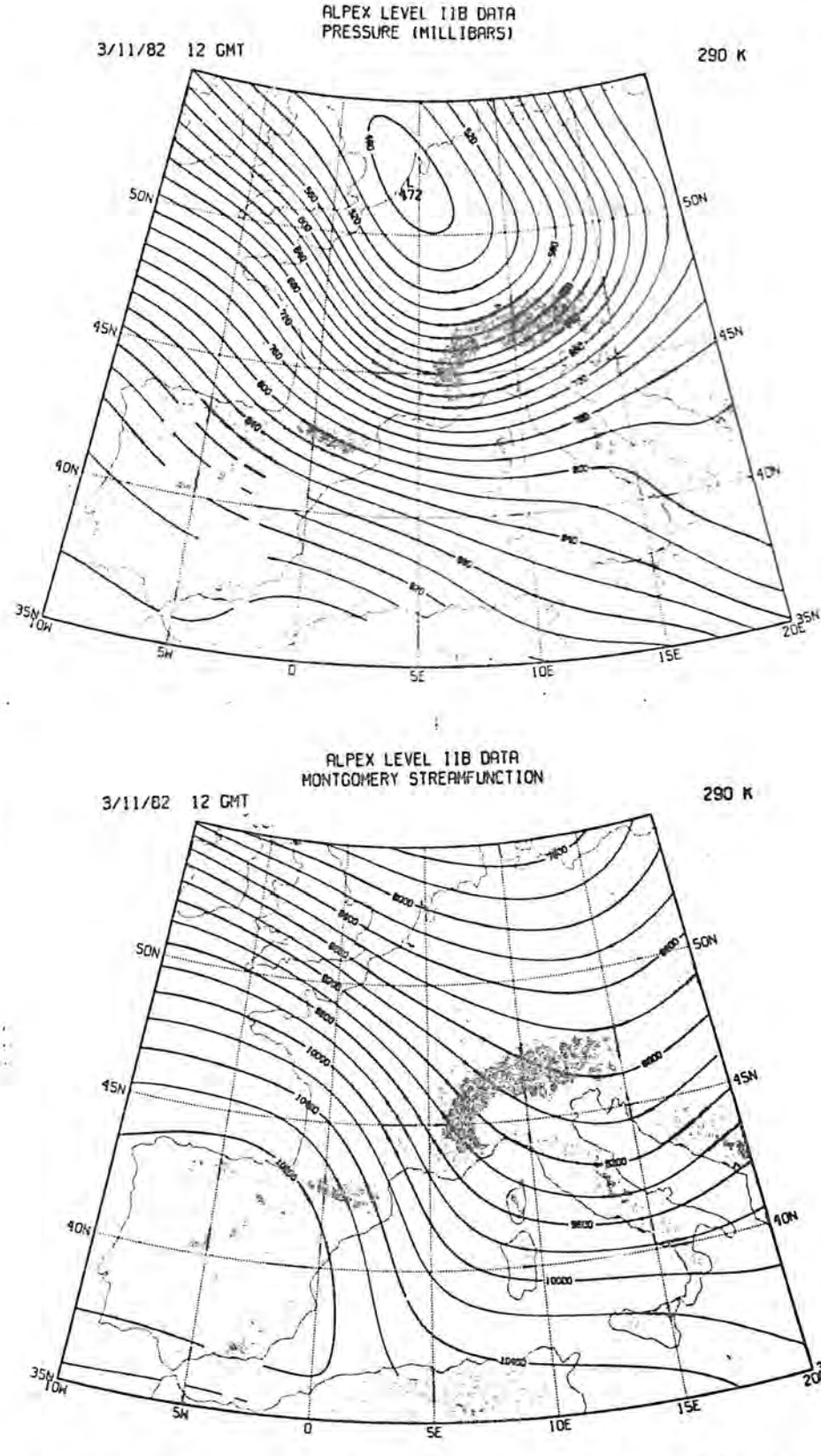

Figure III.8: Isentropic analyses on the 290 K surface: a) pressure at 12 GMT, b) Montgomery streamfunction at 12 GMT, c) potential vorticity at 00 GMT and d) potential vorticity at 12 GMT (analyses by B. Wyman, GFDL). The potential vorticity in c) is aprroximately advected by the streamfunction of b) and shows in d) the effect of the mountain.

c

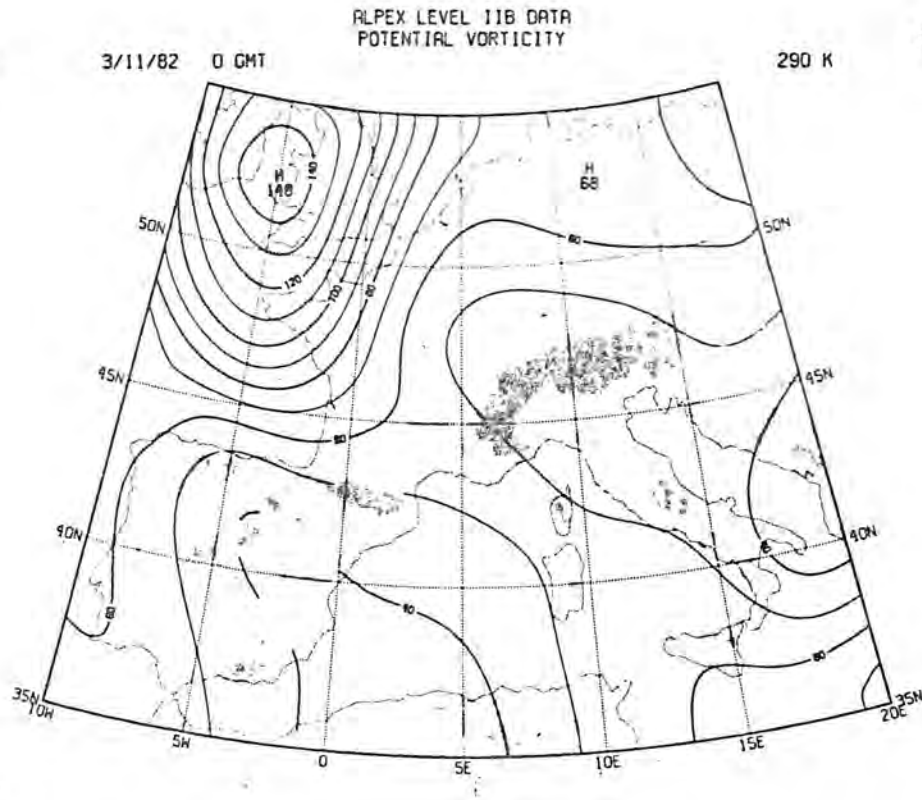

d

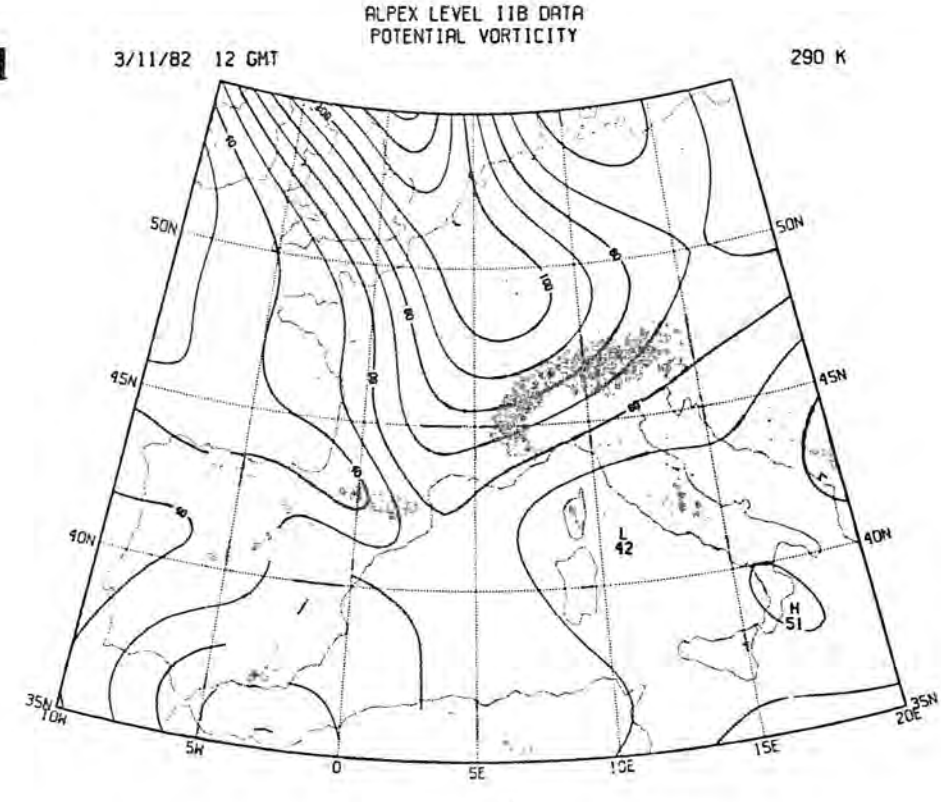

Figure III.8 (continue)

Chapter IV: A simple layer model of the front–mountain interaction

1. INTRODUCTION:

In this chapter we will examine the dynamics of the interaction between the cold front and the mountain using a simple layer model. We will describe the different regimes possible in general and discuss more particularly the case of the Alps.

Our discussion will focus primarily on two aspects of the interaction that have been well established by the observations, but have been the object of few theoretical studies. The first aspect is the effect of the mountain on the progression of the cold front, as compared to its progression over flat terrain. The second is the evolution of the pressure drag during the interaction, which has been discussed in Chapter I, for the observational aspects.

The qualitative effects of orography on fronts has been recognized since for example the work of Bjerkness and Solberg (1921) and are mentioned in the textbook by Pettersen (1941). The mountain is observed to increase the precipitation on the upstream side by a change of the vertical wind field (orographic uplifting) but also by the retardation of the front, because its associated precipitation structure remains longer upstream of the mountain. The phenomenon is well illustrated, for example, by the surface analysis of Steinacker (1981) (see Fig. IV.1.a) that shows the isochrone of a cold front and demonstrates the clear barrier effect of the mountain, the important effect of the valleys where the front penetrates more rapidly and the three dimensional distortion that occur in the later stages. The Alpine Experiment (ALPEX) also provides interesting examples such as the case of March 4, 1982 from Davies (1986), shown in Fig. IV.1.b. The time evolution of the precipitation for the same case in shown in Fig. IV.2, from Phillips (1984), for a series of stations arranged in a

north south cross section in the center of the Alps (Gotthard pass), indicated on the top of the diagram. There is a marked decrease in the propagation speed of the maximum precipitation which remains blocked on the upstream side of the main crest. Smith (1985) also gives references to similar observations in other parts of the world, that include the Rocky Mountains, the South African range, Taiwan... . The most salient feature of all these observations is the retardation of the surface front on the upstream side of the mountain. A different orographic effect is observed when the front is incident perpendicular to the barrier such as in the Andes (Orlanski, 1982) or in the Great Dividing Range of southeastern Australia (Baines, 1980).

It has been shown in Chapter I that all cases of frontal passage during ALPEX are associated with extremely large drag variations occurring in less than 24h (see the composite of drag evolution in Chapter I, Fig. IV.4 or the north-south component for individual cases in Chapter II, Fig. IV.4).

The efforts to understand and model these observations are going in at least two directions. The first approach is to consider that the mountain modifies the frontogenetic circulation and has been taken by Bannon (1984) and Zehnder (1986), who have relied on the semi-geostrophic approximation. Pierrehumbert (1984) used an idealization of the mountain forcing to examine the effect on the frontal circulation. In these studies the mountain is assumed to be broad, so that the Rossby number is small, and the blocking effect is small (Pierrehumbert and Wyman,1985). The case with a narrow mountain will be discussed in Chapter V.

The second approach is to consider the front as a material surface that is blocked and distorted by the mountain and is treated either as a passive tracer as in Smith (1982) or as a dynamically active element in the flow as in the two layer model of Arakawa and Okano (1976) and Davies (1984) (see Fig. IV.3). The same model is also used here because it represents the simplest case in which the ageostrophic effects are represented. It has,

however, the important shortcomings of being unable to reproduce the frontal circulation and also to neglect the effects of vertically propagating gravity waves. With regards to flow blocking, this last omission might not be too consequential because recent numerical experiments have shown a close affinity between the behavior of continuously stratified models and the one layer hydraulic theory (Bacmeister, 1987). This idealized model can also be thought of as an attempt to isolate the first order effect (neglecting the secondary circulation) of the front on the flow.

None of these previous investigations have considered the pressure drag that occur during the front–mountain interaction and this issue will therefore be addressed here.

The representation of a front by a two layer system dates back to Margules (1906) and has since been used in numerous applications. The linear stability of this model was investigated, among others, by Orlanski(1968) and Kasahara and Rao (1972). The model has also been used to numerically study the non-linear development of frontal waves, for example by Stocker (1967) , Kasahara et al. (1965) and Sinton and Mechoso (1984).

Davies (1984) obtained an analytical theory of the orographic distortion of a cold front. An exact non linear solution is obtained if the flow is assumed to remain semi–geostrophic, meaning that the velocity along the front , V, remains geostrophically balanced but not the velocity across the front, U. It is also assumed that the front has initially a uniform potential vorticity, a condition that imposes the initial shape of the interface. The solution is found to depend only on two parameters:

- the rotational Froude number $r = f a / \sqrt{(g'H)}$, where f is the Coriolis parameter, a the total mountain width, g' the reduced gravity across the interface and H the upstream frontal height. "r" represents the ratio of rotational to gravitational effects ,
- the front-mountain vertical aspect ratio $\alpha = H/B$, where B is the mountainheight.

The blocking of the front is strongest when r and α are small as indicated in Fig. IV.4 which represents time isolines (in nondimensional units of the advection time

scale) of the position of the surface front as a function of the front-mountain aspect ratio α and for two different rotational Froude numbers, r. For example in the case $r^2 = 10$, when the mountain is very small compared with the front (e.g. $\alpha = 10$), the front is almost unperturbed during its passage: $x^*(t^*) \approx t^*$, in nondimensional terms. If the mountain height is increased (e.g. $\alpha = 2$) then the front is retarded, $x^*(t^*) < t^*$, on the upstream side, $x^* < 0.5$, and accelerated on the downstream side. If the mountain height is further increased (α decreased) or if the rotational Froude number is increased, then these effects become more important. The hatched region on the diagrams indicates where the solution does not exists. With a detailed analysis of the solution near the boundary of this hatched region, Davies (1984) showed that the solution breaks down because the speed of the surface front becomes infinite. This can happen in the semi-geostrophic theory due to the neglect of the acceleration term in the U-momentum equation that would prevent such a catastrophic breakdown in the full system.

Arakawa and Okano (1976) on the other hand used a numerical model to compute the distortion by a mountain of a front with initially constant slope. They defined differently the three adimensional parameters for the problem as follows:

$Ro' = V_S / f L'$ a Rossby number based on the shear in the along-front velocity V_S, that is initially related to the frontal slope by Margule's formula; L' is half the total length of the mountain

$Ri = g' B / V_S^2$ a Richardson number where g' is the reduced gravity and B is the bottom topography height

$U_0 = U / V_S$ where U is the frontal advection speed towards the mountain.

This choice of the Rossby and Richardson numbers has commonly be adopted in frontal instability studies (see Kasahara and Rao, 1972) but we find preferable here, because we are primarily interested with the mountain effects, to choose the advection speed U as our basic velocity scale. The redefined adimensional parameters are therefore:

$Ro = U / f L$ where $L=L'/2$

$Fr = U / \sqrt{(g' B)}$ the Froude number

with additional geometrical parameters defining the frontal slope. These parameters are now similar to those used by Davies (1984).

Table IV-1

exp #	$Ro'=V_s/ f L'$	$R_i=g'h_m/V_s^2$	$U_0= U/V_s$	$Ro= U/ fL$	$Fr=U/\sqrt{(g'h_m)}$
1	2.0	0.5	0.75	0.75	1.06
2	2.0	1.0	0.75	0.75	0.75
3	4.0	0.5	0.75	1.5	1.06
4	4.0	1.0	0.75	1.5	0.75
5	2.0	0.5	1.5	0.75	2.12
6	2.0	1.0	1.5	0.75	1.5

Arakawa and Okano (1976) present results of six experiments for the parameters indicated in Table IV-1. together with their redefined counterparts. In Fig. IV.5 the surface front velocity is plotted, for each experiment, as a function of the adimensional distance across the mountain (the origin is at the mountain top). We can see in Table IV-1 that the experiments cover a small region of the parameter space for $Ro \approx O(1)$ and $Fr \approx O(1)$ that explain the overall similarity between the curves: the surface front is decelerated on the upstream side of the mountain and accelerated on the downstream side. On closer look, however, important differences can be noticed. For each pair of experiment with the same Rossby number (Ro) (for example 1 and 2) the perturbation velocity is a strong decreasing function of the Froude number (Fr), indicating the important influence of the frontal strength, taken into account in the reduced gravity g', and the mountain height B. Similarly, for each pair of experiments with the same Froude number (for example 1 and 3) the perturbation velocity is a weaker, increasing, function of the Rossby number, indicating that the rotation tends to moderate the decelerations. The experiment with the smallest Ro and the largest Fr ,

experiment 5, is also the one with the weakest frontal perturbation.

In summary these two studies have shown, for a fixed geometry, that:

- for small Rossby number (semi-geostrophic regime) the solution depends only on the rotational Froude number r=Fr/Ro

- for $Fr \approx O(1)$ and $Ro \approx O(1)$ the frontal retardation is an increasing function of Fr and Ro.

In addition a common feature of these two models is the acceleration of the front over the crest of the mountain which is also found by Bannon (1984) and Zehnder (1986).

In this study we address the following remaining questions: what happens in the regimes that have not been explored yet, in particular in the case Ro>1 which is relevant for the Alps; what is the solution in the regimes where the semi-geostrophic approximation predicts a breakdown; what are the differences between this problem and the classical hydraulic theory and in particular is there an analog of the supercritical regime ($Fr < 1$) in which the front would accelerate over the topography. In addition we will examine the influence of other factors such as the steepness of the frontal slope and the height of the mountain.

In section 2 we will present the model and the equations of motion. Following the discussion of the frontal retardation in section 3, we will examine the drag created during the interaction with the mountain and its effect on the cold air flow in section 4 . The principal questions addressed will be: what are the parameters that influence the magnitude of the drag and what are the different effects of this drag on the flow in terms of the momentum budget for a limited domain surrounding the mountain.

Finally in section 5 we discuss the applicability of these results to the Alpine case, the influence of smoothing of the orography on the interaction and discuss the model shortcomings.

2. EQUATIONS OF MOTION:

We consider a one layer model with an interface intersecting the ground, forming a surface front, and study its interaction with a mountain range (see Fig. IV.3). The front is initially in geostrophic balance with its along front velocity V and is advected toward the mountain at the uniform speed U.

If there is no mountain, the front retains its balanced state and simply moves across the domain. The presence of the mountain causes a distortion of the front as it moves over the topography that typically affects the position of the surface front and modify the surface pressure gradient that is initially associated with the frontal structure.

In the following discussion we have made several assumptions, identical to those made by Davies (1984) and Arakawa and Okano (1976). The fluid is assumed to be hydrostatic and homogeneous. The shallow water and f-plane approximations are made. The flow is subject to a reduced gravitational effect (g') and an imposed pressure force P, representing the influence of the warm air upon the cold air flow.

The equations of motion for this system are:

$$\begin{cases} du/dt + g' \partial h/\partial x - f v = - g' db/dx - 1/\rho \ \partial P/\partial x & \text{(IV.1)} \\ dv/dt + f u = - 1/\rho \ \partial P/\partial y & \text{(IV.2)} \\ dh/dt + h \ \partial u/\partial x = 0 & \text{(IV.3)} \end{cases}$$

where:

u,v are horizontal velocities

h is the layer thickness

b is the bottom topography

g' is the reduced gravity at the interface

P is the upper layer pressure forcing

The basic state (represented by capital letters) is a steady translating solution in

geostrophic balance in the absence of the mountain :

$$g' \, dH/dx - f \, V = - 1/\rho \, \partial P/\partial x \qquad \text{(IV.4)}$$

$$f \, U = 1/\rho \, \partial P/\partial y \qquad \text{(IV.5)}$$

$$DH/Dt = 0 \qquad \text{(IV.6)}$$

with

$$U = V = cst \qquad \text{(IV.7)}$$

$$H(x,t) = H(x-Ut) \qquad \text{(IV.8)}$$

$$D/Dt = \partial/\partial t + U \, \partial/\partial x \qquad \text{(IV.9)}$$

3. RETARDATION OF THE SURFACE FRONT:

In this section we describe the effect of the mountain on the position of the surface front. The different regimes possible in our idealized model are discussed and compared, when possible, with the previous studies of Davies (1984) and Arakawa and Okano (1976).

3.1 Linear perturbation theory

By looking at Eq. IV.1 one can see that the solution will be a small perturbation of the basic state in the cases where the forcing term g'db/dx is small, that is, either for a small mountain or for a weak density jump across the interface.

In trying a straightforward expansion where u', v' and h' are the basic state perturbation one easily finds that the approximation $h' << H$ is not uniformly valid near the surface front. On the other hand this expansion gives the classical results of linear hydraulic theory in the post frontal region where H=cst.

In order to study the region close to the surface front, we seek a solution that is uniformly valid and expand the basic state using a strained coordinate, in term of a small parameter ε that will be made precise later. We remark in passing that we have three functions to represent the perturbation:

$$x = s + \varepsilon\, x'(s,t) \qquad \text{(IV.10)}$$

$$h(x,t) = H\,(\,s-Ut\,) \qquad \text{(IV.11)}$$

$$v(x,t) = \quad \varepsilon\; v'(s,t) \qquad \text{(IV.12)}$$

$$u(x,t) = U + \varepsilon\; u'(s,t) \qquad \text{(IV.13)}$$

This expansion is now not uniformly valid in the post frontal region: at a given x the height perturbation is given by $h(x,t) - H(x,t) = - \varepsilon\, dH/dx\; x'$ and therefore the approximation will break down where $dH/dx \approx 0$. A more general form of the perturbation will be required to treat the general case but here we are mainly interested in the dynamics of the frontal zone rather than the post frontal zone and we will assume that $dH/dx \neq 0$.

In order to nondimensionalize the equations we use the following scales:

U for u'

L for all lengths

f L for v' (given by Eq. IV.2)

B for the mountain height

S for dH/dx , typical slope for the front

and we obtain the following system for the perturbation (order ε), retaining the same notation for variables which are now adimensionalized:

$$\begin{cases} Du'/Dt + \dfrac{g'SL}{U^2} dH/dx\; \partial x'/\partial x - \dfrac{f^2L^2}{U^2} v' = -\varepsilon^{-1} \dfrac{g'SL}{U^2} \dfrac{B}{SL}\; db/dx & \text{(IV.14)} \\ \\ Dv'/Dt + u' = 0 & \text{(IV.15)} \\ \\ - dH/dx\; Dx'/Dt + \partial(Hu')/\partial x = 0 & \text{(IV.16)} \end{cases}$$

with $D/Dt = \partial/\partial t + \partial/\partial x$.

The problem depends on three nondimensional parameters: the Rossby number $Ro = U/(fL)$, the Froude number $Fr = U/\sqrt{(g'SL)}$ and the mountain-front vertical aspect ratio

B/(SL). This model will be used mainly to study the limiting regimes and to obtain a preliminary mapping of the parameter space for the numerical experiments described afterward.

3.2 Limiting regimes of the linear model:

The solution of the linear system IV.14-IV.16 is considerably simplified if one of the terms on the l.h.s. of Eq. IV.14 dominates the response to the forcing term on the r.h.s. However the solutions obtained by this simple approach cannot be expected to be uniformly valid in space and time. For example, even if the rotational effects are initially insignificant they will eventually become important for longer times.

Case a) : $Ro \gg 1$, $Fr \gg 1$, $\varepsilon = g'B/U^2$.

Eq. IV.14 reduces to:

$$Du'/Dt = db/dx \, . \qquad \text{(IV.17)}$$

Its solution satisfying the initial condition that $u' = 0$ is:

$$u' = - (b(x) - b(x-t)) \, . \qquad \text{(IV.18)}$$

If the origin of the x axis is the initial position of the surface front then its subsequent undisturbed position is $x_0 = t$. The perturbation velocity at the surface front is therefore $u'_0 = - b(t)$. From the continuity equation (IV.16) one can then compute the perturbed position of the surface front (for which H=0):

$$x'_0 = - \int_0^t b(\tau) \, d\tau \, . \qquad \text{(IV.19)}$$

This perturbed position, plotted in Fig. IV.6 (curve a), shows that the surface front is subject to an increasing retardation that is asymptotically equal to the volume of the mountain, in nondimensional terms. In dimensional terms the deceleration is proportional to $\varepsilon = g'B/U^2$ which shows that the frontal retardation is proportional to both the frontal strength and the mountain height whereas it is inversely proportional to the square of the mean incoming flow speed.

Case b) : $Ro<<1$, $Ro/Fr<<1$, $\varepsilon = g'B/f^2L^2$.

By combining Eqs IV.14 and IV.15 one finds that:

$$u' = - d^2b/dx^2 . \qquad (IV.20)$$

The initial condition, u'=0, cannot be satisfied exactly as it is not in geostrophic balance and we have neglected the terms which permit the rapid initial adjustment to take place. As in the previous case one can now find the perturbed position of the surface front using Eq. IV.16:

$$x'_0 = - db(t)/dx + db(0)/dx. \qquad (IV.21)$$

This function is plotted in Fig IV.6 (curve b) and shows that the surface front is initially retarded as in the previous case but has regained its undisturbed position when it reaches the mountain top. On the lee side of the mountain the surface front is ahead of its undisturbed position. In this regime the frontal retardation is inversely proportional to the square of the mountain width while remaining proportional to the frontal strength and the mountain height.

Case c) : $Fr<<1$, $Ro/Fr>>1$, $\varepsilon = B/SL$.

Eq. IV.14 now gives us:

$$dH/dx \; \partial x'/\partial x = db/dx. \qquad (IV.22)$$

Both the shape of the mountain and the shape of the front enter this equation which is therefore difficult to solve in general. For the purpose of illustration we will further assume that the frontal slope is constant (-1 in adimensional terms):

The solution is then:

$$x' = - b , \qquad (IV.23)$$

for all time. Together with the continuity equation (IV.16) they give:

$$\partial(Hu')/\partial x = - db/dx \qquad (IV.24)$$

which has the solution:

$$u' = (b(x)-b(t)) / (x-t) \qquad \text{(IV.25)}$$

satisfying the boundary condition $Hu'= 0$ at $x=t$. The perturbed position of the surface front is therefore:

$$x'_0= - b(t) \qquad \text{(IV.26)}$$

and is plotted in Fig. IV.6, curve c.

As in the other two cases the front is initially retarded but as in the previous case, regains its undisturbed position, but, this time, when it reaches the base of the mountain on the lee side. In this regime the frontal retardation only depends on the ratio of mountain slope to frontal slope

3.3 Non linear numerical model:

In order to extend the results to more general situations and also to examine the non linear effects, we have also used a numerical model to solve the system IV.1-IV-3. The main originality of this problem is found in the treatment of the surface front, which is a free boundary in the problem. This free boundary can be treated by tracking it using a Lagrangian method,a method that has been used by Houghton and Kasahara (1968) on a similar problem in conjunction with the Lax-Wendroff scheme and by Arakawa and Okano (1976) in conjunction with a Leapfrog scheme but that required frequent spatial smoothing of the solution.

Another possibility is to use a purely Eulerian scheme for the entire problem as suggested by Sielecki (1968, 1970). In this method the free boundary is not tracked explicitly but by its surrounding grid points which are called "underwater" and "underground" respectively, in reference to the initial application of the method to coastal storm surge prediction. All underwater points are updated using the equations of motion. For the underground point we cannot use the entire set of equations of motion because of the instability that would develop as a consequence of the negative depth at the underground

point. Instead, as suggested by Sielecki, one should use the equations of motion in combination with extrapolation from the underwater points.

In this study we have used equivalently both methods and we have verified that they give the same results. A more detailed description and the comparison can be found in . Although the results were equivalent in terms of accuracy, the purely Eulerian scheme was found simpler and more efficient, and was developed in anticipation of the future extension of the model to the case of a three dimensional mountain .

In the full numerical model, the frontal zone is of finite extent and is followed by a post frontal region where the interface height becomes constant . In this case we define our Froude number by $Fr= U / \sqrt{(g' H_F)}$ where H_F is the post frontal interface height. There are now two additional parameters characterizing the frontal zone : L_F / L_M and H_M/H_F , the horizontal and vertical aspect ratio between the front and the mountain.

3.4 Numerical results:

3.4.1 Influence of Ro and Fr on the maximum frontal retardation:

First we examine a series of experiments in which only the Rossby and Froude number are varied. The initial front and the mountain are kept identical in these experiments. An example of the frontal interface at different time is shown in Fig. IV.7 for $Fr=Ro=H_M= 1$. Although rotation is important both an upstream bore and a downstream jump can be observed. Here we concentrate mainly on discussing the retardation of the surface front.

Table IV-2 summarizes the experiments by presenting the maximum frontal retardation (x'; adimentionalized by the mountain length scale L). Fig. IV.8 shows contours of maximum retardation in the Ro-Fr plane based on Table IV-2. One can verify that for large Ro the solution depends only on Fr, in agreement with the linear theory of section 3.2 for small Fr, whereas for small Ro the solution depends only on Fr/Ro, in agreement both with the linear theory and the non linear semi-geostrophic solution of Davies (1984).

Table IV-2

Fr \ Ro	0.2	0.5	1.	2.	4.
0.1	-0.6	-1.0	-3.8		
0.2	-0.3	-0.8	-1.9	-4.8	
0.5	-0.1	-0.3	-0.6	-1.0	-1.2
1.		-0.1	-0.3	-0.4	-0.5
2.			-0.1	-0.1	-0.2

This diagram is also comparable to Fig. IV.14 in Pierrehumbert and Wyman (1985) which represents contours of constant upstream blocking for a uniformly stratified flow. The similarity is remarkable because the stratification, in our idealized model, is concentrated in the frontal zone whereas it is uniform in Pierrehumbert and Wyman and also because the frontal retardation can be temporary, as we have seen.

We now examine in more details the position of the surface front as a function of time, when the Rossby and Froude number are varied.

3.4.2 The time evolution of the surface front position:

In this section we again extend the linear results obtained in section 3.1 and (see in Fig. IV.6) to the non linear regime . Fig. IV.9 present the perturbation of the surface front position relative to the position it would have in the absence of the mountain.

In Fig. IV.9,a we see the influence of the Froude number for a given Rossby number where as Fig. IV.9,b shows the influence of Ro for a given Fr. The non linear curves presented have similarities with the linear limiting regimes, in particular the curves (Fr,Ro)= (.2,2.), (.2,.2) and (.1,1.) with curves a, b and c in Fig. IV.6; these curves are the nearest to the linear regime although they are far from satisfying the conditions required for a strict comparison. These figures also provide some insight into the transition from one limiting

regime into another, for example from small to large Ro in Fig. IV.9,b.

The major non linear effect that is apparent from these figures is the cumulative retardation of the surface front that causes the maximum retardation point to be delayed in time. Consequently, if the front returns to its undisturbed position it is at a later time than predicted by the linear theory.

An extreme behavior is observed in Fig. IV.9.a for Ro=1.and Fr=0.1, when the front becomes totally blocked. In this case the frontal retardation increases linearly with time (proportional to t in adimensional terms). From the equations of motion (IV.1-IV.3) there is a suspicion that this total blocking cannot last forever. If u remains zero in Eq. IV.2 then v accelerates and eventually becomes large enough to possibly overcome the pressure gradient term in Eq. IV.1 and accelerate u back toward its original value. The numerical model cannot settle this question regarding the behavior as $t \rightarrow \infty$ but shows that the time scale for this process is so large so that the front can be considered blocked for all practical purposes.

In Fig. IV.9,c both Ro and Fr are varied but the ratio Fr/Ro is kept constant. This ratio is the parameter that governs the strength of the blocking in the semi-geostrophic limit. The solution of Davies (1984) is indicated by crosses and is in very good agreement with our numerical results for Ro=0.2. Although the precise shapes of the curves change markedly with Ro, the maximum retardation remains almost constant for Ro<1 indicating that the rotational Froude number Fr/Ro control the strength of the frontal retardation for Ro up to 1. For Ro=2 there is a significant departure from the semi geostrophic solution, not only in the maximum but also in the general shape, as the surface front does not overshoot its undisturbed position.

We saw earlier that the semi-geostrophic solution can break down, for sufficiently high mountain, because the surface front speed becomes infinite. The solution presented in Fig. IV.9.c, curve a (Ro=0.2, Fr=0.1) show signs of this behavior although it is not in the breakdown region of parameter space. As the Rossby number is increased one can see how

the rapid return of the surface front to its unperturbed position (and beyond) is progressively attenuated. The speculation by Davies (1984) that the inclusion of the inertia term in the equations of motion would suppress the singular behavior of the semi- geostrophic solution seems verified by these numerical experiments, with increasing Rossby number but constant rotational Froude number (Fr/Ro). Fig. IV.9.d shows an example of the numerical results in a case where the semi–geostrophic theory predicts a breakdown (Fr/Ro = 0.5, H_m= 1.5). Although the surface front is subject to a very large acceleration it is only for a short time and its velocity remains finite.

3.4.3 Influence of the mountain height and the frontal slope:

We have seen, in the linear theory described in section 3.1, that the frontal retardation is directly proportional to the mountain height (B) in all cases, that is if the mountain height is doubled the frontal retardation is doubled. In addition we have seen that the frontal slope plays no role in the surface front retardation if Ro>>1 , Fr >>1 or Ro<<1, Fr/Ro >>1 whereas for Fr<<1, Fr/Ro<<1 the frontal retardation is inversely proportional to the frontal slope, steep fronts being less affected by the mountain than shallow fronts.

Here we consider the extension of these results to the non linear regime using a series of experiments where the mountain height and the frontal slope are varied in turn. The influence of these two parameters on the maximum frontal retardation is presented in Table IV-3 and 4 whereas Figs. IV.10 and 11 represent the accompanying evolution of the frontal interface.

In Table IV-3 we can see that the maximum retardation is still approximately proportional to the mountain height, although the dependence is stronger in the larger Ro case, when the mountain is not too high compared to the front. When the mountain is sufficiently high, however, the front might become temporarily blocked (c.f. discussion above), its retardation is then increasing in time and no maximum retardation can be defined.

This phenomena can be observed in Fig IV.10.

Table IV-3:

(Fr,Ro)\ B	0.25	0.5	1.0	2.0
0.5 , 2.0	-0.4	-1.0	-2.3	< -3.6
0.2 , 0.5	-0.4	-0.8	-1.6	< -3.3

Table IV-4 demonstrates that the frontal slope (characterized by the frontal length scale) has only a weak influence on the frontal retardation although there is a tendency for steep fronts to be less retarded than shallow fronts, in agreement with the linear theory. Fig. IV.11 indicates that the differences between the steep and shallow fronts are mainly in the flow behind the surface front.

Table IV-4:

(Fr,Ro)\ L_f	6	4	2
0.5 , 2.0	-1.2	-1.0	-0.8
0.2 , 0.5	-0.9	-0.8	-0.8

3.4.4 Influence of rotation on upstream propagating bores:

Here we will digress from our discussion of the surface front to briefly describe the influence of rotation on the formation of upstream propagating bore on the frontal interface. It is not our intent here to present an exhaustive account of this phenomena but only to describe a particular example and relate it to previous work on the subject.

In the non rotating case, it is well known (see for example Houghton and Kasahara, 1968) that impulsively started flow of a layer of initially constant depth fluid over an obstacle

can lead to an upstream-propagating wave of elevation and a downstream propagating wave of rarefaction, if the mountain is sufficiently high. Within the non rotating shallow water theory, the wave fronts steepen and eventually break, forming bores and jumps.

When rotation is present, the dispersive effects of the Coriolis force compete with the steepening due to non linear effects. Although they give no rigorous proof that rotation is able to totally suppress the jump formation, both Houghton(1969) and Williams and Hori (1970) give substantial evidence, from scale analysis and numerical experiments, that no jumps form for $Fr > 6.5\ Ro^2$ at least for the finite time of the numerical integration.

In our problem, the rapid passage of the sloping frontal zone across the mountain takes the place of the impulsive start-up employed in the classical problem. Fig. IV.12 shows results of numerical experiments where only the Rossby number is varied. As expected for large Ro an upstream propagating bore is created. On the other hand the stationary jump on the lee side, present in classical theory, does not form simultaneously here due to the absence of cold air on the lee side initially. Some experiments show signs of this jumps reforming after sufficient time (see Fig. IV.7). This formation of jump without the presence of fluid downstream might be explained by the restoring action of the Coriolis force, which tends to reduce the high wind speed on the lee side of the mountain back to the original value.

As Ro is decreased there is marked weakening in the strength of the jump which totally disappears between Ro=0.5 and Ro=0.2. This is in agreement with the boundary of Ro=0.4 predicted by Williams and Hori (1970) for Fr=1. In the latter stages of the interaction the flow pattern resembles the asymmetric subcritical/supercritical transition familiar from hydraulic theory that can be expected from the initial constant depth of the post frontal region.

4. THE PRESSURE DRAG AND ITS EFFECTS ON THE FLOW:

4.1 The pressure drag in the linear model:

The leading term in the drag can easily be found using Eq.IV.4-IV.9 for the surface pressure associated with the basic state:

$$D_0 = \int_{-\infty}^{x_0} [\rho g' H(x-x_0)+P]\, db/dx\, dx \quad + \quad \int_{x_0}^{\infty} P\, db/dx\, dx \qquad \text{(IV.27)}$$

where $x_0 = Ut$ is the position of the surface front.

This drag can also be written as :

$$D_0 = -(\rho g' dH/dx + dP/dx) \int_{-\infty}^{x_0} b\, dx \quad - \quad dP/dx \int_{x_0}^{\infty} b\, dx \qquad \text{(IV.28)}$$

if the frontal slope dH/dx and the upper layer pressure gradient dP/dx are both constant.

In this form it is easy to see the time evolution of the drag, illustrated in Fig. IV.13, between the value - dP/dx V (V: volume of the mountain), when the mountain is entirely located in the warm layer and the value - (ρg'dH/dx + dP/dx) V when it is entirely in the cold layer.

This drag evolution is very similar with the observed drag (Fig. I.4 and Fig. II.4.). However the prefrontal drag (- dP/dx V) is entirely determined by the pressure gradient imposed by the warm layer. In our simple model the warm layer is assumed to remain unperturbed by the mountain and there is therefore no mechanism capable of increasing the prefrontal pressure gradient over its value in flat terrain. But as we have seen in Chapter III this pressure gradient is insufficient to account for the observed pre-frontal drag. A more complete understanding must therefore also include the mountain effect on the warm layer and will be done in Chapter V.

Here we will focus instead on the post-frontal drag created by the cold air flow over the mountain and without loss of generality we will assume that dP/dx = 0. In consequence of this assumption the drag when the mountain is entirely in the warm layer, will be zero, and the drag due to the cold air flow will reduce to:

$$D_0 = \int_{-\infty}^{Ut} \rho g' H(x-Ut)\, db/dx\, dx \;=\; -\int_{-\infty}^{Ut} \rho g' dH/dx\; b\; dx \qquad \text{(IV.29)}$$

This equation indicates that the maximum drag is proportional to the frontal strength (g'), the frontal slope dH/dx, and the mountain volume.

The time evolution for the leading order is determined by the advection speed U and is therefore likely to be modified by the frontal retardation described in the previous section. However, to compute the next order drag correction requires to know the frontal retardation at every point, not only at the surface front, and will not be attempted here. Instead we will discuss these questions in the next section, using the numerical results.

In order to understand the various possible effects of the mountain on the cold air flow, we consider the U-momentum budget for a limited domain surrounding the mountain and for the limiting regimes already discussed in section 3.2. The budgets are based on Eq. IV.14 and summarized in Fig. IV.14. When inertia effects dominate the response (case a, corresponding to the nomenclature of section 3.2) the drag is balanced by a decrease in the U-momentum of the flow, whereas if rotational effects dominate (case b) the drag is balanced by an increased Coriolis force due to an increased V-jet along the mountain. If stratification effects dominate, the drag is balanced by an increase in pressure gradient that is felt at the boundary of the domain.

4.2 Non linear effects on the pressure drag:

In the previous section we have described the drag D_0 created by the pressure gradient associated with the basic state front. This drag and its evolution will provide a reference with

which to compare, in this section, the drag in the numerical results. The question addressed here, that is relevant to the frontal passage observed in the Alps as described in Chapter III, is: under which circumstances can the drag be increased over its reference value D_0, by the non linear processes.

The scale for the reference drag D_0, given by Eq. IV.29, is $\rho g'HB/L$ and will be used to nondimensionalize all the drag values and momentum budget terms discussed here. As a side note we remark that the reference drag in the non-linear model does not asymptotically approach a non zero value, as indicated in Fig. IV.13 for the linear model, because of the finite extend of the frontal zone.

In Fig. IV.15 we present the pressure drag in the numerical model for three cases, compared with the reference drag D_0 which is drawn as a dotted curve:

a) Fr = 1 Ro = 4

b) Fr = .2 Ro = .2

c) Fr = .1 Ro = 2

These experiments were chosen because they are in the non linear regime but with parameters such that there is a dominance of one of the terms in the U-momentum equation (l.h.s. of Eq. IV.1). Before discussing the differences between this cases in details we will first introduce the corresponding U-momentum budget.

These budgets are presented in Fig. IV.16 and can be derived from Eq. IV.1-IV.3:

$$\underset{A}{\partial(hu)/\partial t} + \underset{}{\partial(huu)/\partial t} \quad \underset{B}{- f h v} \quad \underset{C}{+ g'h\, \partial h/\partial x} \quad \underset{D}{+ g'h\, db/dx} = 0 \qquad \text{(IV.30)}$$

In the unperturbed front in flat terrain there is an exact cancellation in the budget between term B and C whereas terms A and D are zero:

$$\underset{B''}{- f H V} \quad \underset{C''}{+ g' H\, dH/dx} = 0 \qquad \text{(IV.31)}$$

This balance has been subtracted from the budget presented in Fig. IV.16 so that all the

terms are zero initially. In Fig. IV.16, term A is represented by a dotted line, term B'=B-B" by a dashed line, term C'=C-C" by a thin solid line and term D by a thick solid line. In Fig. IV.16,a the dominant balance is between terms A and D but as time increases term B' becomes more important. In this case the drag is balanced by a decrease of the U-momentum of the flow inside the domain. In Fig. IV.16,b , the dominant balance is between terms B' and D which means that the drag is balanced by the Coriolis force acting on the mountain induced jet (v–V). In Fig. IV.16,c , after sufficient time, the primary balance is between terms C' and D. In that case the drag is balanced by an increase of pressure gradient at the boundary of the domain. This increase cannot occur instantly at the boundary and there is therefore an adjustment period during which the primary balance is between term A and D.

These budgets of the non-linear experiments confirm the linear analysis of the limiting regimes in the previous section and summarized in Fig. IV.14.

Based on these results the differences in the nondimensionalized drag in Fig. IV.15 can be interpreted as follows. In case a) (Fr=1, Ro=4) the decrease in U-momentum which balances the drag, requires, owing to mass continuity, a rise in the frontal interface in the manner indicated in Fig. IV.12.a. If Fr=O(1) the interface perturbation remains localized on the upstream side of the mountain, creating the observed increase in drag. If Fr>>1, this effect is not significant (except if the mountain is sufficiently high) and if Fr<<1 this interface perturbation rapidly disperses upstream. The increase in height of the interface will eventually become such that the Froude number is locally less than one, allowing upstream propagation in the form of a bore (see section 3.4.4). The flow will subsequently settle into a steady state above the mountain and the drag will reach an asymptotic value equal to that in the classical hydraulic theory, modified by rotation.

In case b) (Fr=.2, Ro=.2) the strong rotational effects prevent the decrease of U-momentum. Instead, the drag is balanced by a V-jet along the mountain and there is no interface rise required by mass continuity. Consequently the drag is very close to its

unperturbed value.

In case c) (Fr=.1, Ro=2.) the dominant stratification effect causes the orographic uplifting of the frontal interface to rapidly disperse upstream thereby reducing the drag over its unperturbed value. The drag evolution in this regime is also very strongly delayed by the frontal retardation.

In summary there can be a substantial drag increase over the reference value D_0 if $Ro > 1$ and $Fr = O(1)$. This increase is due to the accumulation of cold air on the upstream slope of the mountain, caused by blocking. If $Ro \ll 1$ or if $Fr \gg 1$ there is little blocking and therefore little drag increase. If $Fr \ll 1$ the strong upstream dispersion prevents the accumulation of blocked cold air from remaining localized on the upstream slope of the mountain where it contributes to the drag.

5. DISCUSSION:

5.1 Application to the Alps:

First we examine in turn the range of the parameters appropriate for the Alps:

- reduced gravity: $g' = 0.1 - 0.3\ ms^{-2}$ (corresponding to $\Delta T = 3 - 9\ ^{\circ}C$)
- advection speed: $U = 5 - 20$ m/s (based on Hoinka, 1985, estimates)
- frontal height: $H = 4000 - 7000$ m
- mountain width: $L = 50 - 100$ km

The minimum and maximum Rossby number and Froude number that can be derived from these parameters are:

$Fr = 0.1 - 1$ and $Ro = 0.5 - 4.$

Additionally we have the following geometrical parameters:

- mountain height: $B = 2500$ m and therefore $B / H \approx 0.5$
- frontal slope: $S = 1/100$ (typically: f/N)

From these parameters we can deduce the frontal length scale: $L_F = H/S = 400\text{-}700$ km or $L_F/L = 4 - 14$.

These typical values show that frontal passage in the alpine region can be found in a variety of regimes. For example from Fig. IV.8 we can deduce that the maximum frontal retardation is:

L to 2L for (Fr, Ro) = (0.1, 0.5) and $\approx$ 0.5 L for (1.,4.)

with deceleration patterns similar to those in Fig. IV.9.c: long deceleration upstream and rapid acceleration to catch up on the lee side.

The very idealized nature of the model makes a comparison with observations difficult but some signs of this behavior can be observed in Fig. IV.1 the long delay of the central part of the surface front on the upstream slope followed by a rapid catch up of its unperturbed position indicated by the part of the front passing east of the mountain.

The different regimes for the drag created by the Alps can be discussed in reference to Fig. IV.15. For the case Fr=1, Ro=4, corresponding exactly to case a in Fig. IV.15, we can see that the actual drag is 50% larger than expected from the surface pressure gradient associated with the front in flat land. In this case the momentum balance is shown in Fig. IV.16.a. This dynamical drag increase could possibly explain the discrepancy mentioned in Chapter III between the observed drag and the pressure gradients observed upstream of the mountain.

In the case Fr=0.1, Ro=0.5 , we expect a behavior intermediate between cases b and c in Figs. IV.15 and 16, where both stratification and Coriolis effects would be important. As discussed in section 4.2 the drag, in that case, is equal or less than expected from the unperturbed front.

5.2 Influence of orographic smoothing for numerical modelling:

It has been shown by Pierrehumbert (1984), for the linear theory, and Pierrehumbert and Wyman (1985), for the non-linear theory, that for uniformly stratified flow over

topography the maximum upstream deceleration of the flow depends on the mountain height B if Ro>>1 and on the mountain slope B/L if Ro<<1.

No smoothing procedure can retain both the mountain height and the mountain slope and it was argued that conserving the maximum height of the topography offers a good compromise by retaining the blocking effect at large Ro, where it is strong, and ameliorating it at small Ro.

A similar situation is found here for the frontal retardation. Based on our linear analytical results of section 3.1, confirmed by the numerical results of section 3.2, we have the following dependence of the frontal retardation on the mountain dimension, in the different regimes:

B	if Ro>>1, Fr>>1	(regime a))
B/L^2	if Ro<<1, Fr/Ro>>1	(regime b))
B/L	if Fr<<1, Fr/Ro<<1	(regime c))

We are therefore in a similar dilemma here and the situation appears even worse for regime b). There is however an additional constraint if we also insist on reproducing the correct drag, because, as we have seen in section 4.1, the drag is proportional to first order to the mountain volume.

In summary if we adopt a smoothing procedure that conserves the maximum topographic height, we are still faced, in the frontal passage problem, with an insufficient retardation of strong fronts (type c), due to the decrease of the mountain slope, but also with a spurious increase in the pressure drag, due to the increase of the mountain volume. For limited area models we are rapidly approaching the resolution needed to adequately represent mountains such as the Alps and these problems should disappear but in the case of global models, at least in the near future, these effects need to be parameterized.

5.3 Remaining questions:

We will discuss here some elements that are not included in the crude model of this

chapter but that we think might play a role in the problem, although it is still an open question to determine their importance relative to the effects discussed so far:

- the dynamics of the warm layer which are clearly an important part of the problem and necessary in gaining a better understanding of the pre-frontal drag and the pre-frontal foehn,

- the continuous vertical stratification and flow structure, associated with both the mountain and the front, that are eliminated by the shallow water approximation,

- the vertical shear of the frontal advection speed that can create a secondary frontal circulation (Orlanski and Ross, 1977) which might play a role in the interaction with the mountain,

- the finite thickness of the frontal zone which is assumed to be discontinuous here, but is in reality comparable to the mountain width.

These model deficiencies will be addressed in the next chapter by using a more complete numerical model.

To conclude here, we mention other effects that are potentially significant: the three dimensionality of both the frontal system and the mountain, the effect of the boundary layer and moisture, and the effect of complex orography, in particular the valleys. The consideration of these effects is problematic, and will be deferred to future work.

Figure captions for Chapter IV:

Figure IV.1: Isochrones of cold fronts: a) between June 23 and 25, 1978 (from Steinacker, 1981); b) between March 4 and 5, 1982 (from Davies, 1986). The cold front is retarded in the central part of the mountain.

Figure IV.2: Time evolution of the precipitation in the Gotthard section (from Phillips, 1984). The precipitation remain blocked on the upstream side of the mountain.

Figure IV.3: Schematics of the two layer frontal model.

Figure IV.4: Position of the surface front at regular time interval, as a function of the front-mountain aspect ratio and for two rotational Froude numbers ($r^2=1$ and $r^2=10$) in the semi-geostrophic solution of Davies (1984). In the hatched region the solution does not exist.

Figure IV.5: Velocity of the surface front as a function of the distance across the mountain (with origin at the top) in the numerical experiments of Arakawa and Okano (1976)

Figure IV.6: Perturbation of the surface front position as a function of time in the limiting regimes of the linear theory. The perturbation is adimentionalized differently in each case and the corresponding scale is indicated next to the axis. The front reaches the mountain top at $t=2$.

Figure IV.7: Superposition of cross-sections through the mountain and the front at regular time interval ($\Delta t = 1$) for the numerical experiment: Ro = Fr = Hm =1. Changes in line pattern are used to distinguish consecutive times.

Figure IV.8: Contours of maximum frontal retardation in the Ro-Fr plane for fixed mountain and front geometry.

Figure IV.9: Time evolution of the perturbation of the surface front position. The perturbation (vertical axis) is adimentionalized by the mountain width: a) for fixed Ro =1. and varying Fr ; b) for fixed Fr = 0.2 and varying Ro; c) for fixed Fr / Ro and varying Ro. In c) the semi-geostrophic solution of Davies (1984) is indicated by +. For the numerical experiment shown in d) (Ro=0.2, Fr=0.1, Hm=1.5) the semi-geostrophic theory predicts a breakdown.

Figure IV.10: The effect of varying mountain height on the interaction at different times ($\Delta t=1$) for fixed Ro and Fr

Figure IV.11: The difference between steep and shallow front interaction at different times ($\Delta t=1$).

Figure IV.12: The influence of rotation on the formation of upstream propagating bores. For Ro less than 0.2 the bore has completely disappeared.

Figure IV.13: The evolution of the pressure drag in the linear solution.(dP/dx is the pressure gradient imposed by the warm layer, V is the mountain volume and dH/dx is the frontal slope)

Figure IV.14: U-momentum budget in the limiting regimes of linear theory. The r.h.s. represent the pressure drag which is balanced by a different l.h.s. in each limiting case.

Figure IV.15: Non linear effects on the evolution of the pressure drag. The dotted line indicates the drag due to the unperturbed front (see text for definition). The vertical scale is $\rho g'HB/L$.

Figure IV.16: The momentum budget corresponding to the experiments of Fig. 15. The different terms are defined in Eq. IV.30. The thick solid line represents the drag (D), the dotted line the U-momentum term (A), the dashed line the Coriolis term (B) and the thin solid line the pressure gradient term (C).

a

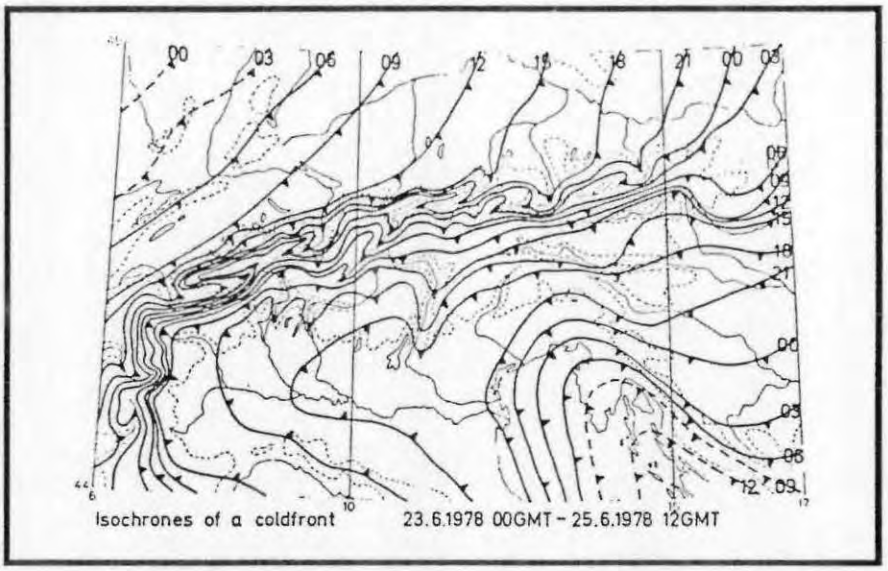

b

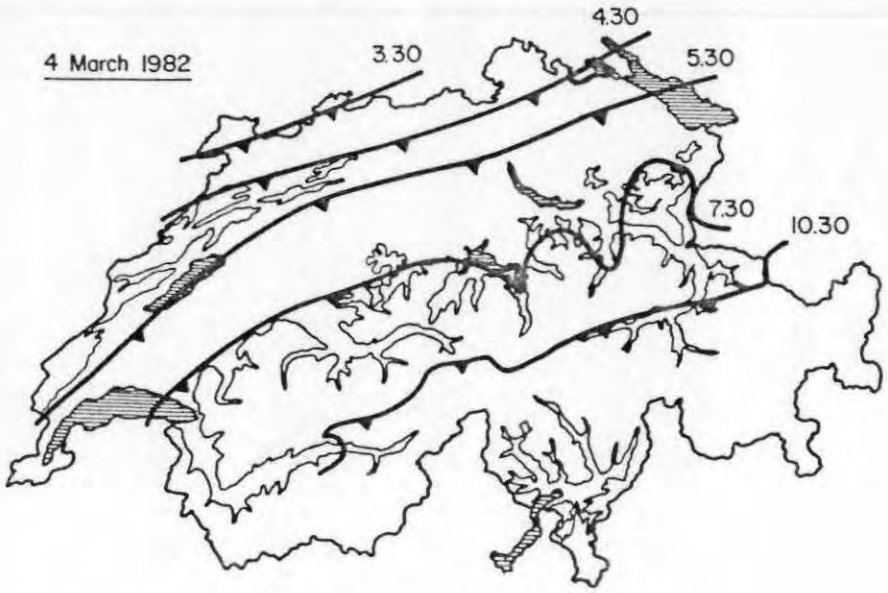

Figure IV.1: Isochrones of cold fronts: a) between June 23 and 25, 1978 (from Steinacker, 1981); b) between March 4 and 5, 1982 (from Davies, 1986). The cold front is retarded in the central part of the mountain.

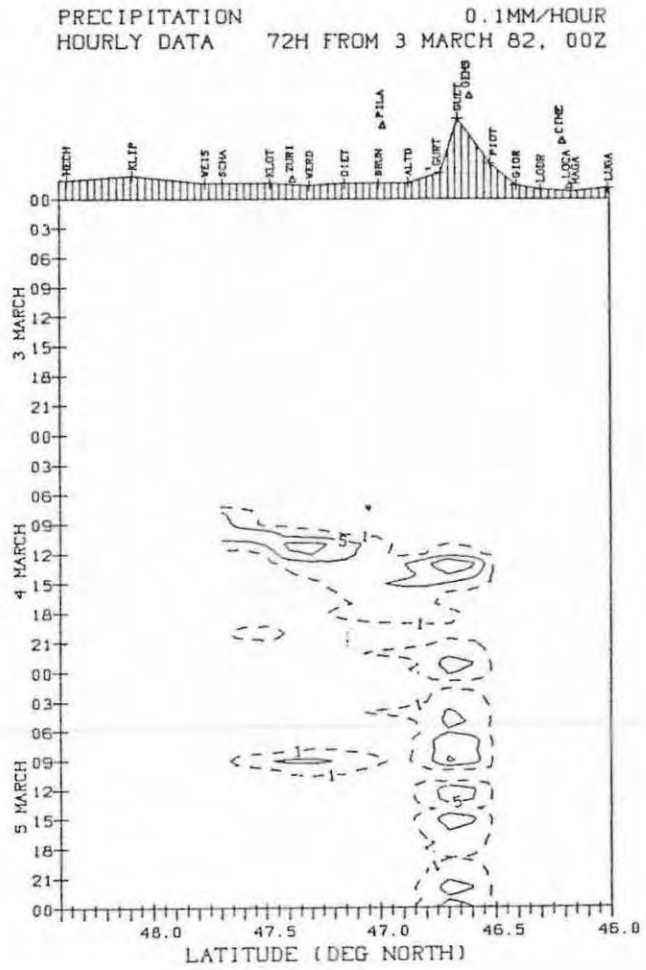

Figure IV.2: Time evolution of the precipitation in the Gotthard section (from Phillips, 1984). The precipitation remain blocked on the upstream side of the mountain.

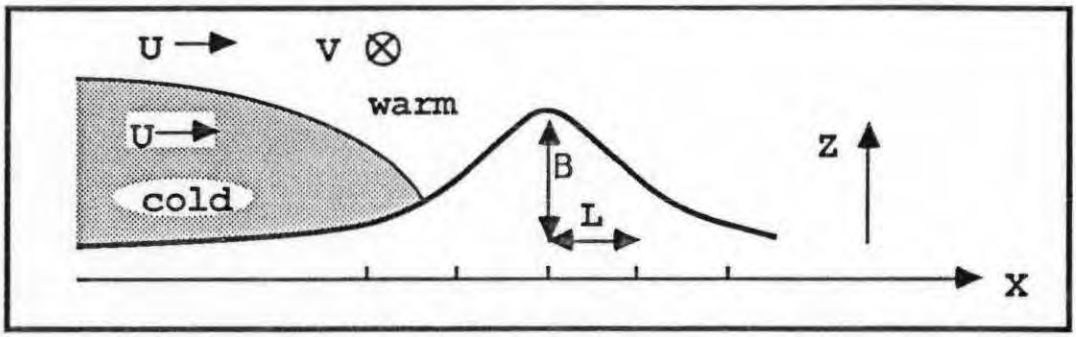

Figure IV.3: Schematics of the two layer frontal model.

Figure IV.4: Position of the surface front at regular time interval, as a function of the front-mountain aspect ratio and for two rotational Froude numbers (r^2=1 and r^2=10) in the semi-geostrophic solution of Davies (1984). In the hatched region the solution does not exist.

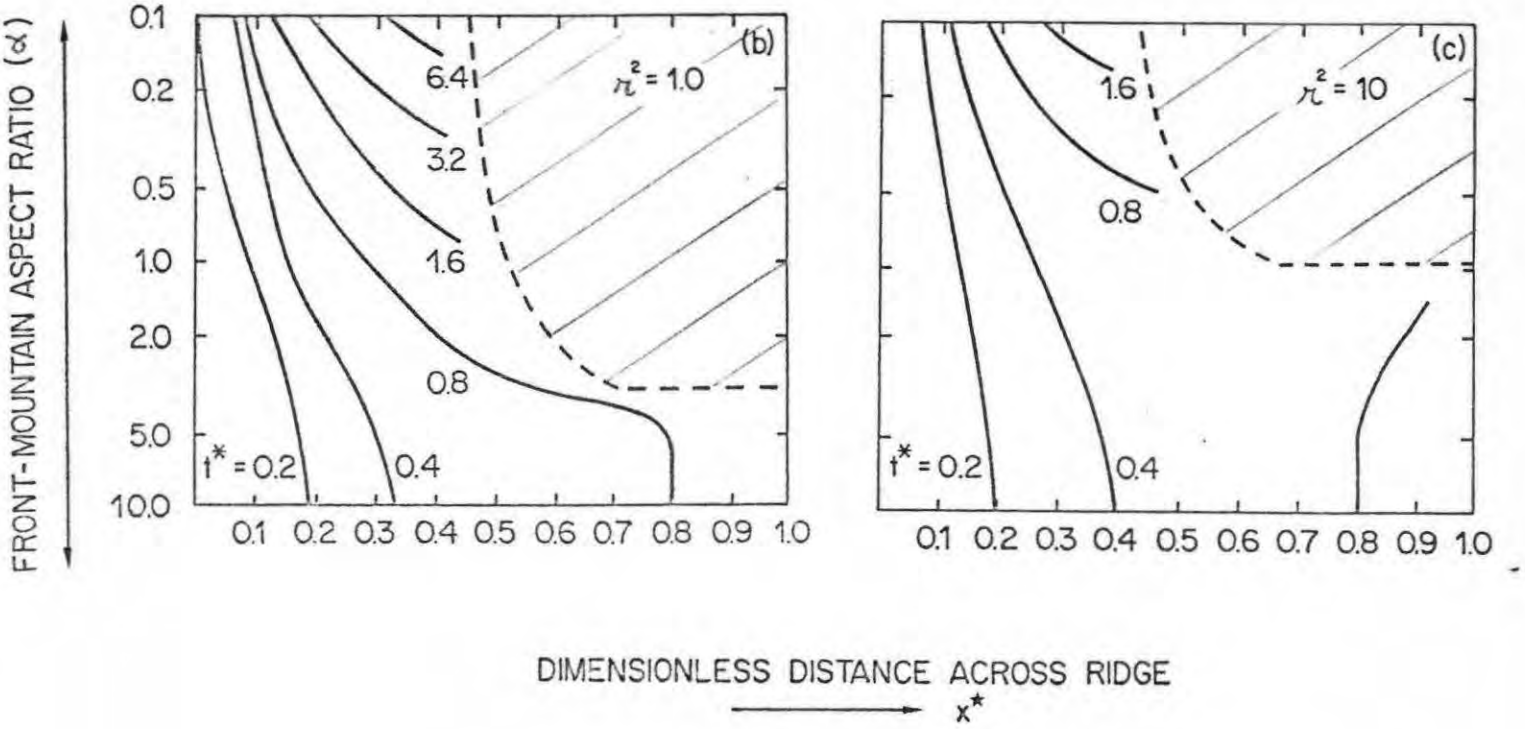

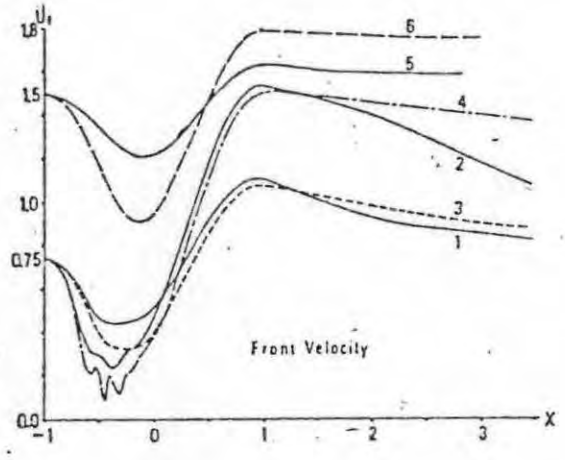

Figure IV.5: Velocity of the surface front as a function of the distance across the mountain (with origin at the top) in the numerical experiments of Arakawa and Okano (1976)

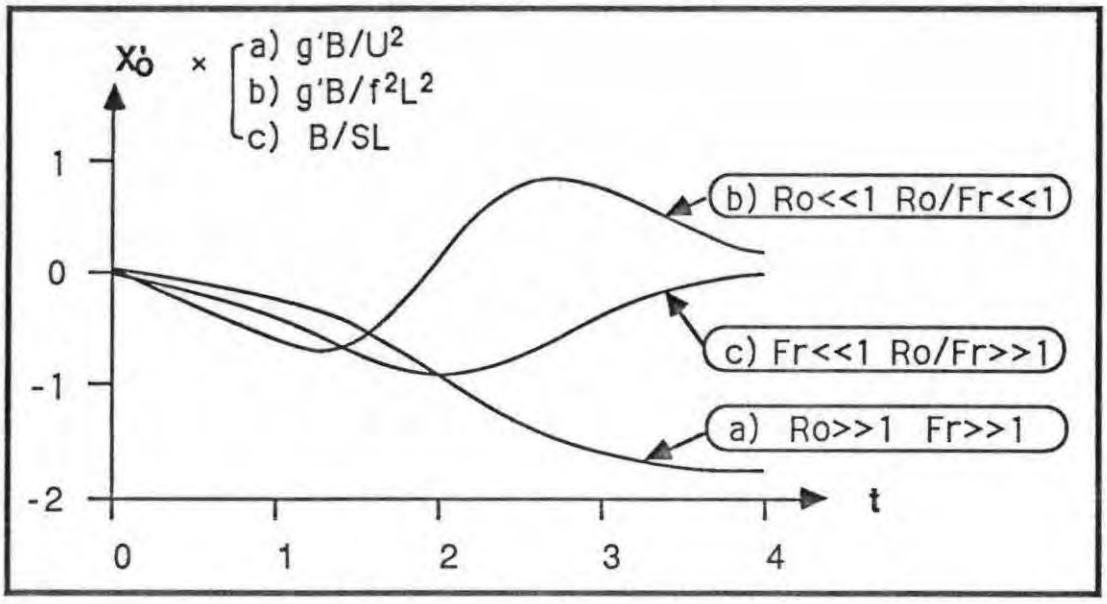

Figure IV.6: Perturbation of the surface front position as a function of time in the limiting regimes of the linear theory. The perturbation is adimentionalized differently in each case and the corresponding scale is indicated next to the axis. The front reaches the mountain top at t=2.

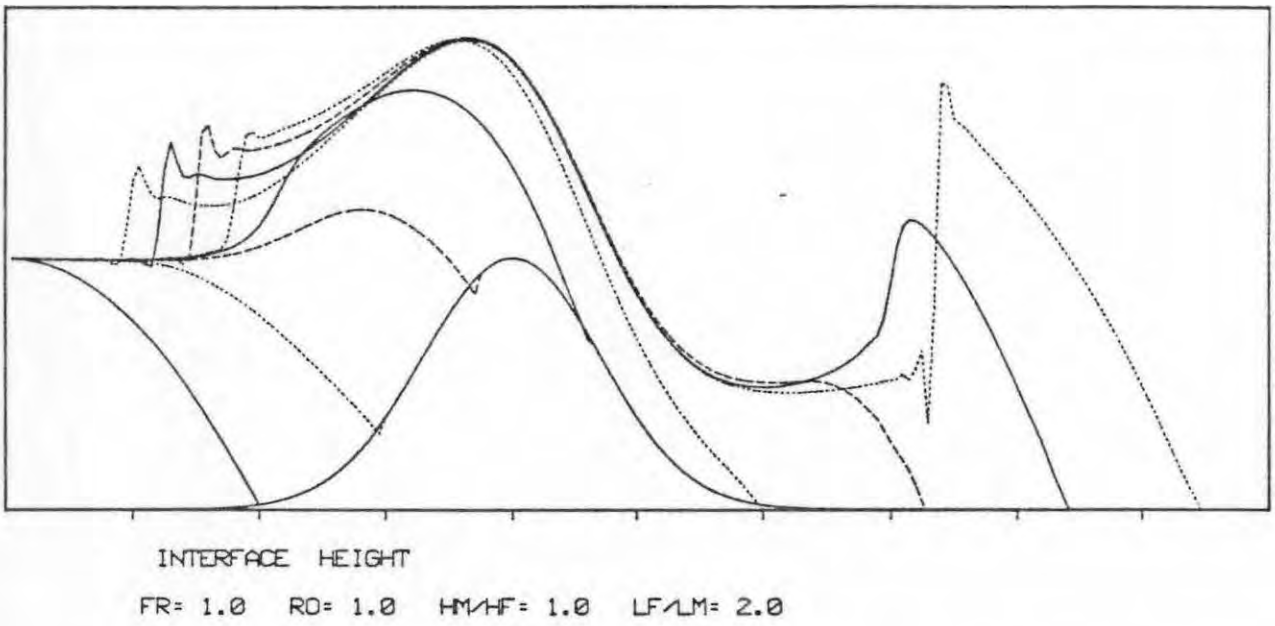

Figure IV.7: Superposition of cross-sections through the mountain and the front at regular time interval ($\Delta t = 1$) for the numerical experiment: Ro = Fr = Hm =1. Changes in line pattern are used to distinguish consecutive times.

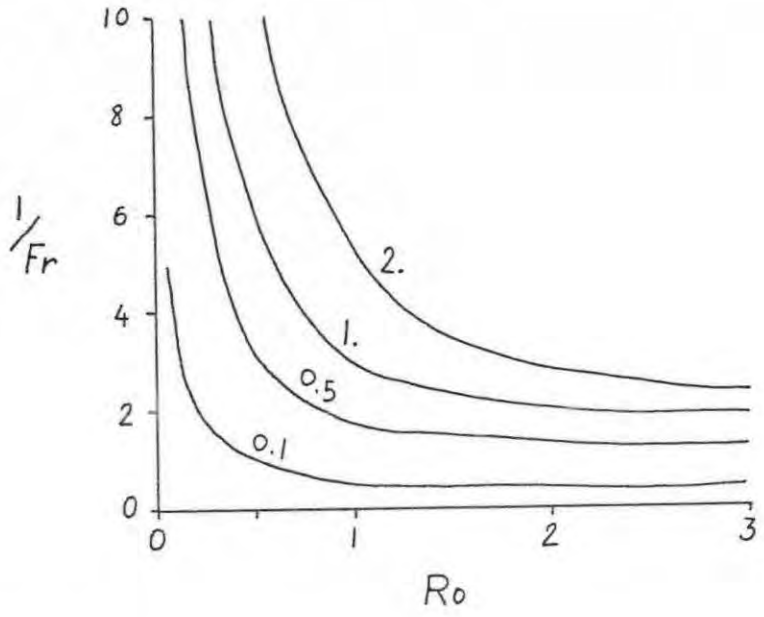

Figure IV.8: Contours of maximum frontal retardation in the Ro-Fr plane for fixed mountain and front geometry.

a

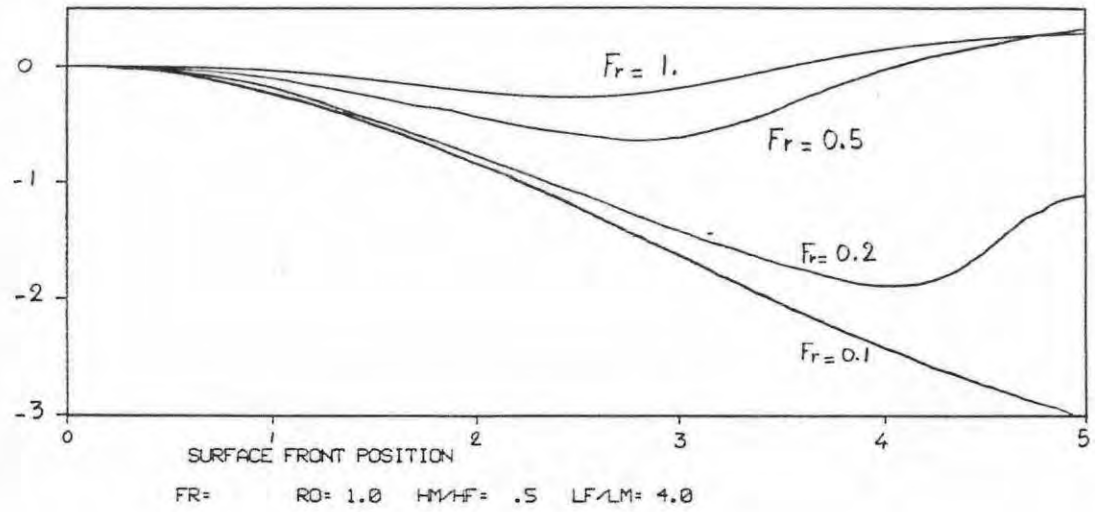

b

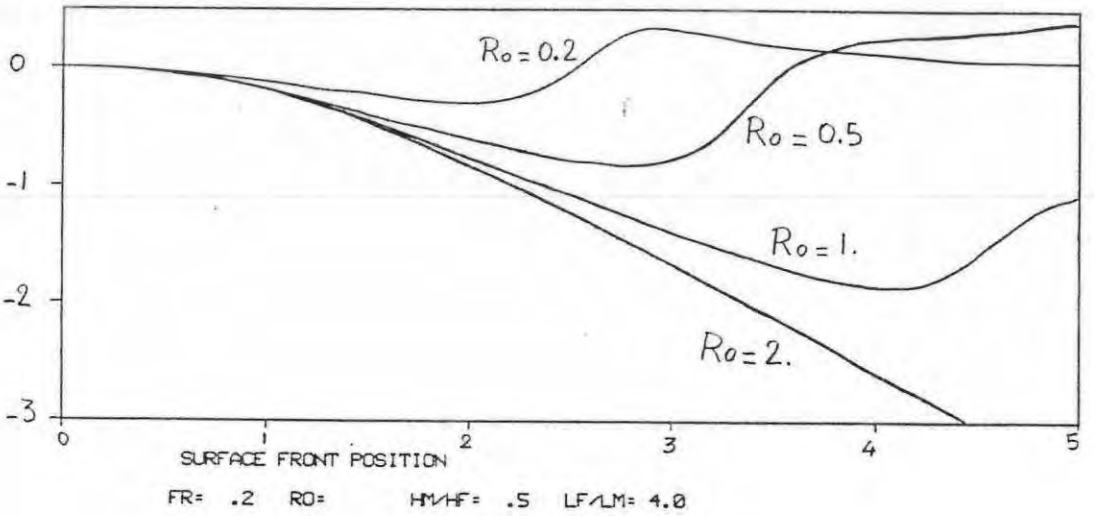

Figure IV.9: Time evolution of the perturbation of the surface front position. The perturbation (vertical axis) is adimentionalized by the mountain width: a) for fixed Ro =1. and varying Fr ; b) for fixed Fr = 0.2 and varying Ro; c) for fixed Fr / Ro and varying Ro. In c) the semi-geostrophic solution of Davies (1984) is indicated by +. For the numerical experiment shown in d) (Ro=0.2, Fr=0.1, Hm=1.5) the semi-geostrophic theory predicts a breakdown.

c

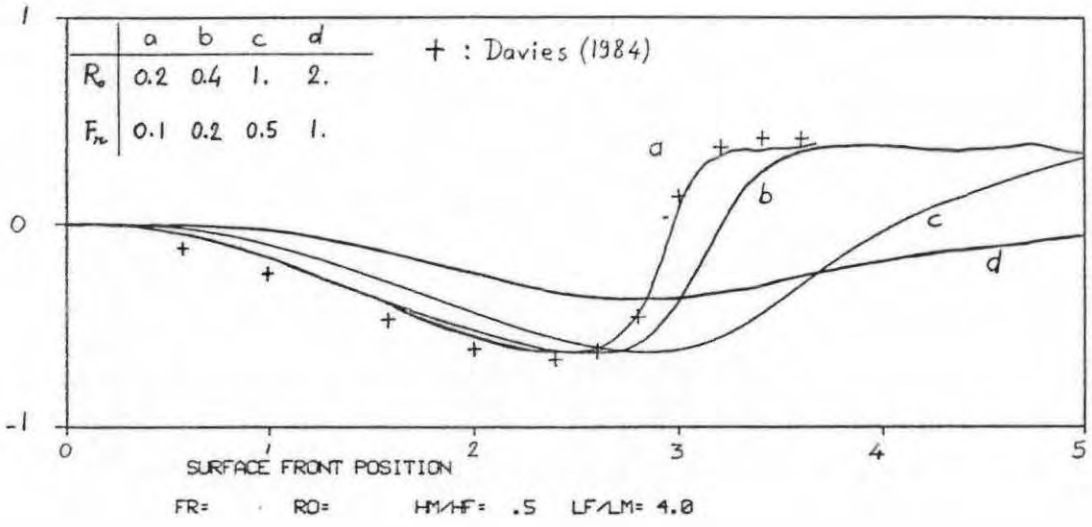

d

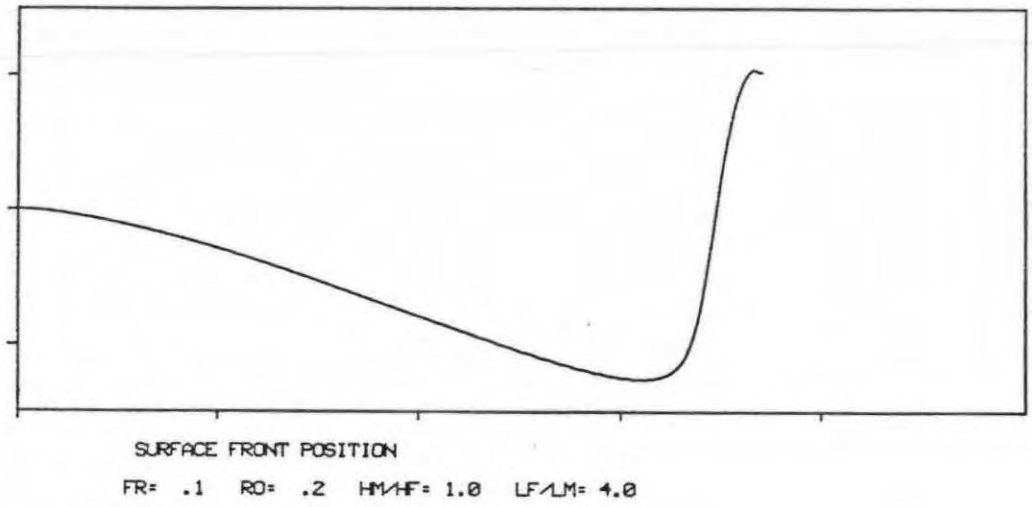

Figure IV.9 (continue)

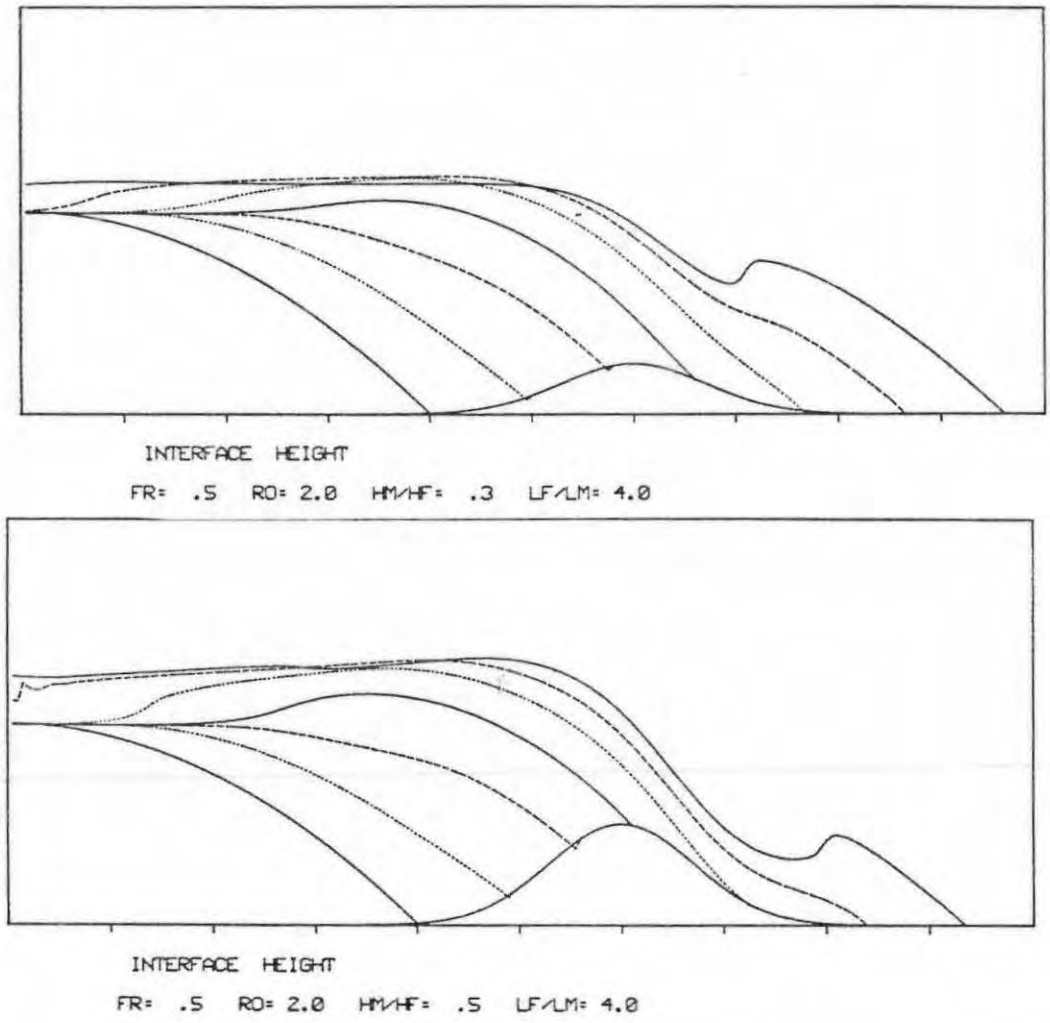

Figure IV.10: The effect of varying mountain height on the interaction at different times ($\Delta t=1$) for fixed Ro and Fr

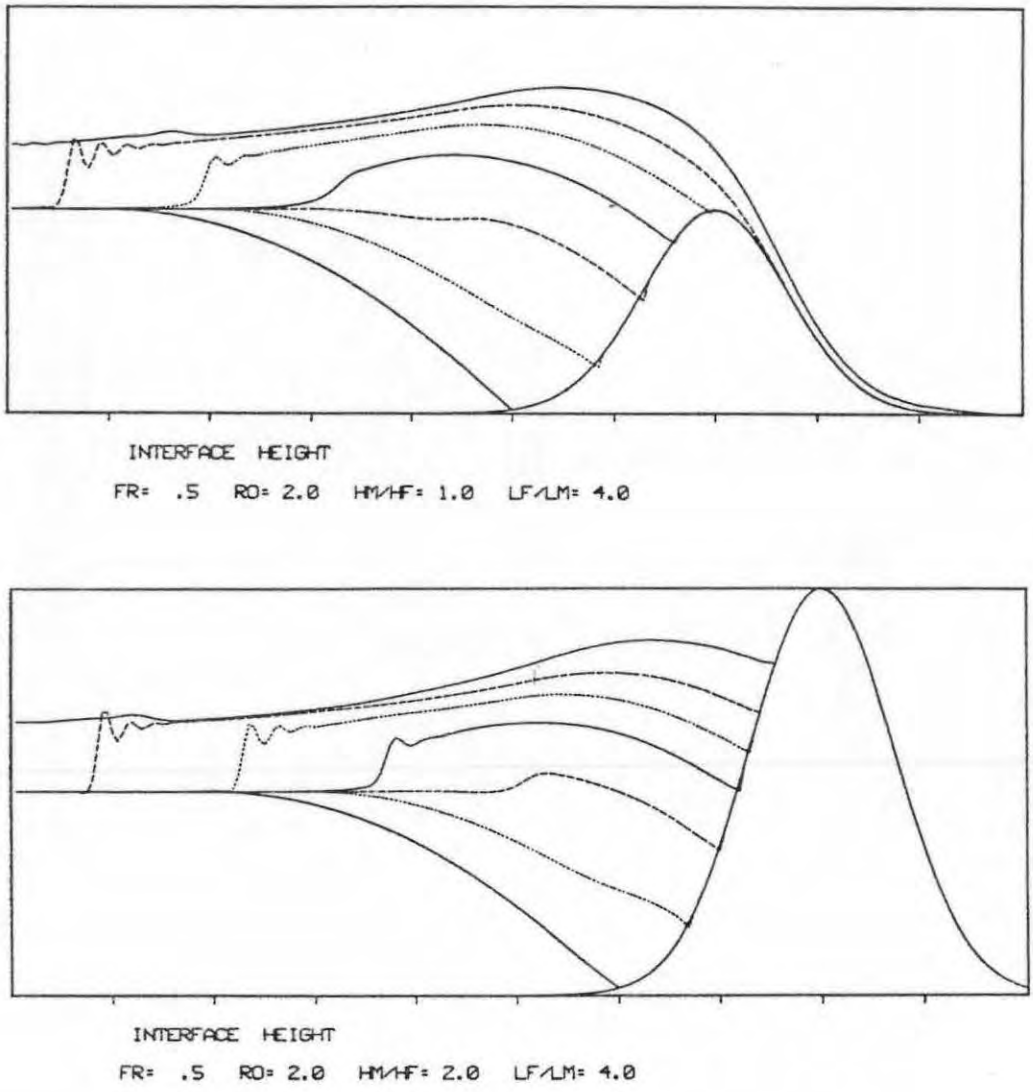

Figure IV.10 (continue)

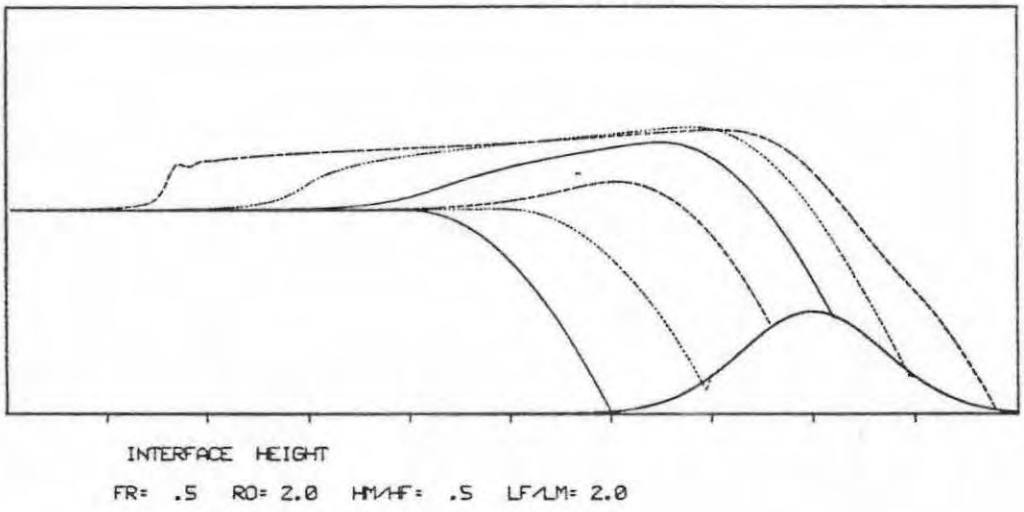

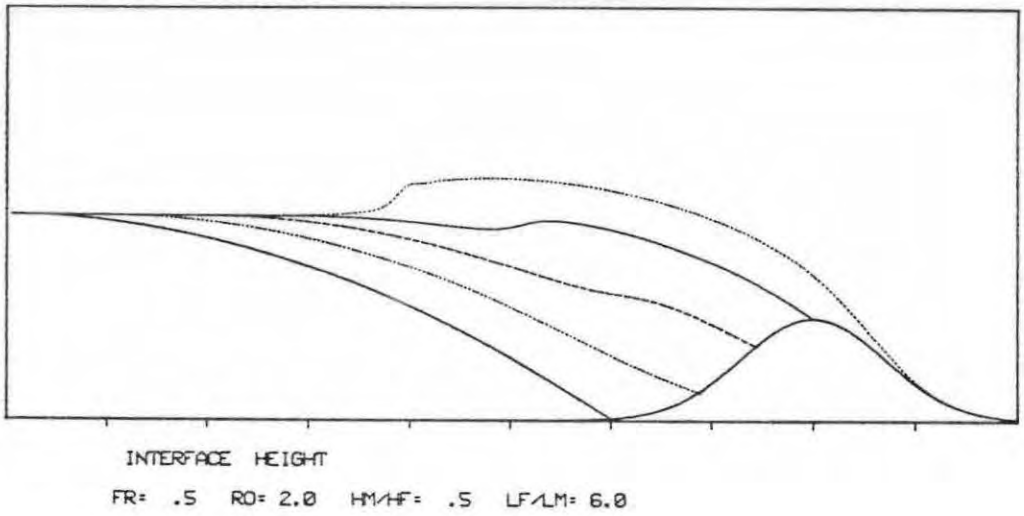

Figure IV.11: The difference between steep and shallow front interaction at different times ($\Delta t=1$).

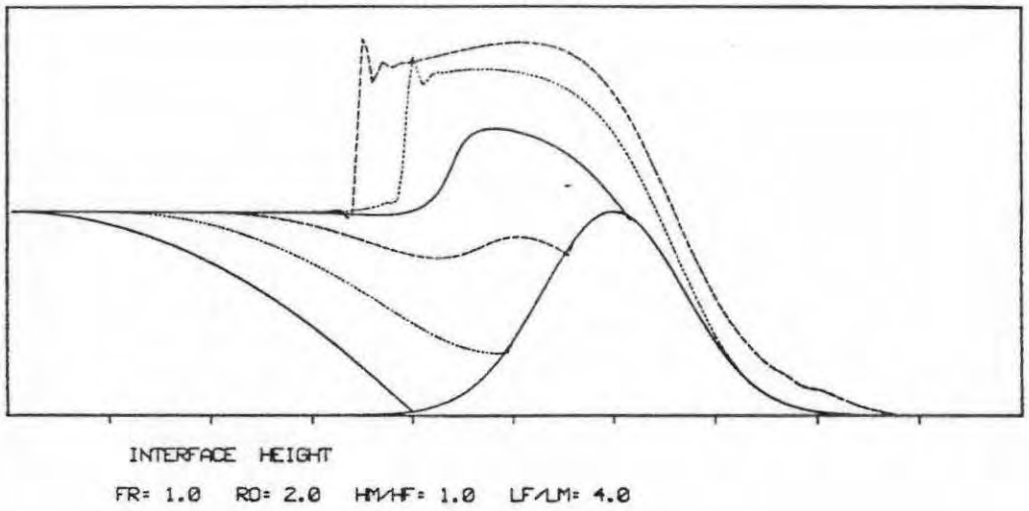

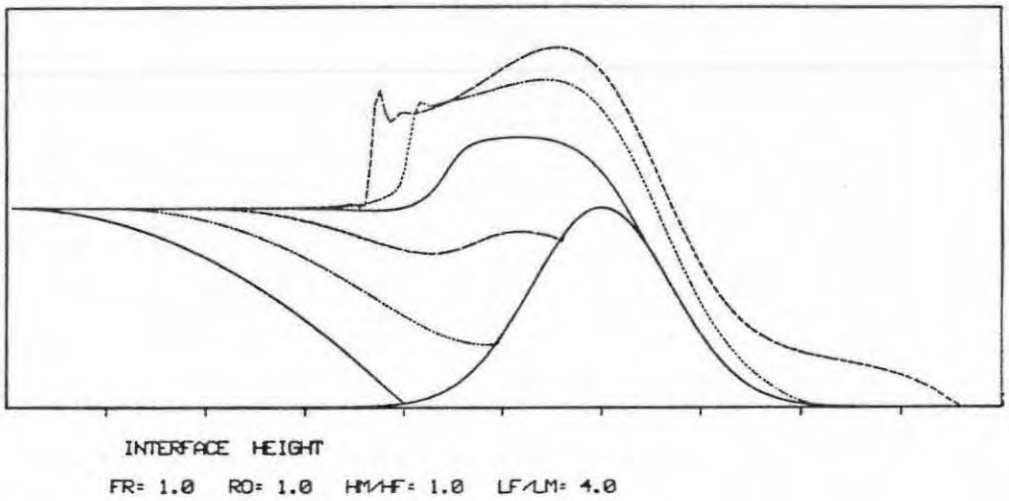

Figure IV.12: The influence of rotation on the formation of upstream propagating bores. For Ro less than 0.2 the bore has completely disappeared.

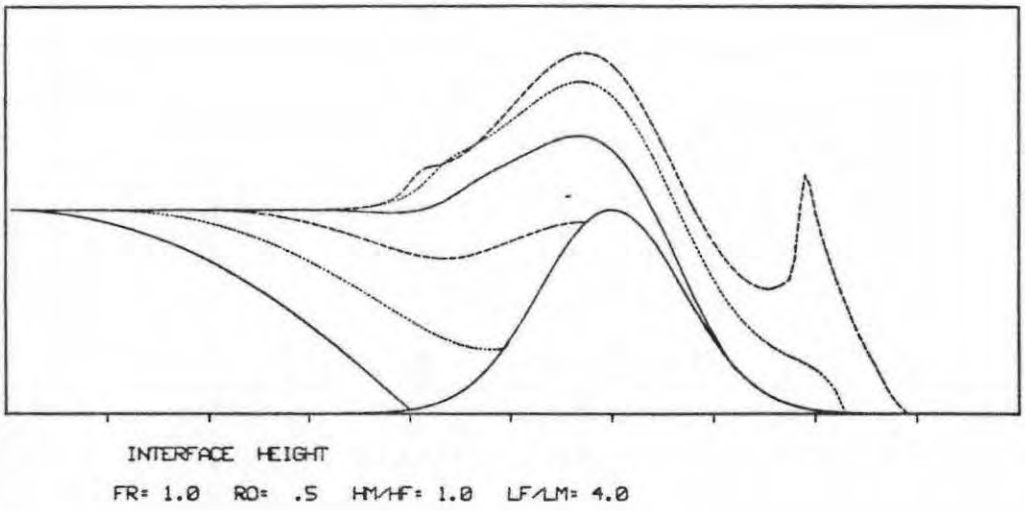

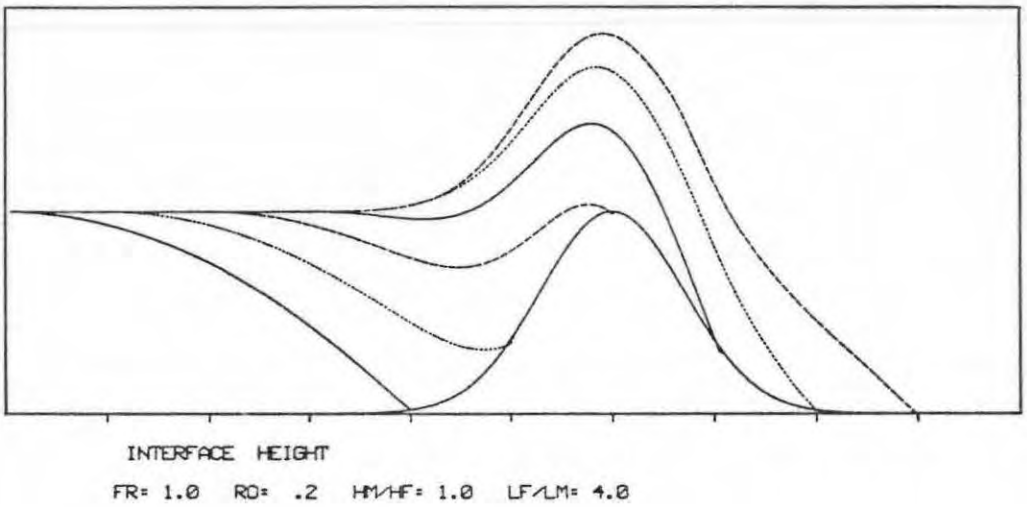

Figure IV.12 (continue)

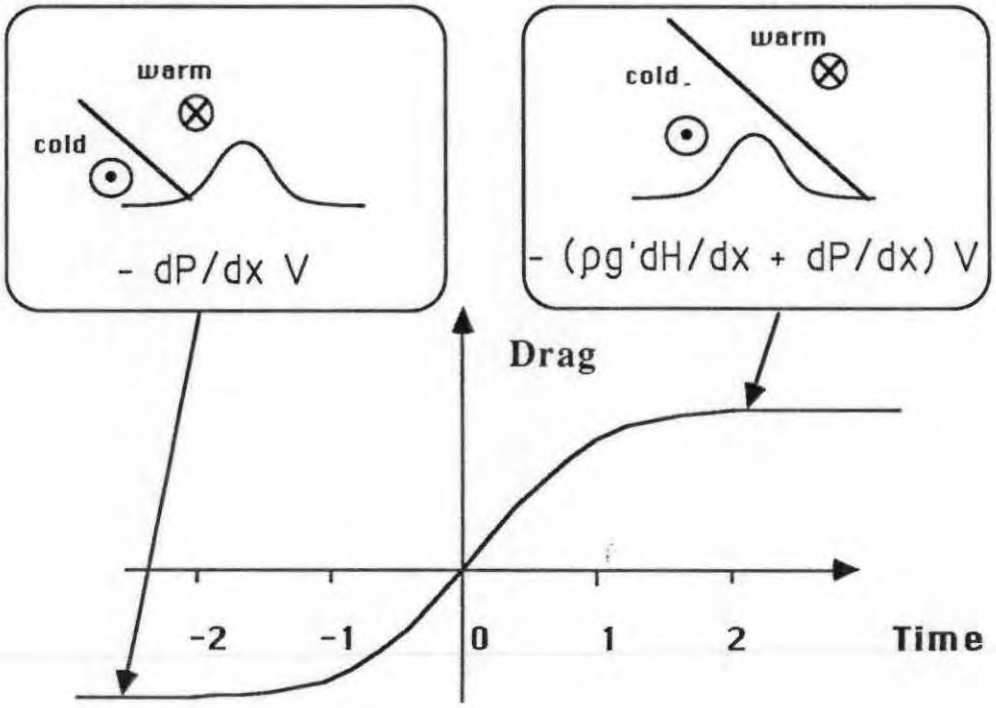

Figure IV.13: The evolution of the pressure drag in the linear solution.(dP/dx is the pressure gradient imposed by the warm layer, V is the mountain volume and dH/dx is the frontal slope)

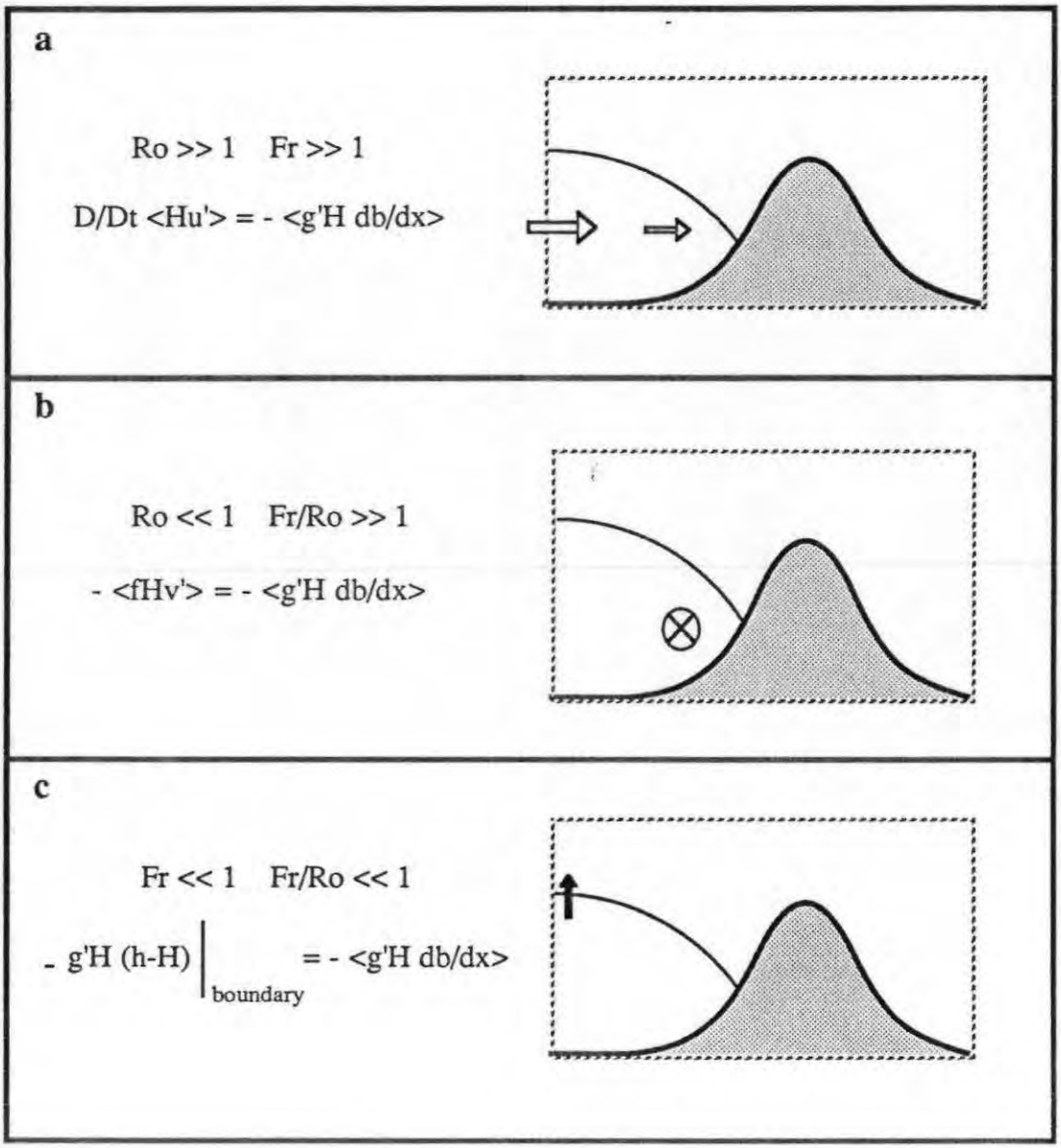

Figure IV.14: U-momentum budget in the limiting regimes of linear theory. The r.h.s. represent the pressure drag which is balanced by a different l.h.s. in each limiting case.

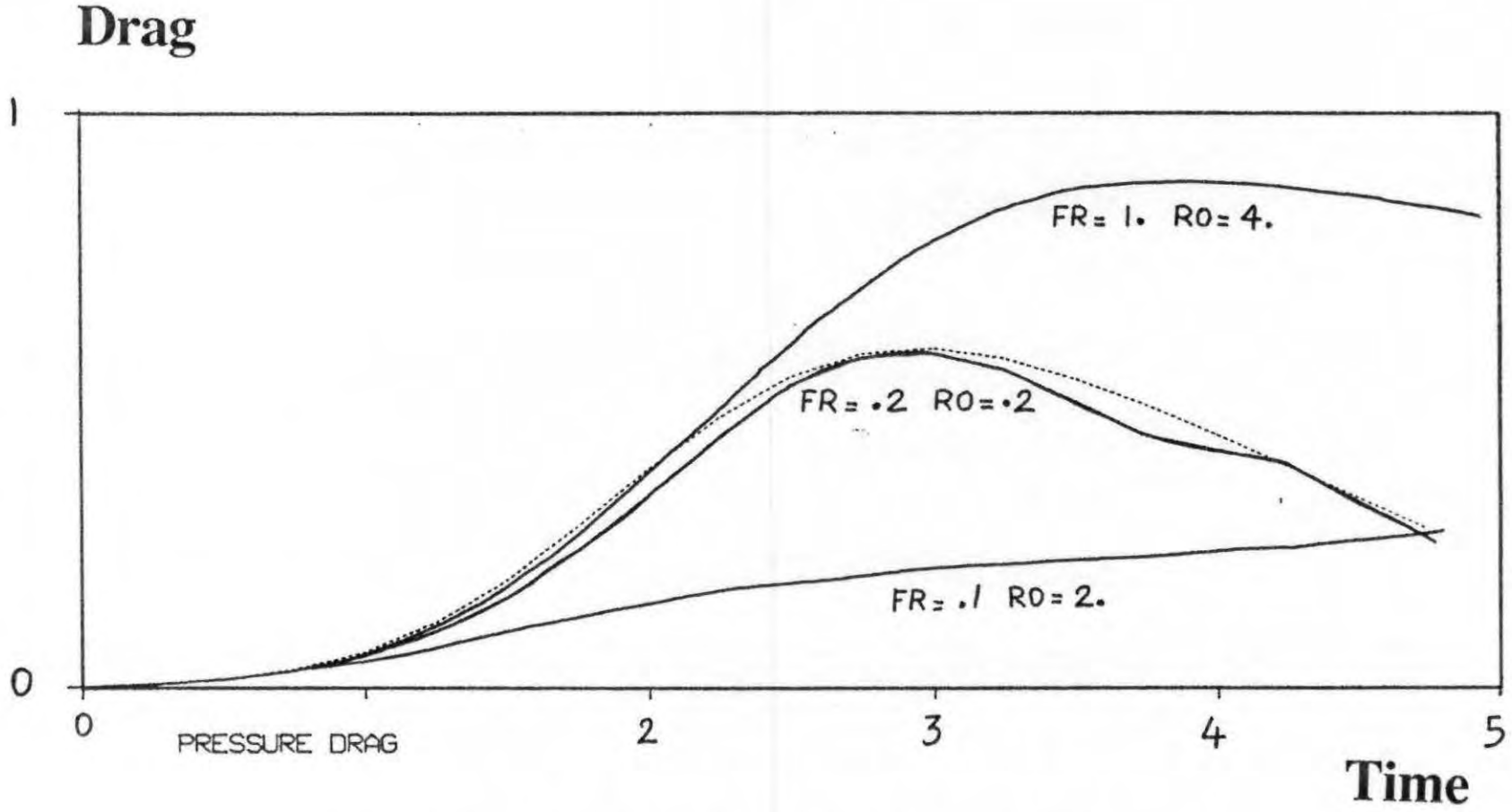

Figure IV.15: Non linear effects on the evolution of the pressure drag. The dotted line indicates the drag due to the unperturbed front (see text for definition). The vertical scale is ρg'HB/L.

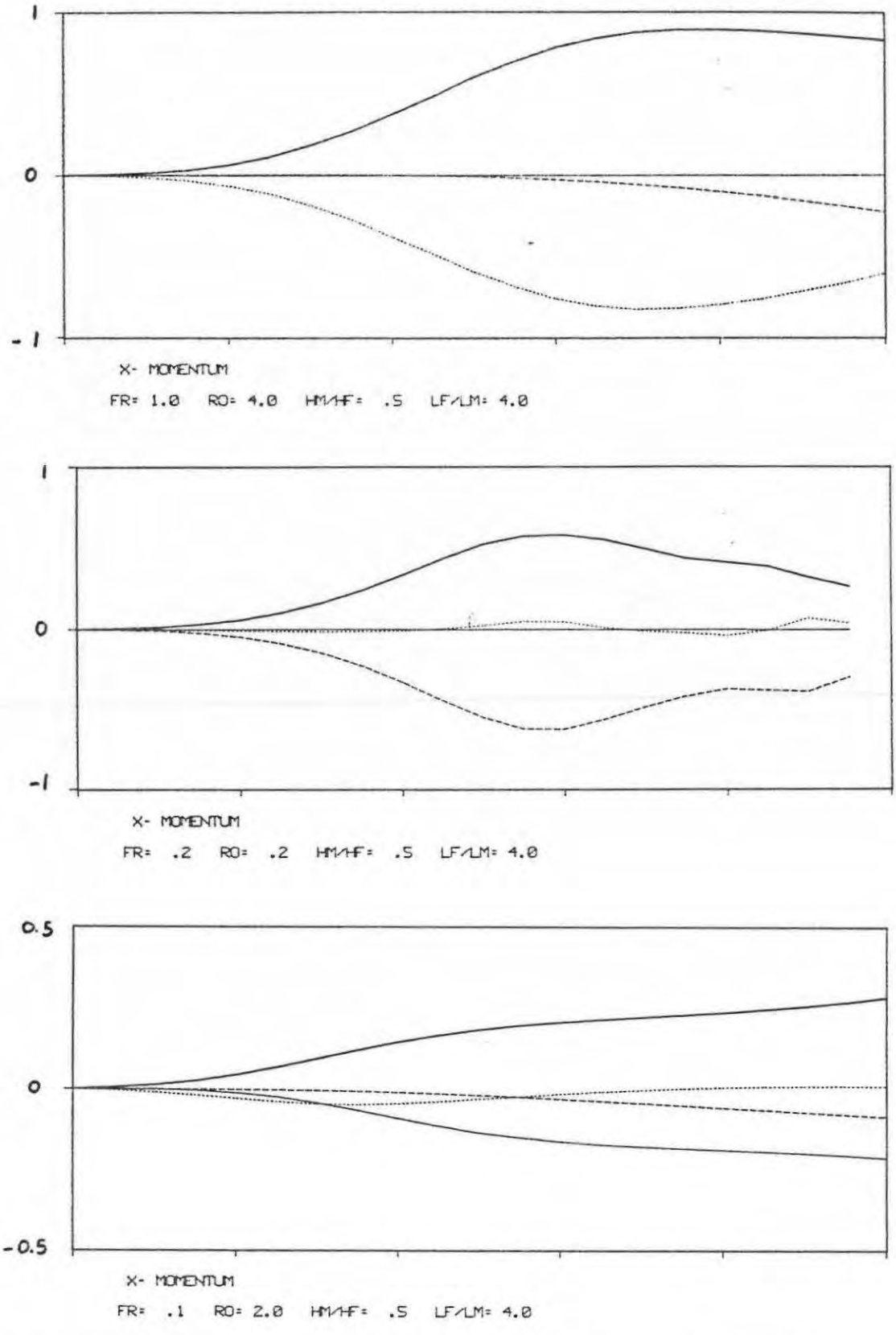

Figure IV.16: The momentum budget corresponding to the experiments of Fig. 15. The different terms are defined in Eq. IV.30. The thick solid line represents the drag (D), the dotted line the U-momentum term (A), the dashed line the Coriolis term (B) and the thin solid line the pressure gradient term (C).

Chapter V: The effect of continuous stratification and secondary frontal circulation on the interaction

1. INTRODUCTION

In this chapter the front-mountain interaction is studied using a two dimensional (x, z) numerical model. The effects of continuous stratification, vertical shear and secondary frontal circulation, neglected in the model of the previous chapter, are investigated. A particular emphasis will again be given to understanding the pressure drag and the evolution of the surface pressure in the model during the interaction and comparing it with the observations. We will not attempt here an extensive study of the entire parameter space but we will rather concentrate on a set of parameters appropriate for the Alpine cases and discuss the differences between simulations with and without front or mountain. In addition the role of the vertical shear in the wind across the front will be investigated.

It has been shown in Chapter I that when a cold front is advected southward across the Alps there is a rapid evolution of the pressure drag between two stages. Before the front reaches the mountain on the north side, the pre-frontal stage, the drag on the atmosphere is very large and directed southward while the upper air flow is westerly and almost parallel to the ridge. At low level there is a southerly shallow foehn. When the front has passed over the mountain, the post frontal stage, the upper air flow is north-westerly and the drag becomes very large and directed northward.

The study of fronts and of flow over mountains have been so far vigorous but separate areas of research. The front mountain interaction is a difficult problem in general due to the variety of possible effects that the mountain can have. For example the observational study of

McGinley (1982) reveals that both the horizontal deformation field as well as the horizontal shear in vertical motion induced by the mountain play a frontogenetic role in different parts of the Alpine range.

Recent progress has been made in the quasi-geostrophic study of Bannon (1983) and the semi-geostrophic studies of Bannon (1984) and Zehnder (1986). In Bannon (1983), the translation speed of the deformation speed is specified so there is no retardation of the front exhibited by the solution. However the first order ageostrophic velocity suggest that the cold front is retarded and weakened on the upwind slope. In Bannon (1984) the less restrictive semi-geostrophic approximation is used but additional approximations have to be used in order to obtain an analytical solution. In this case both warm and cold fronts are retarded on the upstream slope but accelerated in the lee. This behavior is caused by the ageostrophic mountain induced wind field. The maximum retardation of the front is shown to be half the Rossby radius of deformation based on the mountain height ($1/2\ Nh_m/f$) which shows no dependance on the Rossby number (U/fL). The frontal strength is increased on both side and weakened near the mountain peak, in accordance with the divergence pattern of the ageostrophic wind. However the mountain profile has to be specified in the geostrophic coordinate, resulting in a solution that corresponds to different physical mountain profiles at different times. Some of these restrictions have been relaxed by Zehnder (1986) who used a numerical model to obtain the semi-geostrophic solution for an arbitrary mountain height and frontal strength. Both the upstream retardation of the front and its downstream acceleration are now proportional to the mountain slope. As opposed to the results of Bannon (1984), the front is weakened on the upstream slope and Zehnder attributes the difference to an underestimation of the effect of tilting due to vertical motion.

We must emphasize however that all these solutions have been obtained using either the quasi- or semi-geostrophic approximation which are known to be inadequate for the Alps

(for which the Rossby number is 1 or larger). In particular they do not reproduce the strong barrier effect of the mountain. Therefore much remains to be done in extending these results to the full range of ageostrophic effects.

The three studies mentioned so far have been concerned with the frontogenesis due to a large scale horizontal deformation field. However, as pointed out by Orlanski and Ross (1977), such frontogenesis investigations do not provide a complete picture of the circulation within a fully developed front. For example if the frontal system is assumed to have already formed and is initially in geostrophic balance then the vertical shear of the cross front synoptic wind generates a different type of secondary circulation . However, one must say that although the front is in a steady state in the sense of the quasi- geostrophic theory which considers only advection by the geostrophic wind, the ageostrophic circulation is weakly frontogenetic as can been seen in the simulations of Orlanski and Ross (1977).

In this chapter we will similarly study the interaction between a fully developed front and the mountain. This approach is somewhat justified by the observations that show the fronts usually arriving fully formed on the coastal areas far upstream of the mountain. In addition, the structure of the horizontal deformation field is intimately linked to the three dimensional effects of the mountain (McGinley, 1982) which will not be considered here.

In the simulations presented we have chosen a mountain that is deliberately smaller than the Alps. Other experiments have been performed with a two-dimensional mountain of realistic height in which the solution is completely dominated by the mountain forcing, in particular by the wave breaking region in the lee. But there is no observational evidence of such a breaking region in the Alps. The explanation for this discrepancy, if it is real, is still unknown but it might be due to the three dimensional effects which are likely to affect the wave breaking characteristics, or to the surface friction which would possibly decrease the strength of the response and reduce the breaking. However, one caveat in the approach used

here is the underestimation of the barrier effect of the mountain primarily related to its height. Therefore we will not be able to infer from these experiments the importance of the blocking of cold air relative to the other mechanisms, as described in the preceding chapter. This, however is complementary to the study of the previous chapter.

In section 2 the numerical model will be presented together with a description of the diagnostic procedure to compute the surface pressure. The initialization and the presentation of the numerical experiments will be found in section 3. Section 4 will be devoted to the comparison of simulations with and without a front, a mountain or shear in the wind across the front. The pressure drag and the momentum flux during the interaction will be discussed in section 5 and 6, followed by a summary and discussion in section 7.

2. THE NUMERICAL MODEL:

The simulations presented here were run using the numerical model described in Orlanski and Ross (1977) with the modifications presented in Pierrehumbert and Wyman (1985) in order to incorporate a mountain.

This model is two dimensional (x, z) with the y-coordinate parallel to the frontal axis. The dry, hydrostatic, Boussinesq version has been used here. The mountain was introduced by means of a terrain following coordinate: $s = H(z-h(x))/(H-h(x))$ where H is the total height of the model and h the mountain height. A sponge layer at the top of the model prevents the spurious reflection of wave energy likely to be produced by the mountain. Initially the y-velocity jet is in geostrophic balance with the temperature gradient across the front and the frontal system is advected towards the mountain by a synoptic wind U(z). This wind is initially uniform in x so that no large scale frontogenetic horizontal deformation field is present. The solution is assumed to be independent of the y variable except for a y-gradient

of temperature in thermal wind balance with the synoptic wind U and which is kept constant throughout the integration.

The prognostic variables in the model are:

ζ : the vorticity component along the y-axis

v : the y-velocity

θ : the potential temperature

and at each time the streamfunction in the x-z plane is obtained from ζ by solving an elliptic Poisson's equation.

The turbulent fluxes of y-momentum, vorticity and heat are parameterized using a stability dependent eddy diffusivity detailed in Orlanski and Ross (1977). As pointed out by Pierrehumbert and Wyman (1985) such a parameterization allows mountain wave breaking to be handled without explicitly resolving convective mixing. Open boundary conditions are implemented on the sides in which the inflow or outflow behavior of the boundary is set by the direction of the locally determined phase velocity. The model resolution is 10 km in the horizontal and varies in the vertical from 150m near the ground to 350m near the top. The domain dimensions are 1500km length by 20km height. The last 4 km in the vertical are used for the sponge layer.

2.1 Surface pressure computation:

The surface pressure is required to compute the pressure drag in the model. It is also an important element in the comparison with observations as we have discussed in the previous chapters, but one that has not received attention in previous investigations. The pressure is not a prognostic variable in the model and this section describes how it is diagnosed.

The pressure is obtained by downward vertical integration of the hydrostatic relation which is valid in the model. The atmosphere in the model, either in its anelastic version or the Boussinesq used here, is linearized around a reference state of rest. This state remains

constant in time and space and therefore only the pressure perturbations arising from the deviations from this reference state will be considered .

The hydrostatic relation for this perturbed pressure in the Boussinesq approximation is:

$$1/\rho_0 \, \partial p'/\partial z = g \; \rho'/\rho_0 \qquad (5.1)$$

where primes indicate deviations and zeros the reference state.

In order to carry out the vertical integration we need an upper boundary condition on the pressure. The rigid lid approximation used at the top of the model does not readily provide such a condition because it allows arbitrary pressure variations. However a sponge layer has been introduced at the top of the model in order to absorb the perturbations propagating from below and prevent spurious reflection. We will therefore assume that no perturbation actually reaches the boundary and that the pressure remains unperturbed at the top. The validity of this assumption depends of course on the effectiveness of the sponge layer which was found adequate for all cases presented here.

When a front is initially present in the flow there is some ambiguity in defining the reference state which must be horizontally uniform. The reference chosen here for all cases is the initial state at the right boundary of the domain, on the warm side of the front. The surface pressure perturbation p'_s is therefore initially zero on the right boundary. If there is no front p'_s is initially zero everywhere but it reaches a minimum under the surface front otherwise.

3. DESCRIPTION OF THE NUMERICAL EXPERIMENTS:

3.1 Initialization:

In the study by Orlanski and Ross (1977), the front was initialized over flat terrain by prescribing the y-velocity jet and finding the corresponding geostrophicaly balanced

temperature field. Pierrehumbert and Wyman (1985) initialised the model with uniform flow over the topography. The initialization with a frontal zone above the topography is in general a difficult problem. The approach adopted here is to place the front sufficiently upstream of the mountain so that in practice the initialization can be carried out independently for the front and the mountain. The model domain is therefore separated in two parts: one containing the front initialised as in Orlanski and Ross (1977) and the other containing the mountain as in Pierrehumbert and Wyman (1985).

In the presence of vertical shear in the synoptic wind a secondary circulation develops (see e.g. Orlanski and Ross, 1977). The time to spin up this circulation to quasi steady state is on the order of a few hours and is related to the time for gravity waves to leave the region. The circulation can be approximately diagnosed using the Sawyer Eliassen quasi-geostrophic diagnostic equation. There is therefore an issue as to whether such a diagnostic circulation should be used in the initialization of the front. However in the present simulation the initial adjustment of the flow over the topography which is impulsively started, must also be taken into account and there is no immediate diagnostic equation for it. Consequently the approach chosen here is to allow sufficient time for both the secondary circulation to develop and the mountain flow to settle before the interaction.

3.2 Initial conditions:

The initial y-velocity profile is shown in Fig. V.1. a and is similar to the "midtropospheric jet" case in Orlanski and Ross (1977) but with the following modifications. The height of the jet maximum has been increased from 4000m to 7000m while keeping a similar wind at the surface. The jet was also forced to decay faster towards the top of the model so that it will not be affected by the sponge layer.

The corresponding potential temperature profile is shown in Fig. V.1.b. At the right boundary the vertical variation of θ is prescribed to 3. 10^{-3} K m^{-1} below the tropopause

(10 km) and 10. 10^{-3} K m^{-1} above. The maximum temperature difference across the front is close to 10 ºC. The frontal slope is approximately 1/100 as seen in Fig. V.1.a.

The gaussian mountain of half width 50 km and height 1000m is located at 950 km and initially 500 km from the surface front.

The vertical U-wind profile is given by:

$$U = U_0 + (U_\infty - U_0) \tanh (Z / Z_S) \qquad (5.2)$$

with Z_S = 5000 m and $U_0 = U_\infty$ = 10 m/s for the experiment without shear and U_0 = 7.5 m/s and U_∞ = 12.5 m/s for the experiments with shear.

Table V-1

Experiment	front	mountain	shear	Ro	Fr
F	yes	no	no		
F+S	yes	no	yes		
M	no	yes	no	2.0	0.8
M+S	no	yes	yes	1.5	1.1
F+M	yes	yes	no	2.0	0.8
F+M+S	yes	yes	yes	1.5	1.1

In the following six experiments will be discussed: with and without front, mountain or vertical shear. Their characteristics are summarized in Table V-1 (both the Rossby number and the Froude number are based on the low level flow).

4. RESULTS OF THE SIMULATIONS: THE IMPORTANCE OF SECONDARY CIRCULATIONS.

In this section we will present in turn the results of our simulation for the front alone, the mountain alone and the interaction between the two. In each case we will discuss the differences with and without vertical shear in U.

4.1 The front alone (experiments F and F+S)

In the absence of the mountain and of vertical shear in U (F) the front is simply advected through the domain with little modification. This can be verified in Fig. V.2.a showing the potential temperature after 20 h of advection and which is an almost exact translation of the initial condition shown in Fig. V.1.b.

In the corresponding experiment with vertical shear (F+S), a secondary circulation develops in a matter of a few hours and is shown in Fig. V.3.a at 5 h. As discussed by Pierrehumbert (1984) and Orlanski and Ross (1977) this circulation can be diagnosed using the quasi-geosptrophic version of the Sawyer-Eliassen equation:

$$N^2 \partial_{xx}\Psi' + f^2 \partial_{zz}\Psi' = - 2 f \partial_z U \partial_x V \qquad (5.3)$$

where Ψ' is the ageostrophic streamfunction in the x,z plane. For the initial condition shown in Fig. V.1 the vertical scale of the circulation is therefore primarily determined by the shear in U. The strength of this circulation is proportional to $\partial_z U$. This circulation causes an important slow down of the prefrontal flow and can create of shallow region of locally blocked or reversed flow as shown in Fig. V.3.b.

The potential temperature at 20h, in Fig. V.2.b (F+S) , shows the weak frontogenetic influence of this circulation when compared with Fig. V.2.a. One can also notice the formation of a region of weak static stability ahead of the front which has been argued by

Ross and Orlansky (1979) to be favorable to the formation of heavy precipitation and which will be important during the interaction with the mountain.

4.2 The mountain alone (experiments M and M+S):

The experiments for the mountain alone with and without shear (M and M+S) are compared in Fig. V.4 where only small differences are found in the potential temperature at 20 h.

For uniform flow previous investigations have shown that the amplitude of the mountain response depends only on the Froude number (Nh/U) but no similar result exists for the sheared flow. Here in the presence of vertical shear the wave has a slightly smaller amplitude although the Froude number based on the low level flow (indicated on the figures) is larger. On the other hand the Froude number based on the upper level flow is smaller which suggests that it might be more relevant in determining the magnitude of the response. Clearly these questions regarding the effect of the vertical shear on the mountain flow need to be looked at in more details. Presently we will only keep in mind that the effect of the vertical shear adopted is weak in the mountain only case.

In Fig. V.5.a the perturbation stream function reveals the secondary circulation set up by the mountain (for experiment M+S but both experiments M and M+S are similar in this respect). The U-wind field produced by the mountain is shown in Fig. V.5.b. This pattern is quite different from the semi-geostrophic solution in particular for its upstream downstream asymmetry related to the vertically propagating gravity waves.

4.3 The interaction (experiments F+M and F+M+S):

The front mountain interaction is presented here at two representative stages of the evolution: at 10h (after start up) in Fig. V.6 when the front is just upstream of the mountain

and at 20h in Fig. V.7 when the front has just crossed the ridge. The experiments with and without shear (F+M and F+M+S) are shown side by side for comparison.

4.3.1 The prefrontal stage (Fig. V.6):

At 10h the potential temperature (Fig. V.6.a,b) shows some marked differences between the interaction with and without vertical shear. The mountain wave pattern is very weak at low levels in the experiment with shear. At higher level, around 10 km, the wave pattern is very similar in both experiments. The existence, in the shear case, of this wave region decoupled from the low level flow is an indication of the strong transience of the flow. One can also see that the overall strength has been increased in the sheared case and that the static stability has increased behind the front but decreased ahead.

These effects can be better understood by comparing the secondary circulation in the two cases which are presented in Fig. V.6.c,d . In the unsheared case (Fig. V.6.c) there is no secondary circulation associated with the front and the pattern is very reminiscent of the mountain alone experiment shown in Fig. V.5.a . However in the presence of vertical shear there is a strong interaction (Fig. V.6.d) between the secondary circulation due to the front (as seen in Fig. V.3.a) and the mountain which suppresses the wave. The resulting circulation tends to increase the frontal strength and decrease the static stability above the mountain. In the upper troposphere, where the frontal circulation is small, the pattern is again similar to the unsheared case.

The differences introduced by the vertical shear are also well illustrated by the plot of the U-velocity in Fig. V.6.e,f . In the unsheared case (Fig. V.6.e) the vertically propagating wave pattern can clearly be seen with low velocities on the upstream side and high velocities in the lee of the mountain. By contrast, in the sheared case (Fig. V.6.f) there are two nearly symmetric regions of stagnant or even reversed flow on both sides of the mountain. On the

upstream side this reversed flow might explain the southerly shallow foehn observed on the north side of the Alps.

4.3.2 The post frontal stage (Fig. V.7):

A similar comparison is performed at 20h when the front has just passed over the mountain. In the potential temperature for the sheared case one can now observe a wave at low level which is comparable in strength to the unsheared case (Fig. V.7a,b). On the other hand the wave is now weaker in the sheared case in the upper troposphere, a situation opposite to the one discussed above at 10h. The same remark can also be made about the secondary circulation in Fig. V.7.c,d and the U-wind velocity in Fig. V.7.e,f . In the sheared case the wave pattern is starting to rebuild after being disrupted by the prefrontal secondary circulation.

5. THE PRESSURE DRAG DURING THE INTERACTION:

In this section we will compare the pressure drag in each of the experiments previously described. In order to understand better the differences between these cases we will also look at the evolution of the surface pressure in the model. In the next section we will also describe and compare the momentum flux at two different levels in the vertical for each experiment.

The pressure drag is obtained from the surface pressure and topographic gradient by integration over the entire domain, the method also used for the observations described in Chapter I. The drag per unit area presented here is then obtained by considering the mountainous area above 500m which was also considered in the observations. The momentum fluxes are obtained similarly.

The evolution of the pressure drag is presented in Fig. V.8, 9 and 10 for the mountain only (M), and the interaction with and without vertical shear (F+M and F+M+S), respectively. The time runs vertically downward. In parallel with this evolution, Hovmöller

diagrams of the surface pressure as a function of time are also presented. The position of the mountain is indicated in the top margin of these diagrams for reference.

5.1 The drag for uniform flow (M):

In the mountain alone experiment shown in Fig. V.8 , the drag rapidly evolves in a few hours to reach a value of approximately 1.5 Pa. From then on the evolution is very gradual towards a steady state value that can be estimated to roughly 2 Pa. This evolution is similar to other studies which did not include rotational effects (Peltier and Clark, 1979; Bacmeister, 1986). Nevertheless in both studies the drag slightly overshoots its initial steady state value, whereas here it slowly approaches this value asymptotically.

A look at the surface pressure evolution in Fig. V.8 helps to understand how this drag is created. The pressure is falling in the lee while it is rising on the upstream side. This therefore creates a strong pressure gradient across the mountain which is mainly localized on the downstream slope. There is however a weak tendency for the pressure in the simulation to decrease everywhere and it is more evident in the later stages after 15h. This may be due to a model deficiency that we have not been able to isolate.

This behavior of the surface pressure can be related to the flow features seen in the previous section using the Bernoulli relation:

$$B = p/\rho + \mathbf{u}^2/2 + gz = cst \quad \text{along streamlines} \qquad (5.4)$$

In the rotating system considered here this relation is still valid but there is no guarantee that the streamlines remain in the vertical plane of the model as they do in the non rotating case. For example the streamlines are deflected towards the left (in the northern hemisphere) on the upstream side of the mountain, causing particles to move towards lower pressure. However, in the regime of these simulations the v-component of the velocity is weak and the Bernoulli relation holds approximately in the plane of the model. The pressure rise on the

upstream side can therefore be related to the flow deceleration and similarly the pressure drop in the lee to the downslope wind acceleration.

5.2 The pressure drag during the interaction (F+M and F+M+S):

The pressure drag evolution for the front-mountain interaction with and without shear are presented in Fig. V.9 and 10, respectively. We will first describe the features common to both these cases, then compare them to the mountain only experiment, and finally discuss the differences introduced by the vertical shear.

In both Fig. V.9 and 10 the drag starts out positive after the initial adjustment. It then decreases to reach a negative minimum at 12h which approximately corresponds to the prefrontal stage discussed at 10h in the previous section (and shown in Fig. V.6). In this situation the surface front is just upstream of the mountain. Thereafter the drag rapidly increases to reach a positive maximum at 20h, corresponding to the post-frontal stage previously described (see Fig. V.7), when the front has just passed over the mountain.

This evolution of the pressure drag is very similar to that of the observations for the Alps, in particular when compared to the composite of the drag events associated with frontal passage for the period March 1-20, 1982 described in Chapter I . The time scale of this evolution is also of the same order as in the observations, although it corresponds more to a rapid frontal passage such as the one on March 11. Yet in the model this time scale is determined by the advection speed prescribed initially. The observed peak drag magnitudes discussed in Chapter I also agree reasonably well with the model.

To explain this behavior of the drag we turn now to the surface pressure shown in Fig. V.9 and 10 . Upstream of the mountain and early in the interaction the constant frontal propagation towards the ridge can be tracked by the position of the low pressure. The drag is zero at 15h exactly when the low pressure is sitting right over the top of the mountain. The minimum drag arises when the mountain is in the middle of the pressure fall associated with

the arriving front (as seen by a fixed observer). Meanwhile the maximum is reached when the pressure is rising following the passage of the front over the mountain but is reinforced by the high-low pressure pattern found in the mountain alone simulations.

The introduction of the front in the flow affects the drag evolution dramatically as compared with the uniform flow simulation (compare Fig. V.8 and Fig. V.9). The magnitudes are also different: a maximum of 2 Pa for the mountain only and 3-4 Pa for the interaction case, not to mention the drag minimum period which is completely absent without the front.

The surface pressure patterns also reflect these important differences. In order to better isolate the various components in the interaction we have subtracted the effect of the front in the following manner: the reference pattern for the front unperturbed by the mountain is obtained by translating the initial condition using the initial U-wind; this pressure for the unperturbed frontal case only is then subtracted from the pressure in the interaction shown in Fig. V.9 and 10 . The results of this operation are shown in Fig. V.11 and 12 for the unsheared and sheared simulation, respectively. In the unsheared case the difference is strongly reminiscent of the mountain only simulation with similar pattern upstream and downstream of the mountain and also comparable magnitudes. This indicates that without vertical shear the interaction can be thought of, from the surface pressure point of view, as the simple superposition of the frontal propagation and the uniform mountain flow. On the contrary, for the sheared case (Fig. V.12) the difference plot reveals marked differences with the mountain only pattern. In particular a high pressure center can be seen on the lee side at the time of minimum drag. This leads us next to the discussion of the differences introduced by the vertical shear.

From the drag evolution point of view the vertical shear does not affect the qualitative behavior, nevertheless the minimum drag in the sheared case is almost double that in the

unsheared one, while the drag maximum is also larger. The reasons for these differences can be found in the comparison of the pressure plots of Fig. V.9 and 10 and also in the difference plots of Fig. V.11 and 12 , but they are better seen in the sheared–unsheared pressure difference plot shown in Fig. V.13 . In this plot it is apparent that the larger magnitude of the prefrontal drag in the sheared case is attributable to both the high and low pressure centers located on the downstream and upstream side of the ridge, respectively. This situation is the opposite of what is expected when the air is flowing over the mountain in the positive direction (high pressure are upstream and low pressure downstream). We have seen however in the previous section that the main difference introduced by the shear is the secondary frontal circulation, which creates a locally reversed flow over the mountain, thereby explaining the differences found in Fig. V.13 . The larger post frontal pressure drag is on the other hand, attributable to the more pronounced general pressure fall in the lee.

6. THE MOMENTUM FLUX DURING THE INTERACTION:

Given the strong drag variations during the front mountain interaction it is interesting to find out the behavior of the accompanying momentum flux in the model and try to relate it to the observations discussed in Chapter II. In Fig. V.14 the momentum flux is presented at two levels for the three experiments that have just been described for the drag. The solid line represents the momentum flux at low level (2500m) whereas the dashed curve is for the upper level (8000m).

There is generally a large difference in the flux magnitude between the two levels. At the upper level the momentum flux is very small, generally less than 0.5 Pa. At the lower level the magnitudes are much larger and important differences appear in the time evolution. For the mountain only simulation the low level momentum flux agrees well with the surface pressure drag. On the other hand, during the interaction with the front, the peak surface drag

is generally much larger in magnitude than the peak momentum fluxes. These model results are consistent with the observations of momentum flux obtained from aircraft data in Chapter II.This is explained in part by the fact that the surface pressure gradient associated with the front contributes to the drag but not to the momentum flux. At low level the magnitudes are much larger and important differences between the experiments appear in the time evolution.

On theoretical grounds one expects for steady linear mountain waves in uniform flow without rotation, that the momentum flux at low level and the pressure drag are exactly equal in magnitude but opposite in sign. This is easily seen as follows:

- the linearized boundary condition at the ground gives:

$$w' = U\, dh/dx \qquad (5.5)$$

and the linearized Bernoulli relation (5.4) becomes:

$$p'/\rho_0 = - U\, u' \qquad (5.6)$$

these can be combined to give:

$$D = \int p'\, dh/dx\, dx = - \int \rho_0\, u'w'\, dx \qquad (5.7)$$

In the absence of a critical level and if all the other approximations remain valid, the momentum flux is constant with height (a result originally due to Eliassen and Palm, 1961). In the real atmosphere as well as the present numerical simulations the conditions differ drastically from this idealized situation. We will therefore examine in turn the differences and how they might be related to the fluxes shown in Fig. V.14.

First the flow is not strictly in the linear regime because the Froude number (Nh_m/U), a measure of the non linearity of the flow as discussed by Pierrehumbert and Wyman (1985), is greater than 0.8 for all simulations. The nonlinear effects are not very strong either as

shown for example in Fig. V.4, with only weak wave breaking. These simulations can therefore be considered in the weakly nonlinear regime which can partly but probably not totally explain the discrepancy between high and low level momentum fluxes by the weak absorption due to wave breaking.

Another important difference with the idealized situation occur in the presence of rotation. As shown by Jones (1967) for three dimensional stationary linear waves in the presence of vertical shear and rotation, the angular momentum flux, but not the momentum flux, is independent of height. However, a closer look at Jones results reveals that if the waves are two dimensional (such as in these experiments) then the momentum flux is again conserved. The rotation therefore appears to be unable to explain the important momentum flux decrease with height. One must say however, that nothing is known of the case of transient non linear waves.

The effect of transience in the numerical simulations is indeed a strong candidate for explaining the vertical momentum flux decay with height. In a transient system one expects a lag between the response at low and high levels which is related to the time it takes for a disturbance to travel between the two levels. For gravity waves (without rotation) the dispersion relation is:

$$\omega = Uk \pm Nk / m \qquad (5.8)$$

where k and m are the horizontal and vertical wave numbers and N the Brunt–Vaïssala frequency. The vertical group velocity for stationary waves, relevant to determine the propagation of the forced mountain perturbation is therefore:

$$C_{gz} = U^2 k / N \qquad (5.9)$$

For these simulations we have U=10 m/s 1/k = 50 km and N = 0.8 10^{-2} s^{-1} which gives a vertical group velocity of 0.2 m/s. It takes therefore approximately 10 h for a

disturbance to travel to the upper level. Some indication of such a lag is suggested in the mountain only experiment in Fig. V.14.

The effects discussed so far can potentially be found in all three experiments. In the case of the front-mountain interaction experiments both the non uniform stratification in the front and the non uniform U-wind resulting from the secondary frontal circulation can play a role. These effects are not trivial as attested by the differences found in Fig. V.14.

In the interaction without shear the evolution is qualitatively similar at both levels to the mountain only case, but only up to 15h. Thereafter the flux at low level decreases in magnitude approximately by half. We have not been able at this time to fully understand this decrease. In the presence of vertical shear the evolution is completely changed. At the upper level the momentum flux oscillates around zero and no definite trend can be observed as in the other experiments. At low level the momentum flux even changes sign, following the reversal in the drag. At the time of minimum (negative) drag the momentum flux is positive. This difference in the low level momentum flux between the interaction with and without shear can be related to the magnitude difference in the minimum drag already discussed and is attributable to the secondary frontal circulation.

In summary the momentum flux shows in all cases a important decay with height. The candidates to explain this decay include the absorption due to wave breaking, rotation and transience of the flow. In the mountain only simulation the low level momentum flux is opposite to the surface drag, a result which is expected from theory. During the interaction with shear, the secondary frontal circulation gives rise to a pulse of positive low level momentum flux which can be related to the increase in prefrontal drag.

7. SUMMARY:

We have explored the front-mountain interaction in a continuously stratified two dimensional model by comparing simulations with the front only, the mountain only and the interaction between the two with and without vertical shear. The parameters in these experiments were chosen to be typical of the alpine cases, with the exception of the mountain height, which for realistic values was found to produce an unrealistically large response.

There is no large scale horizontal deformation field and in the absence of mountain and vertical shear the initial front (Fig. V.1) is simply advected throughout the domain. In the presence of vertical shear a secondary frontal circulation is created with weak frontogenetic properties (Fig. V.2 and 3). For the mountain only experiment the influence of vertical shear is very weak (Fig. V.4 and 5).

The secondary frontal circulation interacting with the mountain produces marked differences between the front-mountain interaction, with and without shear (Fig. V.6 and 7): the shallow, localized region of very weak or even reversed flow propagating ahead of the front causes a complete collapse of the mountain wave pattern. This local flow is similar to the shallow southerly foehn observed on the north side of the Alps just before the arrival of cold fronts from the north west.

The pressure drag and the surface pressure evolution (Fig. V.8, 9, 10) also reflect the important effect of the secondary circulation. After the initial adjustment the drag decreases towards a minimum of -1 to -2 Pa reached at 12 h and thereafter rapidly increases to reach a maximum of 3 to 4 Pa at 20 h. This behavior is very similar to the observations discussed in Chapter I. The vertical shear causes a doubling of the prefrontal minimum drag that can be related to higher pressure in the lee and lower pressure upstream, attributable to the effect of the secondary circulation (Fig. V.12, 13).

In all experiments the momentum flux decays with height and is less than 0.5 Pa in the upper troposphere. This is consistent with the weak values observed and described in Chapter II. The decay might be related to low level wave breaking, transience of the flow or the effect of rotation. At low level, for the mountain only simulation, the momentum flux is equal in magnitude but opposite in sign to the surface pressure drag, a result expected from theory. Without vertical shear, the introduction of the front in the flow causes little change in the low level momentum flux, indicating that the difference in surface drag is simply due to the advection of the frontal pressure pattern, which does not affect the momentum flux. By contrast the presence of vertical shear during the interaction produces a transient pulse of low level momentum flux causing the observed increase in prefrontal drag and attributable to the secondary frontal circulation.

Figure captions for Chapter V:

Figure V.1: Initial condition for the numerical simulations: a) V-wind (m/s); b) potential temperature (ºC). Distances are in km and time in hours.

Figure V.2: Potential temperature at t= 20 h for the front without the mountain: a) without vertical shear in the wind across the front; b) with vertical shear.

Figure V.3: Secondary frontal circulation (a) and U-wind (b) at t = 5 h for the front simulation without mountain but with vertical shear.

Figure V.4: Potential temperature at t = 20 h for the mountain without front: a) without shear; b) with shear.

Figure V.5: Secondary mountain circulation (a) and U- wind (b) at t = 20 h for the mountain simulation without front and with vertical shear. There is no appreciable difference caused by the vertical shear in this case.

Figure V.6: The pre-frontal stage (at 10 h) of the front mountain interaction. Both simulations without and with vertical shear are compared in the bottom and top frames respectively for: the potential temperature (a and b), the secondary circulation (c and d) and the wind across the front (U) (e and f).

Figure V.7: same as 6 but for the post-frontal stage of the interaction (at t = 20 h).

Figure V.8: Evolution of the surface pressure and drag for the mountain alone experiment.

Figure V.9: same as V.8 but for the front-mountain interaction without shear.

Figure V.10: same as V.8 but for the interaction with vertical shear.

Figure V.11: Difference plot of the surface pressure shown in Fig. V.9 for the unsheared interaction and the pressure due to the reference front (see text for details).

Figure V.12: same as V.11 but for the surface pressure shown in Fig. V.10 for the interaction with vertical shear.

Figure V.13: Difference plot of the surface pressure in the interaction with and without shear (Fig. V.10 and V.9 respectively).

Figure V.14: Time evolution of the momentum flux for: a) the mountain alone, b) the interaction without shear and c) the interaction with shear. The solid line represents the momentum flux in the low troposphere (at 2500 m) and the dashed line in the upper troposphere (at 8000 m)

a)

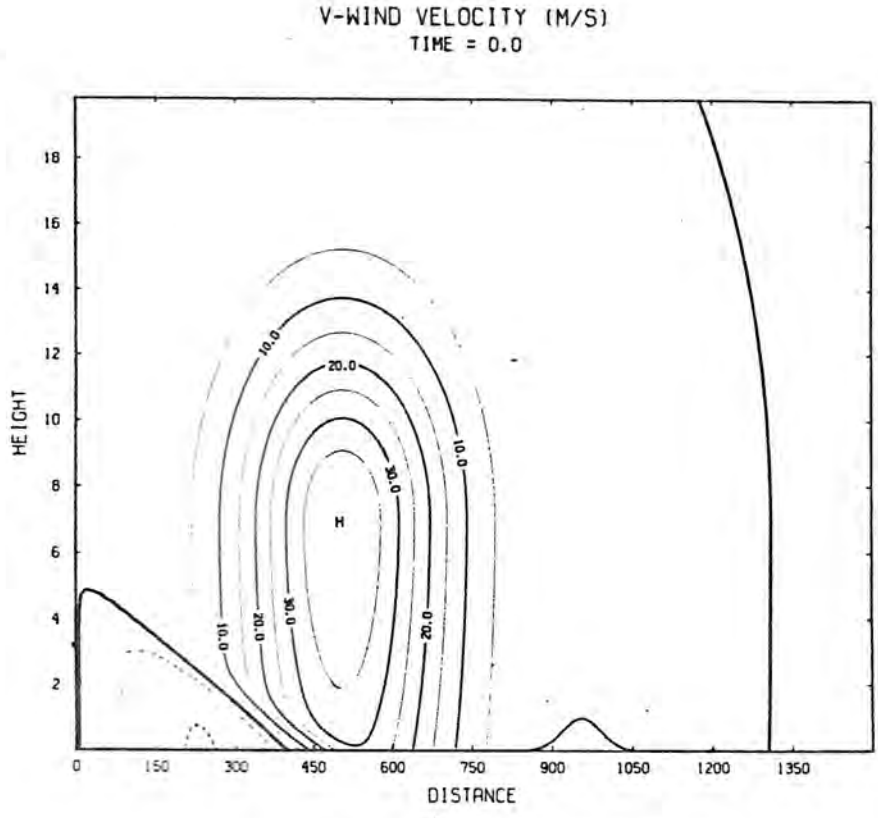

b)

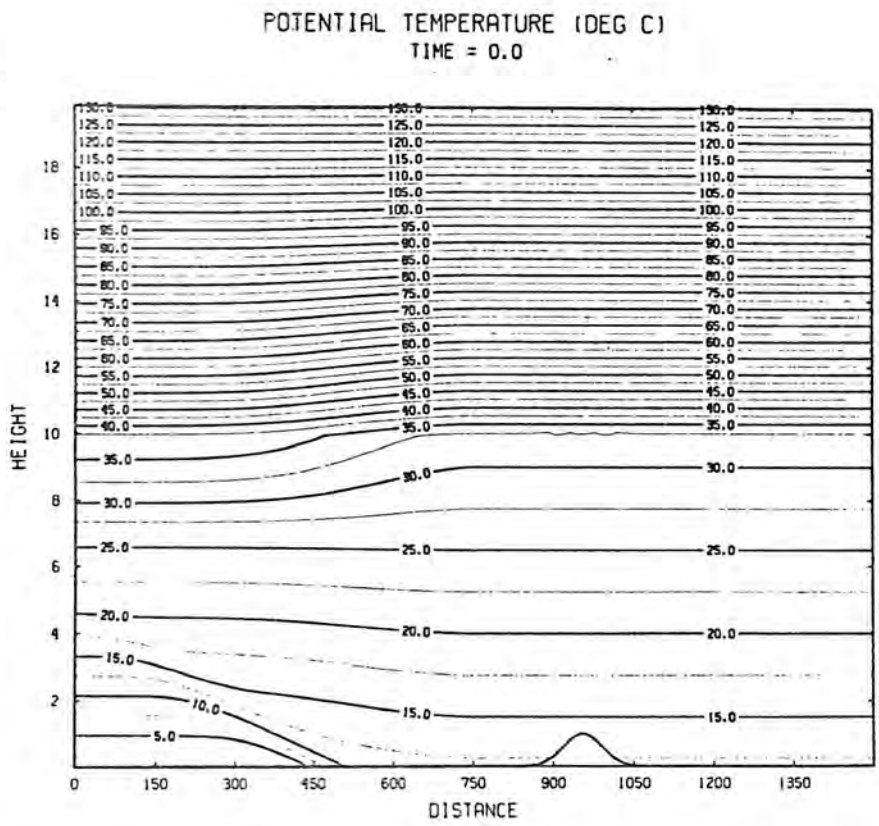

Figure V.1: Initial condition for the numerical simulations: a) V-wind (m/s); b) potential temperature (ºC). Distances are in km and time in hours.

a)

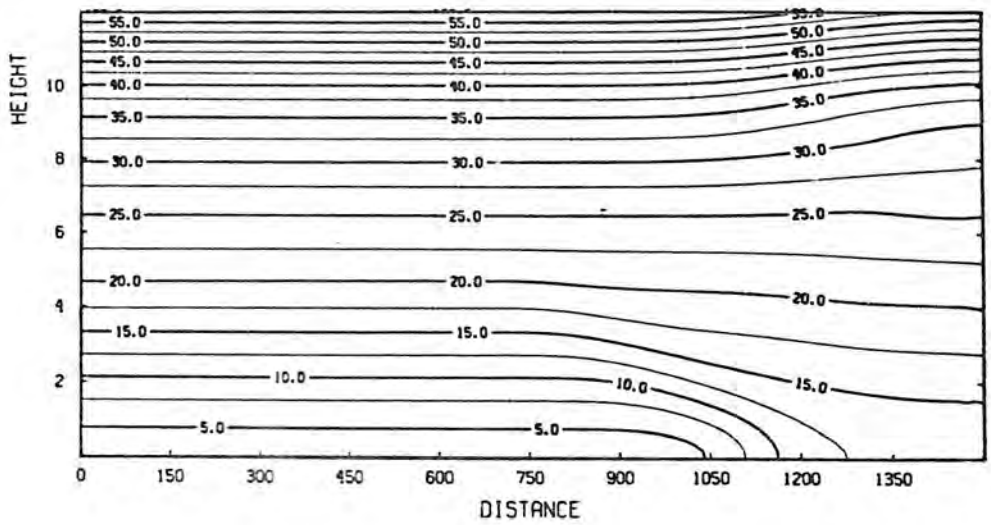

b)

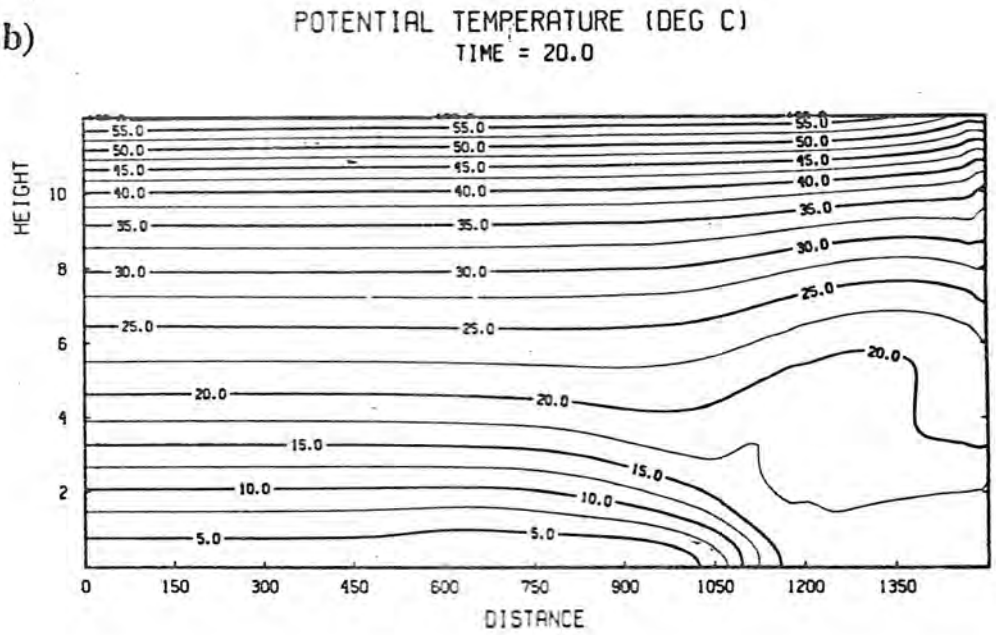

Figure V.2: Potential temperature at t= 20 h for the front without the mountain: a) without vertical shear in the wind across the front; b) with vertical shear.

a)

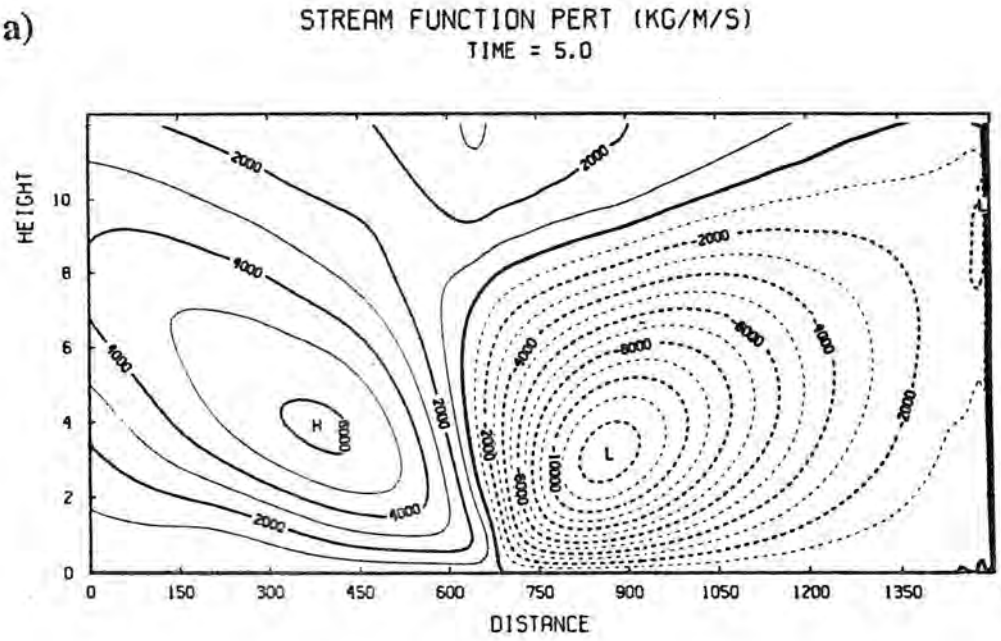

b)

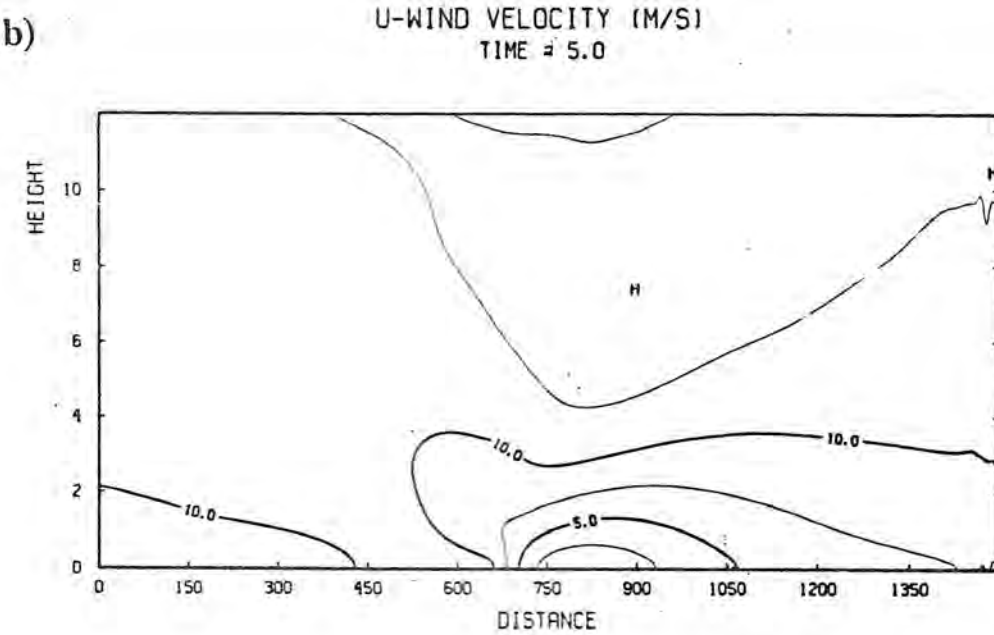

Figure V.3: Secondary frontal circulation (a) and U-wind (b) at t = 5 h for the front simulation without mountain but with vertical shear.

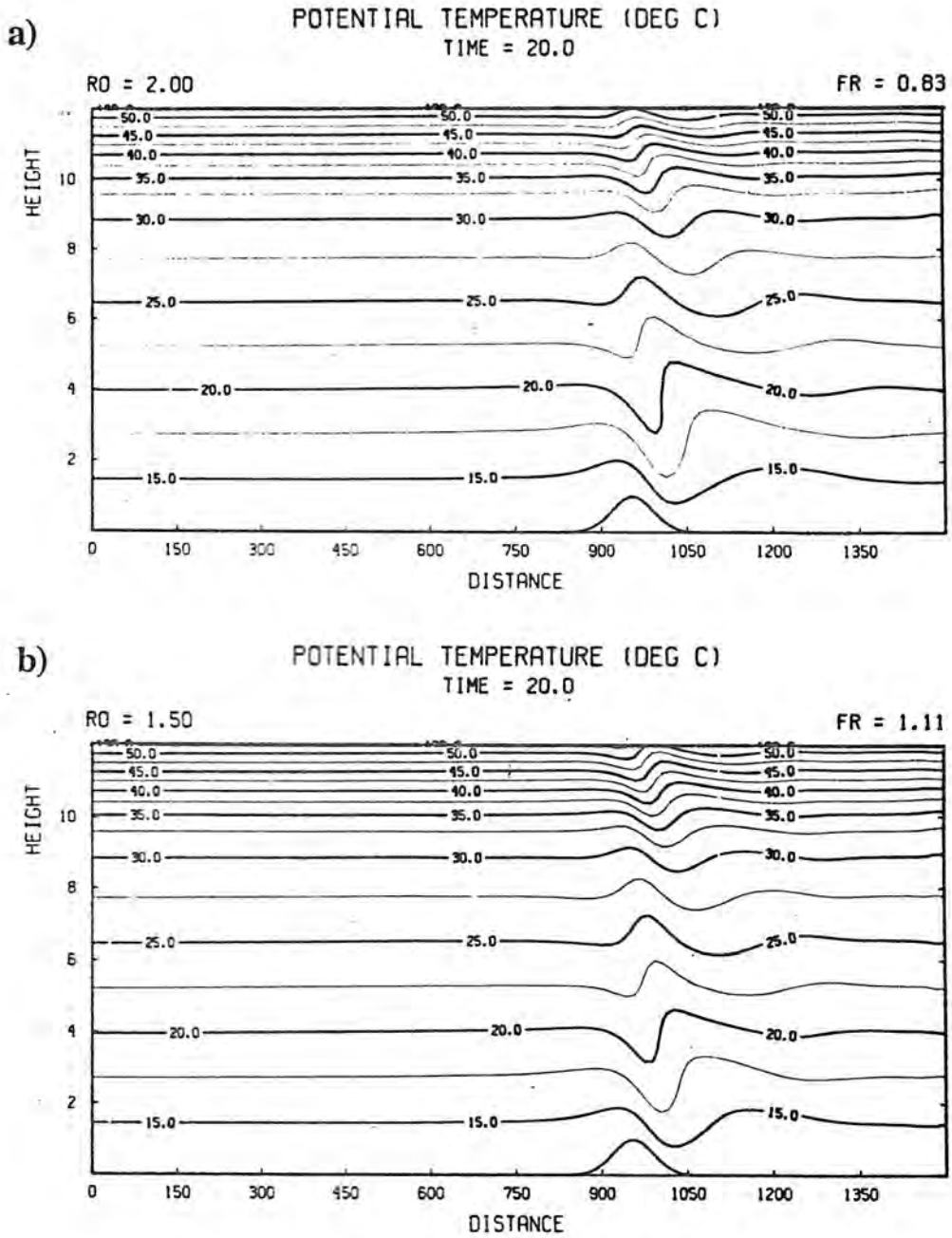

Figure V.4: Potential temperature at t = 20 h for the mountain without front: a) without shear; b) with shear.

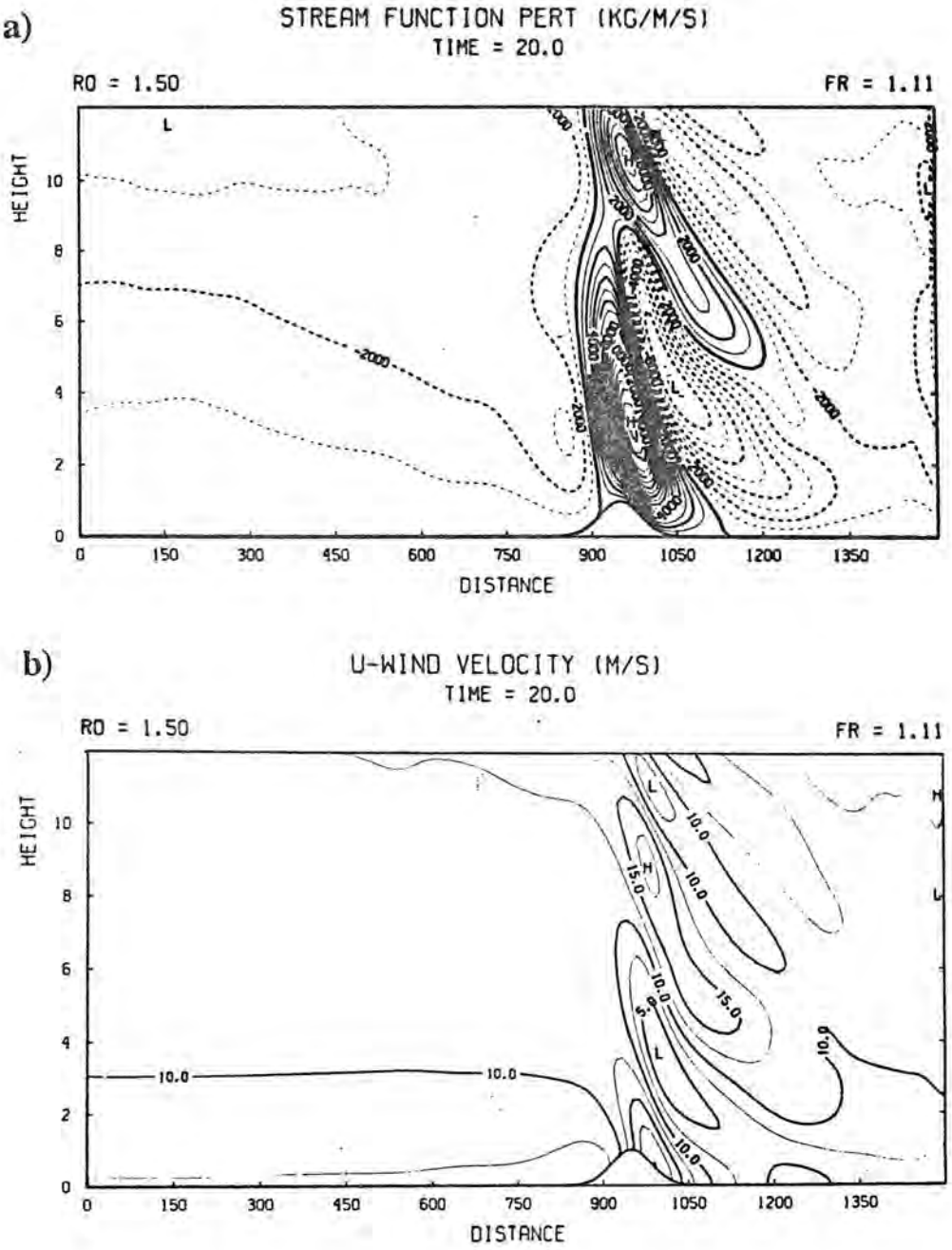

Figure V.5: Secondary mountain circulation (a) and U- wind (b) at t = 20 h for the mountain simulation without front and with vertical shear. There is no appreciable difference caused by the vertical shear in this case.

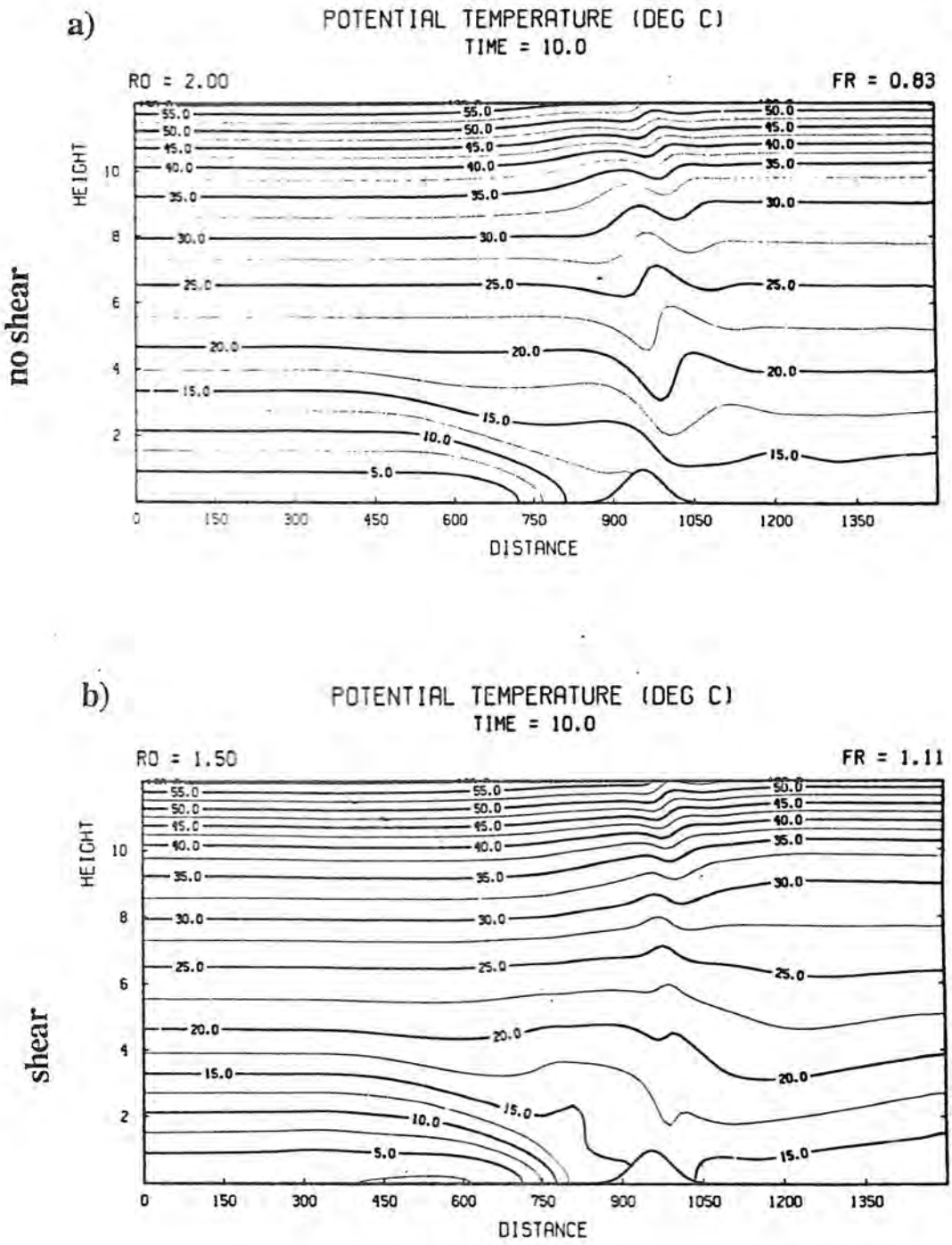

Figure V.6: The pre-frontal stage (at 10 h) of the front mountain interaction. Both simulations without and with vertical shear are compared in the bottom and top frames respectively for: the potential temperature (a and b), the secondary circulation (c and d) and the wind across the front (U) (e and f).

c)

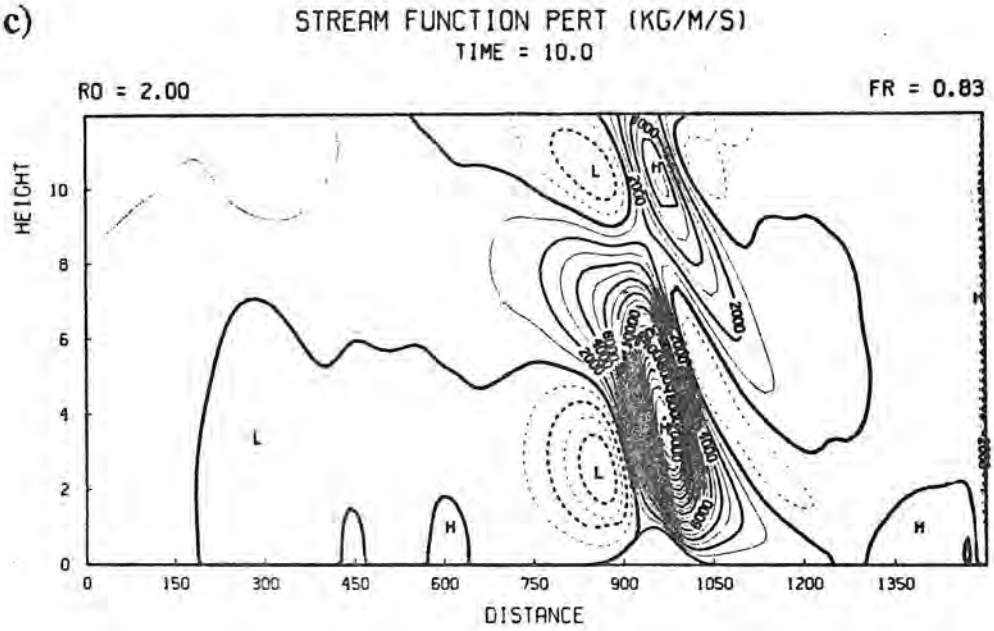

d)

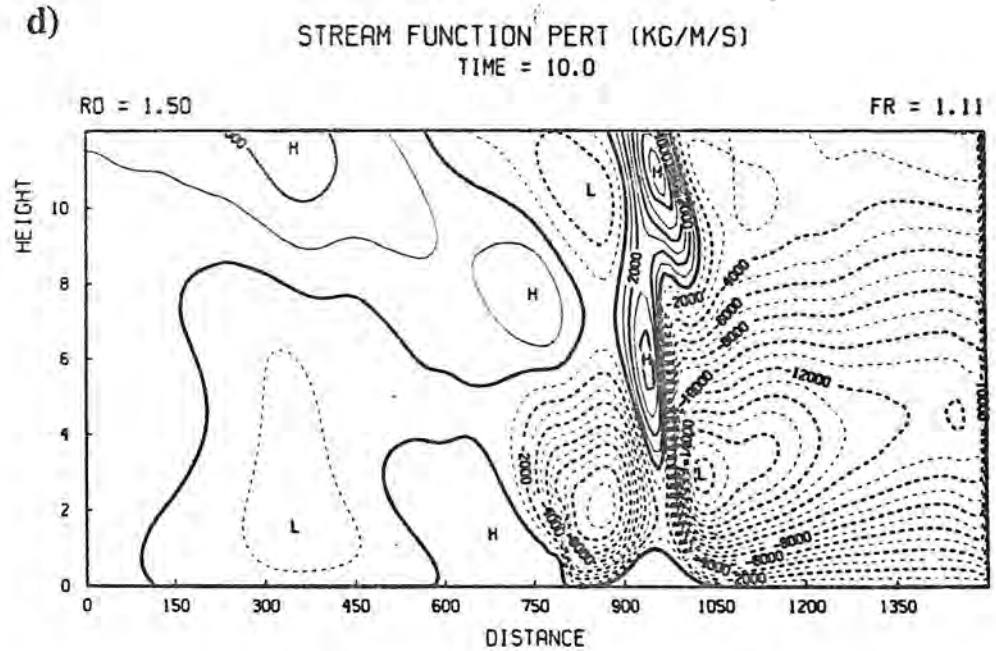

Figure V.6 (continue)

e)

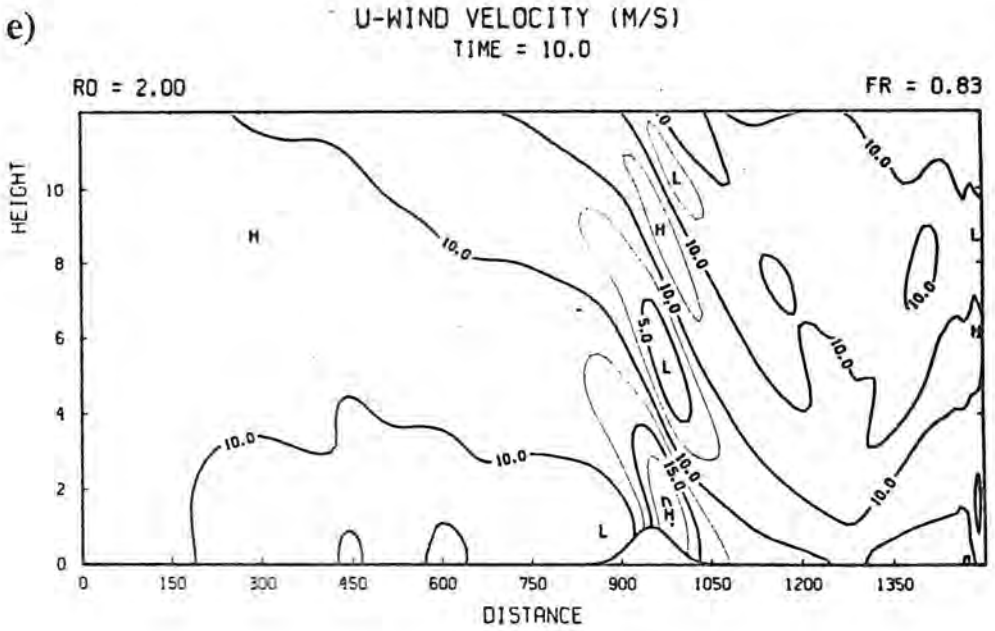

f)

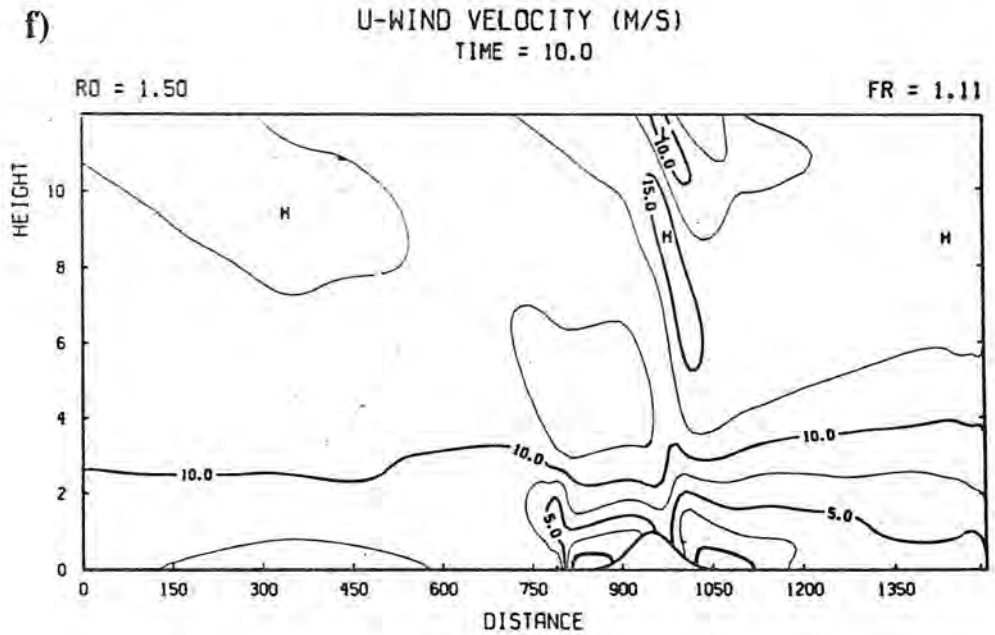

Figure V.6 (continue)

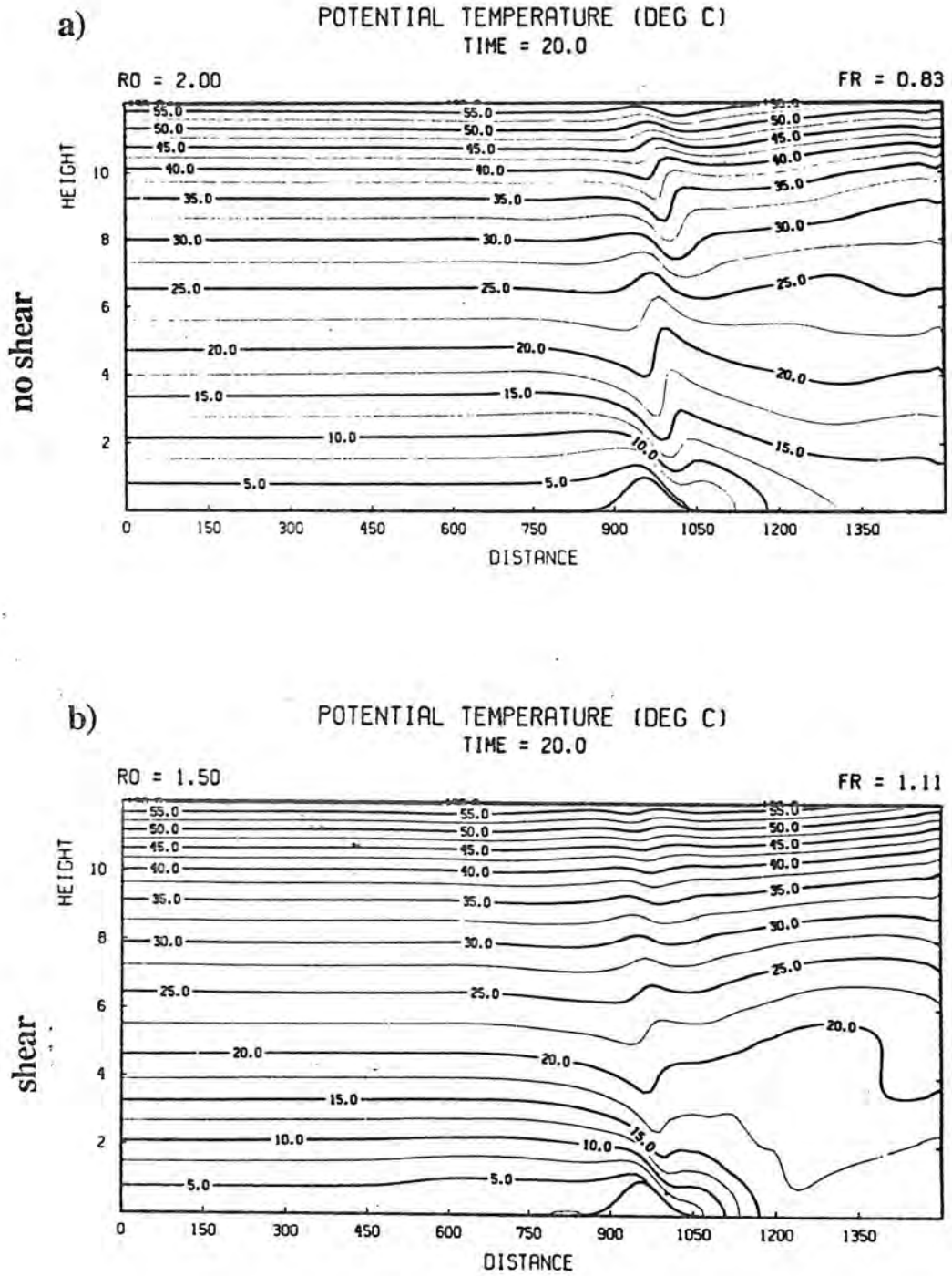

Figure V.7: same as 6 but for the post-frontal stage of the interaction (at t = 20 h).

c)

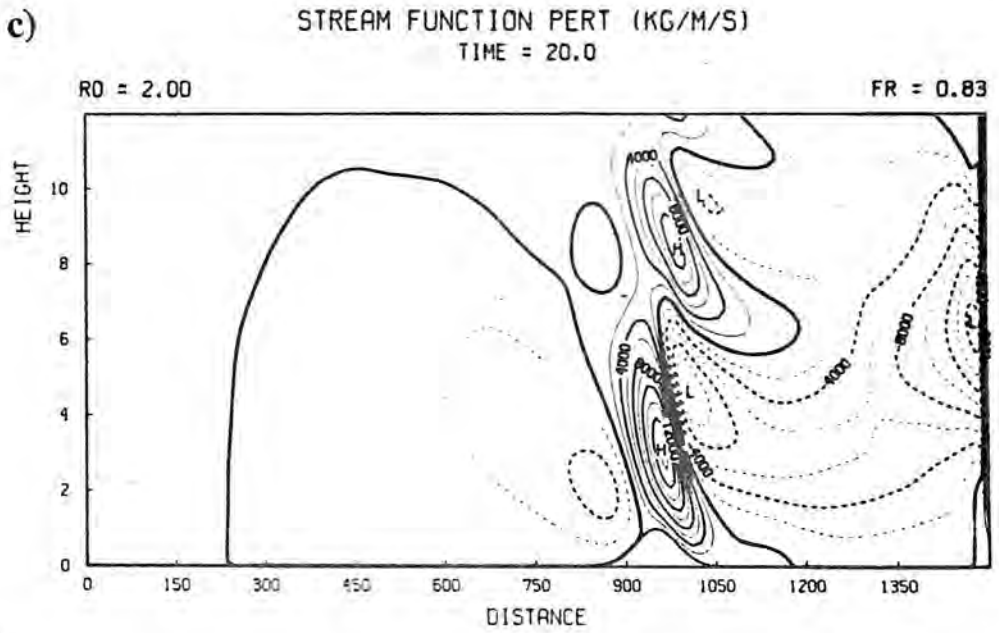

d)

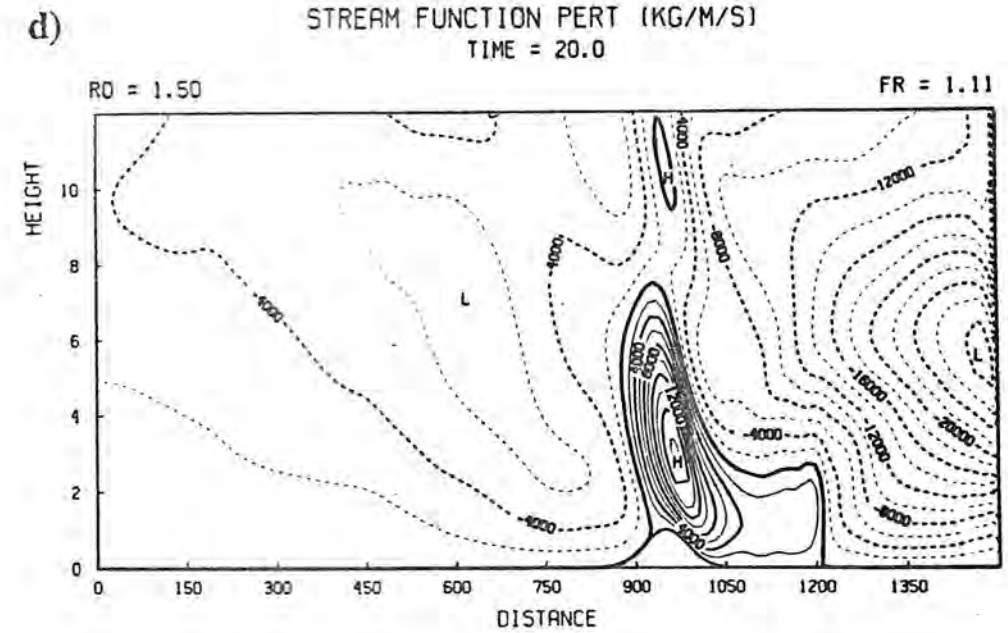

Figure V.7 (continue)

e)

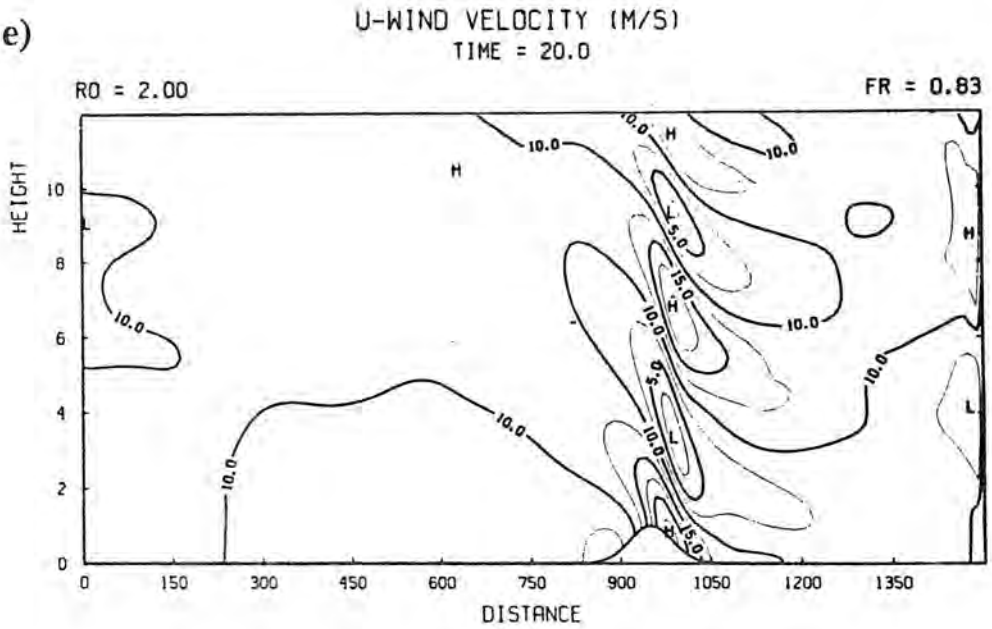

f)

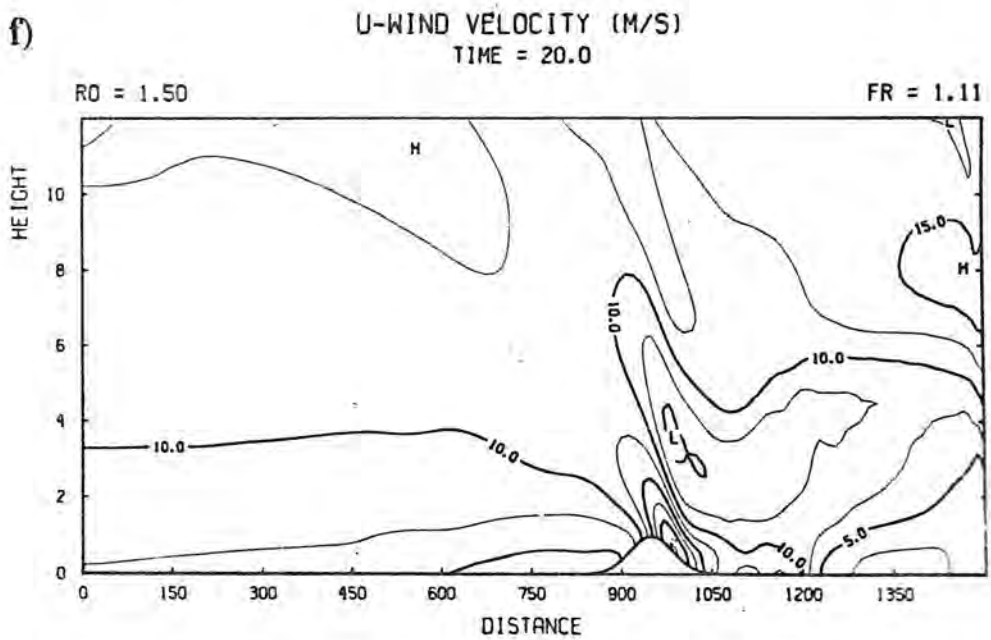

Figure V.7 (continue)

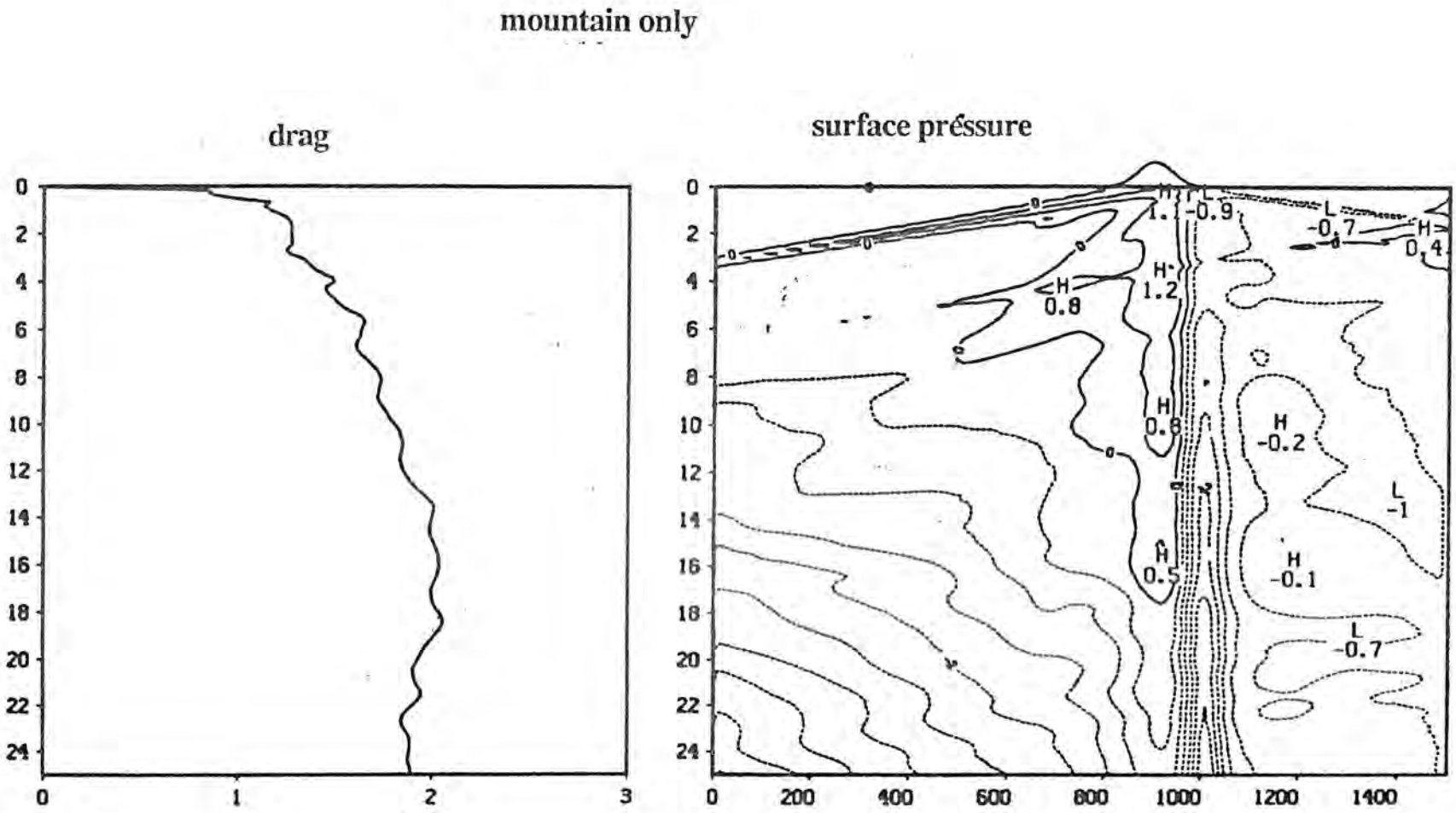

Figure V.8: Evolution of the surface pressure and drag for the mountain alone experiment.

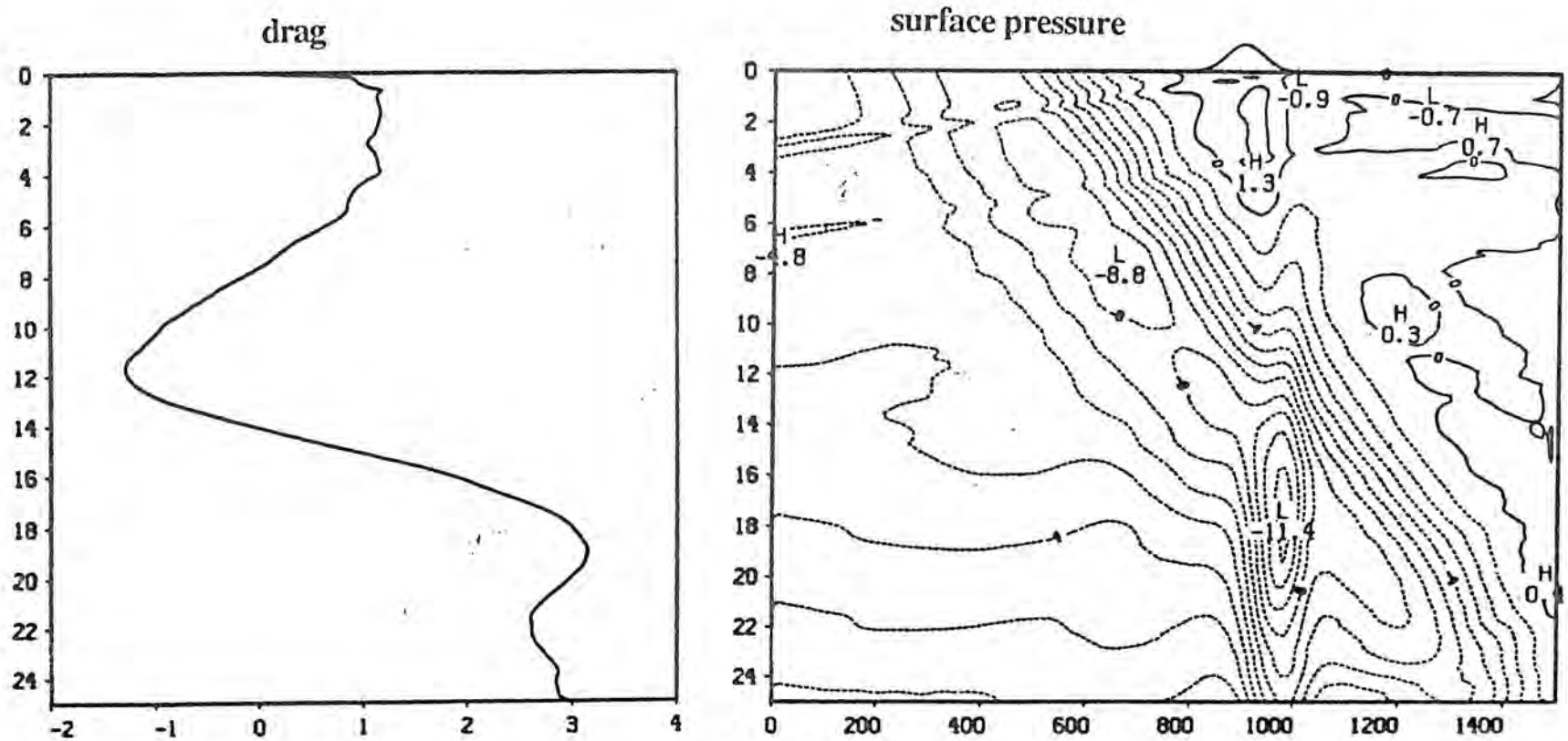

Figure V.9: same as V.8 but for the front-mountain interaction without shear.

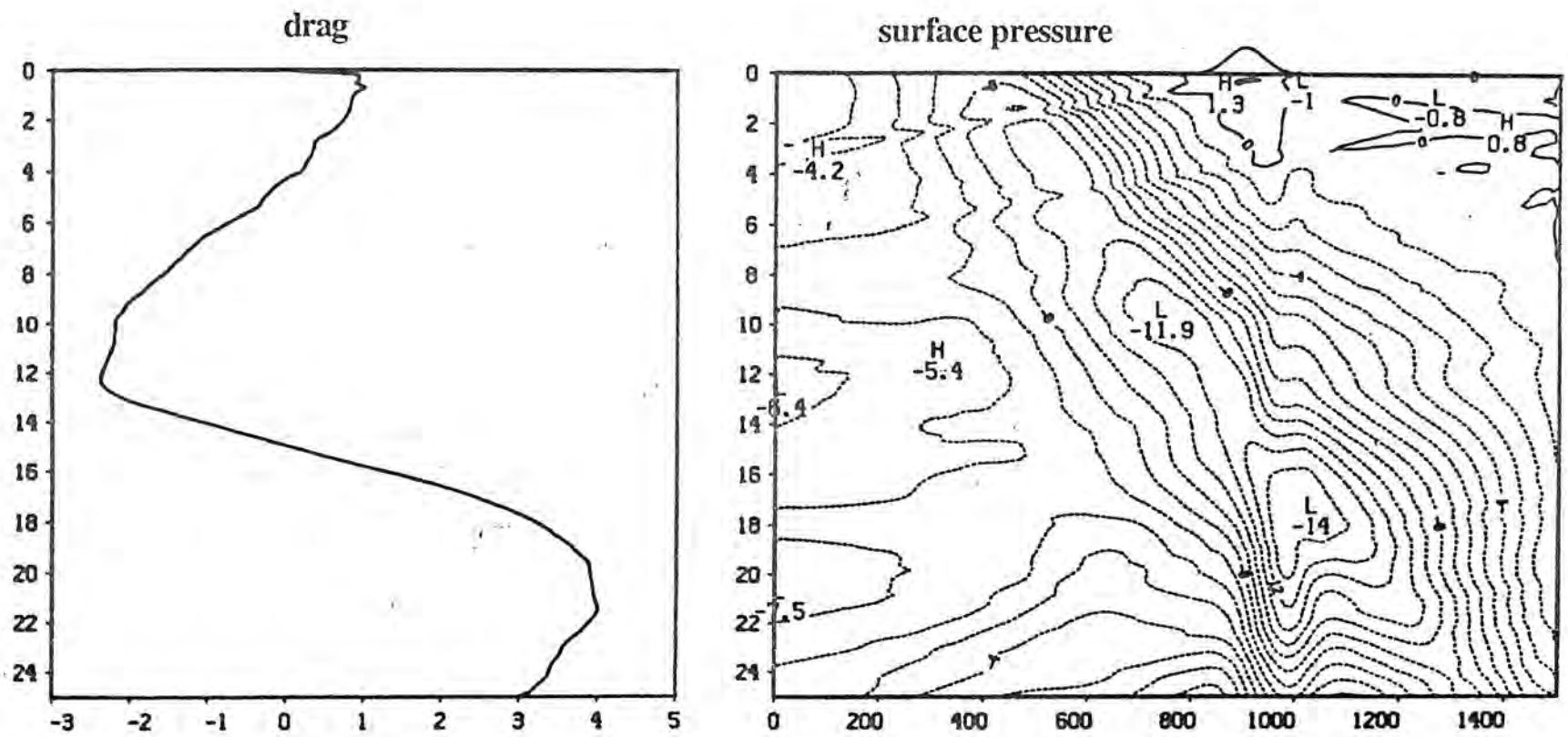

Figure V.10: same as V.8 but for the interaction with vertical shear.

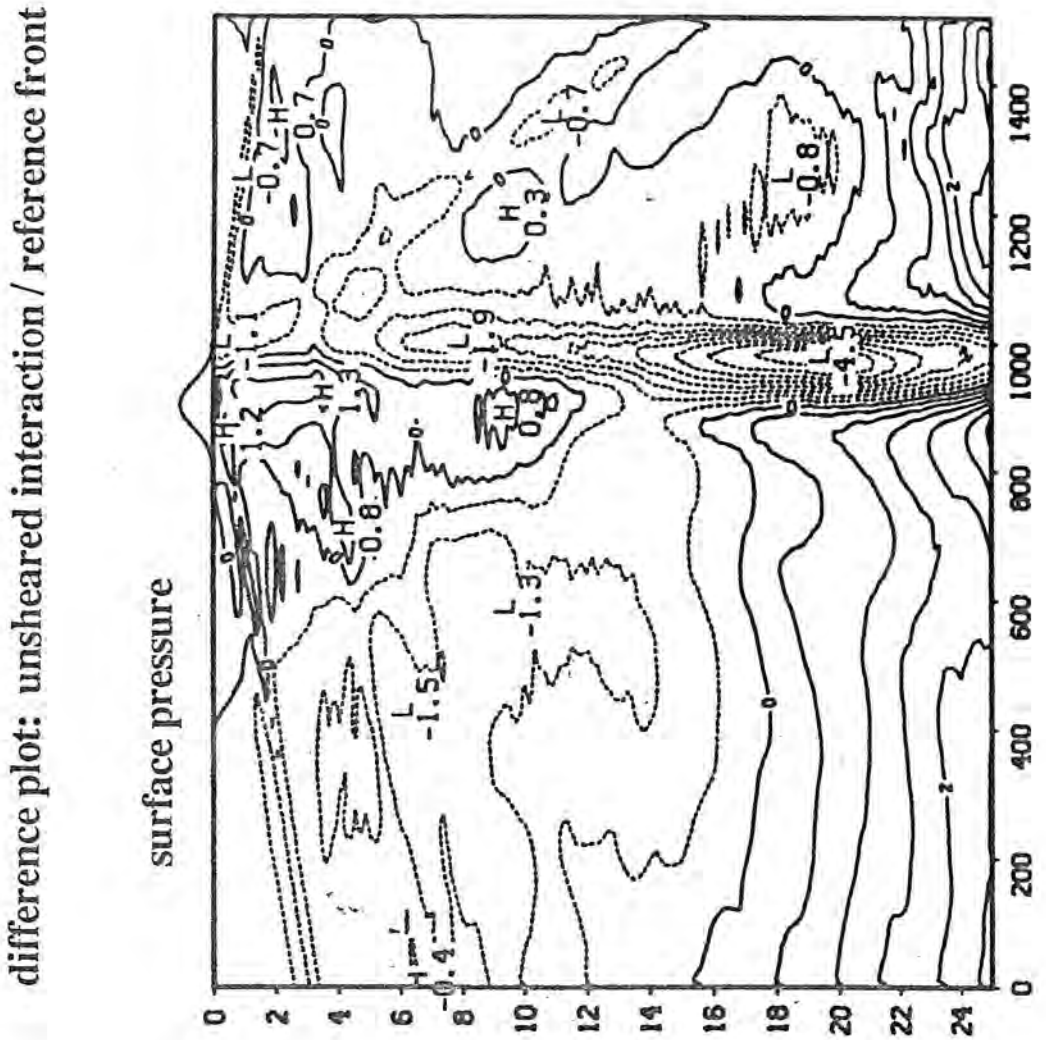

Figure V.11: Difference plot of the surface pressure shown in Fig. V.9 for the unsheared interaction and the pressure due to the reference front (see text for details).

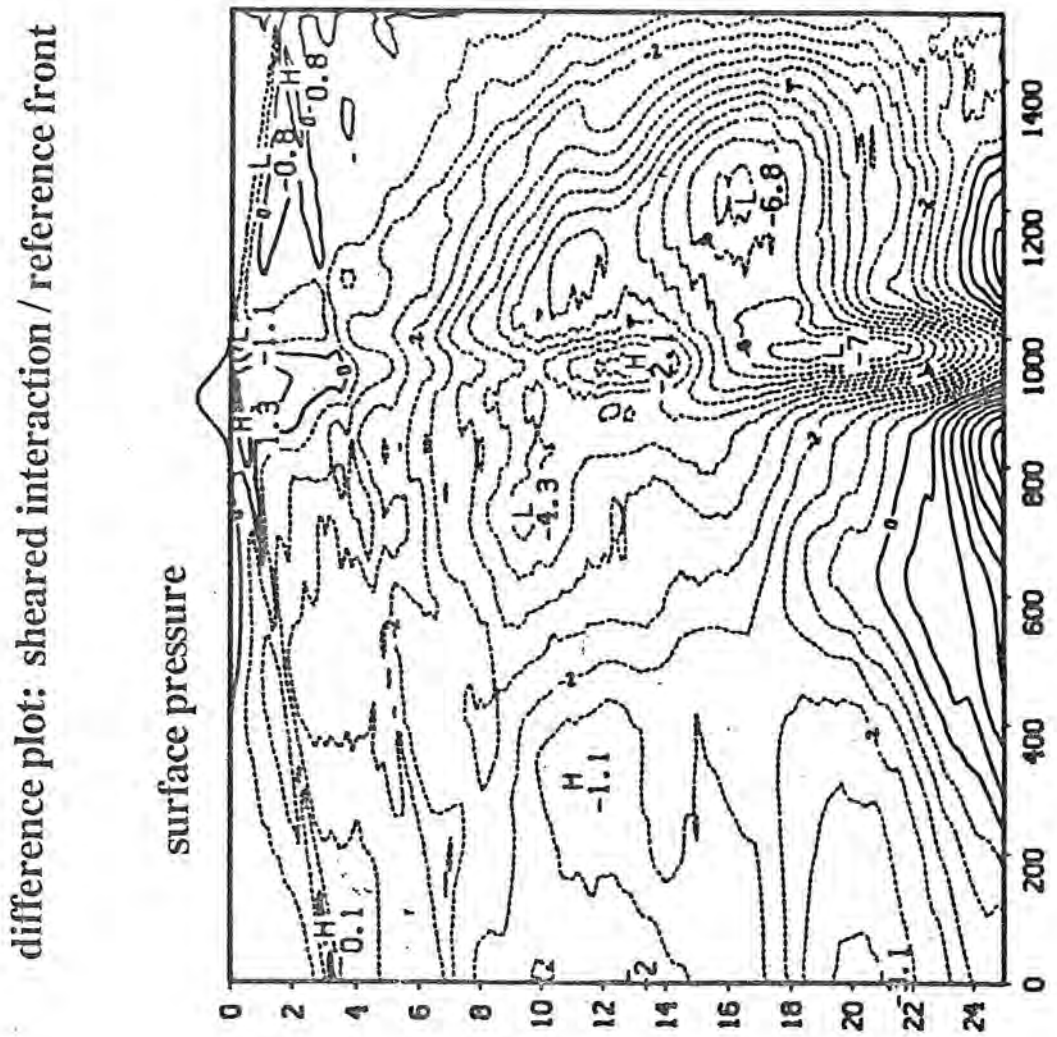

Figure V.12: same as V.11 but for the surface pressure shown in Fig. V.10 for the interaction with vertical shear.

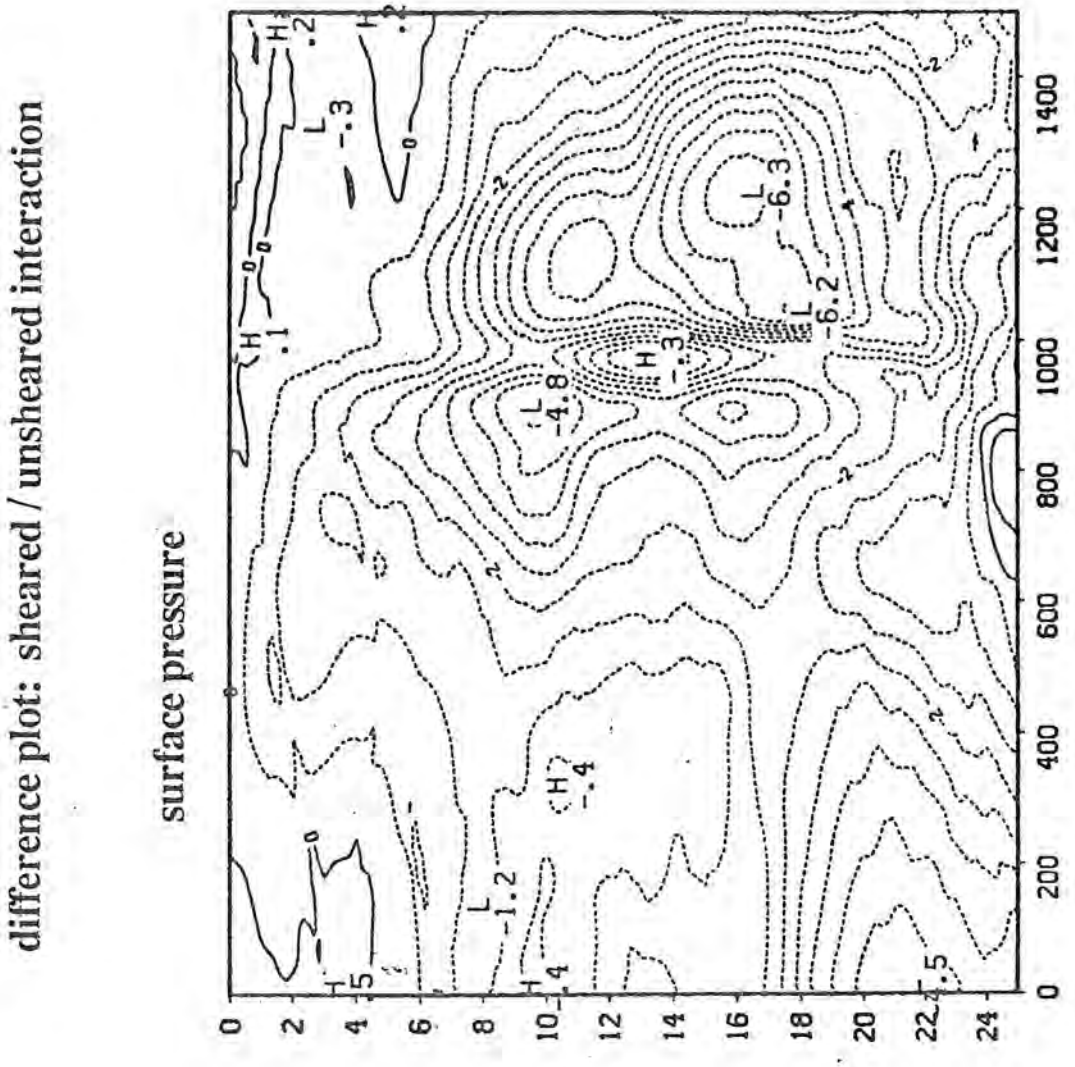

Figure V.13: Difference plot of the surface pressure in the interaction with and without shear (Fig. V.10 and V.9 respectively).

a) mountain only

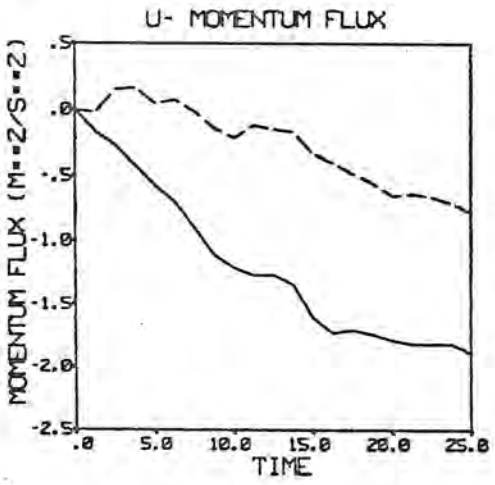

b) interaction without shear

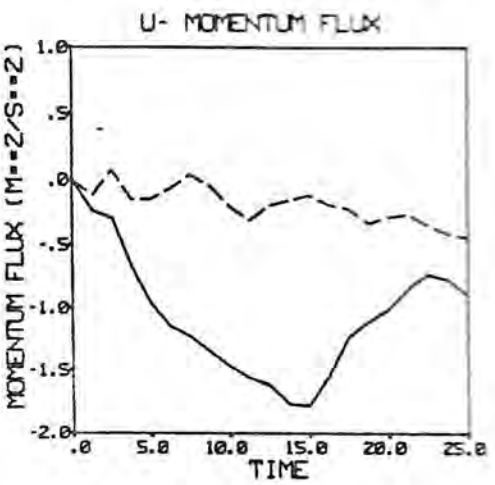

c) interaction with shear

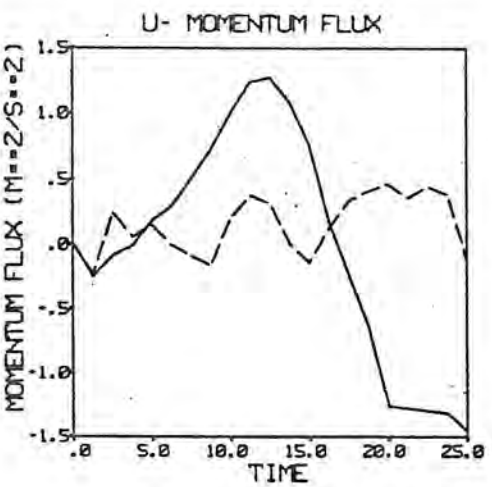

Figure V.14: Time evolution of the momentum flux for: a) the mountain alone, b) the interaction without shear and c) the interaction with shear. The solid line represents the momentum flux in the low troposphere (at 2500 m) and the dashed line in the upper troposphere (at 8000 m)

Conclusions:

In the first chapter the mountain pressure drag on the Alps has been computed every three hours for the two months of the Alpine Experiment (ALPEX) by using the high density network of stations reporting the surface pressure. Compared with previous global estimates, the pressure drag on this limited domain exhibits rapid fluctuations strongly correlated with synoptic events and peak values as large as the hemispheric annual average. The drag obtained here is in very good agreement with previous mesoscale studies and our values fall between the large values obtained from dense microbarograph data by Davies and Phillips (1985) in the central part of the Alps and the smaller values of Hafner and Smith (1985) obtained as in this study for the entire mountain with fewer stations. Peak drag values are found when tight pressure gradients are located above the steep orography and are therefore very sensitive to the analysis resolution: a change of resolution from 200 km to 50 km produces a change of 100 % in magnitude.

As in previous studies, the highest drag values observed during ALPEX occur during frontal passages which lead to cyclogenesis. To emphasize the similarities between these events a composite of the drag evolution for the frontal passage occurring in March is constructed. In this composite the drag first reaches a maximum in magnitude in an almost northerly direction, followed by a rapid rotation to south-easterly direction in which a second maximum is reached. In periods of quiet synoptic activity (in April) the drag time series reveals a clear diurnal cycle, also found in the microbarograph records by Davies and Phillips (1985), which might be related to north-south differences in the solar exposure.

The rapid changes and the large values of the drag provide a good test of the adequate representation of orography in numerical models and has been used here as an example on the simulation of the case of March 4 in ALPEX using a high resolution limited area model and the agreement is good in general.

During ALPEX, instrumented research aircraft provided high resolution data which have been used in Chapter II to estimate the momentum flux above the mountain. These fluxes are small compared with the surface drag (less than 0.5 Pa compared with up to 5 Pa), indicating that they do not play a dominant role in the momentum budget at the surface. These measured fluxes are also compared with those prescribed by the wave drag parameterization under development for the GFDL GCM. The parameterization requires local wind and stratifications which are obtained from aircraft soundings. The values are generally consistent with occasional discrepancies in situations of rapid evolution.

The major source of uncertainty in aircraft measurements comes from estimating the large scale vertical velocity and is discussed using the intercomparison flight between the different aircraft performed during ALPEX. The main conclusion is that contribution to the momentum flux on the scale of the mountain are not resolved by the aircraft and momentum flux results must be taken with caution.

In subsequent chapters (III to V) we have investigated the pressure drag evolution associated with the passage of a cold front from the mesoscale point of view. The observed features of the front -mountain interaction are first reviewed (Chapter III). The time-space evolution of surface pressure, recorded by microbarographs, shows that the pressure fall and rise associated with the front over flat land upstream of the mountain and seen by a fixed observer, is insufficient to account for the peak pressure drag when this pattern has moved over the topography. In other words the pressure drop across the mountain is larger than can be expected from the front alone. The effects of the mountain however, differs significantly from the classical situation of uniform flow across a ridge. For example in prefrontal conditions, when the cold front is still on the north side of the Alps and advected southward, the flow above the mountain top is westerly but the largest drag on the atmosphere is in the north-south direction. In these prefrontal conditions a shallow southerly foehn is also often observed. After the front has reached the mountain the cold air is blocked and temporarily

accumulated on the upstream side of the mountain. This phenomenon has been seen in series of cross sections through the front and by the comparison of low level temperature series on the north and south side of the mountain.

To complement the understanding gained from the observations, a simple layer model of the interaction has been investigated in Chapter IV both by using analytical and numerical methods. The simplicity of this model has allowed an extensive exploration of the different possible regimes of the interaction. In all situations the surface front is initially decelerated on the upstream side of the mountain but the subsequent behavior depends on the relative importance of inertia, stratification or Coriolis effects. For example if Coriolis or stratification effects are strong enough the surface front recovers, after passing over the mountain, the position it would have had without the mountain. The maximum frontal retardation is increased as the Rossby number of the problem is increased and as the Froude number is decreased, a behavior reminiscent of that of uniform flow over topography. Even in this very idealized model the evolution of the pressure drag is qualitatively similar to the observations. Although this model is deficient in simulating the prefrontal stage, the post frontal drag can be substantially increased to more realistic values if the cold air is blocked and remains on the upstream slope of the mountain. This happens in the regime $Ro > 1$ and $= O(1)$ which is the case for the Alps.

The additional effect of continuous stratification and secondary circulation on the interaction has been explored at in Chapter V using a continuously stratified numerical model. A series of six experiments illustrate the differences between cases with and without a mountain, a front or vertical shear in the cross frontal wind. For experiments with the mountain alone or the front alone, the vertical shear has only a small impact. During the interaction, however, the secondary frontal circulation induced by the vertical shear creates a region of reversed flow and weak stability ahead of the cold front which causes the mountain wave pattern to collapse. The model produces a very realistic drag evolution and provides us

with the evolution of surface pressure which compares also well with the observations. The presence of the secondary frontal circulation causes an increase in prefrontal drag and a prefrontal foehn similar to the observations. A discussion of momentum flux in the model has revealed the origin of the increase in pre-frontal drag and also explained some of the features of the observed fluxes.

Remaining questions

Although this study has focused on the contribution of the Alpine region to the global pressure force on the atmosphere, it has raised the important issue of large potential contributions of other mountain ranges.

In addition, the study has established a clear need, from both the theoretical and numerical modelling standpoint, for more reliable and more representative measurements of the momentum flux which cannot be obtained by current aircraft techniques.

Finally, a large number of questions related to the effect of the Alps remain unanswered, among which are the three dimensional effects of the mountain and the influence of surface friction.

Bibliography

Arakawa S., M. Okano, 1976: Numerical experiments on the deformation of cold frontal surfaces due to moutain ranges. J.Met.Res.(Japan) 28, 1-10

Bacmeister J.T., 1987: Non linearity in transient, two dimensional flow over topography. Ph.D. Thesis, Princeton University.

Baines P.G., 1980: The dynamics of the Southerly Buster. Austr.Met.Mag. 28:4, 175-200

Bannon P.R. , 1983: Quasi-geostrophic frontogenesis over topography. J.Atm.Sci. 20, 2266-2277

Bannon P.R. , 1984: A semi-geostrophic model of frontogenesis over topography. Contr.Atm.Phys. 57, 393-408

Bannon P.R. , 1985: Flow acceleration and mountain drag.. J.Atm.Sci. 42, 2445-2462

Bannon P.R. and J. A. Zehnder, 1985: Surface pressure and mountain drag for transient airflow over a mountain ridge. J.Atm.Sci. 42, 2454-2462

Barnes S.L., 1973. Mesoscale Objective Map Analysis using Weighted Time-Series Observations. NOAA Technical Memorandum. ERL-NSSL-62

Batchelor G.K., 1967. An Introduction to Fluid Dynamics. Cambridge University Press.

Bjerknes J. and H. Solberg, 1921: Meteorological conditions for the formation of rain. Geofys.Publik. 2 no 3, pp60

Boer G.J., N.A. McFarlane, R. Laprise, J.D. Henderson and J.P. Blanchet, 1984: The Canadian climate centre spectral atmospheric general circulation model. Atm.Ocean 22, 397-429

Buzzi A. , 1986. Review of the weather phenomena observed during the ALPEX Special Observing Period. (1)

Buzzi A. and S. Tibaldi, 1978: Cyclogenesis in the lee of the Alps: a case study. Quart.J.R.Met.Soc. 104, 271-287

Cox K.W., 1986. Analysis of the Pyrenees Lee Wave Event of 23 March 1982. Mon.Wea.Rev. 114, 1146-1166

Cressman G.P., 1960: An operational objective analysis system.. Mon.Wea.Rev. 87, 367-374

Davies H.C. , 1984: On the orographic retardation of a cold front. Contr.Atm.Phys. 57, 409-418

Davies H.C. , 1986: Diagnostic studies of meso-α scale flow on the Alpine north side (1)

Davies H.C. and P.D. Phillips.1985. Mountain Drag along the Gotthard Section during ALPEX. J.Atm.Sci. 42, 2093-2109

Eliassen A. and E. Palm, 1960: On the transfer of energy in stationary mountain waves. Geofys.Publik. 22, 1-23

Hafner T. and R.B. Smith, 1985: Pressure Drag on the European Alps in Relation to Synoptic Events. J.Atm.Sci. 42, 562-575

Hoinka K.P., 1980: Synoptic-scale atmospheric features and foehn. Contr.Atm.Phys. 53, 486-507

Hoinka K.P., 1984: Observations of a mountain-wave event over the Pyrenees. Tellus, 36A, 369-383

Hoinka K.P., 1985 a): Observation of the airflow over the Alps during a foehn event. Quart.J.R.Met.Soc. 111, 199-224

Hoinka K.P., 1985 b): On fronts in central Europe. Contr.Atm.Phys. 58, 560-571

Hoinka K.P., 1986: Observations of a mountain-wave event over the Pyrenees (corrigendum). Tellus 38A, 93-94

Houghton D.D. and A. Kasahara, 1968: Nonlinear shallow fluid flow over an isolated ridge. Comm.Pure Appl.Math. 21, 1-23

Houghton D.D., 1969: Effect of rotation on the formation of hydraulic jumps. J.Geophys.Res. 74, 1351-1360

Jones W.L., 1967: Propagation of internal gravity waves in fluids with shear flow and rotation. J.Fluid Mech. 30, 429-448

Kasahara A. and D. B. Rao, 1972: Instability of frontal motion in the atmosphere. J.Atm.Sci. 29, 1090-1108

Kasahara A. et.al., 1965: Numerical studies of frontal motion in the atmosphere-I. Tellus 17,261-275

Kennedy P.J. ,Ed., 1982: An ALPEX aircraft atlas. NCAR, pp226

Kennedy P.J. and D. Frey, 1983: ALPEX aircraft data documentation. NCAR, pp 88

Kuettner J.P., 1985 The aim and conduct of ALPEX (1)

LAPETH, 1986. Pressure reduction procedures used by countries participating in ALPEX. Technical note 8609, ETH, Zurich, Switzerland.

Lenshow D., 1982: Memo on present limitations of air motion measurements. Appendix in Kennedy and Frey, 1983.

Lilly D.K. , 1972: Wave momentum flux- A GARP problem. Bull.Am.Meteorol.Soc. 20, 17

Lilly D.K. , 1978: A severe downslope windstorm and aircraft turbulence event induced by a mountain wave. J.Atm.Sci. 35,59-77

Lilly D.K. and P.J. Kennedy, 1973: Observations of a stationnary mountain wave and its associated momentum flux and energy dissipation. J.Atm.Sci. 30, 1135-1152

McGinley J., 1982: A diagnosis of alpine lee-cyclogenesis. Mon.Wea.Rev. 110, 1271-1287

Mesinger F. and R.T. Pierrehumbert, 1985: Alpine lee cyclogenesis: numerical simulation and theory. ICSU-WMO

Orlanski I. , 1968: Instability of frontal waves. J.Atm.Sci. 25, 178-200

Orlanski I. , 1982: Orographically induced vortex centers. Joint U.S.-China Mountain Meteorology Symposium.

Orlanski I. and B. Ross, 1977: The circulation associated with a cold front. Part I : dry case. J.Atm.Sci. 34, 1619-1633

Palmer T.N., G.J. Shutts and R. Swinbank, 1986: Alleviation of a systematic westerly bias in general circulation and numerical weather prediction models through an orographic gravity wave drag parameterization.. Quart.J.R.Met.Soc. 112, 1001-1039

Peltier W.R. and T.L. Clark, 1979: The evolution and stability of finite amplitude mountain waves. Part II: Surface wave drag and severe downslope windstorms. J.Atm.Sci. 36, 1498-1529

Peltier W.R. and T.L. Clark, 1983: Non linear mountain waves in two and three spatial dimensions. Quart.J.R.Met.Soc. 109, 527-548

Pettersen S., 1941: Introduction to Meteorology. McGraw Hill, pp236

Pham H.L., 1985. The role of Alpine mountain representation in lee cyclogenesis simulations (1)

Pierrehumbert R.T. , 1984 a): Linear results on the barrier effect of mesoscale mountain. J.Atm.Sci. 41,1356-1367

Pierrehumbert R.T. , 1984 b): Orographic distortion of fronts. Rev.Met.Aeronaut. 44, 249-263

Pierrehumbert R.T. , 1985: Stratified semigeostrophic flow over two dimensional topography in an unbounded atmosphere. J.Atm.Sci. 42,523-526

Pierrehumbert R.T. , 1987. An essay on the parametrisation of orographic gravity wave drag. (to be published)

Pierrehumbert R.T. and B. Wyman, 1985: Upstream effects of mesoscale mountains. J.Atm.Sci. 42, 977-1003

Queney P., 1948: The problem of airflow over mountains: A summary of theoretical studies. Bull.Am.Meteorol.Soc. 29, 16-26

Richner H., 1985: The relative accuracy of ALPEX aircraft data. LAPETH-23, Zurich, pp 71

Richner H., 1986 . Analysis and quality of ALPEX data. (1)

Sielecki A., 1968: An energy-conserving difference scheme for the storm surge equations.. Mon.Wea.Rev. 96, 150-156

Sielecki A., 1970: The numerical integration of the nonlinear shallow-water equations with sloping boundaries.. J.Comp.Phys. 6, 219-236

Sinton D.M. and C.R. Mechoso, 1984: Non linear evolution of frontal waves. J.Atm.Sci. 41, 3501-3517

Smith R.B. , 1978: A measurement of mountain drag. J.Atm.Sci. 35, 1644-1654

Smith R.B. , 1979: The influence of the earth's rotation on mountain wave drag.. J.Atm.Sci. 36, 177-180

Smith R.B. , 1982: Synoptic observations and theory of orographically disturbed wind and pressure.. J.Atm.Sci. 29, 60-70

Smith R.B. , 1986. Mesoscale Mountain Meteorology in the Alps. (1)

Steinacker R., 1981. Analysis of the temperature and wind field in the Alpine region. Geophys.Astrophys. Fluid Dynamics 17, 51-62.

Stocker J.J., 1967: Water Waves. Willey-Interscience

Tibaldi S. , 1986: Weather regimes and mountain effects in general circulation models. (1)

Tibaldi S. and L. Dell'Osso, 1986. Representation of pressure drag effects in numerical modelling of Alpine cyclogenesis. (1)

Wahr J.M. and A.H. Oort, 1984. Friction and Mountain-Torque estimates from Global Atmospheric Data. J.Atm.Sci. 41, 190-204

Wallace J.M., S. Tibaldi and A. Simmons, 1983. Reduction of systematic forecast errors in the ECMWF model through the introduction of an envelope orography. Quart.J.R.Met.Soc. 109, 683-718

Wallace J.M. and P.V. Hobbs, 1977: Atmospheric Science: An Introductory Survey. Academic Press.

Williams R.T. and A.M. Hori, 1970: Formation of Hydraulic jumps in a rotating system. J.Geophys.Res. 75, 2813-2821

Zehnder J.A. , 1986: A numerical simulation of frontogenesis over a mountain ridge. Ph.D. Thesis, University of Chicago

(1) GARP Publication Series Nº 27. ICSU-WMO